SERVICIO GEOLÓGICO COLOMBIANO

ISSN: 0120-1425 • Junio de 2021

volumen 48
número 1

Boletín Geológico

https://revistas.sgc.gov.co/index.php/boletingeo

Boletín Geológico

Boletín Geológico
Vol. 48, n.º 1, 2021
Periodicidad semestral
ISSN impreso: 0120-1425
ISSN digital: 2711-1318
Servicio Geológico Colombiano

Oscar Paredes Zapata
Director general

Mario Andrés Cuéllar
Director de Geociencias Básicas

Marta Lucía Calvache Velasco
Directora de Geoamenazas

Gloria Prieto Rincón
Directora de Recursos Minerales

Hernán Olaya Dávila
Director de Asuntos Nucleares

Humberto Andrés Fuenzalida
Director de Hidrocarburos

Hernando Camargo
Director de Laboratorios

Victoria Díaz Acosta
Directora de Gestión de Información

Servicio Geológico Colombiano
Diagonal 53 N.º 34-53
Bogotá, Colombia
Teléfono: 220 0200, ext.: 3048
boletingeologico@sgc.gov.co

Mario Maya
Editor
Boletín Geológico

Comité editorial

Germán Alonso Bayona Chaparro
Coorporación Geológica Ares
Bogotá – Colombia

Matthias Bernet
Université Grenoble Alpes
Francia

Antoni Camprubí Cano
Universidad Nacional Autónoma de México
México

Iván Darío Correa Arango
Consultor
Medellín – Colombia

Thomas Heinrich Cramer
Universidad Nacional de Colombia
Bogotá – Colombia

Tobias Fischer
The University of New Mexico
Estados Unidos

Carlos Jaramillo
Instituto Smithsonian de Investigaciones Tropicales
Panamá

John Makario Londoño
Servicio Geológico Colombiano
Manizales - Colombia

María Isabel Marín Cerón
Universidad EAFIT
Medellín – Colombia

Camilo Montes Rodríguez
Universidad del Norte
Barranquilla - Colombia

Héctor Mora Páez
Servicio Geológico Colombiano
Manizales - Colombia

Natalia Pardo
Universidad de los Andes
Bogotá – Colombia

Germán A. Prieto
Universidad Nacional de Colombia
Bogotá – Colombia

Yamirka Rojas Agramonte
Universität Kiel
Alemania

Antonio Romero Hernández, *in memoriam*
Universidad Nacional de Colombia
Medellín – Colombia

John Jairo Sánchez
Universidad Nacional de Colombia
Medellín – Colombia

Luigi Solari
Universidad Nacional Autónoma de México
México

Carlos Augusto Zuluaga Castrillón
Universidad Nacional de Colombia
Bogotá – Colombia

Corrección de estilo en español
Édgar Ordóñez

Traducción y corrección de estilo en inglés
Peerwith

Diseño y diagramación
Leonardo Cuéllar V.

Diseño GIS
Cristian Hernández

Editora general
Carolina Hernández O.

Foto de cubierta
Fotomicrografía en sección delgada de sienita nefelínica, San José del Guaviare, Colombia. Foto por Amaya et al., figura 5a, este número.

Incluida en los siguientes índices y bases de datos:
Ulrich
REDIB
GeoRef
Periódica
Google Scholar

Página web:
https://revistas.sgc.gov.co/index.php/boletingeo

Esta obra está bajo licencia internacional Creative Commons Reconocimiento 4.0

Impresión
Imprenta Nacional de Colombia
Carrera 66 N.º 24-09
PBX: 457 8000
www.imprenta.gov.co
Bogotá, D. C., Colombia

Junio, 2021

Boletín Geológico

SERVICIO GEOLÓGICO COLOMBIANO

CONTENTS

Boletín Geológico

SERVICIO GEOLÓGICO COLOMBIANO

EDITORIAL

Boletín Geológico has published issue 48(1), June 2021, with articles on economic geology, structural geology, and basin evolution (Figure 1).

Arrubla & Silva characterize and classify the gold ore mineral occurrences related to the main intrusive centers of the El Cerro Igneous Complex: Cerro Frontino, Morrogacho and La Horqueta. Information about the distribution, ore mineralogy, structural geology, lithological patterns and gold mineral chemistry of the associated deposits is provided. The authors present the metallogenic characterization of the complex based on petrological and fieldwork data carried out in intrusive bodies and descriptions of the mineralogical, structural and hydrothermal features of gold mineralizations.

Amaya et al. present a lithological, petrographic, geochemical, and geochronological characterization of the San José de Guaviare Syenite (SJGS), unit exposed in an area with Precambrian plutonic igneous and metamorphic rocks, which belong to the crystalline basement of the NW Amazonian Craton. The SJGS consists of nepheline syenites, nepheline monzosyenites, nepheline-bearing alkali-feldspar syenites, syenites, quartz-syenites, quartz-alkali-feldspar syenites, syenogranites, and quartz-rich granitoids. The SJGS intrusion generated a thermal metamorphism, in amphibolite and pyroxene-hornfels facies, in the host rocks of the Guaviare Complex.

Forero et al. propose a methodology for the identification, mapping and analysis of the nature of faults and shear zones. They suggest to characterize structures and fault rocks, define the structural level observed, determine the movement's distribution and kinematics, and assign the relative and absolute ages of deformation, in order to propose some minimum parameters necessary to perform geological-structural studies for acquiring basic information that aids understanding of the tectonic evolution.

López et al. propose a scheme for recording data acquired in the field in a table, which enables sorting by type of fabric element (planar or linear), and the recording of the lineaments always in front of the plane that contains them. In addition, the recording scheme includes data corresponding to the kinematics or direction of movement of faults and shear zones, the indicators that support the kinematics, and a qualitative assessment of the certainty or reliability of the kinematics assigned to the direction of shear zone movement.

Rosello et al. propose a working hypothesis that will generate interest in promoting exploration activities and basic research to confirm or reject a new hydrogeological potential located at greater depths and beneath the structure commonly known as the Puelches aquifer, Argentina.

Figure 1. Location of the areas with contributions presented in *Boletín Geológico*, issue 48(1), 2021.

Boletín Geológico acknowledges the collaboration of the following reviewers and their commitment to the peer-review process involved in this issue:

Umberto Cordani - Universidade de São Paulo, Brazil.
Salomon Kroonenberg - Delft University of Technology, The Netherlands.
Maria Helena Bezerra de Hollanda - Universidade de São Paulo, Brazil.
Uwe Martens - Universidad Nacional Autónoma de México, México.
Eduardo Kruse - Universidad Nacional de La Plata, Argentina.
José Duque Trujillo - Universidad EAFIT, Colombia.
Hernán Barcelona - Universidad de Buenos Aires, Argentina.
Ethel Morales - Universidad de la República, Uruguay.

Marcos Roberto Pinheiro - Universidade de São Paulo, Brazil.
Bruno Vieira Ribeiro - Monash University, Australia.
Carlos Mario Echeverri - Universidade Federal de Campina Grande, Brazil.
Paola Botero Santa - Universidad Nacional Autónoma de México, México.
Orlando Hernández - Universidad Nacional de Colombia, Colombia.
Leonardo Mairink Barão - Universidade Federal do Paraná, Brazil.
Guillermo Camargo - Universidad Nacional de Colombia, Colombia.
Diego Gómez - Universidad EAFIT, Colombia.

Mario Maya
Editor
mmaya@sgc.gov.co
boletingeologico@sgc.gov.co

Boletín Geológico

SERVICIO GEOLÓGICO COLOMBIANO

NOTA DEL EDITOR

In Memoriam: Profesor Antonio Romero Hernández (1954-2021)

Antonio Romero obtuvo su grado de Ingeniero de Minas y Metalurgia en la Facultad de Minas de la Universidad Nacional de Colombia, Medellín, y especialista y doctor de Materias Primas y Energía en la École Nationale Superieure de Géologie, Nancy, Francia.

El profesor Romero enseñó con gran dedicación en la Facultad de Minas de la Universidad Nacional de Colombia donde dirigió un número muy importante de proyectos de grado y posgrado, creó grupos de investigación y contribuyó con una gran cantidad de informes y documentos sobre minería y metalurgia, con énfasis en su impacto tecnológico, social e industrial.

Antonio Romero estuvo al frente de cargos de alta responsabilidad en el Servicio Geológico Colombiano, antes Ingeominas, y fue miembro del Comité Editorial de la revista científica *Boletín Geológico*. Además, fue fundador y director de varias instituciones académicas e industriales y estuvo involucrado en la organización de eventos del sector minero.

En nombre de los comités editoriales del Servicio Geológico Colombiano y del *Boletín Geológico*, enviamos nuestras sinceras condolencias a sus familiares y amigos.

Mario Maya
Editor

EDITOR'S NOTE

In Memoriam: Professor Antonio Romero Hernández (1954-2021)

Antonio Romero obtained his bachelor's degree in Mining and Metallurgy Engineering from the *Facultad de Minas* of the Universidad Nacional de Colombia, Medellín, before going on to complete his postgraduate certificate and PhD. in Raw Materials and Energy from the École Nationale Superieure de Géologie, Nancy, France.

Professor Romero taught with great dedication at the *Facultad de Minas* of the Universidad Nacional de Colombia where he supervised a very significant number of undergraduate and graduate projects, created research groups, and contributed a large number of reports and documents on mining and metallurgy with emphasis on its technological, social and industrial impact.

Antonio Romero was in charge of positions of high responsibility in the Servicio Geológico Colombiano, formerly Ingeominas, and was a member of the Editorial Committee of the journal *Boletín Geológico*. In addition, he was the founder and director of several academic and industrial institutions and was involved in the organization of events in the mining sector.

On behalf of the editorial committees of the Servicio Geológico Colombiano and *Boletín Geológico*, we send our sincere condolences to his family and friends.

Mario Maya
Editor

Boletín Geológico

SERVICIO GEOLÓGICO COLOMBIANO

Boletín Geológico, 48(1), 7-47, 2021
https://doi.org/10.32685/0120-1425/bol.geol.48.1.2021.500

© Author(s) 2020. This work is distributed under the Creative Commons Attribution 4.0 License.

Received: May 15, 2020

Revised: July 4, 2020

Accepted: December 17, 2020

Published online: July 12, 2021

Geology of the Frontino-Morrogacho Gold Mining District and metallogeny of the El Cerro Igneous Complex

Geología del Distrito minero aurífero Frontino-Morrogacho y metalogenia del Complejo Ígneo El Cerro

Felipe **Arrubla-Arango**[1] and Sergio **Silva-Sánchez**[2]

1 Consultant, Bogotá, Colombia
2 Ingetec SAS, Bogotá, Colombia
Corresponding author: Sergio Silva-Sánchez, se.silva11@uniandes.edu.co; Felipe Arrubla-Arango, f.arrubla10@uniandes.edu.co

Abstract

The Frontino-Morrogacho gold district is located on the western flank of the Western Cordillera, NW of Antioquia Province. Gold mineralizations in the area are spatially and genetically associated with the cooling of three mid- to late-Miocene age intrusive centers in the form of stocks and dikes (12-9 Ma): Cerro Frontino, La Horqueta and Morrogacho (El Cerro Igneous Complex). These composite magmatic pulses, with ultramafic to intermediate compositions, vary into diorite-, gabbro- and monzonitic-bearing phases. Mineralization in the complex is present as several structurally controlled fault veins, shear-related veins, sheeted quartz extension veins and quartz-carbonate tabular extension veins, with the development of swarms and nests of veins-veinlets, breccias and stockworks. Structures range from centimeter-wide individual veinlets to several meter-wide swarms of veins developed within broad mineralized structural corridors, with a metallic signature that consists of Au + Ag + Cu + Zn + Pb + As (± Te ± Bi ± Sb ± Hg ± W) assemblages. Veins are composed of multiple stages of mineralization, and the formation of these structures is enhanced by the presence of a local regime of extension and E-trending structures, including evidence of faults and shear zones with right-lateral displacement, which are likely involved in pluton emplacement and cooling. The ore mineralogy is composed of pyrrhotite, pyrite, chalcopyrite, sphalerite, galena and arsenopyrite assemblages formed in two or more mineralization stages, with complex Bi, Te, Sb and Hg mineral specimens associated with Au and Ag. Mineralized structures of the district present a preferential E-strike with dominant vertical to subvertical and occasional subhorizontal S-dips and secondary N- and NW-strikes that are steep to vertically E-dipping.

The Frontino-Morrogacho Gold district presents characteristics related to the architecture, mineralogy and alteration of reduced (ilmenite-series) intrusion-related gold systems but is genetically associated with a parental oxidized magma source. The gold content is associated with three different families involving electrum, tellurides and alloys: gold rich (66 to 78% Au, 22 to 34% Ag),

Citation: Arrubla-Arango, F., & Silva-Sánchez, S. (2021). Geology of the Frontino-Morrogacho Gold Mining District and metallogeny of the El Cerro Igneous Complex. *Boletín Geológico, 48*(1), 7-47. https://doi.org/10.32685/0120-1425/bol.geol.48.1.2021.500

average (50 to 60% Au, 40 to 50% Ag) and silver rich (32 to 40% Au, 60 to 68% Ag). The formation of these bodies is associated with an N-S magmatic-metallogenic trend of Au-Ag-Cu deposits, which extend for more than 300 km along the Western Cordillera of Colombia. Similar plutonic suites span from the south of Chocó Province to the north of Antioquia Province, which indicates that the Frontino-Farallones-Botón arc can be proposed as an individual metallogenic belt.

Keywords: Frontino-Morrogacho gold district, intrusion-related gold System, late mid-Miocene suite of intrusions, metallogeny of the Western Cordillera, metallogenic belt.

Resumen

El Distrito minero Frontino-Morrogacho se localiza en el flanco occidental de la Cordillera Occidental, al NW del departamento de Antioquia. Las mineralizaciones de oro en la zona están espacial y genéticamente asociadas con tres cuerpos intrusivos de edad Mioceno (9-12 Ma) medio a tardío en forma de *stocks* y diques: Cerro Frontino, La Horqueta y Morrogacho (El Complejo Ígneo El Cerro). Corresponden a pulsos magmáticos compuestos con composiciones ultramáficas a intermedias que varían entre dioritas, gabros y fases monzoníticas. Las mineralizaciones en el complejo están presentes como estructuras vetiformes estructuralmente controladas y representadas por vetas de falla, vetas relacionas con zonas de cizalla, vetas laminadas de extensión de cuarzo y vetas de extensión tabulares cuarzo carbonatadas con el desarrollo de nidos de vetas, zonas de brecha y *stockworks*. El espesor de las estructuras varía entre venillas individuales centimétricas a vetas que forman nidos, rejillas y enjambres en corredores estructurales multimétricos, poseen una asignatura metálica compuesta por Au + Ag + Cu + Zn + Pb + As (± Te ± Bi ± Sb ± Hg ± W). Las vetas fueron formadas por diferentes estadios de mineralización. La formación de estas estructuras se encuentra favorecida por la presencia de sistemas locales de extensión y por la presencia de estructuras orientadas hacia el E-, incluyendo la evidencia de zonas de cizalla con desplazamiento lateral-derecho, que están aparentemente relacionadas con el emplazamiento y enfriamiento de los plutones. La mineralogía de la mena en los depósitos está compuesta por pirrotina, pirita, calcopirita, esfalerita, galena y arsenopirita formada en al menos dos estadios de mineralización, con especies minerales de Au, Ag, Bi, Te, Sb y Hg asociados a Au y Ag. Las estructuras mineralizadas del distrito presentan una dirección preferencial de rumbo hacia el E- con buzamientos dominantes hacia el S, sub-verticales y ocasionalmente sub-horizontales, con rumbos secundarios hacia el N- y NW-, buzando verticalmente hacia el E-.

El Distrito minero Frontino-Morrogacho presenta algunas características relacionadas con la arquitectura, mineralogía y alteración de los *Reduced (ilmenite-series) Intrusion-related Gold Systems*, pero están asociados genéticamente con magmas parentales oxidados. El contenido de oro es reconocido en tres distintas familias que involucran *electrum* y teluros: rica en oro (66-78% Au, 22-34% Ag), promedio (50-60% Au, 40-50% Ag) y ricos en plata (32-40% Au, 60-68% Ag). La formación de estos cuerpos está asociada con un cinturón magmático-metalogénico con dirección N-S de depósitos de Au-Ag-Cu, que se extiende por más de 300 km a lo largo de la Cordillera Occidental de Colombia. Complejos de intrusivos similares abarcan desde el sur en el departamento del Chocó hasta el norte en el departamento de Antioquia, evidencia que permite asumir que el arco Frontino-Farallones-Botón puede ser propuesto como un cinturón metalogénico individual.

Palabras clave: Distrito minero aurífero Frontino-Morrogacho, *Intrusion-related Gold System*, intrusiones del Mioceno medio a tardío, Metalogenia de la Cordillera Occidental, cinturón metalogénico.

1. Introduction

In Colombia, the Miocene represents a period of widespread continental subduction-related magmatism, which is represented in the Central and Western Cordilleras. The axis of the magmatism has migrated geographically over the last 20 Ma in both N-S and E-W directions (Leal-Mejía, 2011). The movement of this magmatic arc has developed different arc-related metallogenic belts that have been partially identified. However, this period spanning the last 20 Ma to 30 Ma corresponds to the deposition of the largest gold ore reserves in the country and some of the most explored and studied mineral deposit targets (Shaw et al., 2019).

Previous studies of the Western Cordillera in Colombia have identified a mid- to late-Miocene magmatic arc related to the approximation of the Baudó terrane to the northern Andean

block (Zuluaga and Hoyos, 1978; Cediel and Shaw, 2003; Zapata and Rodríguez, 2011; Rodríguez and Zapata, 2012; Rodríguez and Arango, 2013; Rodríguez-García and Bermúdez-Cordero, 2015; Silva-Sánchez, 2018; Arrubla, 2018; Leal-Mejía et al., 2019; Shaw et al., 2019). In this collision, the Frontino-Botón arc was formed with the additional intrusion of different magmatic bodies on the western flank of the Western Cordillera, NW of Antioquia Province (Rodríguez and Zapata, 2012). Most of these plutons present a shoshonitic to calc-alkaline geochemical signature with medium to high K contents related to a volcanic arc geological setting. The El Cerro Igneous Complex is part of this Miocene arc, and it is associated with individual stocks and dikes and their thermal contact aureole, including Cerro Frontino, Morrogacho, and La Horqueta stocks (Shaw et al., 2019).

The Frontino-Botón arc is represented by the El Botón Volcanic Complex and a suite of mid- to late-Miocene mafic to intermediate plutons. The intrusive bodies were emplaced in the Cañasgordas-Penderisco sedimentary block and occasionally in the El Botón Basalts Volcanic Complex. These intrusives occur as circular-semicircular and N-S elongated stocks, usually isolated, with satellite bodies in the form of apophyses and dikes of different sizes, and they span radially from intrusive centers, such as Perdidas stock, Carauta stock, La Horqueta Monzodiorite stock and Cerro Frontino and Morrogacho stocks (Mejía and Salazar, 1989; González and Londoño, 2002; Buchely et al., 2009; Rodríguez and Zapata, 2012). The cooling history of these plutons is associated with various styles of gold-silver mineralization, with an extensive metamorphic thermal aureole in the surrounding sedimentary rocks. An initial stage of mineralization is related to gold-diopside-garnet-scheelite skarn deposits, and a later stage is related to exsolved fluids that circulated in shear and extensional-dilational zones within the intrusions and wall rocks, thus developing high-grade, structurally controlled, vein-type Au-Ag-Cu-Pb-Zn-As-Mo mineralizations (Escobar and Tejada, 1992; Rodríguez-García and Bermúdez-Cordero, 2015; Shaw et al., 2019). However, Au mineralizations related to the El Cerro Igneous Complex have not been studied in detail. In the present study, these mineralizations related to the El Cerro Igneous Complex are considered to compose the Frontino-Morrogacho district.

The Frontino-Morrogacho district has been exploited for more than 200 years by artisanal miners for lode and alluvial gold. The first semitechnical exploitation was carried out in 1852 when the companies Frontino and Bolivia Gold Mines acquired the San Diego Mine from a local society of miners who discovered the main gold lode of the El Cerro deposit in 1812. During recent decades, lode gold deposits in the region have been intermittently mined in hundreds of underground workings focused in the northern part of the El Cerro Frontino stock, the San Diego-Cuadrazón-Las Hebras mine and the Popales-Morrogacho area.

The term intrusion-related gold system (IRGS) broadly refers to a group of gold deposits that have intimate spatial and temporal relationships with the cooling history of plutonic intrusive centers with volatile-rich magmas (Lang and Baker, 2001; Hart, 2007). These deposits exhibit certain styles of mineralization, such as skarns, replacement mantos, veins and disseminations that are focused in the apex and brittle carapace of small and isolated cylindrically shaped plutons, which are mainly characterized by the presence of arrays of auriferous sheeted quartz veins (Hart, 2007). The tectonic setting of the IRGS involves convergent continental margins with back arc, collisional, postcollisional and magmatic arcs in orogenic belts, which are usually emplaced in sedimentary and metasedimentary country rocks (Goldfarb et al., 2000). The metallic signature involves Au-Te-Bi-Sb-W content in the mineralogy (Hart, 2007), whereas the metallogeny of source plutons is controlled by the associated magma's oxidation state and the degree of fractionation (Ishihara, 1981), which is why the term reduced intrusion-related gold system (RIRGS) was recently established (Hart, 2007).

The present study aims to characterize and classify the gold ore mineral occurrences related to the main intrusive centers of the El Cerro Igneous Complex: Cerro Frontino, Morrogacho and La Horqueta stocks. In particular, information about the distribution, ore mineralogy, structural geology, lithological patterns and gold mineral chemistry of the associated deposits is provided. This paper presents the metallogenic characterization of the complex based on petrological and fieldwork data carried out in intrusive bodies and descriptions of the mineralogical, structural and hydrothermal features of gold mineralizations. It complements the regional and ore deposit geology information on the mid- to late-Miocene magmatic arc segment in the Colombian Western Cordillera, particularly the metallogeny of gold mineralizations hosted and associated with mid- to late-Miocene intrusive bodies.

2. Method

The geological features of the El Cerro Igneous Complex were obtained based on a core fieldwork campaign that consisted

of mapping and sampling through the intrusives and mineralized structures of the study area. Moreover, the present research provides data for the regional characterization of the El Cerro-Farallones Au (Ag, Cu), including the Carauta, Cerro Frontino, Morrogacho, La Horqueta, San Juan stocks and the peripheral parts of the Páramo de Frontino stock. The mineralized structures and mines that have been studied and sampled include Los Chavos, Los Hoyos, El Apique, La Loaiza, Musinga and La Palma N and NW of the El Cerro Frontino stock. Additionally, other mineralized structures were studied and sampled, including Quebrada La Mina and La Trinidad structures in the Carauta stock; El Socorro and Las Camelias in La Horqueta stock; El Mocho, San Donato, El Silencio, La Cascada and Tajo Abierto in the Morrogacho stock; and Media Cuesta, El Duque, La Petaca, and Pizarro, north of Morrogacho stock. However, the results presented here focus on the most relevant mineralized structures and mineralization styles of the El Cerro Igneous Complex: El Apique and Los Hoyos in the El Cerro Frontino stock, Tajo Abierto and La Cascada in Morrogacho stock, and Las Camelias in La Horqueta stock. The main mineralized structures were studied in terms of the structural attitude, alteration, mineralization and distribution to define the magmatic-hydrothermal and genetic processes related to the gold genesis of the Frontino-Morrogacho gold district.

The second stage of the study corresponds to the petrography of the intrusive bodies and mineralization, including the different pulses differentiated in each case. Samples of intrusive bodies were classified according to the nomenclature of plutonic rocks from the IUGS Subcommission (International Union Geological Sciences) on the Systematics of Igneous Rocks (Streckeisen, 1974). Furthermore, the ore and gangue mineralogy, textures, and hydrothermal features were described for each mineralized structure according to the petrographic analysis. This information was complemented with mineral chemistry analyses on selected ore samples by SEM-EDS at the Microscopy Center of Universidad de los Andes. These analyses were carried out to determine and identify the metallic signature of the deposits and the native gold and electrum grain characteristics, including the fineness, size, and mineral association.

Finally, the results are discussed and complemented with geochemical analyses taken from previous studies carried out in the El Cerro Igneous Complex (Rodríguez and Zapata, 2012; Rodríguez-García and Bermúdez-Cordero, 2015). The geochemical data reinterpreted in the present study permitted to characterize the genesis and evolution of the complex.

3. Tectonic framework related to the El Cerro Igneous Complex

The evolution of the Northern Andes Block records a complex geological history associated with the accretion of different tectonic blocks (Figure 1) (Cediel and Shaw, 2003). Therefore, the lithological, structural and geomorphological characteristics of the northern Andes are mainly the result of the processes that occurred during the Mesozoic-Cenozoic orogeny, which are responsible for the features that are currently found in the Western Cordillera, where the Frontino-Morrogacho gold district is located. The geological setting of the study area is related to the Choco arc (Cediel and Shaw, 2003), which is the eastern segment of the Panamá Double arc and consists of the Cañasgordas and Baudó terranes (Etayo-Serna et al., 1983; Duque-Caro, 1990).

The evolution of the northern Andes in the study area presents characteristics related to a highly oblique convergence, where collisions of the Gorgona, Cañasgordas and Baudó terranes took place (Cediel and Shaw, 2003). As the collision of the Panamá-Chocó Terrane ended in the middle Miocene, arc magmatism developed in the middle to late Miocene as a response to the subduction of the Nazca Plate and the accretion of the Baudó Terrane (Cediel and Shaw, 2003). Early stages of this magmatic event are recorded in the intrusion of calc-alkaline bodies along the Cañasgordas terrane, such as the Mistrató-Farallones Batholiths and El Cerro Frontino stock, which mark erratic subduction-related magmatism due to the early approximation of the Baudó terrane at 11 Ma-12 Ma (Maya, 1992; Cediel and Shaw, 2003). These intrusives correspond to the northern calc-alkaline granitoid arc segment associated with Miocene subduction along the Colombian trench and the Farallones-El Cerro-Dabeiba holocrystalline suite (Leal-Mejía, 2011; Leal-Mejía et al., 2019; Shaw et al., 2019).

The result of the accretion of the Panamá-Chocó block is recognized in an N-S trend of monzonitic to granodioritic plutons in the form of isolated batholiths and stocks, from the Torrá and Farallones Batholiths in the south to the Nudillales monzonitic stock located north of Dabeiba, Antioquia Province. The late- to mid-Miocene plutons are commonly found in very steep isolated areas with rugged morphologies that dominate the landscape, with some of them commonly reaching more than 3000 m in altitude. Geomorphological characteristics and prior studies of the Western Cordillera suggest that the

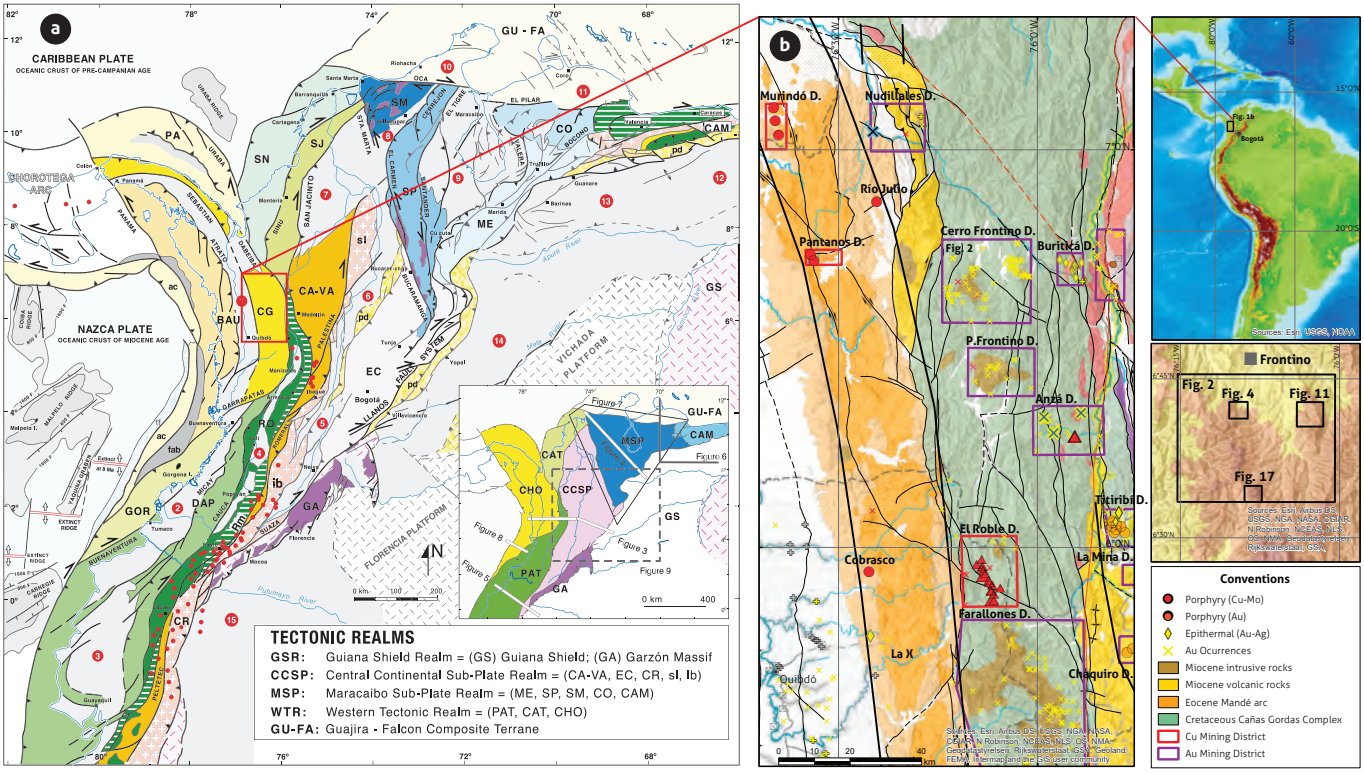

Figure 1. a) Geological terranes of the northern Andes segment (Cediel and Shaw, 2003). b) Geological and metallogenic map of the northern segment, Western Cordillera, with the location of the Frontino-Morrogacho gold district
Modified from Leal-Mejía et al. (2016).

uplift and exhumation of tectonic blocks that host the Miocene intrusives allowed for a higher rate of erosion and surface exposure (Villagómez and Spikings, 2013). Most of these igneous bodies are found intruding the Cañasgordas basement, such as El Cerro Frontino, La Horqueta and Morrogacho stocks, which make up the El Cerro Igneous Complex (Shaw et al., 2019). The intrusion of the El Cerro Igneous Complex developed gold mineralizations that conform to the Frontino-Morrogacho gold district.

After the El Cerro Igneous Complex plutonic event ceased, magmatism shifted eastwards at approximately 8 Ma towards the axis of the Cauca River canyon in the form of shallower porphyritic stocks that are associated with ore deposit genesis in the Middle Cauca Metallogenic Belt, which is the most prolific gold belt in Colombia. The migration of magmatism to the middle Cauca valley is attributed to the progressive shallowing of the subduction angle due to trench clogging by the presence of the subducting Sandra Ridge, which is a buoyant aseismic material (Leal-Mejía et al., 2019). Here, the intrusion of metal fertile plutons led to the genesis of different mineral deposits as well as the migration of hydrothermal fluids associated with epithermal-type deposits. This belt is located along the margin of the Cauca-Romeral fault zone and hosts late Miocene-Pliocene (6-8 Ma) porphyry-related Au-Ag and base metal deposits spanning more than 20 Moz for gold (Maya, 1992), such as La Colosa, Buriticá, Marmato, Miraflores and Nuevo Chaquiro (Gil-Rodríguez, 2010; Leal-Mejía, 2011; Lesage et al., 2013; Bartos et al., 2017).

4. Geological setting

The Frontino-Morrogacho gold district is located along the Cretaceous Cañasgordas complex and associated with the intrusion of El Cerro Frontino, La Horqueta and Morrogacho stocks in the mid- to late-Miocene (Leal-Mejía, 2011; Leal-Mejía et al., 2019; Shaw et al., 2019) (Figure 2). The Cañasgordas complex consists of two different formations: the volcanic sequence of the Barroso Formation and the sedimentary Pende-

risco Formation. The Barroso Formation consists of basaltic and andesitic lava flows with porphyritic and amygdaloidal textures formed in a volcanic arc environment with ages ranging between 85 Ma and 115 Ma and interbedded with tuffs and sedimentary layers (Álvarez and González, 1978; Rodríguez et al., 2016). The Barroso Formation displays two principal geochemical trends within a continuous tendency: one associated with P-MORB (Plateau) and another associated with N-MORB (destructive margins, i.e., subduction) (Geoestudios, 2005).

The Penderisco Formation is divided into two sedimentary members with different lithological characteristics and geographical positions: the Urrao member and Nutibara member (González and Londoño, 2002). The Urrao member is compo-

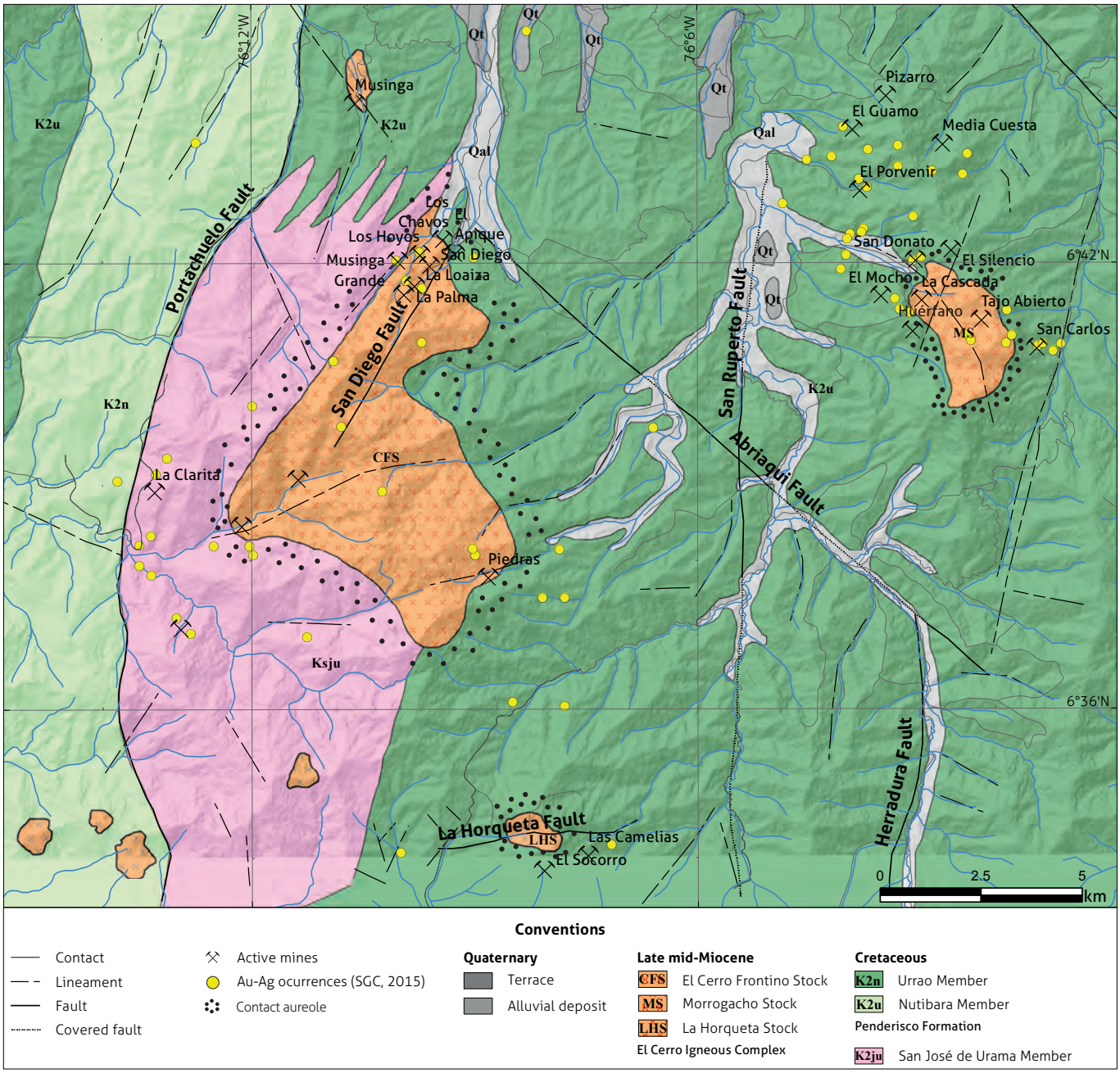

Figure 2. Regional geology of the El Cerro Igneous Complex Modified from González and Londoño (2002).

sed of a sequence of distal and proximal turbidites represented by conglomerates, wackes, lithic sandstones, shale, siltstones and siliceous mudstones. Nutibara members include pelagic and calcareous sedimentary rocks, fine-grained limestones and cherts (Álvarez and González, 1978). The Penderisco Formation was intruded by different Miocene plutons, thus causing contact metamorphism. Therefore, hundreds of meters of wall rocks adjacent to intrusions are commonly found as hornfels in the facies of pyroxene-hornblende-biotite-albite (Álvarez and González, 1978; Rodríguez-García and Bermúdez-Cordero, 2015).

Skarn mineralizations are found in selected areas, where thick calcareous wall rock strata of the Nutibara member were intruded by dioritic pulses, such as the La Loaiza gold-diopside-garnet skarn, which is located in the apex of the El Cerro Frontino stock (Molina and Molina, 1984). La Loaiza skarn is possibly linked genetically and spatially to gold-diopside-garnet skarn mineralization inside the San Diego Mine.

The El Cerro Igneous Complex corresponds to the mid- to late Miocene plutonic suite dated by the K/Ar and Ar/Ar methods in magmatic hornblende and biotite in the range of 12 Ma-10 Ma (Mid-Miocene); however, it has been related to a maximum age of mineralization of 11.8 Ma (Leal-Mejía, 2011; Rodríguez and Zapata, 2012; Shaw et al., 2019). This complex presents a general N-S to NNW-SSE orientation and is associated with Frontino-Botón volcanic arc activity.

The El Cerro Frontino stock has been related to different compositional facies due to the intrusion of more than one pulse and the presence of satellite stocks with areas less than 1 km^2 and ages of 11.8 ± 0.4 Ma (K/Ar) (Leal-Mejía, 2011), 9.87 ± 0.18 Ma and 11.44 ± 0.36 Ma (Ar/Ar) (Rodríguez-García and Bermúdez-Cordero, 2015). Cerro Frontino Monzonite is described by Alvarez and González (1978) as an intrusion of 40 km^2 with equigranular, phaneritic texture, medium grain size, high content of pyrite filling fractures and two main facies: felsic and mafic. The mafic pulse is associated with mineralization processes in the fractures; furthermore, modal classification shows a compositional variation between monzonite and pyroxene diorite.

Rodríguez-García and Bermúdez-Cordero (2015) renamed the pluton to Cerro Frontino Gabbro and described at least three magmatic pulses in a short period of time: (i) an initial facies of gabbros and pyroxenites that is present as xenoliths, (ii) a second and larger facies of gabbros and diorites with variations to pyroxenites and (iii) a final facies of monzonites that intruded the previous pulses. Geochemical data suggest the contribution of a subduction component in magma to the genesis, and this contribution is related to a magmatic arc environment (Rodríguez-García and Bermúdez-Cordero, 2015; Shaw et al., 2019). Evolution started with tholeiitic affinity and ended with alkali enrichment with a shoshonitic geochemical signature. In the San Diego mine, intrusive phases have been described as pyroxenites, pyroxene gabbros and melanodiorites cut by minor auriferous pegmatite dikes containing clinopyroxene, hornblende, biotite and plagioclase crystals (Shaw et al., 2019). Wall rocks show high to low contact metamorphism and are commonly found as hornfels of albite-epidote to pyroxene facies (Álvarez and González, 1978). The closure age of amphiboles in the hornfels indicates that the intrusion was prior to 12.2 ± 4.6 Ma (Rodríguez-García and Bermúdez-Cordero, 2015).

Morrogacho diorite is an elongated and rectangular-shaped stock of approximately 6 km^2 (Álvarez and González, 1978). This intrusion is related to the crystallization of fine- to medium-grained phaneritic equigranular diorites in a single phase with important textural and compositional differences (Álvarez and González, 1978). Wall rocks around the stock are commonly found as hornfels of hornblende and albite facies (Álvarez and González, 1978).

La Horqueta Monzodiorite outcrops in a very prominent hill that has the same name and occurs as a circular-shaped stock spanning approximately 1.2 km^2 (Álvarez and González, 1978). It has been described as a monzonite to pyroxene diorite with a locally high content of biotite related to late hydrothermal K-metasomatic processes without the presence of satellite igneous bodies (Álvarez and González, 1978). Wall rocks around the stock occur as hornfels of albite-epidote facies with a contact aureole of 100 m-200 m width (González and Londoño, 2002). According to Rodríguez and Zapata (2012), La Horqueta and Morrogacho stocks present a hipidiomorphic texture with a mineral assemblage of Pl + Cpx + Opx + Bt ± Or ± Qz and Pl + Cpx + Bt ± Opx ± Ol, respectively.

The Cañasgordas Complex (Penderisco Formation) is highly deformed with the presence of faults and folds that are controlled with a clear morphologic expression (Álvarez and González, 1978; Page, 1986), mainly with a N-S to NW-SE strike. Structurally, the Penderisco Formation in the Farallones-El Cerro area is limited by a set of major terrane boundary faults, which are the Garrapatas-Dabeiba transform fault to the south and east and the Uramita Fault zone to the west.

The most relevant structure in the El Cerro Igneous Complex is the N-striking San Diego Fault (Figure 2) due to its relation with the mineralization processes at the San Diego-La Cuadrazón mine. However, several other preferentially E- and secondary N- and NW-striking mineralized corridors involving fault veins and shear-related structures are commonly found in the district. These structures are considered important for focusing fluid in structurally prepared wall rocks, which also influenced dilatational cooling of extensional structures within the plutonic suites (Hart, 2007). Furthermore, various pre- and postmineral dominantly N-striking fault structures have been described in the area, such as La Herradura, San Ruperto, San Juan-Portachuelo, La Encarnación and Río Verde (Noriega et al., 2012). These structures are affected and displaced by the NW-Cañasgordas, Abriaquí, and Carauta faults. The mentioned structures are not currently related to mineralization processes. La Herradura and San Ruperto faults present neotectonic activity, with sinistral inverse movement related to the regional deformation regime associated with the Panamá-Chocó block push (Noriega et al., 2012).

The Frontino-Morrogacho gold district is classified in the metallogenic map of Colombia as an Au-Ag district in which mineralizations occur in veins and shear zones (Leal-Mejía et al., 2016). Mineralizations have been included in the Buriticá-Frontino district proposed by Leal-Mejía (2011), with gold content not as high as other nearby localities of the Middle Cauca Belt (Lesage et al., 2013)Colombia. It is hosted by the late Miocene Buriticá andesite porphyry, a shallow-level pluton dated at 7.41 ± 0.40 Ma (2σ, MSWD = 2.30; 40Ar/39Ar on hornblende. Shaw et al. (2019) include the El Cerro Igneous Complex in the Oligocene through Pliocene granitoids belonging to this metallogenic epoch in the Colombian Andes. Overall, this district is related to Au (Cu, Zn, Ag, As, W, Co ± PGE) mineralizations hosted in dikes, sheeted veinlets, and contact zones within intrusives and hornfels. Additionally, skarn mineralizations occur along the contact aureole and in sheeted veinlets and stockworks, replacement-style mantos and breccia zones developed in sedimentary rocks of the Penderisco Formation (Shaw et al., 2019).

In the El Cerro Frontino Igneous Complex, the mineralization style is mainly mentioned as nondisseminated textures related to veins and veinlets with coarse-grained native Au and Au-rich electrum that compromise quartz and calcite gangue and two paragenetic phases: Au-molybdenite-scheelite-cobaltite ± lollingite and quartz followed by chalcopyrite-pyrrhotite-sphalerite-quartz ± scheelite (Molina and Molina, 1984; Escobar and Tejada, 1992). Furthermore, the presence of pyrite, pyrrhotite, chalcopyrite, sphalerite, galena and arsenopyrite has been described (Flórez, 1988; Agrominera El Cerro, 1992). The hydrothermal alteration mineralogy consists of late magmatic potassic metasomatism with the replacement of augite and diopside by hornblende and euhedral Fe-rich biotite, local replacement of biotite by chlorite and epidote, and alteration haloes along the veinlet margins marked by biotite coarsening and a calc-silicate mineral assemblage (Shaw et al., 2019). Propylitic alteration is related to chlorite and sericite assemblages developed in small halos (Agrominera El Cerro, 1992).

5. Results

5.1 Geological, metallogenic and exploitation considerations of the El Cerro Igneous Complex

Underground gold mining works in the El Cerro Igneous Complex are related to several mineralized structures with different geometries and styles that are always spatially related to plutonic intrusions. Magmatic intrusions are related to prominent topographic changes in relation to surrounding sedimentary Cretaceous country rocks (Figure 3).

5.1.1 El Cerro Frontino

The El Cerro Frontino stock corresponds to an igneous intrusive body located to the south of the Frontino municipality. Mining activities at the El Cerro Frontino stock can be divided into at least four different zones, which include the Carauta-Orquideas area in the west and southwest, Musinga in the northwest, El Cerro to the north and Piedras to the east. The area of interest of this study corresponds to the northernmost sector of the stock, specifically the mineralized structures located in the El Apique and Los Hoyos mines, north of the San Diego-La Cuadrazón mine, representing a new important mineralized corridor in the El Cerro Frontino area (Figure 4).

Igneous bodies found in the El Apique and Los Hoyos-La Rompida structures vary into gabbroic with high pyroxene content and dioritic phases (Figure 4). Diorite is phaneritic and holocrystalline with leucocratic aspects, small to medium grain sizes and composed of plagioclase of the andesine series (62%), clinopyroxene of the augite-aegirine type (17%), coarse-grained biotite (11%) and quartz (3%). Amphibole is present as primary hornblende and related to the

Figure 3. Panoramic view of the El Cerro Igneous Complex
These profiles show important topographic changes that conform the prominent landforms related to the intrusive centers and the peripheral resistant ridges of hornfels and country rocks. Frontino-Morrogacho gold district.

uralitization of pyroxenes (3%), whereas opaque minerals are mainly identified as disseminated pyrite and magnetite, with the pyrite content being incremented by alteration processes into the host rock in the immediate margin of the veins (4%) (Figure 5). Diorite phases in the Los Hoyos and El Apique areas are found either as thin dikes or as massively N trending elongated outcrops with poor contents of fractures and joints. The textural characteristics of the Los Hoyos diorite are very similar to those in La Palma diorite bodies found in the upper part of the El Cerro, assuming that they are a single widespread phase.

Gabbro corresponds to phaneritic intrusive rocks with fine to medium grain sizes, melanocratic aspects, equigranular and idiomorphic textures, and compounds by plagioclase of the labradorite series (45%), clinopyroxene of the augite-aegirine type (36%), biotite (15%) and orthopyroxene (4%) (Figure 6).

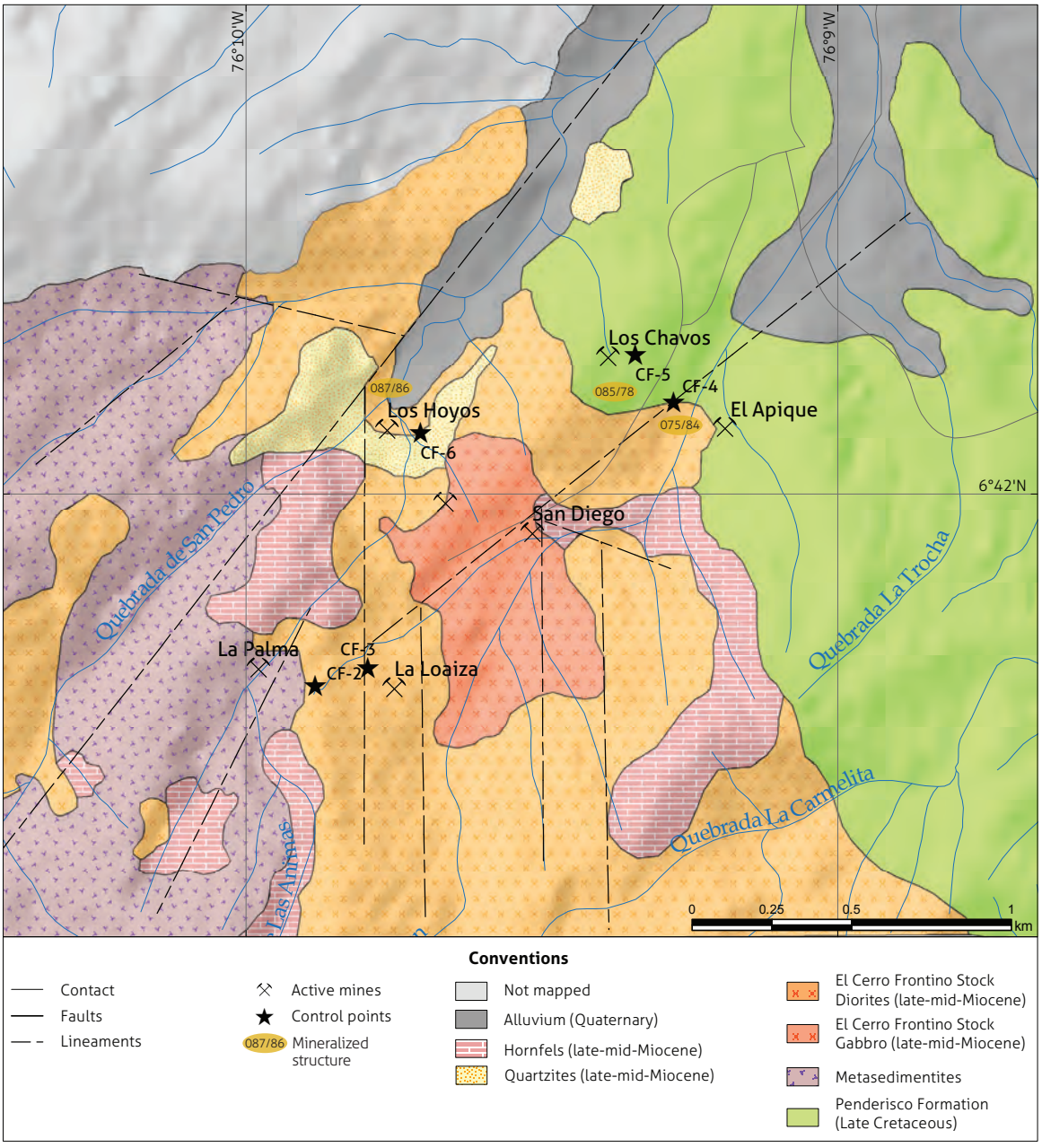

Figure 4. Geological map of the El Cerro Frontino stock with the main mineralized structures relating to this study Modified from Serviminas (2017).

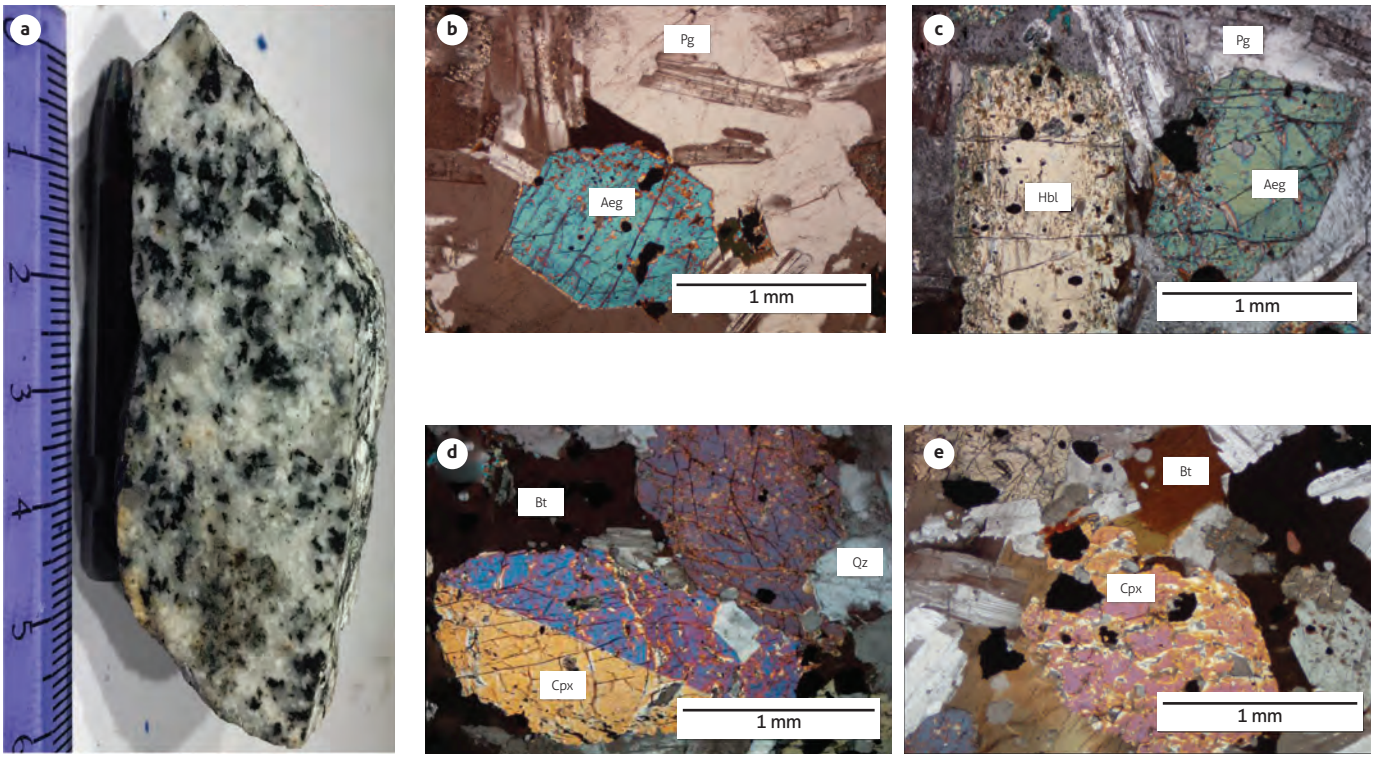

Figure 5. Hand sample and mineralogical composition in thin section. Cerro Frontino diorite
a) Hand-sample. b) Aegirine crystal partially rounded by euhedral plagioclase crystals. c) Presence of hornblende with oxide inclusions and aegirine with plagioclase (andesine). d) Twinned clinopyroxene crystal with quartz. e) Presence of biotite next to plagioclase (andesine) and clinopyroxene crystals. Pg: Plagioclase. Aeg: Aegirine. Hbl: Hornblende. Cpx: Clinopyroxene. Qz: Quartz. Bt: Biotite.

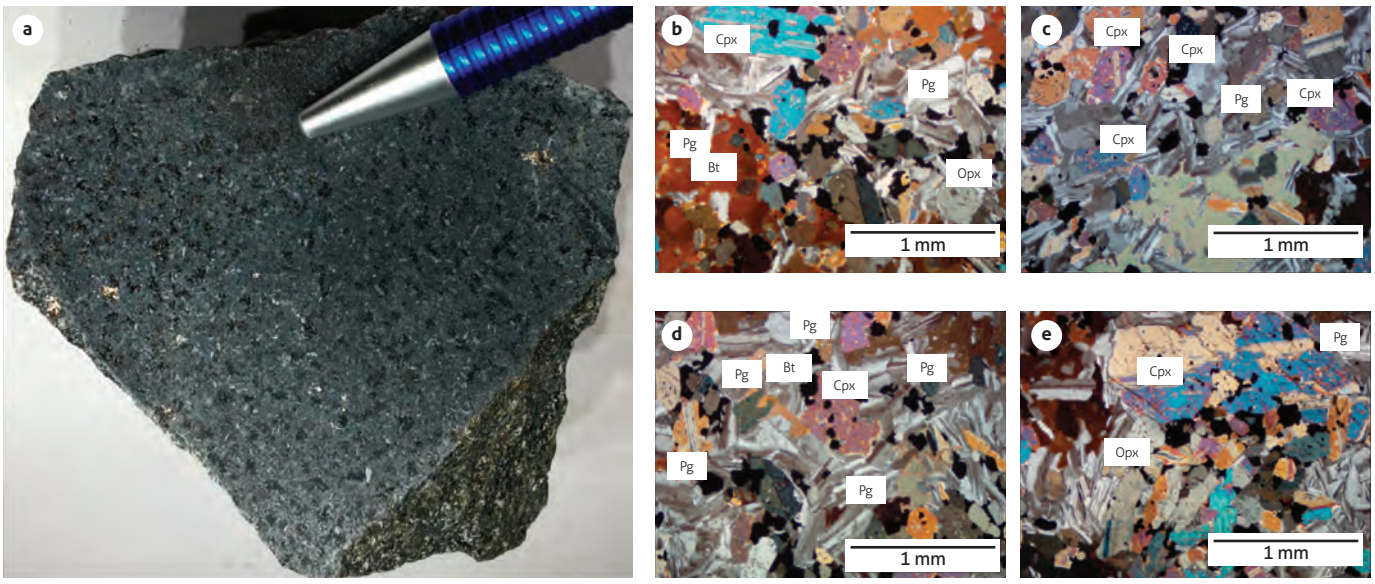

Figure 6. Cerro Frontino gabbro
a) Hand sample. b-c-d-e) High contents of plagioclase (labradorite) and clinopyroxene in the presence of biotite and orthopyroxene. Pg: Plagioclase. Aeg: Aegirine. Hbl: Hornblende. Cpx: Clinopyroxene. Opx: Orthopyroxene. Bt: Biotite.

Minor quantities of amphibole are present as hornblende due to uralitization of pyroxene. Outcrops can be found in the deep zones of El Apique (cm wide coarse biotite) and outcropping along San Pedro Creek (fine biotite). Intrusive relationships show that diorite pulses posterior to the gabbro because several intrusive breccias contain dioritic matrix and mafic clasts.

The intrusion of the El Cerro Frontino stock has generated low-grade contact metamorphic rocks with areas of skarn genesis. Leucocratic diorite intrusions emplaced towards thick calcareous strata with developed pyroxene-albite-chlorite hornfels, chlorite-rich quartzite and impure marble. There are extensive outcrops of metasedimentary rocks west of San Pedro Creek. Furthermore, these metasedimentary country rocks exhibit strong deformation and foliation with subhorizontal to vertical attitudes. Skarn deposits and pyritic mantos replacement are developed along both members of the Penderisco Formation in the area with low-grade mineralization content. Furthermore, the main mineralization style has been related to extensional-sheeted veinlets, extensional veins and shear-related veins found along El Cerro Frontino, where gold exploitation is focused.

Metamorphic and metasomatic thermal aureoles appear as steep resistant cliffs, which commonly indicate vertical and subvertical contact of the pluton and the country rocks. At El Cerro Frontino, the contact aureole presents banding and mineral replacement, with gray and white sequences in the hornfels proximal to the pluton. Hornfels are composed of saccharoidal quartz, diopside, tremolite-actinolite with minor calcite, idocrase, garnet, epidote, sphene, magnetite and disseminated pyrite (Escobar and Tejada, 1992), whereas the distal portions of the country rocks present evidence of grain recrystallization several kilometers away from the contact.

In the El Cerro Frontino area, mineralization is hosted in gabbros and diorites of the main intrusive body and in pyroxene-albite-chlorite hornfels or chlorite-rich quartzites of the contact aureole as a continuous structural corridor. Inside the aureole, there is a significant decrease in sulfide content and a decline in the thickness of the mineralized veins, which are related to shear zones. Conversely, in the igneous body, the mineralization increases in grade where the Los Hoyos and El Apique mines are located. Extension of the mineralization can suffer abrupt thinning and deflection when proximal to foliated metasedimentary rocks that outcrop west of San Pedro Creek, where these units conform to resistant massifs that seem to lack any economic mineralization.

Multiple apophyses of the El Cerro Frontino stock are common in other locations intruding the Cañasgordas basement and developing productive mineralized vein-type structures. For example, the Musinga, Carauta and Orquideas plugs are located northwest, west and southwest, where thin stringers of quartz-sulfide veins are hosted within fine-grained diorite bodies, with narrow cylindrical shapes that constitute clusters of intrusions, each between 0.5 km^2 and 1 km^2 in size, and span radially from the main Cerro Frontino stock.

Mineralization is related to tens of E-trending mineralized corridors across the pluton, with the development of extensional-sheeted veinlets, extensional veins and shear-related veins of different sizes that can form nests of veins and veinlets (a few centimeter-wide individual veinlets, and several meter-wide corridors, up to 3 m). These corridors are found along the axis and borders of the main the El Cerro intrusive body, with several tens of these mineralized zones manifested with widths of 30 m-50 m between individual structural corridors.

Small-scale artisanal activities are commonly represented in hundreds of tunnels dispersed in the area. Gold extraction is carried out using free milling techniques and gravitational separation methods, such as the "Antioquian Mill" or "Molino de Arrastre". This technique consists of a wooden circular recipient acting as a mill that uses water flow to push a set of irregular intrusive rocks inside the mill. Continuous movement of the rocks generates crushing and an ultimate decrease in particle size, with subsequent liberation of gold grains from sulfides and quartz. The process is finished with the use of a wood-based sluice box, where gold is collected as fine-grained particles.

5.1.1.1 El Apique mine

The El Apique mine corresponds to a 1-km-long mineralized structure that has been mined from both east and west in the northern sectors of the El Cerro Frontino stock. It was first exploited by the English company Carmen Valley Limited more than a hundred years ago and was recently reopened by the local society of miners (Hill, 1961; Alarcon, 2008). This mine is developed in rocks of the intrusive body but also in rocks from the surrounding country. Inside the first floor of the mine, there is a transition from the outside rim of the thermal aureole to inner contact with the intrusive body. The stock appears with important textural and compositional differences from fine-grained diorite in the first floor to coarse-grained biotite-bearing gabbros, including high pyroxene content, in the deepest level of exploitation, which is a 120-m-deep shaft.

This lithological variation occurs at altitudes less than a hundred meters and exhibits a mineralizing change between two different magmatic pulses of the El Cerro Frontino stock: an initial mafic pulse and a later dioritic pulse.

The contact between diorites of the El Cerro Frontino stock and the Urrao member of the Penderisco Formation exhibits intense silicification and chlorite alteration towards the border of the intrusion. Mineralization at the contact in the first floor evolves from shear veins to thin extension quartz veins a few centimeters wide hosted in the intrusive zone. Veinlets are included in zones of sheeted quartz veins that converge to a principal vein 10 cm to 20 cm wide and E striking. These veinlets are quite poor in sulfide content, and assays indicate that they are poor on gold, suggesting that auriferous mineralization shows a low grade inside the later dioritic phase of the intrusion. Alterations in this zone consist mainly of weak chlorite selvages a few centimeters near the veins.

The country rocks of the Urrao member appear as fine-grained sandstones, siltstones, and chert, which are strongly metasomatized and with bedding striking E- and vertically dipping mainly to the S. These rocks developed a multifractured EEN-striking shear vein with a vertical to subvertical dip to the S and a right lateral sense of movement evidenced by slickensides and vein displacement (Figure 7). It is possible to appreciate breccia zones partially formed when the fluids exsolved from the pluton were channelized through shear zones. Hydrothermal alteration inside and in the margins of the breccia consists of sericite and chlorite halos proximal to the veinlets. The fractures and joints near the shear zone are usually filled by sheeted quartz veins of a few centimeters wide, with low sulfide content into thin stringers of sheeted veinlets or stockwork textures (Figure 7). The width of the shear vein can vary from a few centimeters to more than a meter in the widest zone, with fine quartz-calcite-sericite hydrothermal breccia that contains fine pyrite and combined sulfide gouge with gold values between 5 ppm and 10 ppm.

Mineralization at the deepest level consists of quartz-calcite extension veins with an E strike with vertical, subvertical and subhorizontal dips to the S. Extension veins exhibit three anastomosed veins with constant thickness changes, averaging 0.5 m, varying from a few centimeters to 1.5 m, where multiple veins converge and form nests. Arrays of veins are not separated more than a meter from the other, and selvages of veins are conformed by bands and patches of coarse-grained sulfide assemblages and high-grade gold values up to several tens of

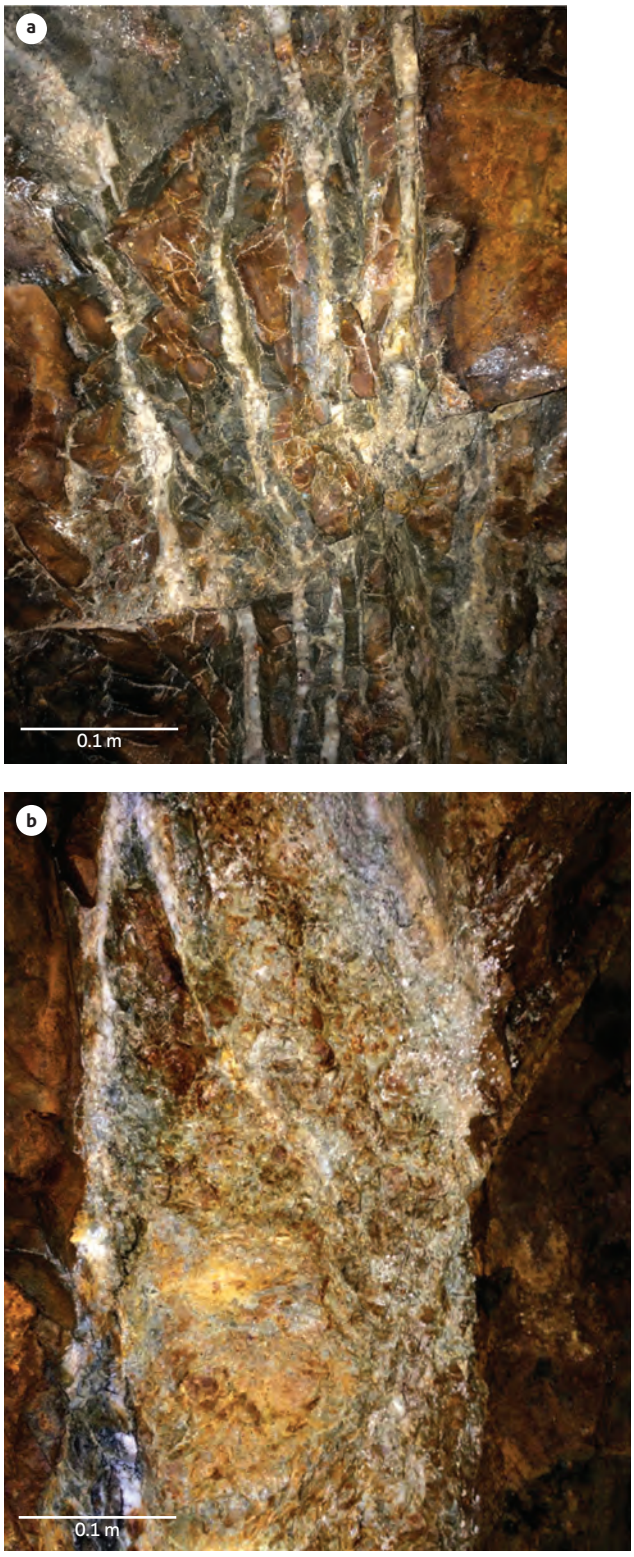

Figure 7. View of the El Apique shear zone located on the first floor of the El Apique mine
Lateral displacement observed in the left photograph related to an extensional shear zone. The shear zone is approximately 1 m wide with the presence of sulfides.

ppm in gold, occasionally visible to the naked eye, with grains several millimeters wide. The vein dip angle varies from vertical and subvertical to subhorizontal (20°-30°) with inclinations towards the S (Figure 8). Minor faults and fractures striking to the NW are displacing the main structure, although the veins appear to be massive and consistent along the strike without internal fracturing.

Both sheared veins and extension veins in El Apique have similar structural control with minor strike deflection from the hornfels to the pluton, which only represent low-order strike changes indicating an oblique sense of the sheared vein with respect to the extension veins. The E-striking direction and S-vertical dip of the shear and extension veins coincide with the E-striking and S-trending dip directions of the stratigraphic planes of the Urrao member country rocks.

Alteration mineralogy in the deepest floors consists mainly of a mild brecciation of the wall rock with the presence of sericite, chlorite and carbonate, with extension of alteration halos spanning a few tens of centimeters around the veins. However, green-colored clay, possibly illite, occurs in some places in the adjacent centimeters near the extension vein-wall rock contact. Extensive pyrite dissemination occurs near the vein margins. Coarsening of the biotite crystals in the gabbro is evident, reaching a few centimeters in size, and it is possibly related to K-rich fluids involving a premineralization event associated with late magmatic metasomatism, which is reflected in the Fe-rich biotite content in this lithotype.

Mineralogy of the vein samples studied from El Apique consists of calcite (occasionally bladed) and quartz. Stage one of mineralization consists of crystallization of pyrrhotite with porosity filled by gold associated with hessite, luangeite, imeterite, calaverite, petzite, galena and Fe-rich sphalerite (Figure 9A). Chalcopyrite occurs as inclusions and exsolutions in pyrrhotite crystals and inside sphalerite with disease textures. Gold grains, gold and silver telluride alloys occur mainly as crystals approximately 10 µm-70 µm in size (Figure 9). The second stage of mineralization consists of quartz and high contents of carbonate, pyrite and galena cutting sphalerite crystals locally (Figure 9b). Finally, a third stage is differentiated by the replacement of pyrrhotite by pyrite in borders. Sulfides appear as sutures within and at the borders of the veins, and they exhibit open space filling textures such as oriented pyramidal quartz crystals and coarse sulfides growing within drusiform cavities. The sulfide content averages 5% and can be as high as 20% of the vein mass.

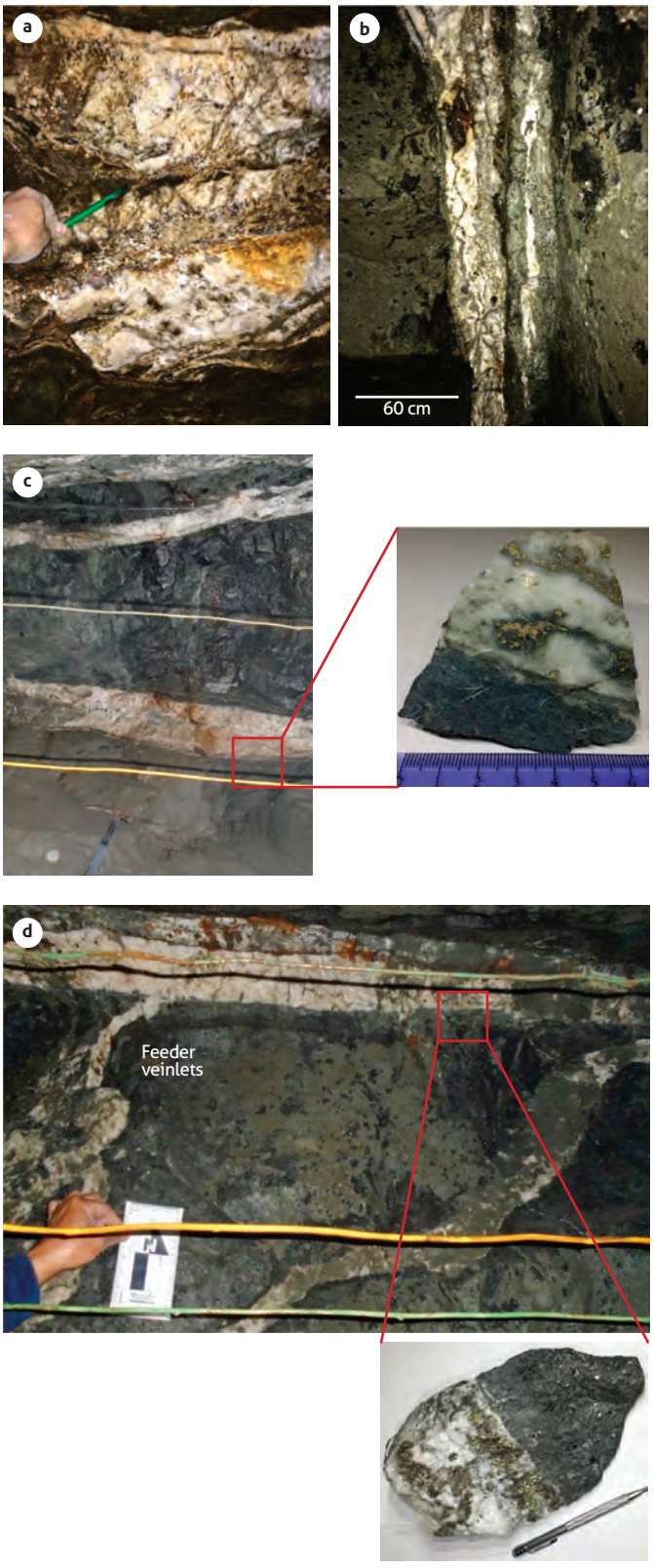

Figure 8. E-W striking extension veins observed in the El Apique mine a-b-c) Quartz-calcite extension vein. d) Mineralized igneous body with chloritization cut by quartz-calcite veins with chalcopyrite, pyrite and sphalerite.

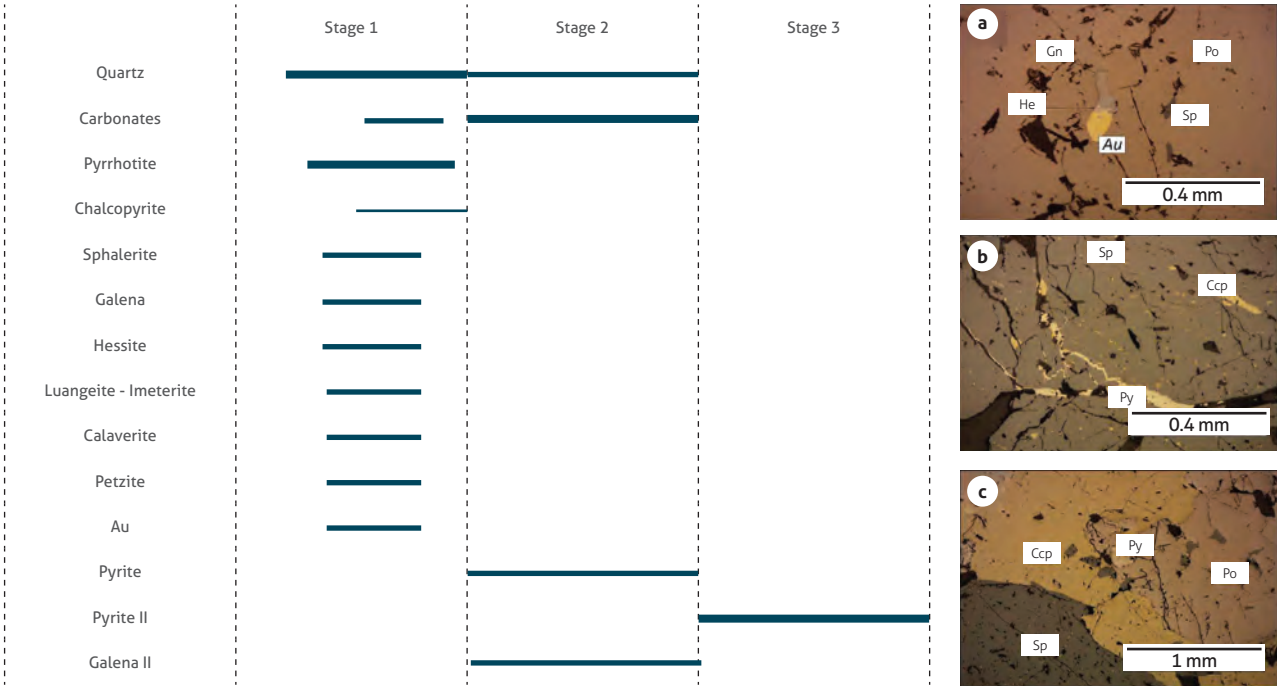

Figure 9. Paragenesis of the El Apique mineralized structure
a) Au, hessite and galena in paragenesis with pyrrhotite. b) Sphalerite cut by pyrite event. c) Chalcopyrite, pyrite, sphalerite and pyrrhotite contents. Ccp: Chalcopyrite, Py: Pyrite, Po: Pyrrhotite, Sp: Sphalerite, He: Hessite, Gn: Galena.

5.1.1.2 Los Hoyos mine

Los Hoyos is an artisanal mining operation that is located on the western part of the northern area of the El Cerro Frontino stock near San Pedro Creek. The most important mining front on Los Hoyos consists of a vertical shaft known as La Rompida. The mineralized structure exploited in La Rompida is thought to be the same as that in El Apique, which can be confirmed in the textural and mineralogical characteristics of the deposit and in the strike of the veins. In this way, these features show that both sets of mineralized vein types correspond to a continuous mineralized structure more than 1 km in length, with at least 200 m in vertical extent.

In the first floor of the Los Hoyos mine, mineralization is related to a set of centimetrically wide subparallel quartz extension veins with low sulfide and gold contents. Veins hosted within a fine-grained diorite show textures and compositions similar to those observed in El Apique. Alterations are mainly characterized by weak chloritization and the presence of clay associated with the wallrock around the mineralization (Figure 10). Host rocks in the deepest part of La Rompida consist of melanocratic gabbro with biotite crystals and green-colored (chlorite content) quartzite, commonly known as Los Hoyos quartzite. Alteration in this area corresponds to narrow selvages of green clay possibly illite, few centimeters adjacent to veins, with wider halos of chlorite spanning tens of centimeters around veins.

Deep in the La Rompida vertical shaft, the mineralized structure has important changes with the location of anastomosed veins with an ENE- to E-striking and S-dipping angle that are vertical to subvertical. The width of the veins varies between 10 cm-30 cm when individually separated to almost 2 m when creating important clusters and nests (Figure 10). In addition to these features, magmatic breccias in the form of dikes can be found surrounding the mineralization, suggesting fractionation processes in the main igneous body.

The ore mineralogy consists of two different phases: the first phase of quartz, pyrite, and galena with high silver contents and the second phase of calcite, pyrrhotite, chalcopyrite and sphalerite selvages, with minor contents of galena and hundreds of ppm gold in selected samples. The sulfide content within the veins averages 5% and can be as high as 30% in selected areas.

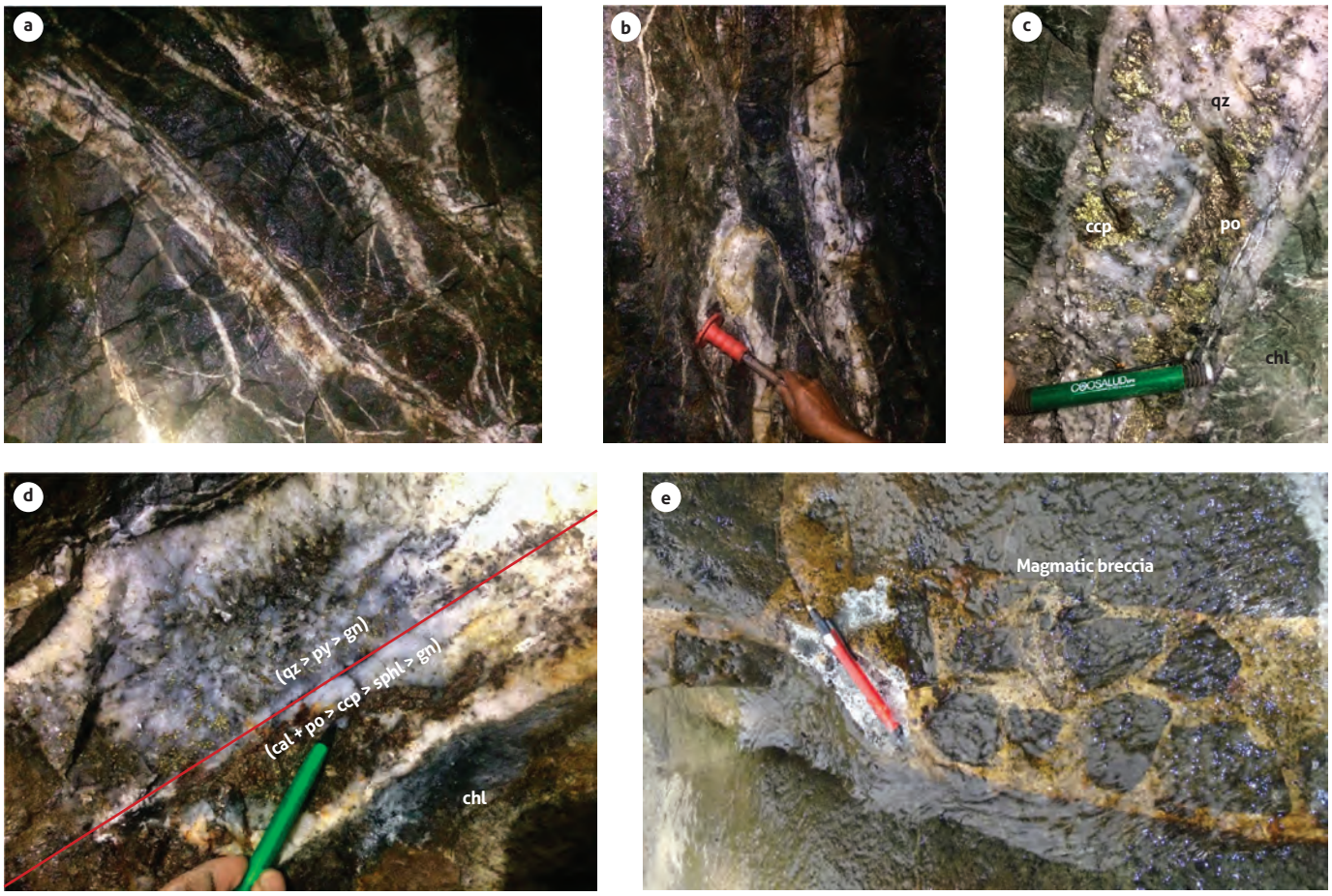

Figure 10. Mineralized structures in Los Hoyos-La Rompida
a-b) Subparallel veins with clay content near the borders. c-d) Decimeter-wide mineralized structures; note the different phases of mineralization and chloritization in host rocks. e) Magmatic-hydrothermal breccia in Los Hoyos creek. po: Pyrrhotite, ccp: Chalcopyrite, gn: Galena, qz: Quartz, py: Pyrite, sphl: Sphalerite, chl: Chloritization.

At least two different mineralization styles were identified in the El Cerro Frontino area. The first is characterized by a set of ENE-striking steeply S- dipping, right lateral displacement, shear-related veins with milky quartz, pyrite, and low contents of sulfides in sericite-dominant gouges that incorporate wall-rock brecciated clasts. Veinlets inside the shear zone are well developed along with tension fractures that sometimes exhibit echelon structures associated with the right-lateral slip of the shear. The second and main mineralization style corresponds to a set of E-striking extension veins with quartz-carbonate gangue, pyrrhotite, pyrite, chalcopyrite, Fe-rich sphalerite and galena with gold in the form of highly concentrated coarse-grained sulfides in vein selvages. Obliquity in the extension vein with respect to the shear veins suggests episodic filling of the dilatational zones generated by the shear forming mineralized corridors.

5.1.2 Morrogacho-Popales

Morrogacho is a NW elongated stock that composes a 3000-meter-high peak that is the apex of the pluton. Mineralizations in the stock are hosted within the pluton (Tajo Abierto and La Cascada mineralized structures) and in the surrounding Urrao member sedimentary wall rocks (El Mocho, San Donato and El Silencio mineralized structures) (Figure 11). Furthermore, other important mineralizations are located north of the stock (Media Cuesta and Pizarro mineralized structures). The area of interest of this study corresponds to the Tajo Abierto and La Cascada mineralized structures and the Media Cuesta and Pizarro areas.

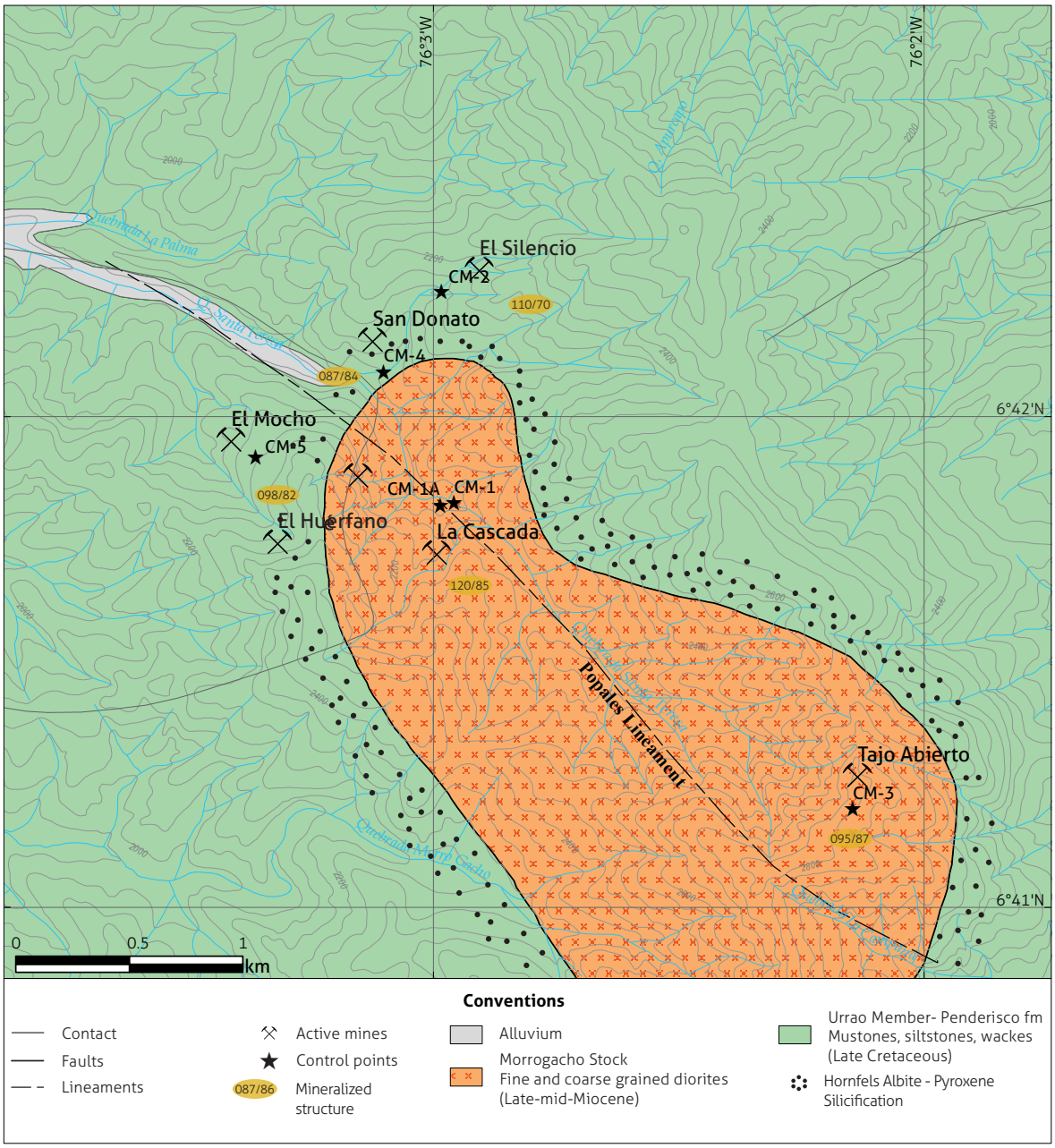

Figure 11. Geological map of the Morrogacho polyphase stock with the main mineralized structures
Modified from González and Londoño (2002), and Fenix Oro (2020).

The Morrogacho stock, as seen in La Cascada mineralized structure in the Popales area and along Santa Teresa Creek, corresponds to a diorite with phaneritic texture of fine to medium grain size. The mineralogy includes plagioclase (andesine series) up to 70%, biotite (12%), clinopyroxene of the augite-aegirine type (15%) and minor quantities of quartz (3%). Opaque minerals occur as disseminated pyrite (Figure 12). Álvarez and González (1978) consider this stock as a single-phase intrusion; however, at least two pulses have been recognized, and they present remarkable textural and compositional changes, one of which is related to dikes and satellite bodies.

Widespread thermal metasomatism traced for at least five hundred meters from the intrusive contact in the facies of hornblende hornfels affects siltstones and shales of the Urrao

member of the Penderisco Formation, whereas distal areas of the country rocks present evidence of grain recrystallization away from the contact.

Mineralizations of Morrogacho stock are mainly distributed in the northern area of the intrusive body but are also located inside the thermal aureole of the pluton along an important E- to NW-striking photogeological lineament, which was named the Popales Lineament in this study (Figure 11), and it is recognized as a cooling structure within the Morrogacho stock. Mining activities have been developed for the last 100 years, with dozens of tunnels found inside and around the stock. Mineralizations near and outside the stock are associated with the movement of fluids that were trapped inside structurally prepared wall rocks.

5.1.2.1 Tajo Abierto mineralized structure

Tajo Abierto corresponds to a mineralized structure located inside the Morrogacho pluton and is related to the apex of the stock, where mineralization occurs as part of the fluid movement that circulates in the cupola and carapace (Hart, 2007). Mineralization hosted in the intrusive consists of a 0.6-m to 1.0-m-wide extension vein with a marked E-strike direction with a vertical S-dipping strike. A dilatational zone observed within the intrusive is hosted of veins of wider margins than others observed in the Frontino-Morrogacho gold district. The sulfide content in the vein is high and reaches 90% of the vein mass. Intersections of SE- and NE-striking branches of veins can generate the occurrence of ore shoots and demonstrate extensional behavior. At this point, veins become massive in sulfide content, with coarse ore mineralogy dominated by pyrrhotite, chalcopyrite, pyrite, arsenopyrite and Fe-rich sphalerite, indicating high temperatures of the mineralizing fluid during precipitation conditions (Figure 13).

The sulfide content in the ore shoots is uncommonly high for the district. Parasitic veinlets several centimeters wide with high contents of pyrite and chalcopyrite orthogonally disposed to the principal set of vertically dipping veins with S-strikes cut the intrusions surrounded by strong chloritic alteration. This condition coincides with the extension processes of the main vein formation (Figure 13). Hydrothermal alteration in Tajo Abierto corresponds to pervasive chloritic alteration near the veins that occur a few tens of centimeters proximate to the back of the veins with sericite, carbonate and widespread strong pyrite dissemination in the host rock. This alteration occurs mainly in fractures and joints along the vein margin, whereas the alteration that is more distal consists of a chloritic assemblage with weak intensity.

The gangue mineralogy of the veins from Tajo Abierto is mainly composed of calcite and quartz. Pyrite and arsenopyrite in the first stage are associated with gangue minerals. Pyrite is highly fractured and brecciated, which are characteristics that indicate the presence of two different stages of mineralization

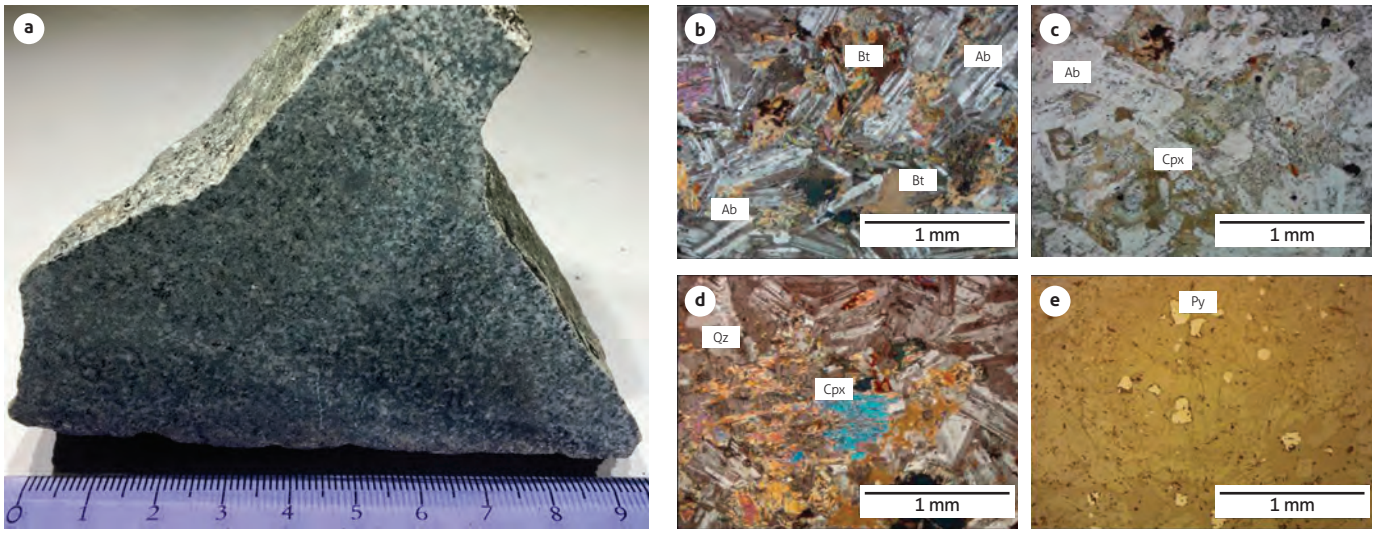

Figure 12. Morrogacho diorite of sample from the La Cascada mineralized structure
a) Hand-sample. b-c-d) Fine-grained holocrystalline diorite constituted by plagioclase of the andesine series, clinopyroxene and biotite. e) Disseminate pyrite crystals in diorite. Bt: Biotite, Pg: Plagioclase, Cpx: Clinopyroxene, Py: Pyrite, Qz: Quartz.

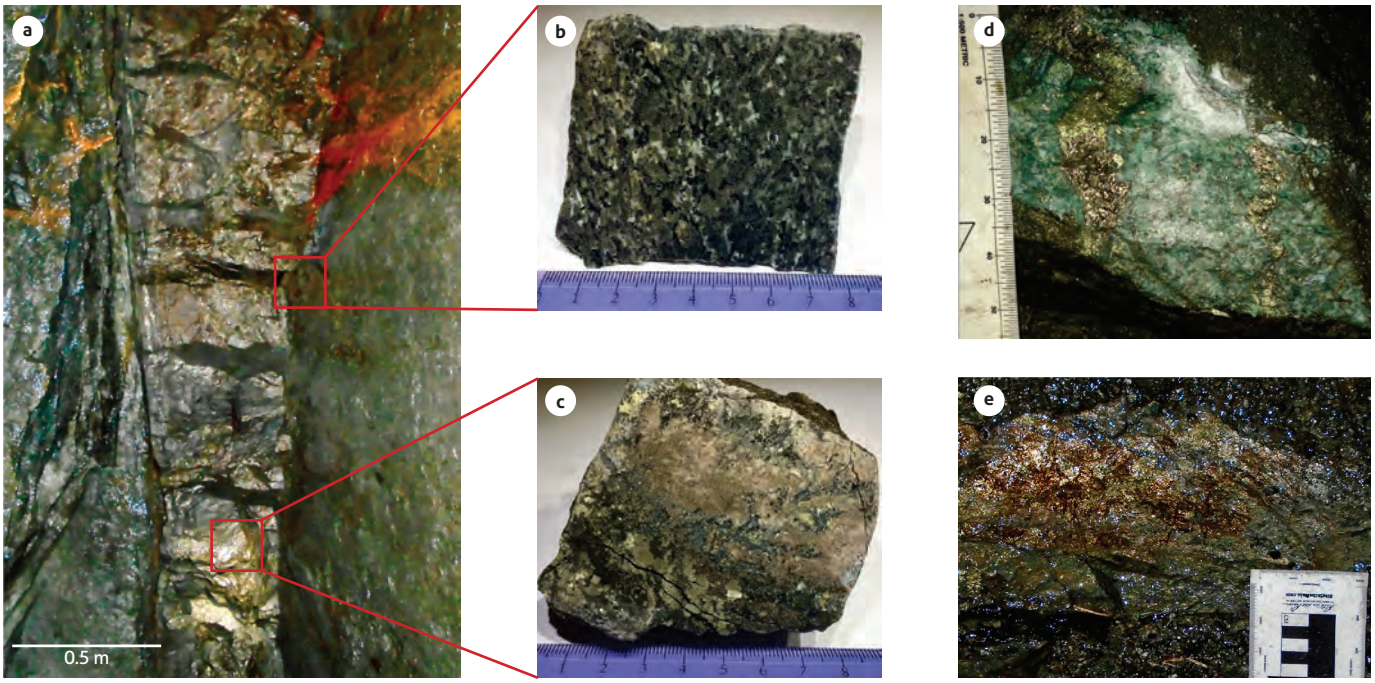

Figure 13. Tajo Abierto mineralized structure
a) Extension veins proximal to the ore shoot with a high content of sulfides. b-c) Hand samples of the mineralized areas with high contents of sulfides. d-e) Chloritic hydrothermal alteration.

(Figure 14 a, b). Gold grains occur mainly as crystals approximately 0.1 mm in size, placed in the rims of brecciated pyrite and associated with pyrrhotite, chalcopyrite, bismuth minerals, tellurides, and silver sulfosalts, such as cuboargirite (Figure 14). Pyrrhotite is the most common sulfide in the second stage. The presence of cubic galena with characteristic triangular pits growing after pyrite is common, and sphalerite seems to be present in a second stage of mineralization and related to gold.

5.1.2.2 La Cascada mineralized structure

The La Cascada mineralized structure includes a series of tunnels near the waterfall of Santa Teresa Creek in the area of Popales inside the dioritic stock (Figure 11). Behind the waterfall is an important NE-striking subvertically S-dipping vein system. The mineralization consists of multiple arrays of sheeted quartz-extension veins and veinlets that are mainly E- and NW-striking with very thin strings of veinlets with different orientations orthogonal between the main trends (Figure 15). It likely developed during the filling of a structural horse tail system because 0.2-m ENE-tabular quartz extension veins appear to join all the zones of planar-sheeted vein arrays with a NW-striking direction.

Quartz veins are a few centimeters thick and hosted in the NW-shoulder zone of the Morrogacho dioritic body, which occurs as a mafic phaneritic fine-grained intrusion. The vein geometry consists of a dense network of tens of subparallel arrays of planar-sheeted milky quartz veinlets and tabular extension veinlets developed inside the dioritic pluton forming massive swarms within a several-meter corridor.

Strong chloritic alteration affects the greenish matrix of the intrusives near the sheeted veins and within the intrusion for tens of centimeters. Quartz occurs in druses and cavities exhibiting the orientation of the extension when growing from the vein margins, and pyrite appears as euhedral cubic crystals representing the most common mineral after chalcopyrite. Vein spacing occurs as a dense array that reaches 6 to 10 veins per meter and suggesting it contains high gold grades (Hart, 2007). Although dissemination is not widespread, mild sulfide dissemination occurs a few centimeters around the veins. Near the mineralized structure, narrow-sheeted quartz veinlets are commonly developed along all outcrops of the intrusive rocks, meaning that mineralization of the sheeting quartz veins is widespread throughout this area.

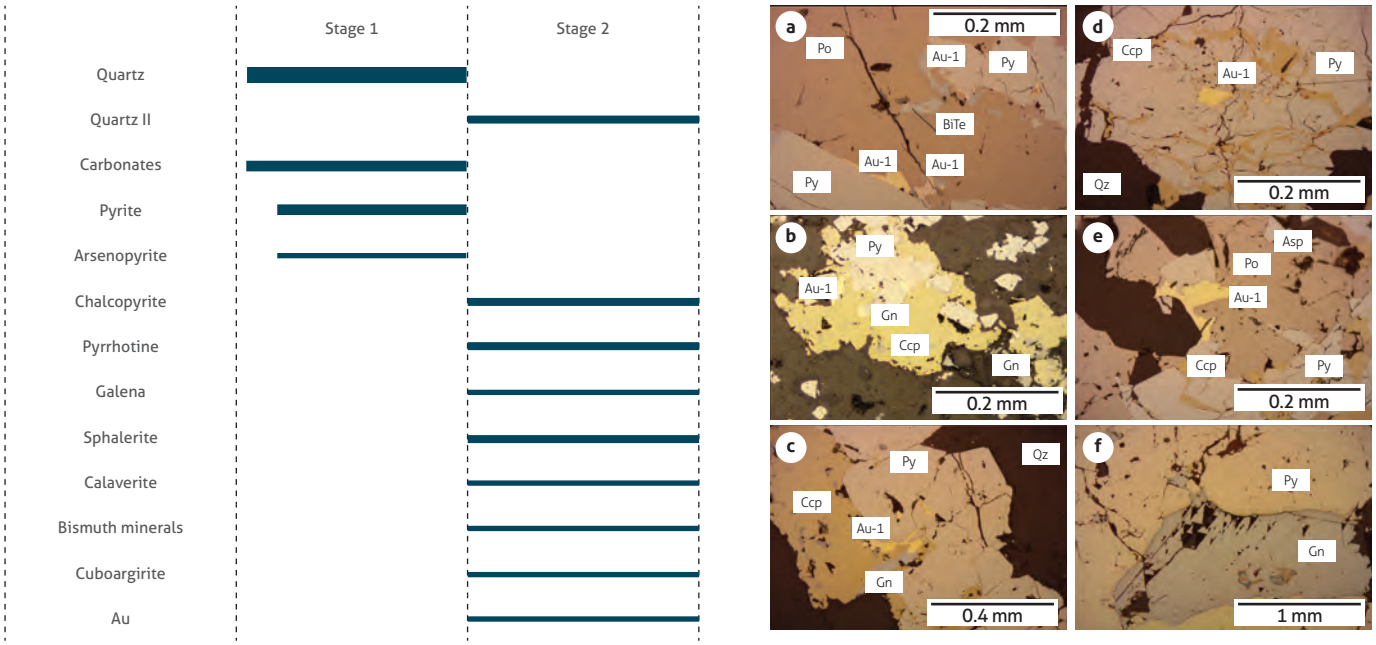

Figure 14. Paragenesis of the Tajo Abierto mineralized structure
a, c, e) Gold crystals associated with BiTe in the rim of brecciated pyrite. b) Gold crystals associated with chalcopyrite and galena. d) Gold crystals associated with chalcopyrite within brecciated previous pyrite. f) Triangular pits in galena next to pyrite crystal. Py: Pyrite, Ccp: Chalcopyrite, Gn: Galena, Asp: Arsenopyrite, Po: Pyrrhotite, BiTe: Bismuth and Tellurium minerals. Au: Gold.

The gangue mineralogy of La Cascada is mainly characterized by quartz. The ore mineralogy includes pyrite and chalcopyrite, which grow after pyrite crystals; sphalerite, which occurs principally after pyrite in minor quantities; and cubic galena is present as small grains growing after chalcopyrite. Samples from this sector do not contain visible gold grains. Important dissemination of the sulfides also occurs as continuous patches from the borders of veins. Propylitic alteration is identified by the strong presence of chlorite staining next to the borders of the veins with the presence of carbonates and sericite in minor quantities. This alteration assemblage suggests replacements of mafic minerals (augite) with chlorite and plagioclase with carbonate and sericite replacements.

5.1.2.3 Media Cuesta and Pizarro mineralized structures

To the north of the Morrogacho stock, several gold mineralizations can be observed in the Media Cuesta and Pizarro areas, which represent a distal expression of mineralizing fluids related to cooling history of the Morrogacho stock (Figure 16) and are associated with satellite bodies of leucocratic pyroxene-bearing fine-grained diorite dykes found in the Media Cuesta area. These mineralizations have different characteristics from those hosted within the intrusive rocks. Vein mineralizations occur mainly hosted in N- to NW-striking vertically dipping, fine-grained siltstone and sandstone sequences of the Urrao member. Gold fault veins and shear veins have dominant N- and NW-striking directions and are steeply E-dipping. These structures are coincident with the right-lateral sense of movement.

Mineralization in the Media Cuesta and Pizarro areas exhibits important fault vein characteristics, with a few centimeters in width in the El Duque mine (Media Cuesta) and up to 0.5-2 m in width in the La Petaca and Pizarro mines. Veins commonly exhibit pyrrhotite dissemination and mild brecciation of the host rock. The gold content in the area is associated with fractures within sulfides involving mineralogy with pyrrhotite, pyrite, arsenopyrite and galena in quartz gangue. The fault vein N- and NW-striking directions coincide with the N-striking, steeply E-dipping stratigraphic planes, a condition that apparently favors vertical shear vein development in the area.

5.1.3 La Horqueta

The La Horqueta stock corresponds to a prominent mountain with an altitude of more than 3600 m associated with a semicircular kilometer-wide intrusion (Figure 17). Mining activities

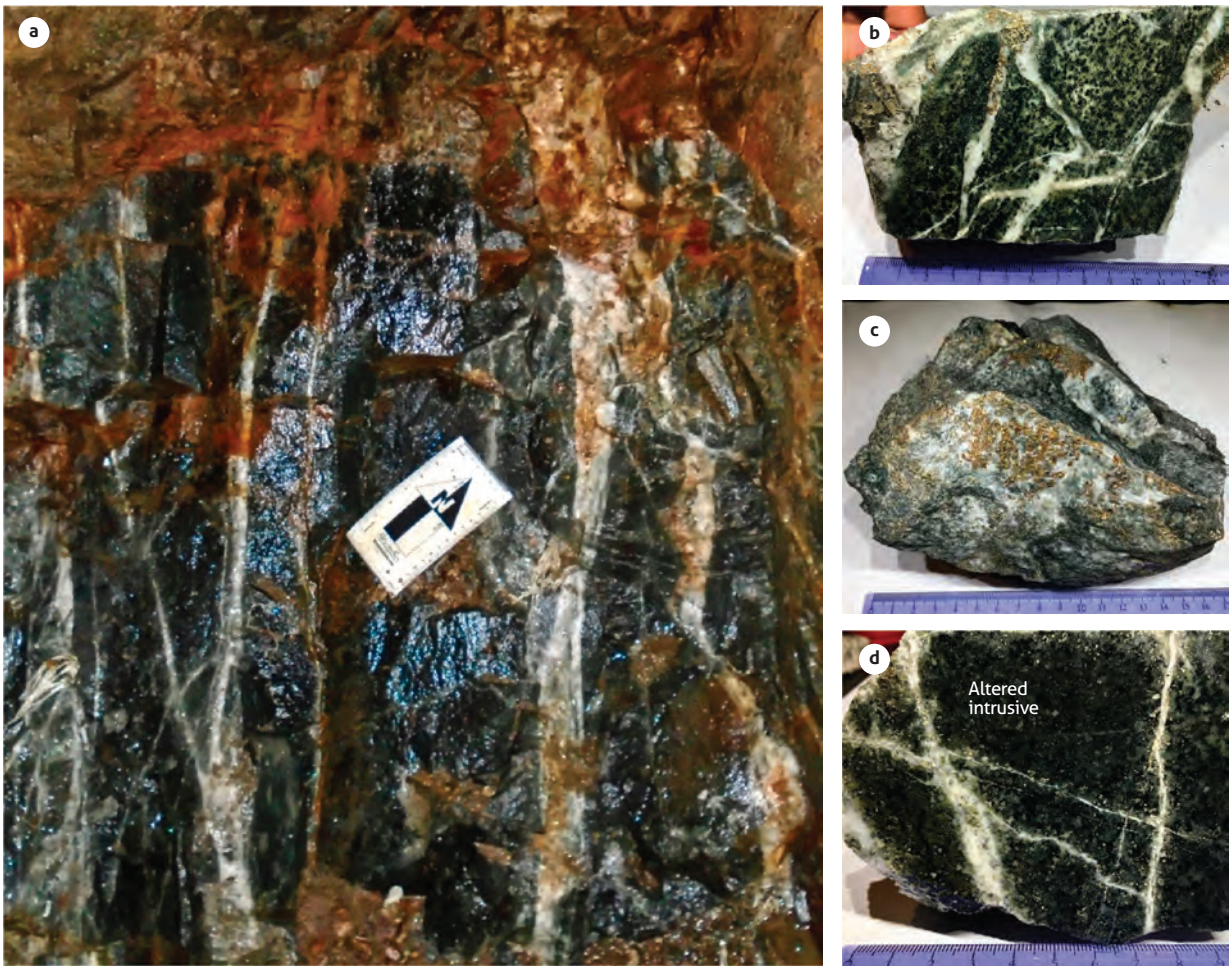

Figure 15. La Cascada mineralized structure
a) Sheeted quartz veins. b-d) Altered intrusions cut by quartz veins with stockwork assemblages. c) Host rock cut by quartz veins with a high content of sulfides.

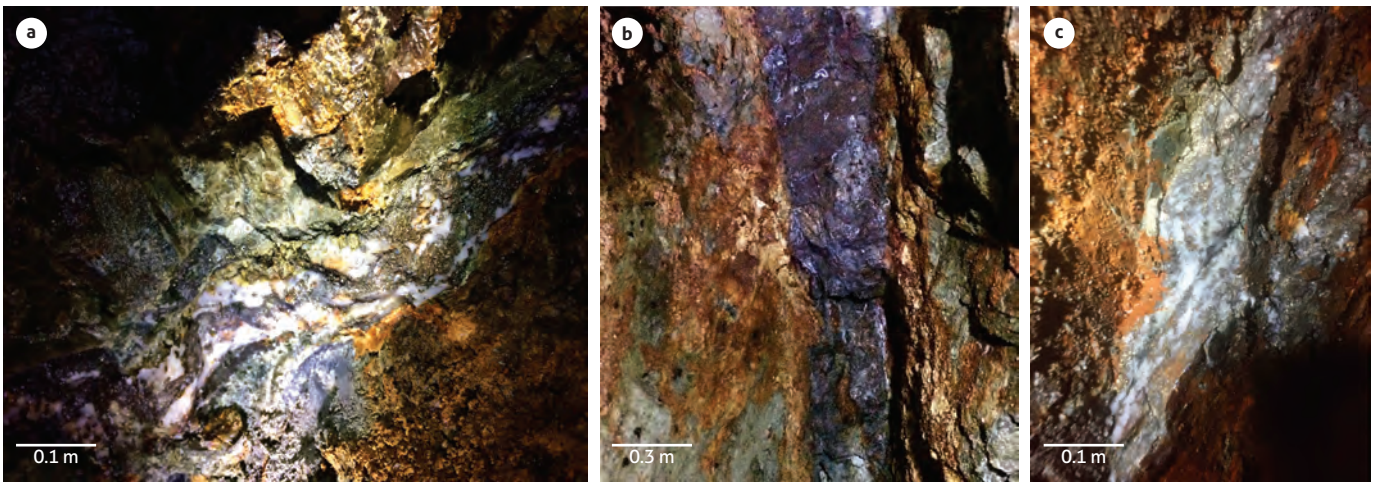

Figure 16. Mineralizing fluids related to cooling of Morrogacho stock
a-b-c) Subordinated N-NW structures in the Pizarro-Media Cuesta area. a-c) Quartz veins and veinlets with sulfide content and local brecciation of the host rock. b) Hydrothermally altered host rock cut by veins with pyrrhotite content.

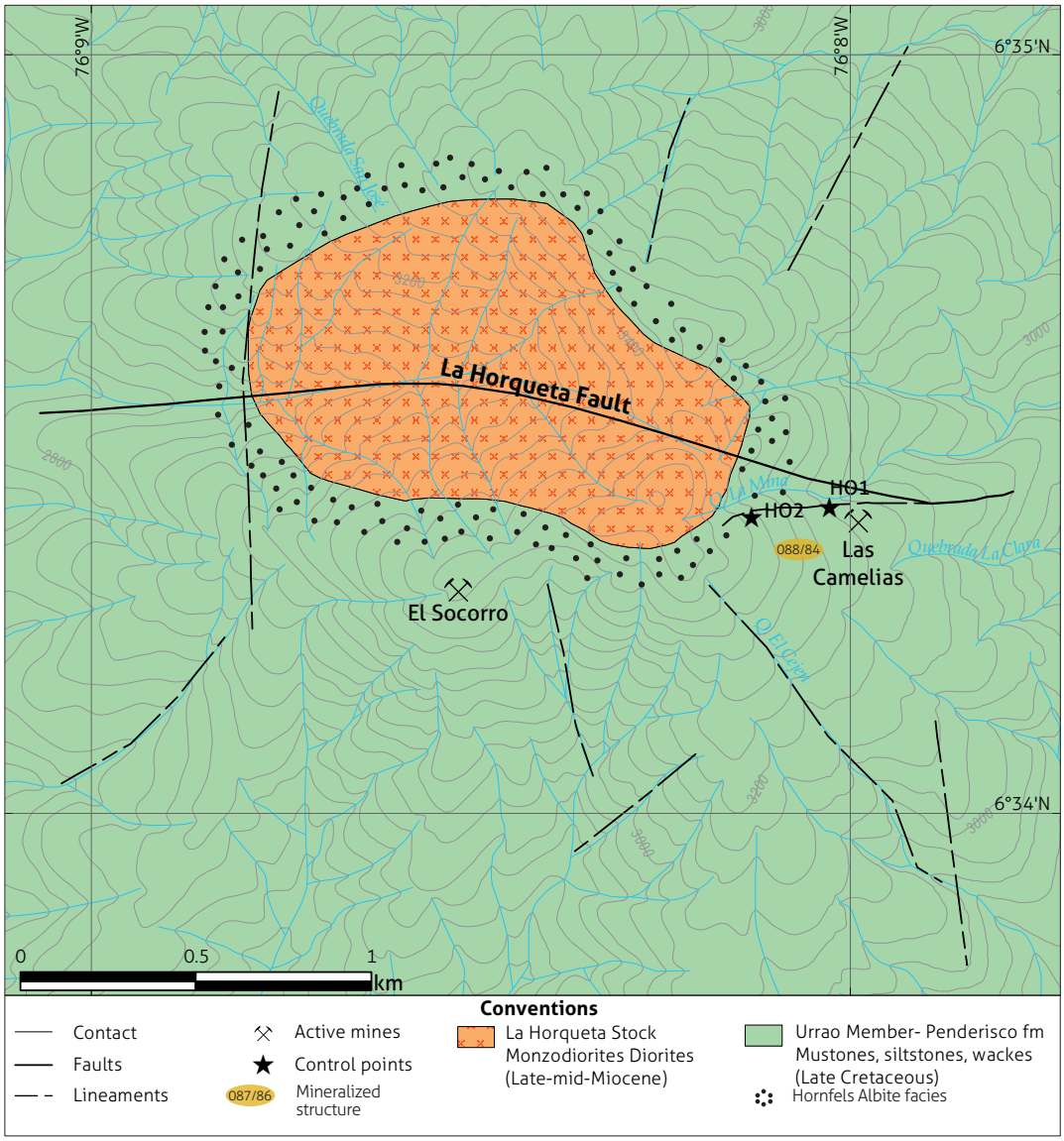

Figure 17. Geological map of the La Horqueta stock with the main mineralized structures
Modified from González and Londoño (2002).

in the pluton are located mainly in the surrounding contact aureole, mineralizations are related to a corridor formed by the La Horqueta Fault inside the plutonic body. The present information is described according to the characteristics of mineralized structures found in the Las Camelias mine, which is a historically productive mine in the Abriaquí area located in the contact aureole of the pluton.

Near the La Horqueta stock, the Urrao sedimentary sequence reflects high tectonic activity, which is evident due to the presence of folds and minor faults. Important exhumation was inferred because of altitude and the prominence of the igneous body since the stock was formed in the late to mid-Miocene. Steeply slope-resistant cliffs of hornfels units as roof zones on top, combined with the steeply dipping E-striking La Horqueta fault, have created an irregular V-shaped peak that gives this mountain its name. This fault exhibits characteristics associated with the cooling and emplacement history of the intrusive and lately associated with the formation of a mineralized corridor that generated hydrothermal veins and faults in the area.

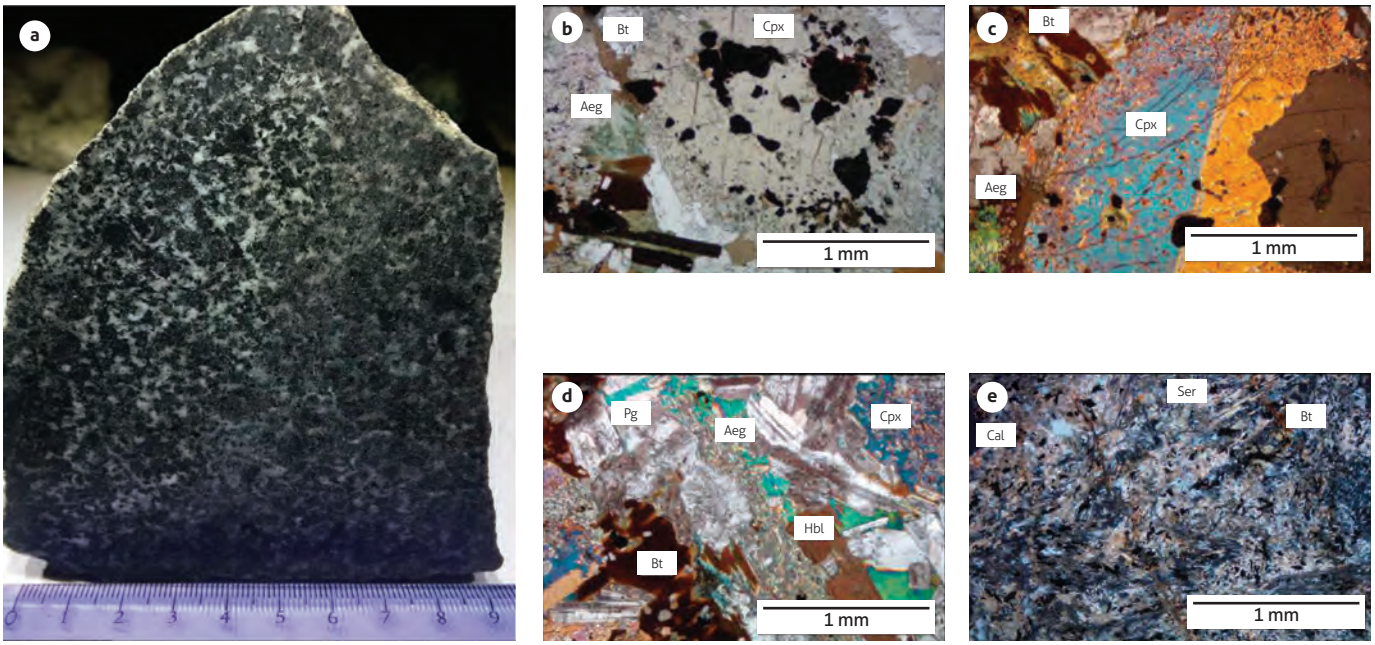

Figure 18. La Horqueta diorite at Las Camelias mineralized structure
a) Hand-sample. b) Presence of opaque minerals as inclusions in the pyroxene crystals. c) Twinned clinopyroxene. d) Plagioclase, hornblende and clinopyroxene crystals. e) Hydrothermal alteration in the presence of sericite and carbonate. Pg: Plagioclase, Aeg: Aegirine, Cpx: Clinopyroxene, Bt: Biotite, Hbl: Hornblende, Ser: Sericite, Cal: Carbonate.

The La Horqueta stock is a phaneritic, intermediate composition pluton with holocrystalline texture and coarse- to medium-sized grains, and it is classified as a diorite with a high content of pyroxene. The pluton is represented by a single intrusive phase that is composed of plagioclase of the andesine series (60%), clinopyroxene of augite-aegirine type (22%), biotite (13%) orthopyroxene (5%), and fewer amounts of k-feldspar, quartz and hornblende (Figure 18). Coarse-grained biotite could be found to be mainly related to hydrothermal processes in addition to sericite and carbonates (Figure 18e). Opaque minerals occur as disseminated pyrite and magnetite constituting up to 10% of the samples locally and are mainly associated with pyroxene crystals (Figure 18b). Some pyroxene crystals show skeletal texture. The emplacement of the stock generated a thermal aureole (Figure 17) that created a zone of hornfels with chlorite-albite facies at least 1 km wide, and country rocks are mainly E-striking with vertical dips and represented by fine-grained siltstone and mudstone strata of the Urrao member.

5.1.3.1 Las Camelias mine

Mineralized structures in the Las Camelias mine are located east of La Horqueta stock, near a fault structure with an E-striking steeply dipping to the S-strike. Mineralization consists of a trend of at least Three subparallel vertically S-dipping veins with E-trending strikes of at least 300 m. Veins are narrow, with thicknesses of approximately 0.1 m-0.2 m and rarely wider. Spacing between the subparallel veins varies from 5 m-20 m (Figure 19). Vein infilling occurs mainly along joints and shear planes with evidence of kinetic movement due to the presence of slickensides with steps along the vein margins that indicate E-right-lateral movement. Mineralization exhibits coarse sulfides and is mainly hosted in hornfels of the contact aureole; nonetheless, principal veins show continuity into the pluton, where the width decreases with no deflection in the strike.

Associated with the shear veins, it is possible to observe local zones that develop a proximate halo of chlorite alteration, with minor carbonate and sericite. In some parts of the mine, a thin late-stage barren quartz veinlet with oxidized pyrite and malachite cuts the dioritic pluton and mineralization. Open space filling textures appear in the veins as drusical cavities with coarse sulfides and oriented pyramidal quartz crystals.

Mineralization consists of quartz and calcite as gangue. The first stage permits crystallization of pyrite and arsenopyrite, which is later remobilized in the second stage of mineralization.

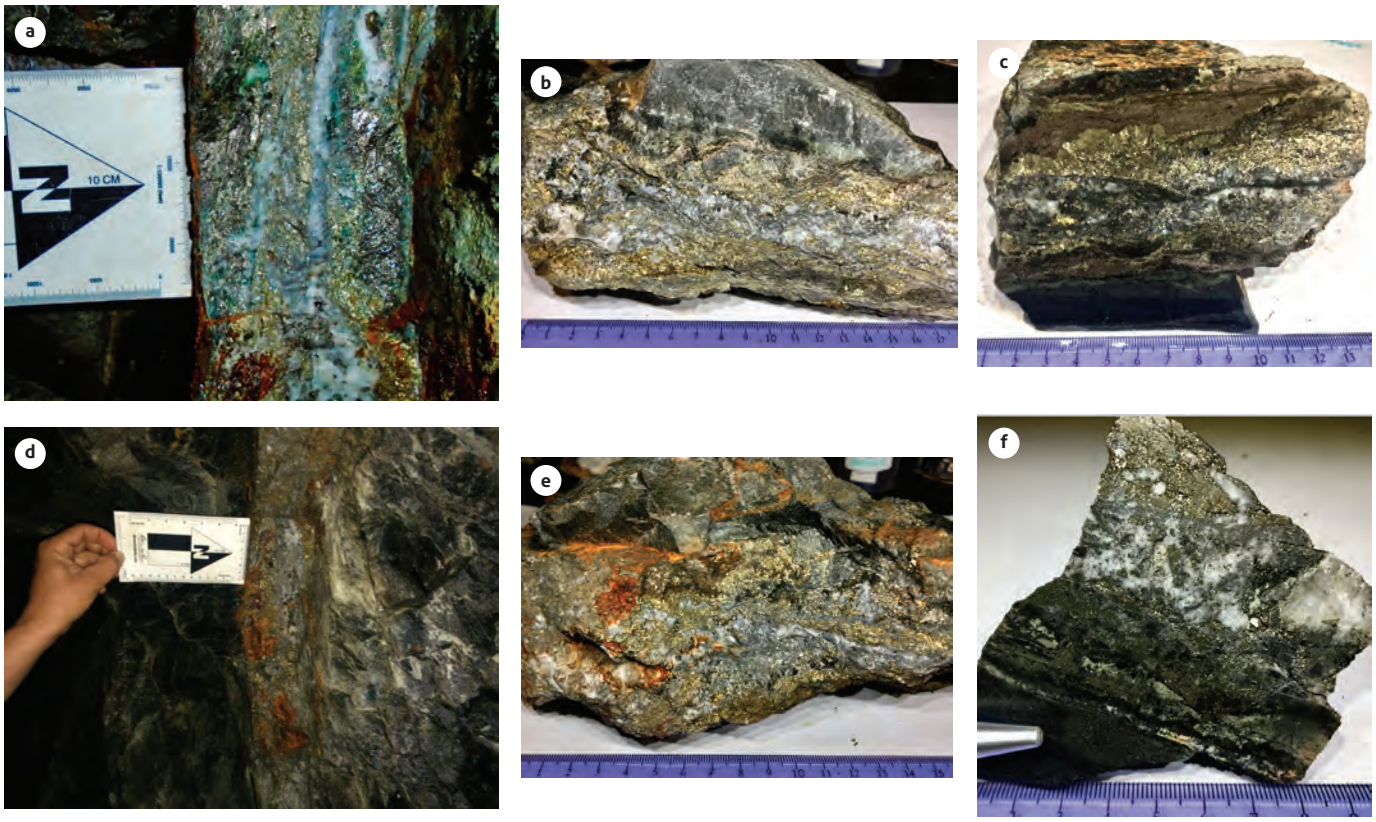

Figure 19. Las Camelias mineralized structure. Subparallel veins with the presence of pyrite, chalcopyrite, arsenopyrite, sphalerite and galena. Host rock corresponds to hornfels with mudstone protolite
a and d) Late quartz-pyrite veins. b-c-e-f) Hand samples of mineralized country rocks and veins with high contents of sulfides and chloritic alteration.

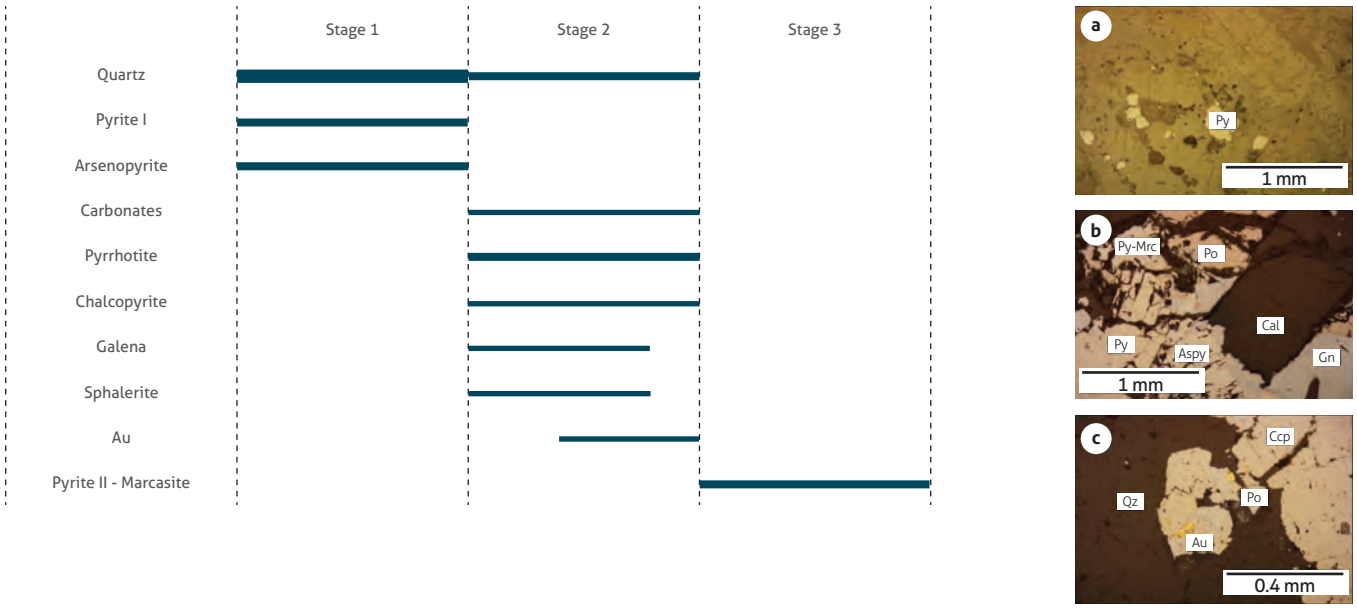

Figure 20. Paragenesis of the Las Camelias mineralized structure
a) Disseminated pyrite content. b) Pyrrhotite and galena with carbonate. c) Gold related to pyrrhotite event. Py: Pyrite, Mrc: Marcasite, Gn: Galena, Aspy: Arsenopyrite, Ccp: Chalcopyrite, Po: Pyrrhotite, Qz: Quartz, Cal: Carbonate, Au: Gold.

This second stage is a compound pyrrhotite and chalcopyrite assemblage with the posterior crystallization of sphalerite and galena, with high contents of carbonates and quartz. Gold grains present sizes of 0.1 mm and are related to pyrrhotite inside brecciated crystals or near their rims (Figure 20). At the final stage of mineralization, pyrrhotite is replaced by pyrite and marcasite. Pyrrhotite is the most common mineral in the ore. The sulfide content averages 10% but can reach up to 80%, with massive pyrrhotite and chalcopyrite crystals concentrated towards the borders of the veins, and no dissemination or very poor brecciation occurs in Las Camelias.

5.2 Mineral chemistry of ore minerals

Mineral chemistry analyses were carried out to analyze the mineral content, composition of the sulfide and gold grain signature and fineness in mines belonging from each of the intrusive centers of the El Cerro Igneous Complex: Tajo Abierto (Morrogacho polyphase stock), Las Camelias (La Horqueta stock) and El Apique (Cerro Frontino polyphase stock) mineralized structures. The results of the gold chemistry plotted in a ternary diagram indicate three families of electrum based on the spectra of the gold grains (Figure 21):

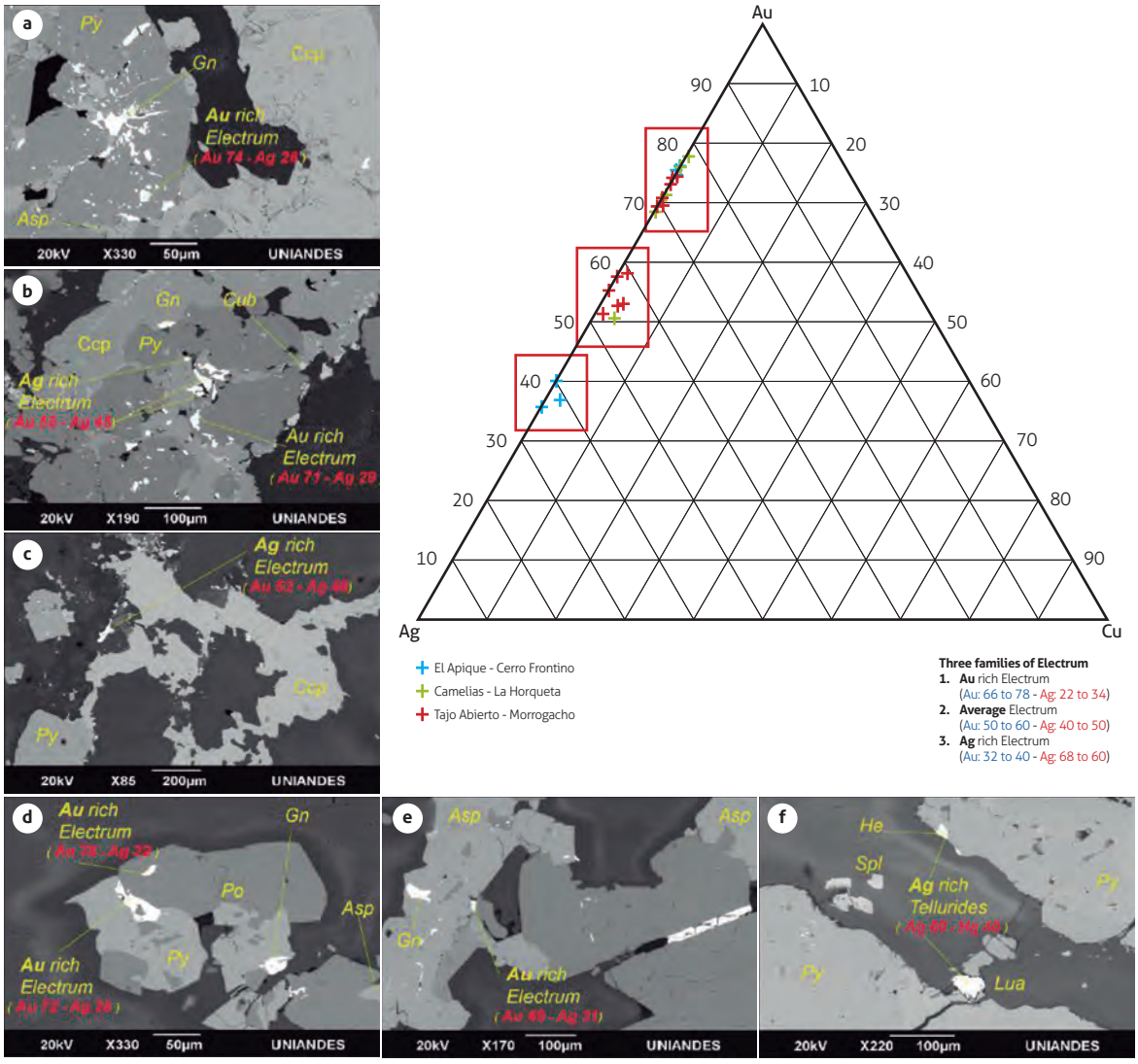

Figure 21. Ternary plot for calculating the gold signature from the Au-Ag-Cu ratio using SEM compositions
Notice the three different families of electrum and tellurides that exist in the area. a-b-c) Tajo Abierto Mineralized structure. d-e) Las Camelias mineralized structure. f) El Apique mineralized structure. Py: Pyrite, Po: Pyrrhotite, Asp: Arsenopyrite, Gn: Galena, Ccp: Chalcopyrite, He: Hessite, Cub: Cuboargirite, Spl: Sphalerite.

- Gold-rich electrum: electrum grains with 66%-78% Au and 22%-34% Ag with sizes ranging from 15 µm to 100 µm. These grains occur in borders of arsenopyrite, chalcopyrite and pyrrhotite crystals and in paragenesis with galena along fractures. Samples of all the mineralized structures present grains of this family, but these are mainly related to Las Camelias and Tajo Abierto mineralized structures.
- Average electrum: electrum grains with 50%-60% Au and 50%-40% Ag. These grains are found in Las Camelias and Tajo Abierto mineralized structures but are mainly related to second.
- Silver-rich electrum: electrum grains with 32%-40% Au and 68%-60% Ag with sizes ranging from 10 µm to 70 µm. These grains are located in the borders of chalcopyrite crystals. The El Apique mineralized structure is the only one with this family of silver-rich electrum grains, which occur as mercury alloys and silver tellurides.

According to the SEM results, vein-type gold fineness in the district ranges between 50% and 80%. The average size of gold grains is between 20 µm and 100 µm; the minimum size is approximately 10 µm; and the maximum size can reach hundreds of micrometers in the form of visible gold. These coarse-grained gold specimens are commonly found in the northern El Cerro Frontino stock at the San Diego-La Cuadrazón and El Apique mines and in the high-grade gold structures of the Morrogacho-Popales area. Gold grains are commonly found as electrum associated with the rims of grains (or within) in chalcopyrite, pyrrhotite, galena, arsenopyrite, native gold grains and silver tellurides, close sulfosalts and mercury-gold-silver alloys, specimens that include cuboargirite, imeterite, stützite, petzite, luangeite, hessite and calaverite, with consistent Bi, Te and Sb contents. Gold is mainly refractory, hosted within sulfides and rarely present as free grains in quartz or carbonates; conversely, it is found filling fractures within sulfides, with tabular, semicircular and elongated shapes and occasionally with a circular shape.

6. Discussion

6.1 Geochemical comparison, Frontino-Morrogacho arc and Middle Cauca Belt (MCB)

After the emplacement of the El Cerro Igneous Complex intrusive suite, Frontino arc magmatism ended and plutonism shifted eastwards, where arc migration was associated with the genesis of the Middle Cauca Belt (MCB) (Leal-Mejía et al., 2019; Shaw et al., 2019). In the present study, we present a geochemical comparison between both arcs according to lithogeochemical data of the intrusions in the El Cerro Igneous Complex, presented in the Cordillera Occidental project of the Servicio Geológico Colombiano (Rodríguez and Zapata, 2012; Rodríguez-García and Bermúdez-Cordero, 2015) (Annex 1), and lithogeochemical data from MCB intrusions: Buriticá andesite and La Colosa cluster (Gil-Rodríguez, 2010; Lesage et al., 2013) (Annexes 2 and 3).

According to the alumina saturation index (Shand, 1943), the El Cerro Igneous Complex intrusive suite corresponds to the metaluminous series (Figure 22a), which is consistent with the mineralogy of the intrusives. The elemental behavior of the El Cerro Igneous Complex intrusions exhibits a shoshonitic

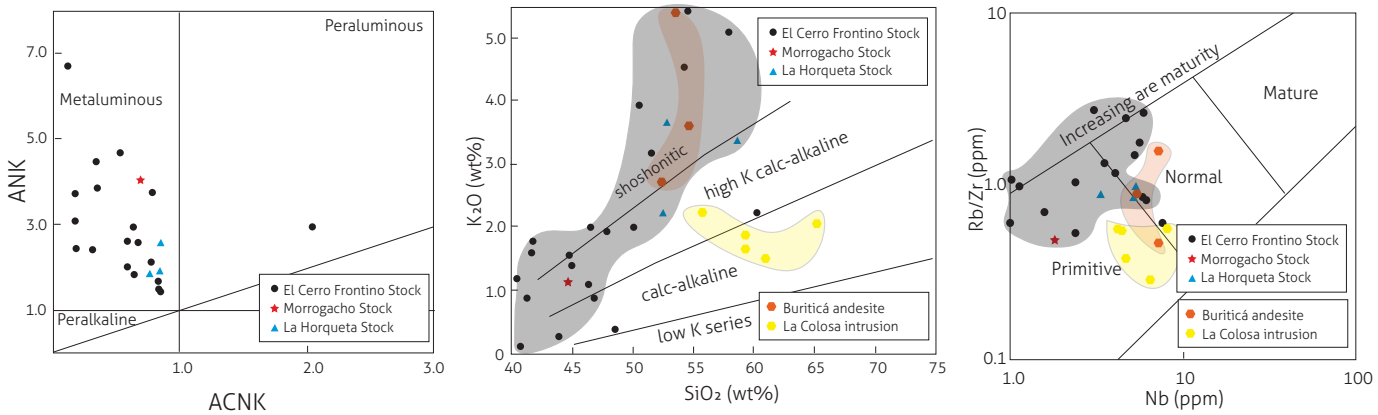

Figure 22. a) Alumina saturation index after Shand (1943). b) Relationship between SiO_2 and K_2O content-Peccerillo and Taylor (1976). c) Arc maturity discrimination diagram after (Brown, 1984)
Geochemical data from Gil-Rodríguez (2010); Rodríguez and Zapata (2012); Lesage et al. (2013), and Rodríguez-García and Bermúdez-Cordero (2015).

to high-K calc-alkaline geochemical signature, which marks a high content of K in the parental magma, which is evident locally by the high content of biotite (Figure 22b). Furthermore, detailed petrographic studies show late magmatic K metasomatism along the Cerro Frontino intrusive, which can also be associated with K enrichment. This alteration is reflected in the replacement of augite and diopside by hornblende and euhedral Fe-rich biotite (Escobar and Tejada, 1992; Shaw et al., 2019), with alteration haloes along the veinlet margins marked by the coarsening of biotite and by calc-silicate mineral assemblage. Late hydrothermal effects include local replacement of biotite by chlorite and epidote (Escobar and Tejada, 1992; Shaw et al., 2019). Similarly, Buriticá andesite plots in the shoshonitic series with a sample close to the high-K calc-alkaline series, which is related to an increase in K- content due to potassic hydrothermal alteration (Lesage et al., 2013)Colombia. It is hosted by the late Miocene Buriticá andesite porphyry, a shallow-level pluton dated at 7.41 ± 0.40 Ma (2σ, MSWD = 2.30; 40Ar/39Ar on hornblende. The porphyry intrusion of the La Colosa deposit shows a decrease in K_2O content in comparison to Buriticá and El Cerro Igneous Complex suite intrusions (Figure 22b). Maturity discrimination diagrams display Rb/Zr and Nb compositions related to a primitive to mature arc that is associated with the presence of an initial stage of plutonism in the volcanic arc formed after the Baudó terrane collision (Figure 22c).

Multielemental trace element composition diagrams were used to compare Frontino arc intrusions with some porphyry intrusive samples of the early, intermediate and late units of the La Colosa deposit presented by Gil-Rodríguez (2010) and porphyritic intrusions of the Buriticá Andesite. REE normalized diagrams show a great similarity between the middle Cauca belt and El Cerro Igneous Complex, in certain patterns (Figure 23a). There is enrichment in LREEs with respect to HREEs, which is shown in the decreasing slope with generally flat HREE values, indicating enrichment in LREEs and fractionation of the intrusion that is consistent with the fertile intrusive bodies in both arcs, as expected (Figure 23b). The plotted REE data show that these magmatic arcs were formed as a response to a main tectonic event of Baudó terrain accretion, as they share general REE characteristics. Conversely, spider diagrams show a clear impoverishment, with negative anomalies of Ba, Rb, Th, U, Zr, Nb and Ta in the El Cerro Igneous complex in comparison to the Middle Cauca Belt intrusive suites. These discrepancies could be related to the more evolved composition in the magmatic arc environment, with possible crustal contamination higher in the middle Cauca Belt due to U, Th, and Pb anomalies.

In this way, the El Cerro Igneous Complex in relation to the MCB is a less developed and undifferentiated magmatic arc that formed from a more mafic and impoverished source with less crustal contamination (negative Th, U, Zr, Nb and Ta anomalies). Frontino arc magmatism preceded the formation of the Middle Cauca Belt for at least 3 Ma, when the axis of the magmatic arc migrated eastwards towards the Romeral shear zone. Although the general geochemical signatures of both arcs are similar, the El Cerro Igneous Complex intrusions have formed in a postcollisional extensional regime with different slab conditions than those associated with the MCB (Leal-Mejía et al., 2019; Shaw et al., 2019).

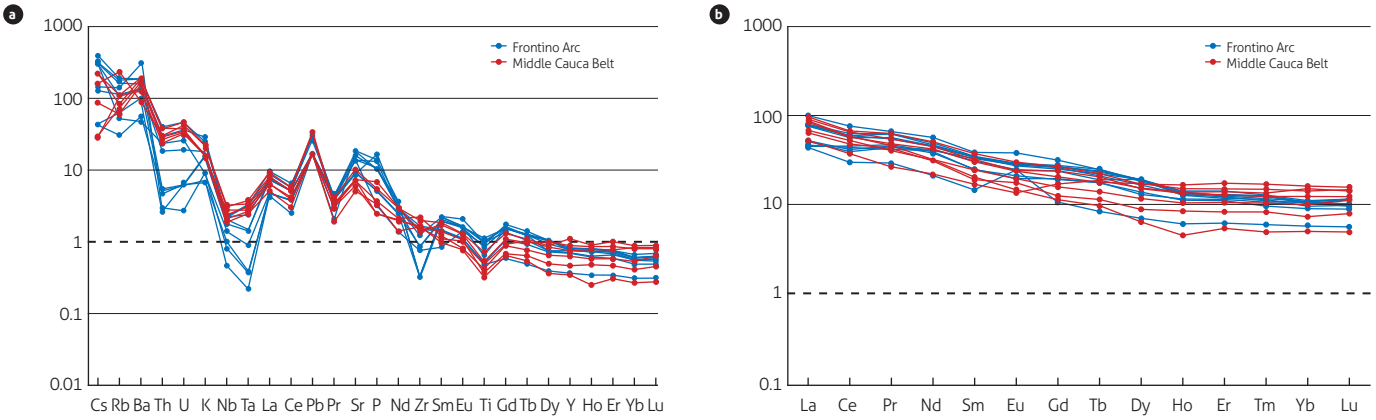

Figure 23. Spider and rare earth element (REE) discrimination diagrams normalized to N-MORB and chondrite, respectively (Sun and McDonough, 1989) Geochemical information from Rodríguez-García and Bermúdez-Cordero (2015); Rodríguez and Zapata (2012); Lesage et al. (2013) and Gil-Rodríguez (2010).

6.2 Metallogenic characteristics and deposit classification

Mineralizations in the El Cerro Igneous Complex are present as a series of shear-related veins, subparallel planar-sheeted quartz extension veins, and quartz-carbonate tabular-shaped extension veins spanning from a few centimeters to several meters in width. The metallic signature consists of Au + Ag + Cu + Zn + Pb + As (± Te ± Bi ± Sb ± Hg ± W) assemblages. Mineralization occurs as breccias in shear zones with important sulfide contents, massive milky quartz extension veins filling fractures as arrays, and rarely as stockworks. The mineralogy consists of quartz and calcite as gangue with pyrrhotite, pyrite, chalcopyrite, Fe-rich sphalerite, galena and arsenopyrite, and it includes more than two mineralization stages. General features of the mineralogy indicate common assemblages; however, mineralization in the El Cerro igneous complex corresponds to fine- to coarse-grained gold and electrum grains.

The most common hydrothermal alteration is chloritization proximate to the back of the veins in discrete selvages. Additionally, there are high quantities of sericite, carbonate, pyrite, and illite and a replacement of coarser biotite by chlorite and rare epidote in the margin of the veins. Extension veins are hosted in the intrusives and fault-shear veins in the country rocks. The contact aureole of the intrusives developed albite-chlorite-pyroxene-hornblende hornfels. The alteration of the distal sector in the thermal aureole occurs as interstitial silica dominant-grain recrystallization of the sedimentary country rocks. The presence of skarn mineralizations in the El Cerro Frontino stock with high tungsten concentrations has been described in the La Loaiza area (Molina and Molina, 1984; Escobar and Tejada, 1992). Dikes and breccias with low sulfide and gold contents occur along the El Cerro Frontino stock related to differentiation processes during intrusion.

Mineralized structures of the Frontino-Morrogacho district have preferential E-strikes, dominant subvertical (60°-90°) to rarely subhorizontal (20°-50°) S-dipping angles, and secondary N- and NW-striking, steeply to vertically E-dipping structures in the Media Cuesta-Pizarro area. Subhorizontal structures allowed the fluid percolation of the subvertical structures in zones such as El Apique, and the E-striking vertical and subvertical dip of the stratigraphic bedding in the country rocks allows it, which is coincident with the trend of mineralization and should contribute to the formation of debility planes along the strata. The presence of these structures corresponds to the main fractures and alignments of the intrusives in the El Cerro Igneous Complex, which are related to pre-syn-mineral structural processes associated with the cooling of the plutons. There is a consistent similarity in the vein and fault orientations over the complex with a general E-strike for extension veining and ENE-, N- and NW-strikes in oblique fault and shear-related veins, indicating E-W shortening at the time of mineralization (Figure 24).

Sheeted and tabular auriferous extension veins in the complex show no displacement, with unstrained orthogonally growing pyramidal quartz crystals in the vein borders indicating a position of the minimum principal stress σ_3 with a subhorizontal broadly N-S extension orientation (Stephens et al., 2004). Intermediate σ_2 and maximum σ_1 are broadly E-W oriented with vertical orientations, which coincides with thinned zones of the intrusions. Veins do not have any evident deflection across the pluton-country rock transition, showing consistent stress trajectories. Consequently, the emplacement and crystallization of the stocks occurred at the time of vein formation. A ductile-brittle transition in the formation of the veins is evidenced by tensile failure in the bulk rock resulting in the formation of σ_1 parallel to E-striking extension veins and orthogonal to pure σ_3 extension (Sibson, 1992). N- and NW-trending fault veins are thought to be misoriented with respect to σ_1 and are likely developed related to N-S regional trending structures that formed pre- or early synmagmatic. However, increased fluid pressure after plutonic suite boiling could generate re-failure episodes of the N- and NW-structures found in Pizarro and Media Cuesta (Figure 25).

Plutons were emplaced during the collision of the Baudó terrane and record less oxidized and more alkaline signatures than those found in the intrusions of the Middle Cauca Belt in a deeper epizonal environment. According to the mineralogical and structural characteristics, the Frontino-Morrogacho gold district could be classified as an intrusion-related gold system (IRGS) (Lang and Baker, 2001; Hart, 2007). Intrusives associated with IRGs are emplaced in an extensional postcollisional regime in the form of isolated, cylindrical-shaped and elongated plutons that reflect structural controls during emplacement (Mair et al., 2006; Hart, 2007). Hydrothermal processes in the systems are related to the cooling history of the plutons with exsolved fluids circulating near a brittle cupola-carapace in the roofs of plutons, allowing the fluid to focus in the apex, such as in the Tajo Abierto Mine. At the El Cerro Igneous Complex, intrusions occur as cylindrical-shaped isolated stocks with steep sides and domed or cupola-like roofs where fluid focusing is

enhanced due to the pluton geometry (Hart, 2007). Furthermore, sharp shoulders in igneous bodies are related to structural and rheological contrast that enhances the development of fluid focusing structures (Stephens et al., 2004).

The presence of carbonates and pyrrhotite in the mineralization and chlorite-sericite-carbonate-pyrite alteration assemblages in discrete margins of the veins indicates a considerably reduced fluid with neutral to alkaline pH and high CO_2 con-

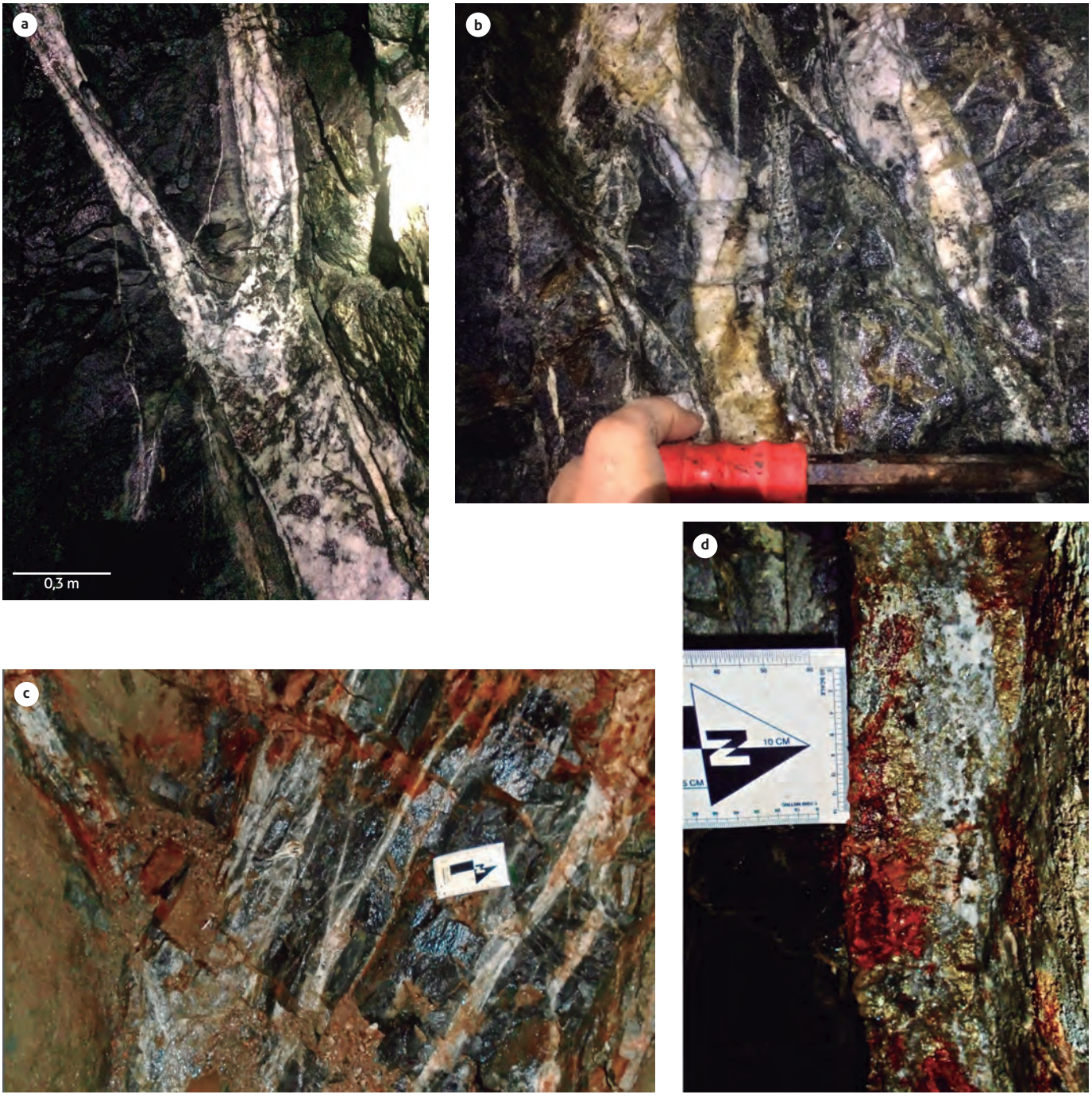

Figure 24. Principal arrangements of high-grade gold veins in the Frontino-Morrogacho gold district
a) Extensional vein bifurcation in Los Hoyos mine. b) Nest of veins and veinlets in Los Hoyos mine. c) Multimeter-wide horse-tail splay of sheeted veins in Morrogacho-Popales. d). Massive sulfide vein hosted in hornfels in La Horqueta.

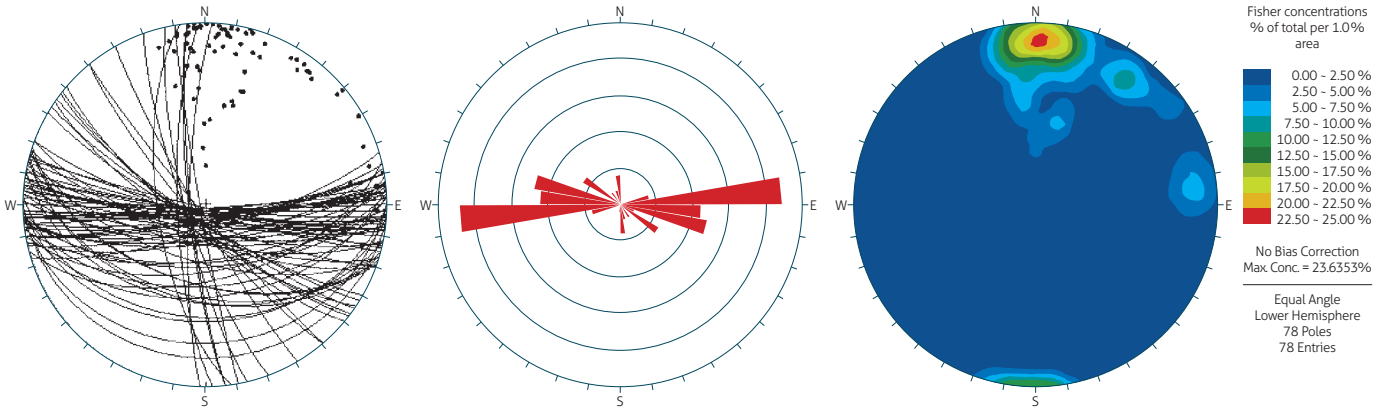

Figure 25. Main structural characteristics for the mineralized structures of Frontino-Morrogacho gold district, according to the structural attitude of 78 mineralized veins. Horsetail with main structural orientations of the veins

tent, in which $Au(HS)_2$ was probably the ligand and transport media (Mikucki, 1998; Goldfarb et al., 2004). The metal assemblage shows the presence of gold with As, Te and Bi with general low- to high-grade gold and sulfide contents less than 10% on average. The gold-silver ratio is variable from 10:1 and 1:1.

Concentric metal zoning was found as Au-Cu ± Bi ± Te extensional sheeted veins in the center and shoulders of the intrusions, As-Au assemblages mainly in the contact aureole, and Au-Ag-Pb-Zn mineralizations in peripheral-distal fault vein structures, such as those observed in the El Mocho mine, peripherally located in the Morrogacho stock. In this way, the Frontino-Morrogacho district shows some characteristics related to the reduced (ilmenite-series) intrusion-related gold systems, although it is associated with magnetite-bearing plutons with magmatic pyrite, indicating oxidizing conditions of the redox state (Ishihara, 1981; Hart, 2007).

6.3 Evolution of the El Cerro Igneous Complex

The magmatic and tectonic evolution of the El Cerro Igneous Complex is associated with late- to mid-Miocene erratic subduction-related magmatism due to the approximation of the Baudó terrane at 11-12 Ma (Maya, 1992; Cediel and Shaw, 2003). This complex is part of calc-alkaline to shoshonitic geochemical series plutons (Rodríguez and Zapata, 2012), with intermediate to mafic compositions, high pyroxene contents and the presence of secondary biotite as a product of potassic metasomatism. The high-K content of the intrusives is related to a late magmatic K-metasomatism event associated with the cooling of the pluton (Escobar and Tejada, 1992; Shaw et al., 2019), which is considered to be premineralization due to the textural relationship shown in veins and veinlets in the El Cerro Frontino gabbro. Cerro Frontino and Morrogacho stocks show different intrusion phases that are overprinted. At least two phases of the El Cerro Frontino stock are described in the present study: a mafic initial gabbroic pulse with high pyroxene content and a later dioritic pulse, both hosting mineralized structures. The Morrogacho stock is related to different intermediate- to felsic intrusions with local dioritic dikes and satellite bodies that host mineralized structures, such as Media Cuesta. The presence of these igneous phaneritic bodies represents part of the deepest mid- to late-Miocene magmatic arc, with elevated morphologies due to the high rates of exhumation and erosion that took place since the late Miocene (Villagómez and Spikings, 2013).

The tectonic setting of the El Cerro Igneous Complex emplacement is related to the subduction of the young and hot Nazca Plate during the beginning of the flattening of the slab below the South American Plate in the mid- to late Miocene (Pennington, 1981; Hardy, 1991; van der Hilst and Mann, 1994; Gutscher et al., 2000a). In this setting, the initial volcanism stages presented a calc-alkaline affinity with a later increase in alkalis related to slab melting due to the steepness of the subducted slab (Barberi et al., 1974; Gutscher et al., 2000b). Oblique convergence of the Baudó terrane during the accretion gave place to rotation and fragmentation with uplift and faulting during the stabilization of the arc in a local postcollisional extensional regime (Karig, 1974), in which the El Cerro Igneous Complex plutons were emplaced (Figure 26). The posterior evolution of the arc allowed the enrichment of the intrusions where several alteration and mineralization proces-

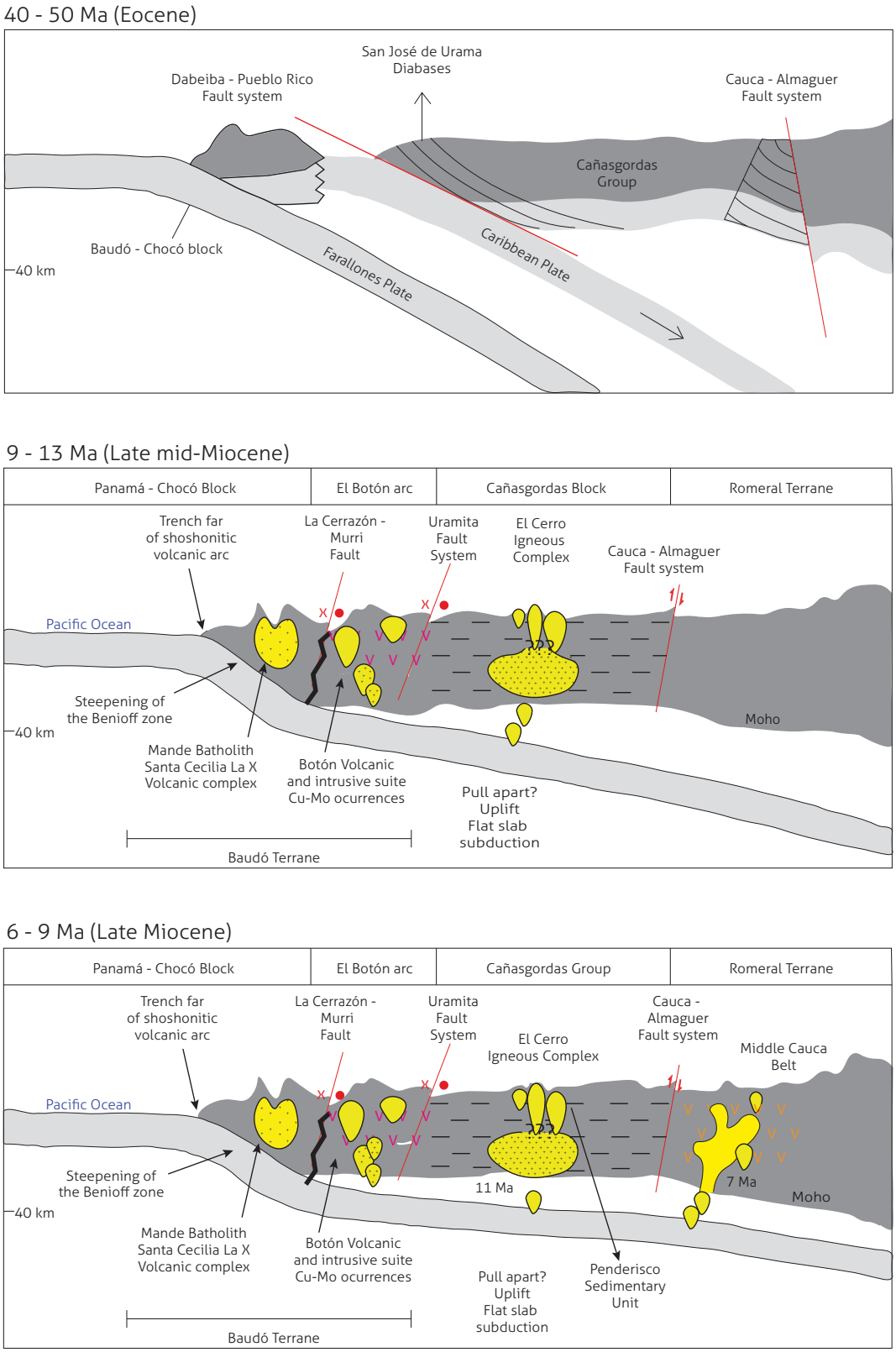

Figure 26. Regional tectonic evolution during the emplacement of the late- to mid-Miocene plutons, and 9-13 Ma emplacement of the El Cerro Igneous Complex with an unknown main magma source

ses occurred and genesis of the Frontino-Morrogacho district took place.

7. Conclusions

The magmatic and structural features of the Frontino-Morrogacho gold district allow us to classify it as an intrusion-related gold system (IRGS), which is spatially associated with the presence of the late- to mid-Miocene El Cerro Igneous Complex. Petrographic, mineral chemistry and field studies suggest the presence of concentric metal zoning in the district with a general Au + Ag + Cu + Zn + Pb + As (± Te ± Bi ± Sb ± Hg ± W) metallic assemblage. The mineralized structures are dominantly E- and steeply S-dipping, with reactivated N- and NW-striking structures in the form of extension veins, shear veins and fault veins and with the presence of extensional duplex and horse tails in broad mineralized zones.

The Frontino-Morrogacho district is an underexplored metallogenic area of late- to mid-Miocene age that holds great potential for the exploration of gold-silver deposits. Corresponding to an independent arc episode that marks the existence of an individual metallogenic belt spreading for at least 300 km, from the south of Chocó Province to the north of Antioquia Province. The presence of multiple unroofed and roofed plutonic suites hosting gold, silver and copper mineralization is commonly observed in the vicinities of the Frontino-Morrogacho gold district in rocks of similar age and characteristics. This type of mineralization is observed in extensional sheeted vein zones in the apex of the San Juan stock, fault veins containing gold-base metal sulfides in shear and breccias peripheral to the Páramo Frontino stock and Cu-Au-Ag porphyry style mineralization associated with intrusive phases of the Carauta stock (Arrubla and Silva-Sánchez, 2019). In the genesis of the Frontino-Morrogacho gold district, there is probably a key role associated with the redox state during the enrichment of Au-Ag in volatile phase separation to produce economic concentrations during the crystallization of the magmas.

The gold content in the Frontino-Morrogacho district is similar in several of the mineralized structures; hence, gold identified in three different families is mainly associated with the presence of pyrrhotite, chalcopyrite, tellurides and alloys with a high presence of Bi and Sb. The first family is characterized by Au-rich electrum with gold contents varying from 66 to 78 Au % wt, the second family presents average electrum with gold contents varying from 50 to 60 Au % wt, and the third family is characterized by Ag-rich electrum and tellurides with gold contents varying from 32 to 40 Au % wt.

An important magmatic relationship exists between the Middle Cauca Belt and the Frontino Arc/Frontino-Morrogacho gold district. Frontino Arc was formed in a low-angle postcollisional environment as a precursor of posterior middle Cauca belt magmatism. In this way, the Frontino-Morrogacho magmatic event is related to an initial stage of plutonism that migrated to the east after the El Cerro Igneous Complex Intrusive event ended at an uncertain age, with magmatic genesis initiating afterwards in a sector of the Middle Cauca Belt. Subsequently, the mineral assemblages and mineralization styles are quite different due to the differences between the geochemical signature of the plutons and the geodynamical setting of both arcs.

Further studies concerning fluid chemistry should include detailed microthermometry and Raman spectroscopy of fluid inclusions to determine the temperature and pressure of the fluid associated with the different events of mineralization. In this way, the fluid salinity and sulfur compositions in the magmatic fluids can be determined. Zircon U/Pb, molybdenite Re-Os, Sm/Nd, and sericite-muscovite Ar-Ar geochronological data analyses will be useful to find the absolute timing relationship between plutonism and mineralization, with Pb, S, H and O isotopic data to determine the source of the mineralization fluids. Stable isotopic oxygen analyses will assist in constraining the magmatic and country rock continuum to establish a possible interaction between fluid phases. Finally, combined pluton thermal metamorphic, pluton crystallization and mineralization ages should aid in identifying the evolution of the mineral process and identifying new targets.

Supplementary Data

Supplementary data for this article can be found online at https://doi.org/10.32685/0120-1425/bol.geol.48.1.2021.500

Acknowledgments

In the memory of our friend Alcibar Alcaraz Puerta, former mining inspector and gold refiner of the Frontino, Abriaquí, Cañasgordas and Buriticá districts over a period of 40 years. His multiples decades of work and trajectory with local artisanal miners allowed access to the gold mines, while his knowledge provided a basis for the geological understanding of this underexplored gold mining district. Special greetings to Frank

Vanegas, gold refiner and jeweller, and to his family the Vanegas, victims of the Colombian Armed Conflict that opened their doors to the researchers. Furthermore, the authors are truly thankful for the observations and comments of Juan Sebastián Durán, an economic geologist. The authors are grateful to the anonymous reviewers for their valuable suggestions and recommendations that helped to improve this manuscript.

References

Agrominera El Cerro. (1992). *Estudio técnico-económico de la Mina el Cerro*. Solicitud de Crédito de Fomento.

Alarcón, J. (2008). *Reconocimiento y exploración preliminar del prospecto aurífero El Cerro. Municipio de Frontino, Departamento de Antioquia*. Universidad Industrial de Santander.

Álvarez, E., & González, H. (1978). *Geología y geoquímica del cuadrángulo I-7*. Ingeominas.

Arrubla, F. (2018). *Geology and Geochemistry of the Frontino-Morrogacho Gold District*. Universidad de los Andes, Colombia.

Arrubla, F., & Silva-Sánchez, S. (2019). Geología de las mineralizaciones auríferas de tipo Intrusion-Related en el Distrito Minero Frontino-Morrogacho. *XVII Congreso Colombiano de Geología*. Santa Marta.

Barberi, F., Innocenti, F., Ferrara, G., Keller, J., & Villari, L. (1974). Evolution of Eolian arc volcanism (southern Tyrrhenian Sea). *Earth and Planetary Science Letters*, *21*(3), 269-276. https://doi.org/10.1016/0012-821X(74)90161-7

Bartos, P. J., García, C., & Gil, J. (2017). The Nuevo Chaquiro Cu-Au-(Mo) Porphyry Deposit, Middle Cauca Belt, Colombia: Geology, Alteration, Mineralization. *Economic Geology*, *112*(2), 275-294. https://doi.org/10.2113/econgeo.112.2.275

Brown, G. C., Thorpe, R. S., & Webb, P. C. (1984). The geochemical characteristics of granitoids in contrasting arcs and comments on magma sources. *Journal of the Geological Society*, *141*(3), 413-426. https://doi.org/10.1144/gsjgs.141.3.0413

Buchely, F., Parra, E., Castillo, H., González, F., Dávila, C., & Romero, O. (2009). *Realización de la cartografía geológica y muestreo geoquímico en las planchas 144, 145, 128, 129, 113 y 114*. Ingeominas.

Cediel, F., & Shaw, R. P. (2003). *Tectonic Assembly of the Northern Andean Block*. In C. Bartolini, R. T. Buffler, & J. Blickwede (eds.), *The Circum-Gulf of Mexico and the Caribbean: Hydrocarbon habitats, basin formation, and plate tectonics: AAPG Memoir 79*, pp. 815-848.

Duque-Caro, H. (1990). The Choco Block in the northwestern corner of South America: Structural, tectonostratigraphic, and paleogeographic implications. *Journal of South American Earth Sciences*, *3*(1), 71-84. https://doi.org/10.1016/0895-9811(90)90019-W

Escobar, L. A., & Tejada, N. (1992). *Prospección de Platino en Piroxenitas y de Oro en Skarn en la Mina Don Diego, El Cerro, Frontino (Antioquia)*. (B. Sc. thesis). Universidad Nacional de Colombia, Facultad de Ciencias.

Etayo-Serna, F., Barrero, D., Lozano, H., Espinosa, A., González, H., Orrego, A., Ballesteros, I., Forero, H., Ramírez, C., & Zambrano, F. (1983). *Mapa de terrenos geológicos de Colombia*. Publicación Geológica Especial, 14. Ingeominas.

Fenix Oro. (2020). *Fenix Oro Launches Drill Program at Abriaqui*. Technical report.

Flórez, M. (1988). *Monografía de los distritos mineros de El Cerro, La Antigua, Popales, Musinga y Mediacuesta en Frontino, Abriaqui y Cañasgordas en el departamento de Antioquia*. Ingeominas.

Geoestudios. (2005). *Complementación geológica, geoquímica y geofísica de la parte occidental de las planchas 130 Santa Fé de Antioquia y 146 Medellín occidental. Escala: 1:100.000*. Ingeominas.

Gil-Rodríguez, J. (2010). *Igneous petrology of the Colosa gold-rich porphyry system (Tolima, Colombia) (PSM/EG Thesis)*. University of Arizona.

Goldfarb, R. J., Ayuso, R., Miller, M. L., Ebert, S. W., Marsh, E. E., Petsel, S. A., Miller, L. D., Bradley, D., Johnson, C., & McClelland, W. (2004). The late Cretaceous Donlin Creek gold deposit, Southwestern Alaska: Controls on epizonal ore formation. *Economic Geology*, *99*(4), 643-671. https://doi.org/10.2113/gsecongeo.99.4.643

Goldfarb, R., Hart, C., Miller, M, Miller, L., Farmer, G. L., & Groves, D. (2000). The Tintina Gold Belt: A global perspective. In *The Tintina Gold Belt: Concepts, exploration, and discoveries*, special volume 2. British Columbia and Yukon Chamber of Mines.

González, H., & Londoño, A. (2002). *Catálogo de las unidades litoestratigráficas de Colombia, Granodiorita de Nudillales, Cordillera Occidental, Departamento de Antioquia*. Ingeominas.

Gutscher, M. A., Maury, R., Eissen, J. P., & Bourdon, E. (2000a). Can slab melting be caused by flat subduction? *Geology*,

28(6), 535-538. https://doi.org/10.1130/0091-7613(2000)28<535:CSMBCB>2.0.CO;2

Gutscher, M., Spakman, W., Bijwaard, H., & Engdahl, E. R. (2000b). Geodynamics of flat subduction: Seismicity and tomographic constraints from the Andean margin. *Tectonics*, *19*(5), 814-833. https://doi.org/10.1029/1999TC001152

Hardy, N. C. (1991). Tectonic evolution of the easternmost Panama Basin: Some new data and inferences. *Journal of South American Earth Sciences*, *4*(3), 261-269. https://doi.org/10.1016/0895-9811(91)90035-J

Hart, C. J. R. (2007). Reduced intrusion-related gold systems. In Goodfellow, W. D. (ed.), *Mineral deposits of Canada: A Synthesis of Major Deposit Types, District Metallogeny, the Evolution of Geological Provinces, and Exploration Methods*. Special Publication 5. Geological Association of Canada, Mineral Deposits Division.

Hart, C. J. R., McCoy, D., Goldfarb, R. J., Smith, M., Roberts, P., Hulstein, R., Bakke, A. A., & Bundtzen, T. K. (2002). Geology, exploration and discovery in the Tintina gold province, Alaska and Yukon. In *Integrated Methods for Discovery: Global Exploration in the Twenty-First Century*. Special Publication 9. Society of Economic Geologists. https://doi.org/10.5382/SP.09.12

Hill, G. (1961). *Brief report on the Carmel Vallet Mines with special reference to the Las Hebras Lode.*

Ishihara, S. (1981). The granitoid series and mineralization. In *Seventy-Fifth Anniversary Volume*, Economic Geology Publishing Company. https://doi.org/10.5382/AV75

Karig, D. E. (1974). Evolution of arc systems in the western Pacific. *Annual Review of Earth and Planetary Sciences*, *2*(1), 51-75. https://doi.org/10.1146/annurev.ea.02.050174.000411

Lang, J. R., & Baker, T. (2001). Intrusion-related gold systems : the present level of understanding. *Mineralium Deposita*, *36*, 477-489. https://doi.org/10.1007/s001260100184

Leal Mejía, H., Shaw, R. P., & Malgarejo Draper, J. C. (2019). Spatial-temporal migration of granitoid magmatism and the Phanerozoic tectono-magmatic evolution of the Colombian Andes. In Cediel, F., & Shaw, R. P. (eds), *Geology and Tectonics of Northwestern South America. Frontiers in Earth Sciences.* (pp. 253-410). Springer. https://doi.org/10.1007/978-3-319-76132-9_5

Leal-Mejía, H. (2011). *Phanerozoic Gold Metallogeny in the Colombian Andes: A Tectono-Magmatic Approach* (Ph.D. Thesis). Universitat de Barcelona.

Leal-Mejía, H., Celada C. M., Luengas, C., Velásquez, L., Prieto, D., Moyano, I., Prieto, G., López I., J. A., & Sepúlveda, J. (2016). *El mapa metalogénico de Colombia v. 2016: Un avance en la compilación e integración de información reciente de los depósitos minerales del país y el conocimiento de los recursos del subsuelo* [Conference paper]. XVI Congreso Colombiano de Geología and III Simposio de Exploradores, Santa Marta, Colombia.

Lesage, G., Richards, J. P., Muehlenbachs, K., & Spell, T. L. (2013). Geochronology, geochemistry, and fluid characterization of the late miocene buriticá gold deposit, Antioquia department, Colombia. *Economic Geology*, *108*(5), 1067-1097. https://doi.org/10.2113/econgeo.108.5.1067

Mair, J. L., Goldfarb, R. J., Johnson, C. A., Hart, C. J. R., & Marsh, E. E. (2006). Geochemical constraints on the genesis of the Scheelite Dome intrusion-related gold deposit, Tombstone gold belt, Yukon, Canada. *Economic Geology*, *101*(3), 523-553. https://doi.org/10.2113/gsecongeo.101.3.523

Maya, M. (1992). Catálogo de dataciones isotópicas en Colombia. *Boletín Geológico*, *32*(1-3), 127-187.

Mejía, M., & Salazar, G. (1989). Memoria explicativa de la Geología de la Plancha 114 (Dabeiba) y parte W de la 115 (Toledo). Ingeominas.

Mikucki, E. J. (1998). Hydrothermal transport and depositional processes in Archean lode-gold systems: A review. *Ore Geology Reviews*, *13*(1-5), 307-321. https://doi.org/10.1016/S0169-1368(97)00025-5

Molina, C., & Molina, A. (1984). *Estudio de la génesis y paragénesis de la mina San Diego el Cerro, Frontino (Antioquia).* Universidad Nacional de Colombia.

Noriega, S., Caballero-Acosta, J. H., & Rendón-Rivera, A. (2012). Estudio morfotectónico de un tramo del río Herradura entre los municipios de Frontino y Abriaquí, Departamento de Antioquia, Cordillera Occidental de Colombia. *Geología Colombiana*, *37*, 49-50.

Page, W. (1986). *Geología sísmica y sismicidad en el noroccidente colombiano*. ISA-Integral. Woodward & Clyde Consultants.

Peccerillo, A., & Taylor, R. (1976). Geochemistry of eocene calc-alkaline volcanic rocks from the Kastamonu area, Northern Turkey. *Contributions to Mineralogy and Petrology*, *58*(1), 63-81. https://doi.org/10.1007/BF00384745

Pennington, W. D. (1981). Subduction of the eastern Panama Basin and seismotectonics of northwestern South America.

Journal of Geophysical Research: Solid Earth, *86*(B11), 10753-10770. https://doi.org/10.1029/JB086iB11p10753

Rodríguez García, G., & Arango Mejía, M. (2013). Formación Barroso: Arco volcánico toleitico y Diabasas de San José de Urama: Un prisma acrecionario T-Morb en el segmento norte de la Cordillera Occidental de Colombia. *Boletín de Ciencias de La Tierra*, *33*, 17-38.

Rodríguez García, G., & Bermúdez-Cordero, J. G. (2015). Petrografía, geoquímica y edad del Gabro de Cerro Frontino. *Boletín de Ciencias de la Tierra*, *38*, 25-40. https://doi.org/10.15446/rbct.n38.46053

Rodríguez, G., & Zapata, G. (2012). Características del plutonismo mioceno superior en el segmento norte de la cordillera occidental e implicaciones tectónicas en el modelo geológico del noroccidente colombiano. *Boletín de Ciencias de La Tierra*, *31*, 5-22.

Rodríguez, G., Cetina, T., & María, L. (2016). Caracterización petrográfica y química de rocas de corteza oceánica del Complejo Quebradagrande y comparación con rocas de la Unidad Diabasas de San José de Urama. *Boletín de Geología*, *38*(3), 15-29. https://doi.org/10.18273/revbol.v38n3-2016001

Servicio Geológico Colombiano (SGC). (2015). *Mapa metalogénico de Colombia*. Convenio especial de cooperación SGC-MDRU.

Serviminas. (2017). Reporte técnico interno Mina San Diego.

Shand, S. J. (1943). *Eruptive rocks: their genesis, composition, classification, and their relation to ore deposits with a chapter on meteorites*. T. Murby & co.

Shaw, R. P., Leal-Mejía, H., & Malgarejo Draper, J. C. (2019). Phanerozoic metallogeny in the Colombian Andes: a tectono-magmatic analysis in space and time. In *Geology and Tectonics of Northwestern South America* (pp. 411-549). Springer.

Sibson, R. H. (1992). Implications of fault-valve behaviour for rupture nucleation and recurrence. *Tectonophysics*, *211*(1-4), 283-293. https://doi.org/10.1016/0040-1951(92)90065-E

Silva-Sánchez, S. (2018). *Geochemical and petrographic analyses of mutatá basalts and its relationship with the volcanic expressions of the Colombian northwest, tectonic implications (Bachelor thesis)*. Universidad de los Andes.

Stephens, J. R., Mair, J. L., Oliver, N. H. S., Hart, C. J. R., & Baker, T. (2004). Structural and mechanical controls on intrusion-related deposits of the Tombstone Gold Belt, Yukon, Canada, with comparisons to other vein-hosted ore-deposit types. *Journal of Structural Geology*, *26*(6-7), 1025-1041. https://doi.org/10.1016/j.jsg.2003.11.008

Streckeisen, A. (1974). Classification and nomenclature of plutonic rocks recommendations of the IUGS subcommission on the systematics of igneous rocks. *Geologische Rundschau*, *63*(2), 773-786. https://doi.org/10.1007/BF01820841

Sun, S. S., & McDonough, W. F. (1989). *Chemical and isotopic systematics of oceanic basalts: implications for mantle composition and processes*. Special Publications 42. Geological Society. https://doi.org/10.1144/GSL.SP.1989.042.01.19

Van der Hilst, R., & Mann, P. (1994). Tectonic implications of tomographic images of subducted lithosphere beneath northwestern South America. *Geology*, *22*(5), 451-454. https://doi.org/10.1130/0091-7613(1994)022<0451:TIOTIO>2.3.CO;2

Villagómez, D., & Spikings, R. (2013). Thermochronology and tectonics of the Central and Western Cordilleras of Colombia: Early Cretaceous-Tertiary evolution of the northern Andes. *Lithos*, *160-161*, 228-249. https://doi.org/10.1016/j.lithos.2012.12.008

Zapata, G., & Rodríguez, G. (2011). Basalto De El Botón, Mioceno Volcanic Arc of Shoshonitic Affinity To the North of Cordillera Occidental of Colombia. *Boletín de Ciencias de La Tierra*, *30*, 77-92.

Zuluaga, J., & Hoyos, P. (1978). *Estudio geológico del Grupo Cañasgordas: Sección Boquerón del Toyo- Dabeiba*. Universidad Nacional de Colombia.

ANNEXES

Annex 1. Lithogeochemical data taken from the Cordillera Occidental Project of the Servicio Geológico Colombiano (Rodríguez and Zapata, 2012; Rodríguez-García and Bermúdez-Cordero, 2015)

		Analyte Symbol	SiO_2	Al_2O_3	$Fe_2O_3(T)$	MnO	MgO	CaO	Na_2O	K_2O	TiO_2	P_2O_5	LOI	Total
		Unit Symbol	%	%	%	%	%	%	%	%	%	%	%	%
		Detection Limit	0.01	0.01	0.01	0.001	0.01	0.01	0.01	0.01	0.001	0.01	0.01	0.01
Geological unit	Classification	Analysis Method	FUS-ICP	FUS-ICP	FUS-ICP	FUS-ICP	FUS-ICP	FUS-ICP	FUS-ICP	FUS-ICP	FUS-ICP	FUS-ICP	FUS-ICP	FUS-ICP
La Horqueta Diorite	Diorite	JZU0094	57.46	16.65	7.69	0.156	2.43	6.12	3.16	3.29	0.63	0.36	0.12	98.066
La Horqueta Diorite	Granodiorite	AAT1611	52.19	21.76	6.38	0.1	2.05	9.41	3.68	2.19	0.588	0.23	0.85	99.428
La Horqueta Diorite	Monzonite	GGC4687	52.54	18.02	8.73	0.193	3.23	7.48	3.52	3.61	0.833	0.71	0.55	99.416
Cerro Frontino Monzonite	Monzonite	BCZ3296	49.85	15.05	11.89	0.204	4.55	10.08	3.28	1.98	1.079	0.63	0.71	99.303
Cerro Frontino Monzonite	Diorite	EAG0878	54.14	19.11	6.91	0.145	2.36	6.29	3.99	4.52	0.701	0.54	0.99	99.696
Cerro Frontino Monzonite	Pyroxene Diorite	EAC3382	54.4	18.9	6.92	0.143	2.19	5.42	4.04	5.55	0.672	0.54	0.63	99.405
Cerro Frontino Monzonite	Pyroxene Diorite	EEB0102	41.4	15.97	15.96	0.217	6.37	14.5	1.51	0.85	1.428	0.93	0.88	100.015
Cerro Frontino Stock	Hornfels	GR5566	60.1	16.99	8.82	0.075	4.02	1.38	2.07	2.21	0.92	0.1	3.16	99.845
Cerro Frontino Stock	Quartzdiorite	GR5567	47.54	17.7	10.25	0.195	4.77	10.74	2.93	1.9	1.142	0.94	1.12	99.227
Cerro Frontino Stock	Gabbro	GR5568	40.25	10.55	17.21	0.247	10.11	15.81	0.67	1.17	1.395	1.12	0.75	99.282
Cerro Frontino Stock	Quartzdiorite (?)	GZG5662A	46.25	12.53	10.71	0.244	6.98	17.62	1.42	0.84	0.646	1.04	0.44	98.72
Cerro Frontino Stock	Diorite-Quartzdiorite	JFG0054B	51.16	17.88	9.5	0.16	3.58	8.09	3.08	3.1	0.906	0.75	0.8	99.006
Morrogacho Diorite	Diorite	GGC3113	44.24	17.71	13.04	0.222	6.22	11.61	1.97	1.09	0.875	0.76	1.24	98.977
Cerro Frontino Stock	Diorite Contact	HGI12689	44.97	17.03	13.47	0.24	5.72	11.45	2.64	1.36	1.18	0.94	0.67	99.67
Cerro Frontino Stock	Diorite-Monzodiorite	HGI12690A	48.73	6.98	12.24	0.352	8.97	20.13	0.9	0.36	0.478	0.68	0.27	100.09
Cerro Frontino Stock	Granodiorite-Monzodiorite	HGI12691	46.85	16.21	12.54	0.21	6.06	11.68	2.48	1.98	1.073	0.79	0.61	100.483
Cerro Frontino Stock	Diorite-Gabbro	HGI12692A	40.69	4.07	22.9	0.261	11.88	17.63	0.31	0.09	1.459	0.11	< 0.01	99.4
Cerro Frontino Stock	Diorite-Gabbro	HGI12692B	37.75	5.65	22.14	0.247	11.81	16.9	0.39	1.09	1.593	2.1	0.28	99.95
Cerro Frontino Stock	Diorite-Gabbro	HGI12692C	45.13	6.19	14.09	0.174	13.85	16.76	0.54	1.54	1.172	0.12	0.88	100.446
Cerro Frontino Stock	Diorite-Gabbro	HGI12692D	42.06	8.87	21.56	0.221	8.91	13.65	1.09	1.76	1.423	0.27	0.73	100.544
Cerro Frontino Stock	Diorite-Gabbro	HGI12692E	41.77	15.76	14.79	0.237	7.79	14.28	1.02	1.57	1.328	1.02	0.56	100.125
Cerro Frontino Stock	Diorite-Gabbro	HGI12692F	44.33	15.68	10.59	0.179	7.17	19.32	0.81	0.26	0.77	1.19	0.5	100.799
Cerro Frontino Stock	Diorite-Gabbro	HGI12692H	50.71	16.36	10.52	0.212	4.24	9.11	2.87	3.93	0.892	0.81	0.66	100.314
Cerro Frontino Stock	Diorite-Gabbro	HGI12693A	57.04	17.39	6.65	0.186	2.04	4.69	3.97	5	0.504	0.42	0.58	98.47
Cerro Frontino Stock	Diorite-Gabbro	HGI12693B	46.93	19.97	11.54	0.181	4.73	11.18	2.52	1.07	1.006	0.61	1.25	100.987

		Analyte Symbol	Sc	Be	V	Cr	Co	Ni	Cu	Zn	Ga	Ge	As	Rb	Sr	Y	Zr	Nb
		Unit Symbol	ppm	ppm	ppm	ppm	ppm	ppm	ppm	ppm	ppm	ppm	ppm	ppm	ppm	ppm	ppm	ppm
		Detection Limit	1	1	5	20	1	20	10	30	1	0.5	5	1	2	0.5	1	0.2
Geological unit	Classification	Analysis Method	FUS-ICP	FUS-ICP	FUS-ICP	FUS-MS	FUS-MS	FUS-MS	FUS-MS	FUS-MS	FUS-MS	FUS-MS	FUS-MS	FUS-MS	FUS-ICP	FUS-MS	FUS-MS	FUS-MS
La Horqueta Diorite	Diorite	JZU0094	16	2	155	40	13	< 20	30	100	19	1.4	< 5	105	916	20.4	123	5.2
La Horqueta Diorite	Granodiorite	AAT1611	14	2	194	30	14	< 20	30	70	23	0.8	< 5	52	1239	10.4	58	3.3
La Horqueta Diorite	Monzonite	GGC4687	18	2	226	< 20	23	< 20	90	130	24	1.6	< 5	90	1287	24.7	91	5.4
Cerro Frontino Monzonite	Monzonite	BCZ3296	29	3	348	40	38	< 20	150	160	25	1.8	< 5	60	891	30	410	8.4
Cerro Frontino Monzonite	Diorite	EAG0878	11	2	157	< 20	15	< 20	220	90	20	1	< 5	90	1542	18.7	33	5.9
Cerro Frontino Monzonite	Pyroxene Diorite	EAC3382	10	2	156	< 20	17	< 20	80	90	21	1.6	< 5	110	1636	20.3	61	5.7
Cerro Frontino Monzonite	Pyroxene Diorite	EEB0102	40	2	496	< 20	43	< 20	110	130	22	1	< 5	17	1224	24.4	32	2.4
Cerro Frontino Stock	Hornfels	GR5566	33	2	254	180	22	50	70	140	18	1.4	< 5	90	189	22.3	107	6.2
Cerro Frontino Stock	Quartzdiorite	GR5567	26	2	332	20	34	< 20	1450	140	21	1.5	< 5	63	1644	24.3	25	4.7
Cerro Frontino Stock	Gabbro	GR5568	58	1	588	70	56	30	260	130	16	1.7	< 5	35	781	23.1	33	1.1
Cerro Frontino Stock	Quartzdiorite (?)	GZG5662A	42	1	329	40	34	30	40	110	17	1.8	< 5	21	961	26.7	34	1
Cerro Frontino Stock	Diorite-Quartzdiorite	JFG0054B	19	2	236	20	21	< 20	150	70	17	1	< 5	84	1217	19.4	98	5.9
Morrogacho Diorite	Diorite	GGC3113	30	2	485	20	42	< 20	140	180	22	1.1	< 5	30	1441	19.5	62	1.9
Cerro Frontino Stock	Diorite Contact	HGI12689	30	2	390	30	41	< 20	80	130	20	1.3	< 5	35	1545	25.7	26	3.6
Cerro Frontino Stock	Diorite-Monzodiorite	HGI12690A	57	1	224	< 20	40	40	80	90	11	2.2	< 5	9	338	18.2	47	0.8
Cerro Frontino Stock	Granodiorite-Monzodiorite	HGI12691	33	2	323	60	32	< 20	50	110	18	1.5	< 5	78	1345	21.7	65	4.1
Cerro Frontino Stock	Diorite-Gabbro	HGI12692A	88	2	831	70	69	40	20	140	15	2	< 5	4	134	15.9	29	0.5
Cerro Frontino Stock	Diorite-Gabbro	HGI12692B	71	2	743	80	72	40	50	130	15	1.9	< 5	37	283	25.5	32	1
Cerro Frontino Stock	Diorite-Gabbro	HGI12692C	80	1	415	160	56	70	20	80	10	1.9	< 5	49	207	10.9	24	0.8
Cerro Frontino Stock	Diorite-Gabbro	HGI12692D	67	2	708	30	34	30	20	80	13	0.6	< 5	44	408	14.7	41	2.4
Cerro Frontino Stock	Diorite-Gabbro	HGI12692E	42	1	487	50	48	< 20	100	140	20	1.7	< 5	51	1350	24.5	18	3.1
Cerro Frontino Stock	Diorite-Gabbro	HGI12692F	45	1	370	30	32	20	40	70	16	1.5	< 5	7	1342	18.8	26	0.7
Cerro Frontino Stock	Diorite-Gabbro	HGI12692H	22	2	280	20	27	< 20	120	110	17	1.3	< 5	87	1428	21.9	58	5.2
Cerro Frontino Stock	Diorite-Gabbro	HGI12693A	10	3	116	< 20	13	< 20	60	90	18	1.4	< 5	140	889	23.1	231	7.7
Cerro Frontino Stock	Diorite-Gabbro	HGI12693B	26	2	370	20	27	< 20	100	120	20	1.2	< 5	23	1907	14.5	33	1.6

		Analyte Symbol	Mo	Ag	In	Sn	Sb	Cs	Ba	La	Ce	Pr	Nd	Sm	Eu	Gd	Tb	Dy
		Unit Symbol	ppm	ppm	ppm	ppm	ppm	ppm	ppm	ppm	ppm	ppm	ppm	ppm	ppm	ppm	ppm	ppm
		Detection Limit	2	0.5	0.1	1	0.2	0.1	3	0.05	0.05	0.01	0.05	0.01	0.005	0.01	0.01	0.01
Geological unit	Classification	Analysis Method	FUS-MS	FUS-MS	FUS-MS	FUS-MS	FUS-MS	FUS-MS	FUS-ICP	FUS-MS	FUS-MS	FUS-MS	FUS-MS	FUS-MS	FUS-MS	FUS-MS	FUS-MS	FUS-MS
La Horqueta Diorite	Diorite	JZU0094	< 2	< 0.5	< 0.1	< 1	< 0.2	2.7	1108	19.1	35.9	4.55	17.8	3.77	1.19	3.94	0.65	3.35
La Horqueta Diorite	Granodiorite	AAT1611	2	< 0.5	< 0.1	< 1	< 0.2	2.2	1021	10.8	19.1	2.77	10.1	2.24	1.44	2.22	0.33	1.78
La Horqueta Diorite	Monzonite	GGC4687	10	0.6	< 0.1	1	2.8	2.1	957	21	42.3	5.9	23.6	5.5	1.75	5.48	0.82	4.29
Cerro Frontino Monzonite	Monzonite	BCZ3296	2	2.3	< 0.1	1	1	0.8	720	20.6	40	5.73	23.3	5.62	1.62	5.97	0.93	4.89
Cerro Frontino Monzonite	Diorite	EAG0878	3	< 0.5	< 0.1	< 1	< 0.2	1.1	1558	20.7	39.4	5.56	20.4	4.35	1.67	4.28	0.61	3.02
Cerro Frontino Monzonite	Pyroxene Diorite	EAC3382	4	< 0.5	< 0.1	< 1	0.7	1.1	1745	20.4	39.8	5.37	20.4	4.45	1.76	4.51	0.67	3.37
Cerro Frontino Monzonite	Pyroxene Diorite	EEB0102	32	< 0.5	< 0.1	< 1	< 0.2	0.3	354	12.2	26.8	4.26	18.9	5.19	1.66	5.4	0.86	4.38
Cerro Frontino Stock	Hornfels	GR5566	< 2	< 0.5	< 0.1	< 1	< 0.2	5.5	3316	14.2	29.3	3.63	14	3.28	0.867	4.03	0.71	4.19
Cerro Frontino Stock	Quartzdiorite	GR5567	< 2	1.4	< 0.1	1	< 0.2	0.9	840	24	47.8	6.3	26.2	5.91	2.18	6.51	0.92	4.68
Cerro Frontino Stock	Gabbro	GR5568	< 2	0.6	< 0.1	< 1	< 0.2	0.3	612	11.6	27.7	4.29	19.7	5.29	1.57	5.73	0.92	4.74
Cerro Frontino Stock	Quartzdiorite (?)	GZG5662A	< 2	< 0.5	< 0.1	2	< 0.2	0.3	979	14	28.2	4.81	19.6	5.1	1.46	5.33	0.92	4.79
Cerro Frontino Stock	Diorite-Quartzdiorite	JFG0054B	< 2	< 0.5	< 0.1	< 1	< 0.2	0.9	1051	17.9	34.6	4.52	17.5	4.01	1.24	4.09	0.65	3.44
Morrogacho Diorite	Diorite	GGC3113	42	0.7	< 0.1	< 1	< 0.2	2.1	294	19.2	38.9	5.83	23.1	5.25	1.59	4.84	0.72	3.49
Cerro Frontino Stock	Diorite Contact	HGI12689	< 2	< 0.5	< 0.1	< 1	< 0.2	0.3	1001	23.1	45.7	6.22	25.4	6.06	2.08	6.55	0.98	4.99
Cerro Frontino Stock	Diorite-Monzodiorite	HGI12690A	< 2	< 0.5	< 0.1	< 1	< 0.2	0.2	102	8.44	19.4	3	13.3	3.59	0.972	4.34	0.68	3.65
Cerro Frontino Stock	Granodiorite-Monzodiorite	HGI12691	< 2	< 0.5	< 0.1	< 1	< 0.2	1	1883	18.7	38.1	5.2	21.4	5.07	1.61	5.36	0.81	4.2
Cerro Frontino Stock	Diorite-Gabbro	HGI12692A	< 2	< 0.5	< 0.1	< 1	< 0.2	< 0.1	47	2.84	9.01	1.7	9.3	2.96	0.921	3.57	0.61	3.26
Cerro Frontino Stock	Diorite-Gabbro	HGI12692B	< 2	< 0.5	< 0.1	< 1	< 0.2	0.3	499	15.3	35.6	5.36	23.7	6.14	1.76	6.66	1.05	5.19
Cerro Frontino Stock	Diorite-Gabbro	HGI12692C	< 2	< 0.5	< 0.1	< 1	< 0.2	0.4	558	2.81	7.92	1.41	7.77	2.38	0.754	2.7	0.44	2.3
Cerro Frontino Stock	Diorite-Gabbro	HGI12692D	< 2	< 0.5	< 0.1	< 1	< 0.2	0.5	408	5.59	13.7	2.1	10.6	2.79	0.916	3.17	0.53	2.86
Cerro Frontino Stock	Diorite-Gabbro	HGI12692E	2	< 0.5	< 0.1	< 1	< 0.2	0.6	740	17	35.9	5.15	22.5	5.7	1.77	5.93	0.96	4.86
Cerro Frontino Stock	Diorite-Gabbro	HGI12692F	< 2	< 0.5	< 0.1	< 1	< 0.2	0.1	97	9.62	22.3	3.48	16.3	4.38	1.41	4.84	0.75	3.82
Cerro Frontino Stock	Diorite-Gabbro	HGI12692H	< 2	< 0.5	< 0.1	< 1	0.5	0.7	1092	21	41.6	5.5	21.8	4.93	1.67	5.28	0.8	4.08
Cerro Frontino Stock	Diorite-Gabbro	HGI12693A	< 2	< 0.5	< 0.1	< 1	< 0.2	1.7	785	23.2	43.9	5.3	19.3	4.23	1.11	4.55	0.71	3.84
Cerro Frontino Stock	Diorite-Gabbro	HGI12693B	3	< 0.5	< 0.1	< 1	< 0.2	1	547	15.3	30.1	4	16.1	3.61	1.47	3.9	0.52	2.74

		Analyte Symbol	Ho	Er	Tm	Yb	Lu	Hf	Ta	W	Tl	Pb	Bi	Th	U
		Unit Symbol	ppm	ppm	ppm	ppm	ppm	ppm	ppm	ppm	ppm	ppm	ppm	ppm	ppm
		Detection Limit	0.01	0.01	0.005	0.01	0.002	0.1	0.01	0.5	0.05	5	0.1	0.05	0.01
Geological unit	Classification	Analysis Method	FUS-MS	FUS-MS	FUS-MS	FUS-MS	FUS-MS	FUS-MS	FUS-MS	FUS-MS	FUS-MS	FUS-MS	FUS-MS	FUS-MS	FUS-MS
La Horqueta Diorite	Diorite	JZU0094	0.64	1.92	0.288	1.84	0.288	3.2	0.43	< 0.5	0.24	8	< 0.1	4.7	2.07
La Horqueta Diorite	Granodiorite	AAT1611	0.35	1.03	0.152	0.97	0.144	1.6	0.12	< 0.5	0.18	< 5	< 0.1	2.23	0.9
La Horqueta Diorite	Monzonite	GGC4687	0.78	2.25	0.325	2.05	0.314	2.1	0.31	< 0.5	0.29	8	0.1	3.48	1.66
Cerro Frontino Monzonite	Monzonite	BCZ3296	0.95	2.78	0.42	2.65	0.415	8.1	0.54	< 0.5	0.23	< 5	< 0.1	2.78	1.5
Cerro Frontino Monzonite	Diorite	EAG0878	0.58	1.7	0.256	1.62	0.221	1	0.17	< 0.5	0.13	7	< 0.1	1.57	0.71
Cerro Frontino Monzonite	Pyroxene Diorite	EAC3382	0.65	1.89	0.272	1.67	0.262	1.4	0.24	< 0.5	0.18	13	< 0.1	1.61	1.03
Cerro Frontino Monzonite	Pyroxene Diorite	EEB0102	0.8	2.29	0.313	1.83	0.259	1.1	0.05	< 0.5	< 0.05	< 5	< 0.1	0.64	0.28
Cerro Frontino Stock	Hornfels	GR5566	0.83	2.47	0.381	2.5	0.396	3.1	0.49	0.8	0.75	< 5	< 0.1	4.57	1.84
Cerro Frontino Stock	Quartzdiorite	GR5567	0.79	2.14	0.295	1.73	0.25	0.9	0.2	1.2	0.12	< 5	0.1	0.59	0.29
Cerro Frontino Stock	Gabbro	GR5568	0.8	2.12	0.279	1.67	0.251	1.5	0.03	< 0.5	< 0.05	< 5	< 0.1	0.35	0.13
Cerro Frontino Stock	Quartzdiorite (?)	GZG5662A	0.86	2.41	0.337	2.05	0.304	1.2	0.05	< 0.5	< 0.05	< 5	< 0.1	0.96	0.42
Cerro Frontino Stock	Diorite-Quartzdiorite	JFG0054B	0.62	1.79	0.258	1.61	0.248	2.5	0.35	< 0.5	0.16	< 5	< 0.1	2.47	1.03
Morrogacho Diorite	Diorite	GGC3113	0.63	1.77	0.251	1.51	0.226	1.7	0.05	0.8	0.17	9	< 0.1	2.75	1.22
Cerro Frontino Stock	Diorite Contact	HGI12689	0.86	2.33	0.325	2	0.289	1	0.15	< 0.5	0.06	< 5	< 0.1	0.47	0.19
Cerro Frontino Stock	Diorite-Monzodiorite	HGI12690A	0.64	1.77	0.261	1.7	0.285	1.8	0.03	< 0.5	< 0.05	< 5	< 0.1	0.7	0.37
Cerro Frontino Stock	Granodiorite-Monzodiorite	HGI12691	0.74	1.99	0.283	1.72	0.259	1.8	0.19	< 0.5	0.19	< 5	< 0.1	0.88	0.31
Cerro Frontino Stock	Diorite-Gabbro	HGI12692A	0.57	1.53	0.212	1.25	0.188	1.4	< 0.01	< 0.5	< 0.05	< 5	< 0.1	0.08	0.03
Cerro Frontino Stock	Diorite-Gabbro	HGI12692B	0.87	2.35	0.314	1.76	0.257	1.4	0.03	< 0.5	0.05	< 5	< 0.1	0.46	0.16
Cerro Frontino Stock	Diorite-Gabbro	HGI12692C	0.39	1.01	0.136	0.8	0.116	1.1	0.02	< 0.5	0.07	< 5	< 0.1	0.2	0.1
Cerro Frontino Stock	Diorite-Gabbro	HGI12692D	0.51	1.42	0.204	1.25	0.182	1.5	0.14	1.1	< 0.05	< 5	< 0.1	0.61	0.3
Cerro Frontino Stock	Diorite-Gabbro	HGI12692E	0.84	2.25	0.312	1.85	0.268	0.9	0.12	< 0.5	0.09	< 5	< 0.1	0.22	0.09
Cerro Frontino Stock	Diorite-Gabbro	HGI12692F	0.64	1.7	0.219	1.27	0.188	1.1	< 0.01	< 0.5	< 0.05	< 5	< 0.1	0.53	0.21
Cerro Frontino Stock	Diorite-Gabbro	HGI12692H	0.7	1.96	0.282	1.73	0.258	1.8	0.28	< 0.5	0.1	< 5	< 0.1	1.37	0.64
Cerro Frontino Stock	Diorite-Gabbro	HGI12693A	0.72	2.19	0.341	2.29	0.373	5.9	0.52	< 0.5	0.17	8	< 0.1	16.4	4.94
Cerro Frontino Stock	Diorite-Gabbro	HGI12693B	0.47	1.3	0.181	1.1	0.154	1	0.07	< 0.5	0.11	< 5	< 0.1	1.48	0.65

Annex 2. Lithogeochemical data taken from Lesage et al. (2013)

	Analyte Symbol	SiO_2	Al_2O_3	$Fe_2O_3(T)$	MnO	MgO	CaO	Na_2O	K_2O	TiO_2	P_2O_5	LOI	Total
	Unit Symbol	%	%	%	%	%	%	%	%	%	%	%	%
	Detection Limit	0.01	0.01	0.01	0.001	0.01	0.01	0.01	0.01	0.001	0.01	0.01	0.01
Geological unit	Classification	Analysis Method	FUS-ICP	FUS-ICP	FUS-ICP	FUS-ICP	FUS-ICP	FUS-ICP	FUS-ICP	FUS-ICP	FUS-ICP	FUS-ICP	FUS-ICP
Buriticá Andesite	Plagioclase-Hornblende-Phyric Andesite	08-Bu-79	53.87	16.31	7.05	0.22	2.18	5.65	2.27	5.75	0.06	0.037	5.01	<0.5
Buriticá Andesite	Plagioclase-Pyroxene-Phyric Andesite	08-Bu-93	54.7	15.06	8.34	0.29	4.53	7.28	3.05	3.59	0.67	0.4	1.63	0.6
Buriticá Andesite	Plagioclase-Hornblende-Pyroxene-Phyric Andesite	09-Bu-242	52.41	16.03	8.86	0.18	3.23	8.15	2.81	2.68	0.8	0.4	3.52	1

	Analyte Symbol	Ag	As	Ba	Be	Bi	Br	Cd	Co	Cr	Cs	Cu	Ga	Ge
	Unit Symbol	ppm	ppm	ppm	ppm	ppm	ppm	ppm	ppm	ppm	ppm	ppm	ppm	ppm
	Detection Limit	0,5	1	1	1	0,1	0,5	0,5	0,1	0,5	0,1	1	1	0,5
Geological unit	Classification	Analysis Method	MULT INAA/TD-ICP	INAA	FUS-ICP	FUS-ICP	FUS-ICP	INAA	TD-ICP	INAA	INAA	FUS-MS	TD-ICP	FUS-MS	FUS-MS
Buriticá Andesite	Plagioclase-Hornblende-Phyric Andesite	08-Bu-79	<0.5	22	1115	2	<0.1	<0.5	<0.5	12.8	12.7	0.6	24	19	1.5
Buriticá Andesite	Plagioclase-Pyroxene-Phyric Andesite	08-Bu-93	0.6	53	1295	2	0.1	1.5	7.5	31	94.4	0.4	148	17	1.2
Buriticá Andesite	Plagioclase-Hornblende-Pyroxene-Phyric Andesite	09-Bu-242	1	38	2084	1	0.7	1.2	1	26.1	25.7	0.2	63	17	1.6

	Analyte Symbol	Hf	Hg	In	Ir	Mo	Nb	Ni	Pb	Rb	S	Sb	Sc	Se
	Unit Symbol	ppm	ppm	ppm	ppm	ppm	ppm	ppm	ppm	ppm	%	ppm	ppm	ppm
	Detection Limit	0,1	1	0,1	1	2	0,2	1	5	2	0,001	0,1	0,01	0,5
Geological unit	Classification	Analysis Method	FUS-MS	INAA	FUS-MS	INAA	FUS-MS	FUS-MS	TD-ICP	TD-ICP	FUS-MS	TD-ICP	INAA	INAA	INAA
Buriticá Andesite	Plagioclase-Hornblende-Phyric Andesite	08-Bu-79	3.2	<1	<0.1	<1	<2	6.9	5	8	186	0.93	4.1	13	<0.5
Buriticá Andesite	Plagioclase-Pyroxene-Phyric Andesite	08-Bu-93	2.6	<1	<0.1	<1	3	5.3	40	12	78	0.67	8.1	20.5	<0.5
Buriticá Andesite	Plagioclase-Hornblende-Pyroxene-Phyric Andesite	09-Bu-242	2.4	<1	<0.1	<1	<2	6.6	11	<5	45	3.43	8.8	18.9	<0.5

	Analyte Symbol	Sn	Sr	Ta	Th	U	V	W	Y	Zn	Zr	La	Ce	Pr
	Unit Symbol	ppm	ppm	ppm	ppm	ppm	ppm	ppm	ppm	ppm	ppm	ppm	ppm	ppm
	Detection Limit	1	2	0,01	0,05	0,05	5	1	1	1	1	0,05	0,1	0,02
Geological unit	Classification	Analysis Method	FUS-MS	FUS-ICP	FUS-MS	FUS-MS	FUS-MS	FUS-ICP	INAA	FUS-ICP	MULT INAA/TD-ICP	FUS-MS	FUS-MS	FUS-MS	FUS-MS
Buriticá Andesite	Plagioclase-Hornblende-Phyric Andesite	08-Bu-79	<1	577	0.4	4.37	2.36	148	<1	20	100	122	29.2	56.8	7.2
Buriticá Andesite	Plagioclase-Pyroxene-Phyric Andesite	08-Bu-93	1	849	0.3	3.33	1.97	215	<1	17	949	94	20.6	40	5.35
Buriticá Andesite	Plagioclase-Hornblende-Pyroxene-Phyric Andesite	09-Bu-242	2	724	0.4	2.59	1.55	243	<1	21	104	107	18.1	32.4	4.23

	Analyte Symbol	Nd	Sm	Eu	Gd	Tb	Dy	Ho	Er	Tl	Tm	Yb	Lu
	Unit Symbol	ppm	ppm	ppm	ppm	ppm	ppm	ppm	ppm	ppm	ppm	ppm	ppm
	Detection Limit	0,05	0,01	0,005	0,02	0,01	0,02	0,01	0,01	0,05	0,005	0,01	0,002
Geological unit	Classification	Analysis Method	FUS-MS	FUS-MS	FUS-MS	FUS-MS	FUS-MS	FUS-MS	FUS-MS	FUS-MS	FUS-MS	FUS-MS	FUS-MS	FUS-MS
Buriticá Andesite	Plagioclase-Hornblende-Phyric Andesite	08-Bu-79	25.7	5.3	1.56	4.38	0.71	4.15	0.8	2.33	1.61	0.35	2.23	0.34
Buriticá Andesite	Plagioclase-Pyroxene-Phyric Andesite	08-Bu-93	19.7	4.2	1.25	3.54	0.55	3.19	0.61	1.76	1.07	0.26	1.62	0.25
Buriticá Andesite	Plagioclase-Hornblende-Pyroxene-Phyric Andesite	09-Bu-242	18	4.09	1.25	3.83	0.63	3.67	0.72	2.09	0.23	0.32	2.18	0.32

Annex 3. Lithogeochemical data taken from Gil-Rodríguez (2010)

Analyte Symbol	FeO	SiO_2	Al_2O_3	Fe_2O_3	MnO	MgO	CaO	Na_2O	K_2O	TiO_2	P_2O_5	LOI	TOTAL
E1b	4.99	55.91	17.01	1.45	0.066	3.47	6.69	3.57	2.29	0.799	0.27	3.08	99.59
E2b	3.45	59.43	16.61	2.32	0.033	2.5	4.7	4.24	1.66	0.814	0.25	3.32	99.33
I1a	4.44	59.43	16.7	1.13	0.042	2.61	5.84	4.38	1.86	0.554	0.24	1.69	98.92
I2a	3.8	61.16	16.97	2.14	0.108	2.78	6.51	4.03	1.5	0.589	0.25	1.06	100.9
DAa	2.19	65.33	16.01	1.2	0.034	1.07	3.88	4.74	2.04	0.414	0.17	2.21	99.29

Geological unit	Classification	Analyte Symbol	Sc	Be	V	Cr	Co	Ni	Cu	Zn	Ga	Ge	As	Rb	Sr	Y	Zr	Nb	Mo	Ag
Early unit-Colosa Intrusive	Diorite	E1b	23	1	232	<20	40	<20	160	60	20	2.2	10	54	533	18.3	97	4.6	<2	<0.5
Early unit-Colosa Intrusive	Diorite	E2b	16	2	142	30	9	<20	250	70	20	0.7	6	68	557	17.9	113	7.9	<2	<0.5
Intermineral unit-Colosa Intrusive	Diorite	I1a	15	1	126	50	11	<20	240	30	19	1.7	<5	57	567	17.1	101	4.3	6	<0.5
Intermineral unit-Colosa Intrusive	Diorite	I2a	15	1	136	50	8	<20	30	<30	18	1.5	<5	34	669	18	88	4.7	<2	<0.5
Late unit-Colosa Intrusive	Quartz Diorite	DAa	5	2	69	20	<1	<20	40	30	22	1.4	<5	46	650	9.7	165	6.5	<2	<0.5

Geological unit	Classification	Analyte Symbol	In	Sn	Sb	Cs	Ba	La	Ce	Pr	Nd	Sm	Eu	Gd	Tb	Dy	Ho	Er	Tm
Early unit-Colosa Intrusive	Diorite	E1b	<0.1	1	<0.2	1.4	1112	16.3	31.3	4.17	15.8	3.74	1.2	3.5	0.63	3.28	0.69	1.97	0.3
Early unit-Colosa Intrusive	Diorite	E2b	<0.1	1	0.2	2.9	664	18.7	33.6	4.46	15.9	3.4	1.01	3.12	0.55	2.96	0.6	1.84	0.287
Intermineral unit-Colosa Intrusive	Diorite	I1a	<0.1	<1	4.1	1.3	909	17.4	34.5	4.02	15.7	3.62	1.07	3.3	0.51	2.88	0.56	1.66	0.25
Intermineral unit-Colosa Intrusive	Diorite	I2a	<0.1	<1	1	1.2	985	20.7	38.6	5.15	18.4	3.78	1.15	3.39	0.56	3.05	0.6	1.84	0.285
Late unit-Colosa Intrusive	Quartz Diorite	DAa	<0.1	<1	0.4	1.5	1158	15.5	30.1	3.9	14.5	3.13	0.85	2.36	0.36	1.65	0.26	0.91	0.127

Geological unit	Classification	Analyte Symbol	Yb	Lu	Hf	Ta	W	Tl	Pb	Bi	Th	U
Early unit-Colosa Intrusive	Diorite	E1b	1.87	0.279	2.8	0.3	3.4	0.55	7	2.1	3.15	1.59
Early unit-Colosa Intrusive	Diorite	E2b	1.85	0.272	3	0.59	10.8	0.63	<5	0.1	4.04	1.71
Intermineral unit-Colosa Intrusive	Diorite	I1a	1.61	0.255	2.6	0.31	6.6	0.42	<5	<0.1	4.38	1.45
Intermineral unit-Colosa Intrusive	Diorite	I2a	1.77	0.267	2.7	0.31	1.1	0.11	<5	<0.1	4.21	1.71
Late unit-Colosa Intrusive	Quartz Diorite	DAa	0.84	0.127	4.4	0.36	6.3	0.25	<5	0.3	3.61	1.63

El Capricho hill, San José del Guaviare. Author: Amaya et al.

Boletín Geológico

SERVICIO GEOLÓGICO COLOMBIANO

Boletín Geológico, 48(1), 49-79, 2021,
https://doi.org/10.32685/0120-1425/bol.geol.48.1.2021.503

© Author(s) 2021. This work is distributed under the Creative Commons Attribution 4.0 License.

Received: May 15, 2020

Revised: July 12, 2020

Accepted: October 9, 2020

Published online: July 12, 2021

San José de Guaviare Syenite, Colombia: Repeated Ediacaran intrusions in the northwestern Amazonian Craton

Sienita de San José de Guaviare, Colombia: Intrusiones repetidas durante el Ediacárico en el noroeste del Cratón Amazónico

Carolina **Amaya López**[1], Marion **Weber Scharff**[2], Mauricio **Ibáñez Mejía**[3], Federico Alberto **Cuadros Jiménez**[4], Jorge Julián **Restrepo Álvarez**[1], Nilson Francisquini **Botelho**[4], Mario **Maya Sánchez**[5], Orlando Manuel **Pérez Parra**[6], Carlos **Ramírez Cárdenas**[7]

1 Universidad Nacional de Colombia, Medellín, Colombia
2 Departamento de Geociencias y Ambiente, Universidad Nacional de Colombia, Medellín, Colombia
3 Department of Earth and Environmental Sciences, University of Rochester, New York, USA
4 Instituto de Geosciências, Universidade de Brasília, Brazil
5 Servicio Geológico Colombiano, Bogotá, Colombia
6 Université Grenoble-Alpes, France
7 Faculty of Earth Sciences, Universitat de Barcelona-UB, Spain
Corresponding author: Carolina Amaya, caro.geologia@gmail.com

Abstract

The Neoproterozoic igneous rocks found in the municipality of San José del Guaviare include several isolated plutonic bodies that protrude from the Phanerozoic sedimentary cover in belts aligned NW-SE. Limited to the Guaviare department, these intrusions stretch from the La Lindosa mountain range to the *corregimiento* El Capricho. These plutonic bodies consist of nepheline syenites, nepheline monzosyenites, nepheline-bearing alkali-feldspar syenites, syenites, quartz-syenites, quartz-alkali-feldspar syenites, syenogranites, and quartz-rich granitoids, which have been grouped and termed the San José de Guaviare Syenite unit (SJGS).

The intrusion of the unit occurred in the Ediacaran (604 ± 7 Ma and 620.5 ± 7.5 Ma) by mantle-derived alkaline magmas formed in anorogenic settings, most likely in rift-like stretching zones. The silica-subsaturated magma may have reacted with host rocks at the crust level, producing some silica-saturated igneous rocks, such as syenogranites and quartz-syenites, which are found in the El Capricho and Cerritos bodies.

Keywords: Nepheline Syenite, Neoproterozoic, Intraplate, Geochemistry, Geochronology.

Citation: Amaya L., C., Weber S., M., Ibáñez M., M., Cuadros, F. A., Restrepo A., J. J., Botelho, N. F., Maya S., M., Pérez P., O. M., & Ramírez C., C. (2021). San José de Guaviare Syenite, Colombia: Repeated Ediacaran intrusions in the northwestern Amazonian Craton. *Boletín Geológico*, *48*(1), 49-79. https://doi.org/10.32685/0120-1425/bol.geol.48.1.2021.503

Resumen

Las rocas ígneas neoproterozoicas presentes en el municipio de San José del Guaviare están representadas por varios cuerpos plutónicos aislados que se extienden en franjas de sentido NW-SE y sobresalen de la cobertura sedimentaria fanerozoica. Restringidos al departamento de Guaviare, dichos intrusivos se extienden desde la serranía de La Lindosa hasta el corregimiento El Capricho. Estos cuerpos plutónicos están compuestos por sienitas nefelínicas, monzosienitas nefelínicas, sienitas de feldespato alcalino con nefelina, sienitas, cuarzosienitas, cuarzosienitas de feldespato alcalino, sienogranitos y granitoides ricos en cuarzo, que se agruparon en la unidad denominada Sienita de San José de Guaviare (SSJG).

La intrusión de esta unidad tuvo lugar en el Ediacárico (604 ± 7 Ma y 620,5 ± 7,5 Ma) a partir de magmas alcalinos que se formaron en ambientes anorogénicos manto-derivados, probablemente en zonas de distensión tipo *rift*. Este magma subsaturado en sílice habría reaccionado a nivel cortical con la roca encajante produciendo algunos magmas saturados en sílice, como los sienogranitos y cuarzosienitas que se presentan en los cuerpos El Capricho y Cerritos.

Palabras clave: Sienita nefelínica, Neoproterozoico, intraplaca, geoquímica, geocronología.

1. Introduction

The San José de Guaviare Syenite is located in eastern Colombia, in an area with exposed Precambrian plutonic igneous and metamorphic rocks, which belong to the crystalline basement of the NW Amazonian Craton. This unit forms several isolated bodies aligned NW, some of which are structurally controlled and related locally to Mesoproterozoic metamorphic rocks known as the Guaviare Complex (*Complejo Guaviare*), which shows contact metamorphism superimposed by the syenite intrusion (Maya et al., 2018).

Different studies have reported a total of four plutonic bodies (B) in the SJGS, of which the two northernmost bodies (La Pizarra B and Las Delicias B), located in La Lindosa mountain range, were identified and studied by Trumpy (1943, 1944), Gansser (1954), Pinson et al. (1962), Vesga and Castillo (1972), Galvis et al. (1979), and Arango et al. (2011, 2012). The two southernmost bodies (El Capricho B and Cerritos B), located near El Capricho corregimiento, have been explored in more recent studies such as those of Maya et al. (2018), Franco et al. (2018), and Muñoz Rocha et al. (2019).

Previous studies have focused on reporting Paleozoic or Precambrian syenite intrusive rocks located in the mountain range west of San José del Guaviare, Guaviare department, Colombia, belonging to the crystalline basement of the Amazonian Craton (Trumpy, 1943, 1944; Gansser, 1954; Pinson et al., 1962; Galvis et al., 1979). The most detailed early studies were performed by Vesga and Castillo (1972), followed by Arango et al. (2011, 2012). These authors focused on describing textures and structures and the petrography, geochemistry, and geochronology of northern SJGS bodies. Other studies, such as those of Franco et al. (2018) and Muñoz Rocha et al. (2019), have complemented the age records of syenite rocks and their geochemistry.

In this study, southern syenite bodies were mapped at a 1:25000 scale (Maya et al., 2018), previously not possible for all bodies of the SJGS. We also studied their macroscopic and microscopic characteristics, geochemistry for major and trace elements, and U-Pb zircon geochronology. The existence of both feldspathoid and quartz rocks and the range of geochronological ages of the SJGS had not been previously reported. They will be essential to define the conditions under which events gave rise to the unit.

2. Methods

2.1 Field geology and petrography

The field work was conducted in the Colombian Amazon region, between the municipalities of San José del Guaviare and El Retorno, in the Guaviare department, within the framework of the geologic mapping of Plate 372, El Retorno, performed by Serviminas S.A.S. from 2017 to 2019 for the Servicio Geológico Colombiano (SGC). The geological survey made use of the Instituto Geográfico Agustín Codazzi 1:25 000-scale topographic maps, following the parameters for collecting data in a field book established by Caicedo (2003) and updated by Serviminas S.A.S. (Maya et al., 2019). In total, 29 field stations were established in the SJGS, collecting 41 rocks samples of nepheline syenite, nepheline monzosyenite, quartz-syenite, syenite, syenogranite and hornfels, among others, of which 41 thin sections and two polished sections were prepared for analysis

by transmitted and reflected light microscopy, respectively, counting 300 points per sample. The composition and texture of the minerals were described according to Heinrich (1965), Bowie and Simpson (1977), and Winter (2001), and the rocks were classified based on their composition using the Quartz, Alkali feldspar, Plagioclase, Feldspathoid (QAPF) diagram of plutonic rocks by Streckeisen (1976).

The materials used and generated during this research, such as field maps, thin sections, polished sections, rock samples, and discards, have been deposited at the Servicio Geológico Colombiano, Bogotá headquarters.

2.2 Geochemistry

Geochemical analyses of major and trace elements, including rare-earth elements (REE), were performed by X-ray fluorescence (XRF) and by inductively coupled plasma mass spectrometry (ICP-MS), respectively, at ALS Global Ltd., in accordance with internal code specifications of the laboratory (ME-XRF26 and ME-MS81). The samples were crushed and pulverized to collect the < 200-mesh-size fraction. The analyses were performed following laboratory standards, including the melting of samples with $LiBO_2$ and acid digestion for ICP-MS.

2.3 Total-rock isotope analysis

Sm, Nd, and Sr isotope analyses were performed at the Geochronology and Isotope Geochemistry Laboratory of the University of Brasilia. The analytical procedures applied in this study to determine the $^{147}Sm/^{144}Nd$ and $^{143}Nd/^{144}Nd$ isotope ratios were those described by Gioia and Pimentel (2000). ^{149}Sm and ^{150}Nd spike solutions were added to the crushed and pulverized rock. Sm and Nd were separated on cation exchange columns. Two drops of 0.025 N H_3PO_4 were added to the resulting fractions, which were then evaporated. The residue was dissolved in 1 µl of 5% HNO_3 and mounted on a double Re filament on a Finnigan MAT 262 thermal ionization mass spectrometer with seven collectors in static mode. The uncertainties of the $^{147}Sm/^{144}Nd$ and $^{143}Nd/^{144}Nd$ isotope ratios were lower than 0.2% and 0.0033% (2σ), respectively, based on the analysis of the international standard BHVO-2. The $^{143}Nd/^{144}Nd$ ratio was normalized using a $^{146}Nd/^{144}Nd$ ratio =0.7219 and a decay constant of 6.54×10^{-12} a^{-1} (Lugmair and Marti, 1978).

The procedures followed for Sr isotope analysis were those presented by Gioia et al. (1999). The samples were pulverized and subjected to acid dissolution and separation on cation exchange columns. Subsequently, the Sr-containing fractions were deposited together with 1 µl of H_3PO_4 on a Ta filament in the mass spectrometer described above. Based on the analysis of the international standard NBS-987, the uncertainties of the $^{87}Sr/^{86}Sr$ ratio were lower than 0.0069% (2σ). The $^{87}Rb/^{86}Sr$ ratio was calculated based on the Rb and Sr concentrations of the samples assessed by ICP-MS (Annex 1), according to the procedure of Faure and Mensing (2005).

2.4 LA-ICP-MS U-Pb zircon geochronology

The samples were initially prepared at the EAFIT University (originally *Escuela de Administración, Finanzas e Instituto Tecnológico*), where zircon crystals were separated following standard crushing, sieving, and mineral concentration methods. Subsequently, at the University of Rochester, several crystals of each sample were mounted in epoxy resin and polished to expose an internal face, on which the textural and isotopic analyses were performed. Cathodoluminescence images, taken to reveal the internal structure of the study zircons and to guide the geochronological analyses, were acquired under a JEOL 7100FT field-emission scanning electron microscope with a Deben panchromatic cathodoluminescence detector at the Mackay Microbeam Laboratory, University of Nevada, Reno.

The U-Pb isotope analyses were performed at the University of Rochester on an Agilent 7900 ICP-MS coupled to a Photon Machine Analyte G2 laser ablation system. This contained a HelEx2 rapid purge cell and generated pulses lasting approximately 8 ns using an excited ArF excimer. During the analyses, the laser was operated at a repetition rate of 7 Hz and a spot size of 30-µm diameter, generating a constant energy density of approximately 7 J/cm^2 on the surface of the crystals. The ablations were conducted under an ultrahigh-purity He atmosphere, and the same gas was used to transport the ablation aerosol to the ICP-MS. Each analysis consisted of 15 s of an "analytical blank" measurement with the laser off, immediately followed by a 20-s measurement of the isotope composition of the crystals with the laser on. The isotopes ^{202}Hg, $^{204}(Pb+Hg)$, ^{206}Pb, ^{207}Pb, ^{208}Pb, ^{232}Th, and ^{238}U were measured on the mass spectrometer. The instrumental bias was corrected using the standard-sample bracketing method with fragments of a Sri Lankan zircon (SL2) with a known age of 563.6 ± 3.2 Ma, assessed by isotope dilution thermal ionization mass spectrometry (ID-TIMS), as the primary reference material (Gehrels et al., 2008).

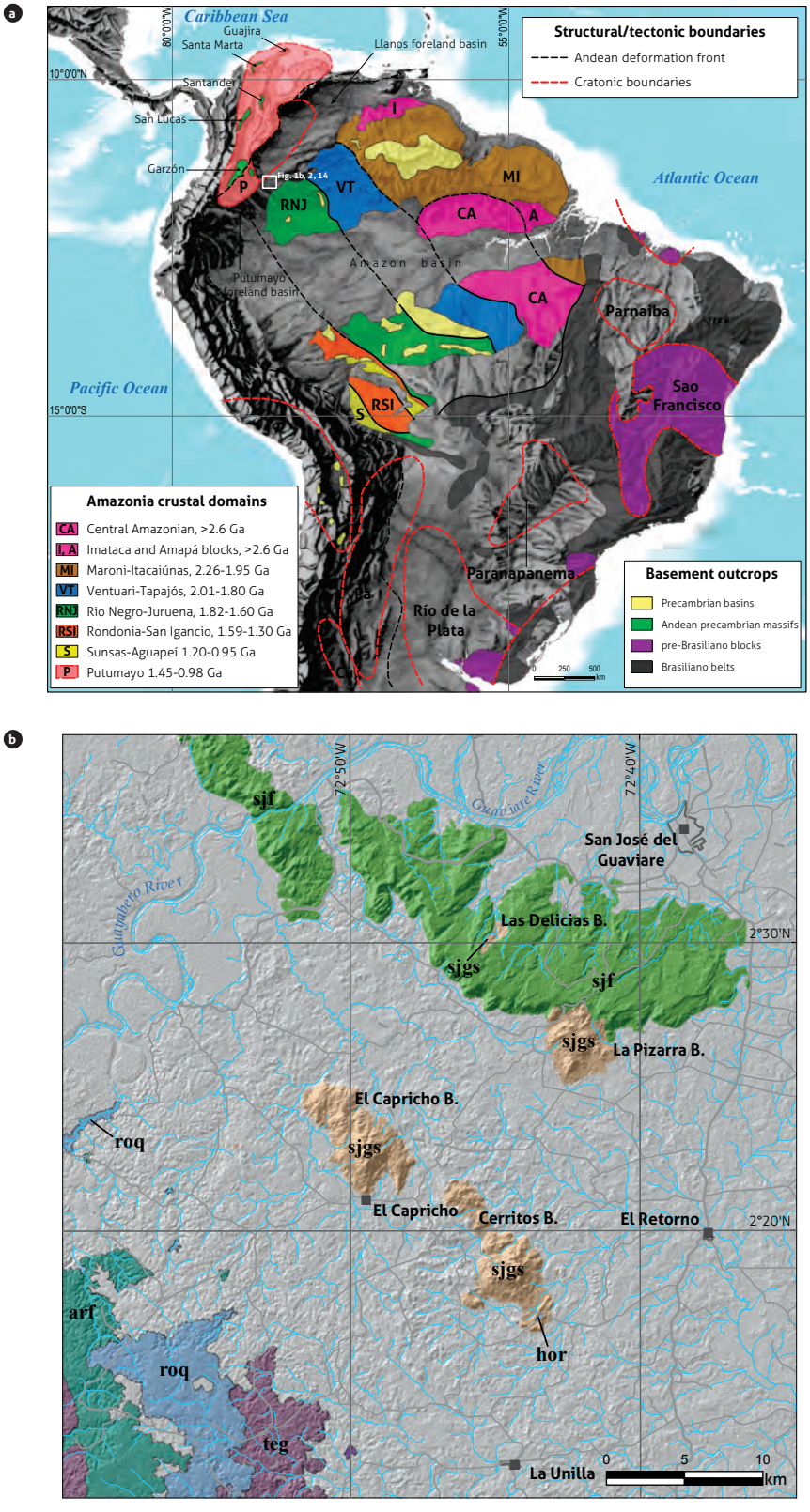

Figure 1. Map showing the locations of the syenite bodies and neighboring geological units
teg: Termales Gneiss; roq: La Rompida Quartzite; sjgs: San José de Guaviare Syenite; arf: Araracuara Formation; sjf: San José Formation. Source: adapted from Nivia et al. (2011), Maya et al. (2018), and Ibáñez Mejía and Cordani (2019).

U-Pb data were processed using the procedures and algorithms described by Pullen et al. (2018) to make the necessary linearity corrections of the detection system. In addition to the primary reference material and to zircons from the San José de Guaviare Syenite, during our analytical session, several Plešovice and FC-1 zircon fragments (Duluth Gabbro Complex, Minnesota) were also analyzed to assess the precision, accuracy, and reproducibility of the method. Said secondary materials yielded weighted average ages of $^{206}Pb/^{238}U$=335.0 ± 1.2/3.9 (2σ, n=21, MSWD=0.8) for Plešovice and $^{207}Pb/^{206}Pb$=1098 ± 8/11 (2σ, n=23, MSWD=0.3) for FC-1 zircons. The first level of uncertainty reported represents only internal analytical uncertainties, and the second level of uncertainty includes the propagation of systematic uncertainty and standardization sources. By including the systematic uncertainties, the values assessed in our analytical session become indistinguishable from the reference ages of 337.13 ± 0.37 Ma for Plešovice (Sláma et al., 2008) and 1099.96 ± 0.58 Ma for FC-1 (Ibáñez-Mejía and Tissot, 2019), determined by CA-ID-TIMS, which confirms that the geochronological results reported in this study are accurate and that the analytical uncertainties have been correctly assigned.

3. Geological framework

The SJGS represents a period of tectonism-related intrusions after the Precambrian bodies of the Amazonian Craton basement (Pinson et al., 1962; Vesga and Castillo, 1972), and this magmatic event was the last relevant igneous activity that occurred in the western section of the Amazonian craton (Galvis et al., 1979).

According to the K-Ar and Rb-Sr biotite ages assessed by Pinson et al. (1962), these rocks would be Paleozoic, dated between the Early Ordovician and the Late Ordovician, with different episodes of intrusion, although the K-Ar and Rb-Sr biotite dating methods used actually indicate a cooling below approximately 300 °C. Toussaint (1993) indicates that the nepheline syenite bodies correspond to the last early Paleozoic magmatism of the Autochthonous Block (*Bloque Autóctono*), resulting from local partial melting of the base of the continental crust of the Eastern Range (*Llanos Orientales*), which would have been affected by a stretching movement that increased the thermal flow in the region.

Nevertheless, the U-Pb zircon age assessed by Arango et al. (2012) dated the unit to the Ediacaran (Neoproterozoic), with a proposed origin from anatexis processes of migmatitic metamorphic rocks, which are related to the Pan-African event during the Cambrian in the continent Gondwana. The U-Pb ages assessed in the study conducted by Franco et al. (2018) are similar, but the authors diverge in their interpretation of the origin of these rocks, which indicates that the intraplate alkaline magmatism of the Neoproterozoic-Cambrian, east of Colombia and absent from the Colombian Andes, could have derived from Pan-African orogeny during the accretion of mobile belts in the NW continental margin of Gondwana.

The SJGS rocks are overlaid by sedimentary formations deposited in unconformity over the unit, such as the San José Formation from the Cretaceous (Figure 1) (Arango et al., 2011, 2012) and the Caja Formation from the Neogene (Maya et al., 2018). Furthermore, in the southern section of the Cerritos body, the SJGS is in contact with Proterozoic metamorphic rocks (Maya et al., 2018), where igneous rocks intrude into metamorphic rocks, creating a thermal effect, evidenced in the recrystallization to hornfels and in the formation of injection migmatites. Approximately 6 km west of the El Capricho body, a small syenite outcrop (Figure 2) shows that the extent of the unit is mostly under the sedimentary cover.

Approximately 15 km southwest of the syenite bodies, basement rocks, named the Guaviare Complex by Maya et al. (2018) (Termales Gneiss and La Rompida Quartzite), as well as the Araracuara Formation (Figure 1) crop out, and there are no other syenite bodies in this section.

4. Results

4.1 Lithology

The San José de Guaviare Syenite, in the southern section, encompasses two bodies aligned NW-SE located in the El Capricho and Cerritos sectors (Figure 2). In general, these bodies correspond to holocrystalline, phaneritic, hypidiomorphic rocks, ranging from equigranular (Figure 3A) to inequigranular. They are leucocratic, with a medium to coarse grain size, up to pegmatitic (7 cm) (Figure 3B), with a low to medium color index (7-20%) and with white, gray, and pink hues mottled with black. The El Capricho body is the most homogeneous in both composition and texture. The Cerritos body tends to be heterogeneous, with locally dark-gray fine-grained facies, which preserve the mineralogical composition, as well as rocks oriented by a mafic mineral flow (Figure 3 A, C).

In the southern section of the Cerritos body, SJGS intrusion generated a contact aureole in the regional metamorphic rocks of the Guaviare Complex, forming hornfels covering an area of

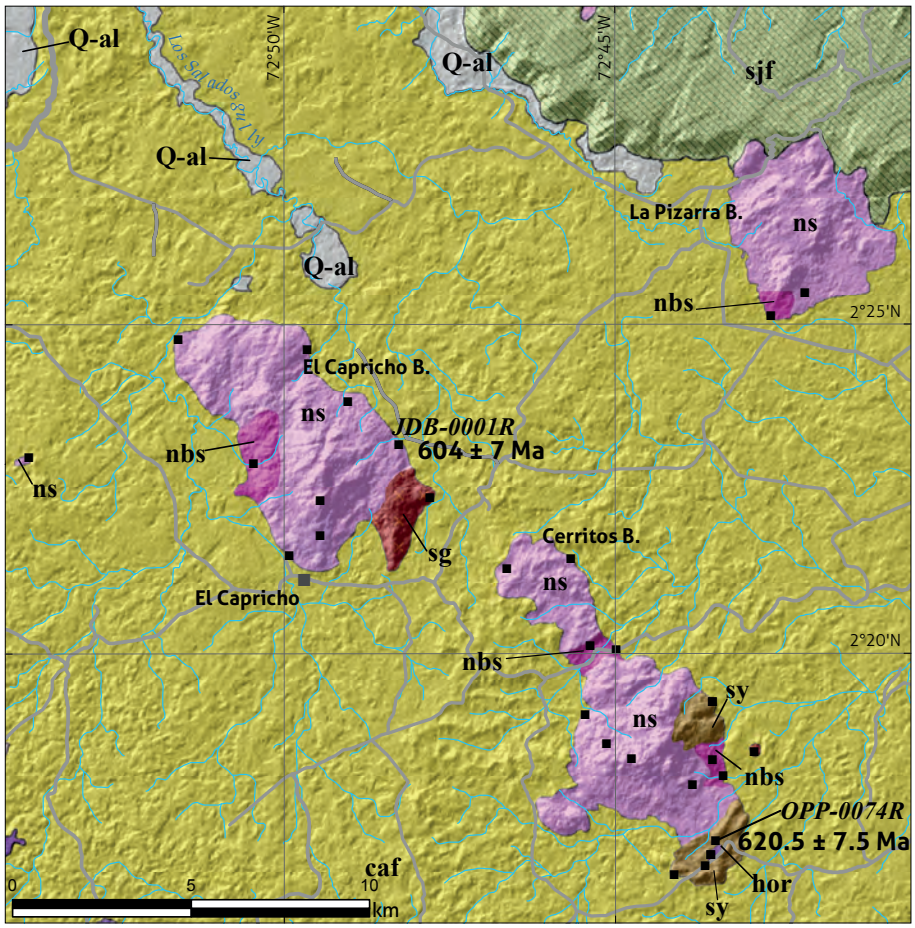

Figure 2. SJGS compositional distribution
ns: nepheline syenite; nbs: nepheline-bearing alkali-feldspar syenite; sg: syenogranite; sy: syenite; hor: hornfels; sjf: San José Formation; caf: Caja Formation; Q-al: alluvial deposits; ■: samples.

0.1 km^2. Although this type of rock only crops out in this zone, it provides considerable information about the origin of the syenites. The hornfels have a fine to medium grain, with black, gray, and red hues, some of which show banding and vestiges of the original orientation of the rock. At the same place, the rocks show silicification and form injection migmatites (Figure 3D), with stromatic textures. They are also characterized by the presence of syenite dikes, intersecting the injection migmatites and enveloping hornfels xenoliths.

4.2 Petrography

4.2.1 Syenites

San José de Guaviare syenite comprises mostly rocks with nepheline-like feldspathoids (Annex 2). Unlike the northern bodies, described by Arango et al. (2011, 2012), the southern bodies contain quartz (Figure 4). The nepheline-bearing rocks are petrographically classified according to Streckeisen (1976) into nepheline syenite, nepheline monzosyenite, and nepheline-bearing alkali-feldspar syenite (Figures 4 and 5a). Two lithological facies are recognized in these rocks (Figure 2): one with a nepheline content higher than 15.7% (facies 1-F1) and another impoverished in nepheline, with amounts lower than 11.0% (facies 2-F2). Two samples analyzed in this study, collected in the southernmost section of the La Pizarra body, in the El Turpial sector, are also nepheline-bearing lithological facies.

The rocks with quartz correspond to syenogranite, syenite, quartz-syenite, and quartz-alkali feldspar syenite (Figure 4). According to the quartz content, two facies are differentiated (Figure 2): facies 3 (F3) is rich in quartz (>19.4%), and facies 4 (F4) is impoverished in it (<9.3%). Both facies are characteri-

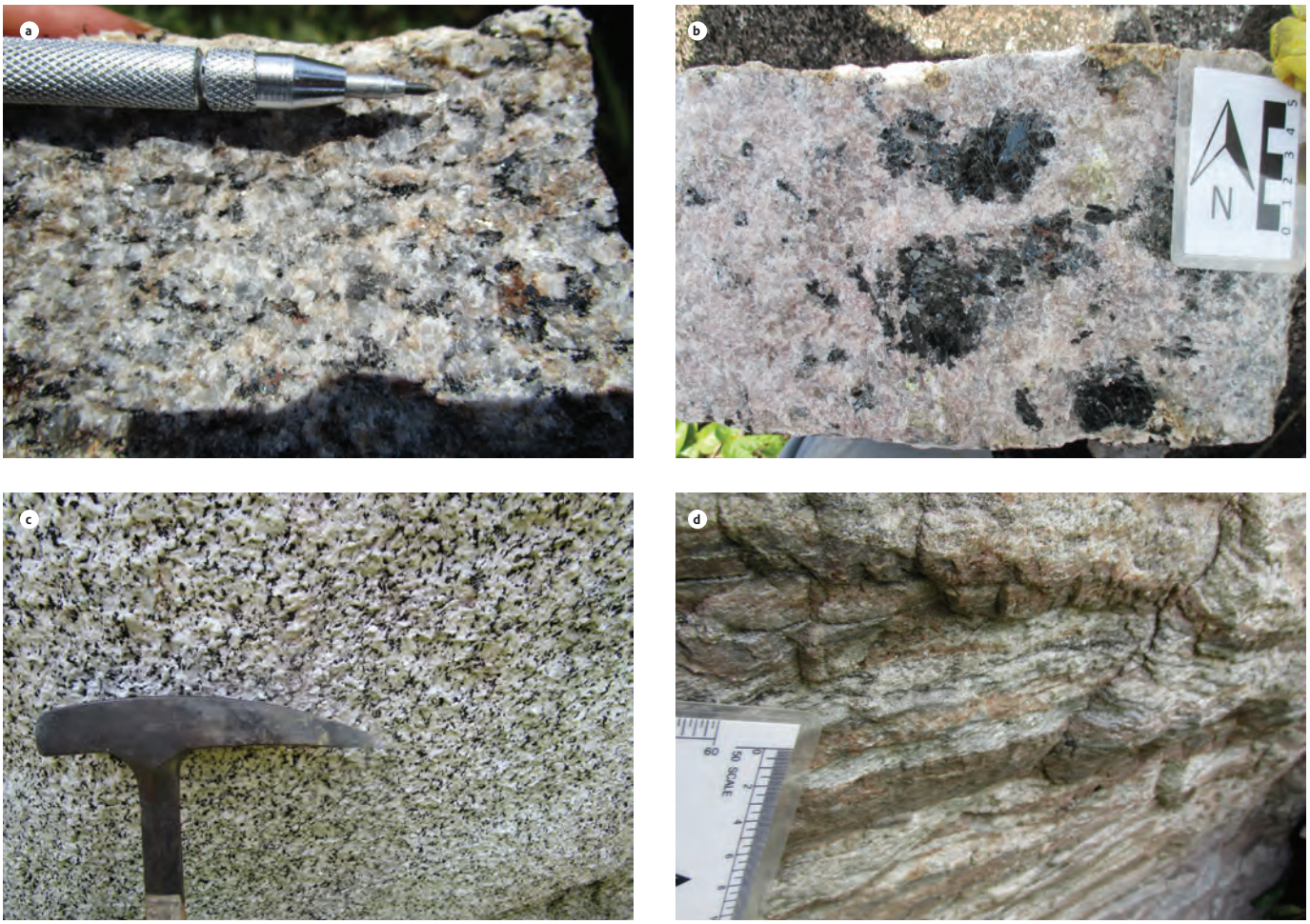

Figure 3. Texture and lithology of macroscopic samples from the SJGS
a) Equigranular, medium grain, slightly oriented; b) Pegmatitic biotite crystals; c) Slight orientation through mafic mineral flow; d) Injection migmatites.

zed by the occurrence of arfvedsonite-like amphibole (Figure 5b). The zone of contact between the SJGS and metamorphic rocks of the Guaviare Complex shows silicification (Qz>68%), most likely through host rock assimilation; this sample was classified as a quartz-rich granitoid (Figure 4).

In general, these rocks have a holocrystalline, hypidiomorphic, inequigranular to equigranular texture, with a medium to coarse grain. Some samples show mineral orientation, defined by biotite, and others show recrystallization with a polygonal granoblastic texture (Figure 5c). Mineralogically, they consist of microcline, plagioclase, nepheline or quartz, biotite, arfvedsonite, and aegirine.

Microcline presents as subhedral to anhedral, tabular crystals with gridiron and Carlsbad twinning, which implies formation from orthoclase. Sometimes the microcline forms an exsolution (perthite and mesoperthite) and myrmekitic fan texture, with plagioclase, nepheline, biotite, and calcite inclusions, and is slightly altered to clays and sericite. Albite to oligoclase plagioclase, determined using the Michel-Levy method, forms individual subhedral to euhedral, tabular, zoned crystals with albite, albite-Carlsbad, and Carlsbad twinning and with mesoperthitic and anti-perthitic textures, along with wedge-shaped lamellae and with calcite and biotite inclusions, sometimes altered to sericite and recrystallized along the grain boundaries, which causes the loss of extinction that is characteristic of this mineral.

Nepheline is found in subhedral to euhedral crystals with shapes ranging from rectangular to hexagonal, with simple twinned crystals and microcline, plagioclase, biotite, and calcite inclusions in poikilitic textures, showing slight alteration to

sericite, cancrinite, and natrolite. Quartz is found in colorless, clean, uniformly distributed anhedral crystals with undulose extinction, forming granular mosaics of complete contact with microcline and plagioclase.

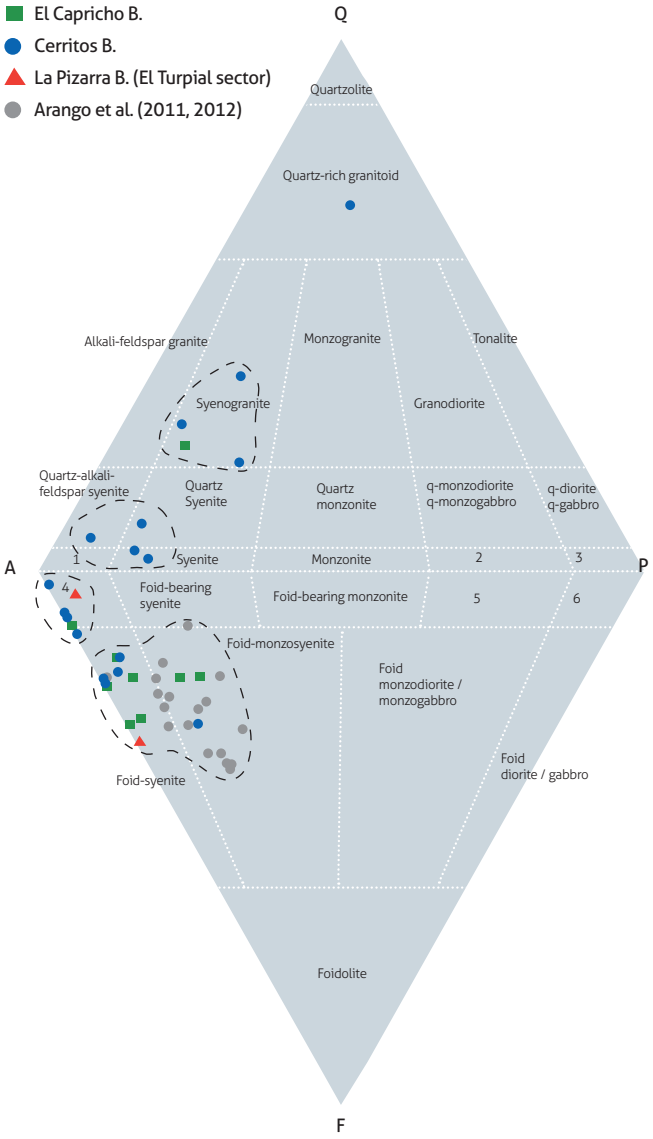

1 Alkali-feldspar syenite

2 Monzodiorite Monzogabbro

3 Diorite, gabbro

4 Foid-bearing alkali-feldspar syenite

5 Foid-bearing monzodiorite/ monzogabbro

6 Foid-bearing diorite/gabbro

Figure 4. Classification of the SJGS samples in the QAPF diagram (Streckeisen, 1976)

Biotite is found in subhedral to euhedral, tabular crystals with strong pleochroism with X (α): pale yellowish brown, Y (β)=Z (γ): dark reddish or greenish brown, simple twinning, and bird's eye and undulose extinction. Sometimes the biotite shows a preferential orientation in undeformed clustered laths, which is therefore interpreted as the flow orientation. Some crystals have pleochroic halos around inclusions of zircon, while others are embayed, skeletal crystals, and they are replaced by muscovite, sericite, and chlorite along the grain boundaries.

Arfvedsonite amphibole forms subhedral to anhedral, columnar to hexagonal crystals, with simple twinning and strong pleochroism with X (α): bluish green, Y (β): greenish brown, and Z (γ): olive green, in columnar aggregates with biotite, titanite, and zircon. It is replaced by biotite towards the edges and fractures. Pyroxene-like aegirine is found in short, columnar, subhedral to anhedral crystals with strong pleochroism with X (α): dark green, Z (γ): brownish yellow, and Y (β): green. Aegirine is associated with arfvedsonite through possible transformation to amphibole. Cleavage planes are filled by opaque minerals possibly due to oxidation.

The primary accessory minerals correspond to granular opaque minerals, with sharp rhombic, square shapes or with skeletal textures, which correspond to pyrite and magnetite/ilmenite, in addition to titanite with simple twinning, some fractured and overgrown zircons, calcite-like carbonate, epidote, apatite, tourmaline, allanite, pyrochlore, and garnet, possibly melanite. Franco et al. (2018) mention that the syenites contain large magmatic zircons with a partly metamictic character.

Secondary accessory minerals, such as cancrinite, sericite, and natrolite, result from the alteration of nepheline in the cleavage planes, edges, and fractures of the host mineral. Sericite aggregates with carbonates are also an alteration product from the interior and edges of microcline, plagioclase, and biotite crystals.

4.2.2 Hornfels

The different types of hornfels identified by petrographic analysis highlight how the compositional variation of the host rock was affected by thermal metamorphism during the SJGS intrusion. Thus, pelitic and mafic protolith hornfels were initially subjected to regional metamorphism within the Guaviare Complex and later to thermal metamorphism in amphibolite facies (previously hornblende hornfels) and pyroxene hornfels. In addition, feldspar-quartz hornfels correspond to a syenite

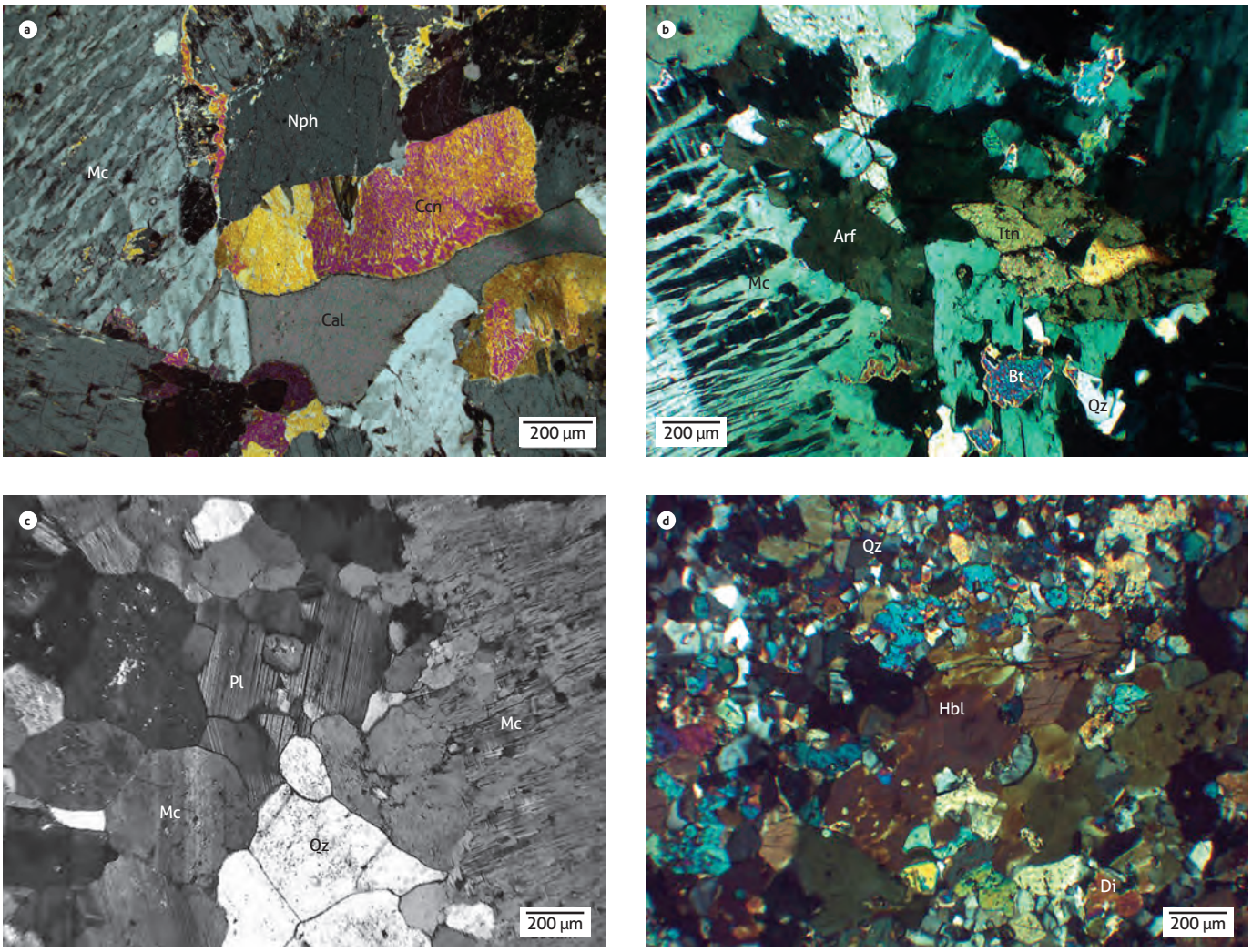

Figure 5. Mineralogy and textures of SJGS rocks
a) Nepheline (Nph)-, microcline (Mc)-, cancrinite (Ccn)-, and calcite (Cal)-bearing, hypidiomorphic, holocrystalline nepheline syenite; b) Syenite with aggregates of arfvedsonite (Arf), titanite (Ttn), and biotite (Bt); c) Syenite with recrystallized zone in polygonal granoblastic mosaics with straight edges of plagioclase (Pl), quartz (Qz), and microcline (Mc); d) Mafic hornfels with quartz-feldspathic domains and mafic domains (Di: diopside; Hbl: hornblende).

material recrystallized through intrusive processes, which occurred at various stages during the period of magmatism that originated the SJGS, as also shown by the wide range of ages assessed by geochronology and the many multielement and REE patterns found in geochemistry.

These rocks have a polygonal granoblastic texture and occasionally relict orientation derived from the original rock. The feldspar-quartz hornfels mineralogically consist of microcline, plagioclase, quartz, biotite, muscovite, and epidote (Annex 2), with zircon, calcite, apatite, titanite, fluorite, and opaque minerals as accessory minerals. The pelitic hornfels have a similar composition to that of feldspar-quartz hornfels but contain andalusite and sillimanite. The mafic hornfels (Figure 5d) show banding with mafic and quartz feldspar domains, compositionally differing in the occurrence of hornblende and clinopyroxene.

Quartz is detected as xenoblast crystals, with undulose extinction and granoblastic to polygonal texture. Microcline is identified as subidioblastic to xenoblastic, tabular crystals with gridiron twinning and slight sericitization. Albite and oligoclase plagioclase, as determined using the Michel-Levy method, ranges from subidioblastic to idioblastic and is tabular,

with albite twinning, apatite inclusions, and slight alteration to saussurite. Biotite ranges from subidioblastic to idioblastic and is laminar with strong pleochroism, X(α): very pale yellow to Y(β)=Z(γ): dark brown, some with mimetic orientation, whereas others are disordered. Occasionally, they exhibit irregular boundaries and moderate chloritization. Muscovite is identified as xenoblastic to subidioblastic, laminar crystals with irregular boundaries and without any orientation, in intergrowths of biotite.

Hornblende is subidioblastic, columnar, with strong pleochroism X(α): pale yellow, Z(γ): dark green, Y(β): greenish yellow, forming aggregates with titanite. Clinopyroxene (diopside) is found associated with hornblende in xenoblasts with slight pleochroism X(α): pale bluish green, Z(γ): pale brownish green, Y(β): pale brownish yellow. Hornblende appears to replace clinopyroxene, most likely due to retrogression. Epidote is associated with biotite, suggesting epidotization, whereas zircon is found in inclusions, forming pleochroic halos in biotite. The opaque minerals are identified as pyrite, ilmenite, and magnetite.

4.3 Geochemistry

Eighteen representative samples of the petrographic groups were selected to analyze major, minor, and trace elements (Annex 1). The rocks from the San José de Guaviare Syenite are classified as nepheline syenites, syenites, and granites, according to the classification diagram of plutonic rocks by Cox et al. (1979) (Figure 6). They were subdivided into three groups according to their major and trace elements. In general, the rocks are peralkaline, according to the alkalinity index by Maniar and Piccoli (1989), but some rocks are placed in the metaluminous (group 3, mainly) or peraluminous (group 2) fields (Figure 7).

The samples included in group 1 are classified as nepheline syenites (Figure 6) and characterized by their low SiO_2 (53.58-55.40%), CaO (0.44-1.04%), MgO (0.21-0.80%), and P_2O_5 (0.01-0.04%) and high Al_2O_3 (20.08-22.81%) and Na_2O contents (7.51-8.98%). These samples have a lower Zr content (61-259 ppm) than the samples from groups 2 and 3 (134-4070 ppm).

The samples from group 2 are mostly classified as nepheline syenites, one of which is classified as syenite (Figure 6). They show a higher SiO_2 content than those of group 1 (56.35-63.86%) and are characterized by their low CaO (0.04-0.49%), MgO (0.03-0.46%), and P_2O_5 (<0.01-0.09%) and high Al_2O_3 (18.53-22.76%) and Na_2O contents (6.10-9.56%).

Some samples have abnormally high concentrations of Zr (4070 and 1970 ppm). These values may be related to the abundance of zircon. In this group, the high Nb content is also notable (up to 625 ppm in sample JDB-0011R), which can be explained by the presence of trace pyrochlore contents in the rock. The rocks of groups 1 and 2 are generally impoverished in TiO_2, and the samples from group 2 have a very low modal proportion or do not contain titanite in their mineralogy, in contrast to those from groups 1 and 3.

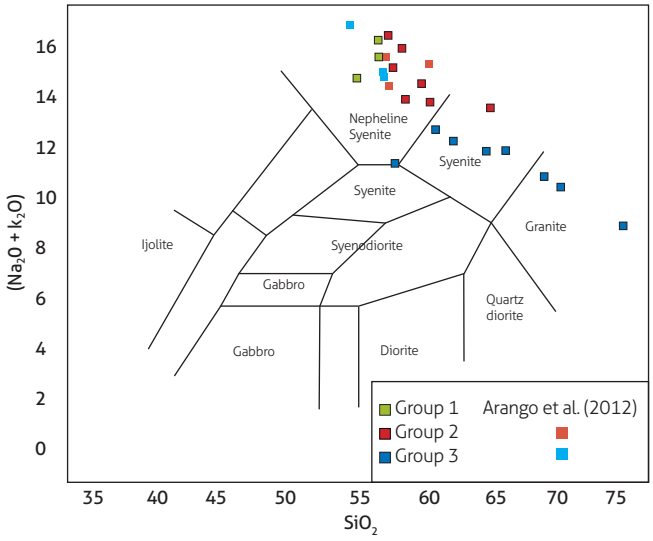

Figure 6. Total alkali-silica (TAS) diagram (Cox et al., 1979) of SJGS rocks, divided into three compositional groups

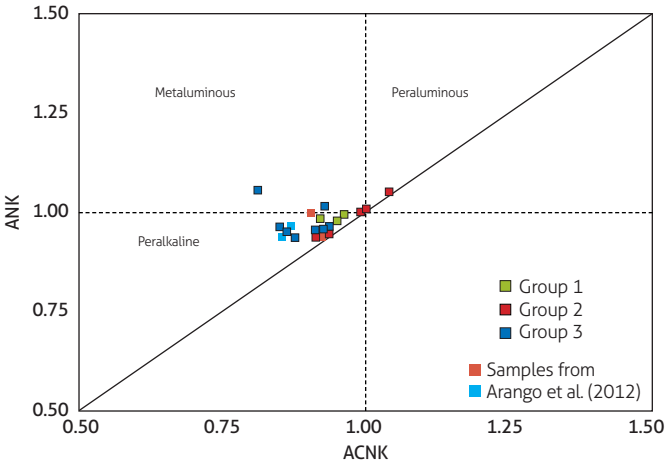

Figure 7. Alkalinity index (Maniar and Piccoli, 1989) of SJGS rocks
The rock samples mainly belong to the peralkaline field.

The samples associated with group 3 include rocks saturated and subsaturated with SiO_2 (56.31-74.20%). They are mainly classified as syenites and granites (Figure 6). In contrast to the rocks from the two previous groups, these rocks are impoverished in Al_2O_3 (12.63-18.53%) and Na_2O (3.30-6.63%) and enriched in CaO (0.26-3.60%), MgO (0.13-1.82%), and P_2O_5 (0.02-0.53%).

When graphed on primitive mantle-normalized multielement diagrams (McDonough et al., 1992) (Figure 8), group 1 is homogeneous, showing negative U, Th, and light rare-earth elements (LREE) anomalies and a slightly positive Sr anomaly. Group 2 is heterogeneous and shows a pointed pattern, with negative Ba anomalies and positive U, K, Sr, and Zr anomalies in some samples. Group 3 shows a relatively coherent pattern, with negative Sr and Ti anomalies and with some variability in elements such as Ba, Th, U, and LREE.

In chondrite-normalized REE patterns (Figure 8), group 1 shows enrichment in LREE over middle (MREE) and heavy rare-earth elements (HREE), and the slope of the curve is relatively gentle $(La/Yb)_N$=19.2-23.2. Group 2 displays a "reverse spoon" pattern, showing a relative impoverishment in MREE [$(La/Sm)_N$=4.0-11.1 $(Sm/Yb)_N$=0.2-2.9] compared to LREE and HREE; some samples show a slight (CAL-0023R and CAL-0017R) to strong positive Eu anomaly (ENA-0036R), which

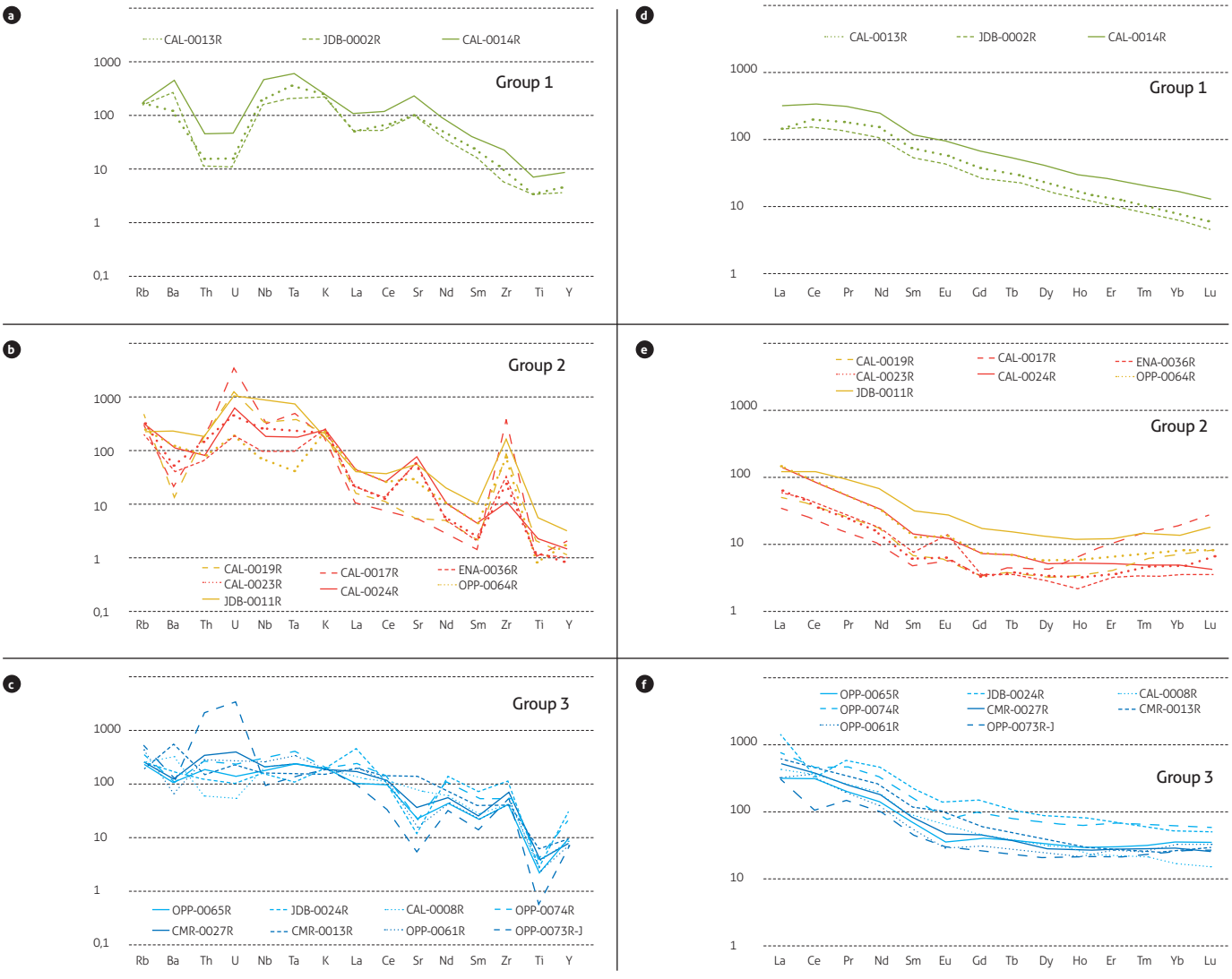

Figure 8. Primitive mantle- (McDonough et al., 1992) (a, b and c) and chondrite- (McDonough and Sun, 1995) (d, e and f) normalized multielement diagrams of SJGS rocks

indicates a possible plagioclase accumulation during the magmatic history or the inheritance of this pattern from the original source. Group 3 is less homogeneous than the other groups and shows an enrichment in LREE in relation to HREE, with a relatively gentle slope [$(La/Yb)_N$=8.9 - 28.0]; these samples show a negative Eu anomaly, except two samples (CAL-0008R and CMR-0013R) had a slightly positive Eu anomaly. Most likely, the REE patterns reflect early differentiation of titanite and consequent loss of these magmatic elements.

The phase diagram of the $NaAlSiO_4$-$KAlSiO_4$-SiO_2 system (Hamilton and Mackenzie, 1965) (Figure 9) shows that the Si-subsaturated rocks of the San José de Guaviare Syenite are defined by a crystallization sequence in which, once the temperature decreases, two pathways occur: one in which nepheline crystallizes first, and another in which potassium feldspar crystallizes first, as shown by the textural relationships of euhedral nepheline inclusions in feldspar crystals, whereas other samples exhibit feldspar crystals in nepheline. In both cases, the residual liquid corresponds to nepheline syenite magma.

Si-saturated magmas (especially in group 3), which are found at the top of the Ab-Or line, when the temperature decreases, initially crystallize alkali feldspar or quartz. As the temperature decreases, the liquid increases or decreases in Si. The final outcome of the fractionation corresponds to granite magma. These paths are reflected in granitic rocks in which quartz is the last crystallization phase.

Rocks with intermediate compositions between both compositions, which correspond to syenites, should tend towards either of the previous two during the fractional crystallization process, meaning the abundance of these rocks results from magma mixing (Storey et al., 1989), assimilation of continental crust (Motoki et al., 2010), or absorption of previously precipitated cumulus feldspar material by new magma inside the magma chamber (Wolff, 2017).

The Silica Saturation Index (SSI) vs. $(K^+Na)/Al$ diagram (Figure 10a) shows that the rocks from groups 1 and 2 are classified as alkaline rocks, whereas the rocks from group 3 primarily belong to the nonalkaline field. In general, the samples define a linear pattern, especially those of group 3, in which $(K^+Na)/Al$ does not decrease when transitioning from a SiO_2-subsaturated (SSI<0) to a SiO_2-saturated (SSI>0) magma, which indicates crust assimilation, possibly alkaline. The patterns observed in the Rb/K vs. Nb/Y diagram (Figure 10b) suggest that the samples from group 1 are the least evolved and the closest to the original composition of the magma and that the samples from groups 2 and 3 were mainly formed by fractional crystallization and assimilation of continental crust, respectively.

The fractioning of titanite and zircon is noticeable in the diagrams of Figure 10c, d, e, in which the samples of the three groups are clearly separated. The anomalies observed in the REE patterns are also expressed in the diagrams of Figure 10f,

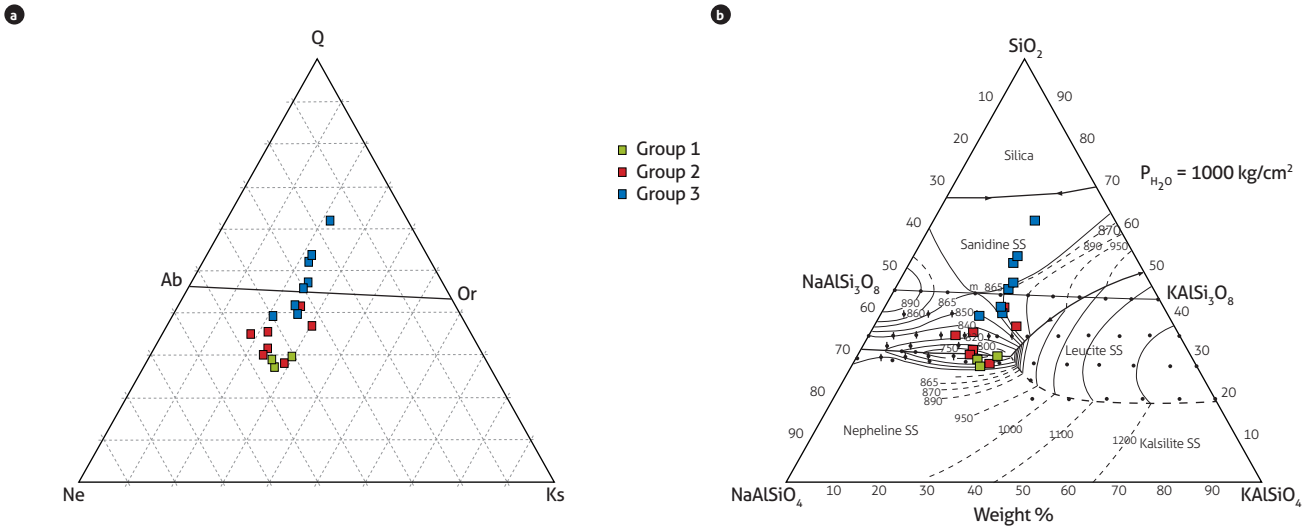

Figure 9. a) Rock composition in the Q-Ne-Ks system; b) Equilibrium phase diagram for the $NaAlSiO_4$-$KAlSiO_4$-SiO_2 system at 1 kbar
Source: adapted from Hamilton and Mackenzie (1965).

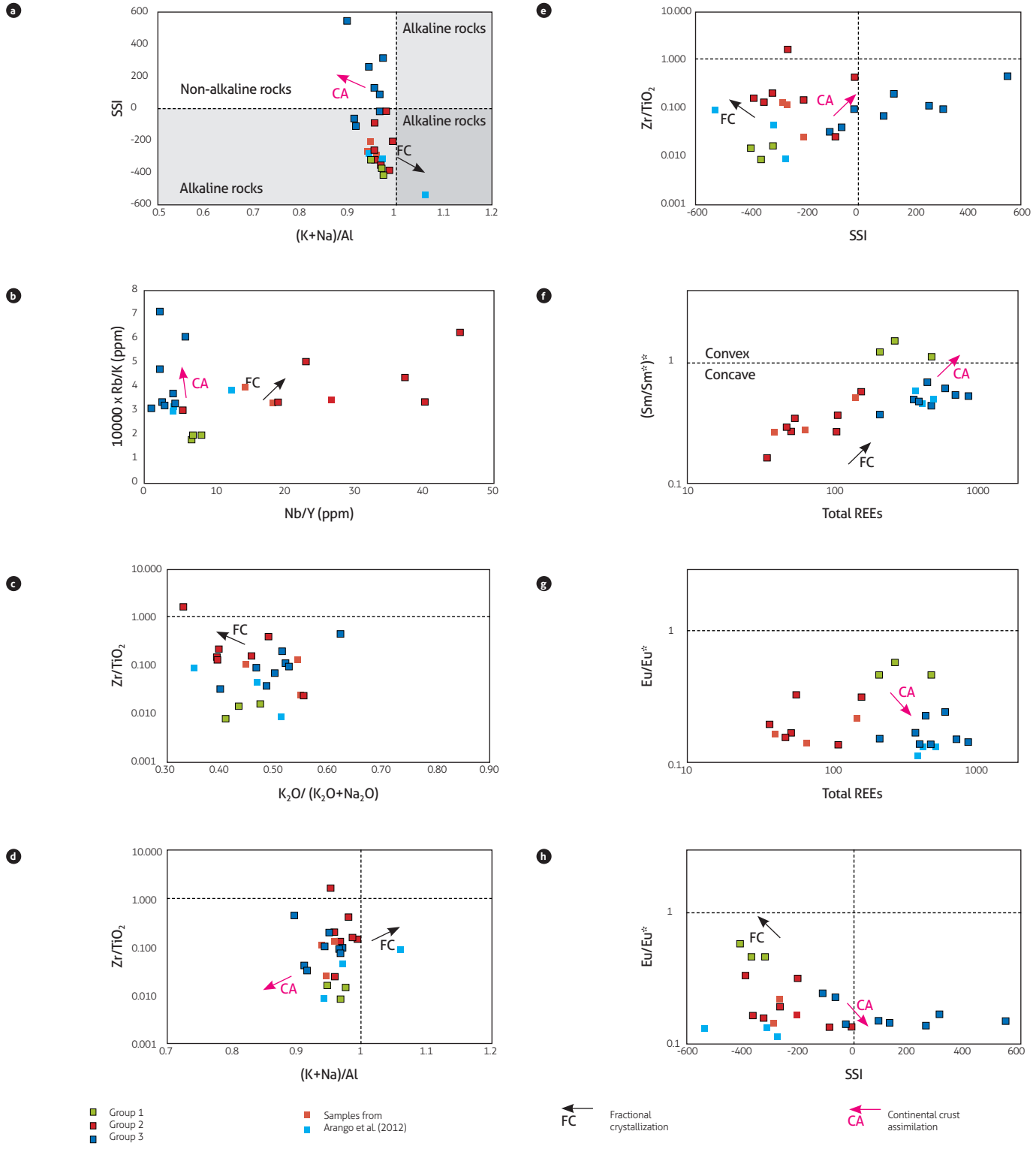

Figure 10. Compositional variation diagrams of SJGS rocks
a) Silica saturation index (SSI) vs. (K+Na)/Al; b) Rb/K vs. Nb/Y; c) Zr/TiO_2 vs. $K_2O/(K_2O+Na_2O)$; d) Zr/TiO_2 vs. (K+Na)/Al; e) Zr/TiO_2 vs. SSI; f) (Sm/Sm*)* vs. Total REE; g) Eu/Eu* vs. Total REE; h) Eu/Eu* vs. SSI. Source: adapted from Motoki et al. (2015). The diagram also shows data from Arango et al. (2012).

g, h, which show the effect of assimilation processes of the continental crust in addition to fractional crystallization processes. In the latter, the samples of groups 1 and 2 are connected by trends of fractional crystallization, albeit opposite to those observed in Figure 10b.

Field relationships showed the presence of metamorphic xenoliths partly absorbed in syenites in the southern section of the body. These xenoliths comprise rocks rich in SiO_2, which include the Si-saturated rocks of group 3. However, the relationship between the rocks of groups 2 and 3 is not limited to a simple assimilation model. The patterns observed in the diagrams presented by Motoki et al. (2010, 2015) indicate combined processes of fractional crystallization in groups 1 and 2 and assimilation in group 3.

In the Rb vs. (Y+Nb) tectonic discrimination diagram (Pearce et al., 1984), all rocks are placed in the within-plate granite (WPG) field (Figure 11), which corroborates the findings of other studies on the same unit, conducted north of the study area (Arango et al., 2011, 2012).

The comparison analysis of syenite rocks identified to the south and those to the north of SJGS reported in the study by Arango et al. (2011, 2012) shows that the compositional variation is higher in the southern SJGS rocks, which include nepheline syenites, syenites, and granites, whereas the northern SJGS rocks consist of only nepheline syenites (Figure 6).

In the multielement and REE diagrams (Figure 12), the northern SJGS (Arango et al., 2011, 2012) shows geochemical patterns similar to those of groups 2 and 3, defined for southern SJGS rocks; three samples show geochemical patterns similar to those of group 2, and the other three, to those of group 3. Sample 5000421 is deviates slightly from the pattern because it is impoverished in HREE relative to the group 3 field.

Although the composition of northern SJGS rocks is restricted to nepheline syenites, the main geochemical characteristics are similar to those of southern SJGS rocks, as are the concave-upward REE patterns, resulting from the impoverishment in MREE, slightly positive Eu anomaly, and positive Sr and Zr anomalies in group 2 and the relative enrichment in LREE in relation to the other groups, slightly negative Eu anomaly, and negative Sr and Zr anomalies in group 3.

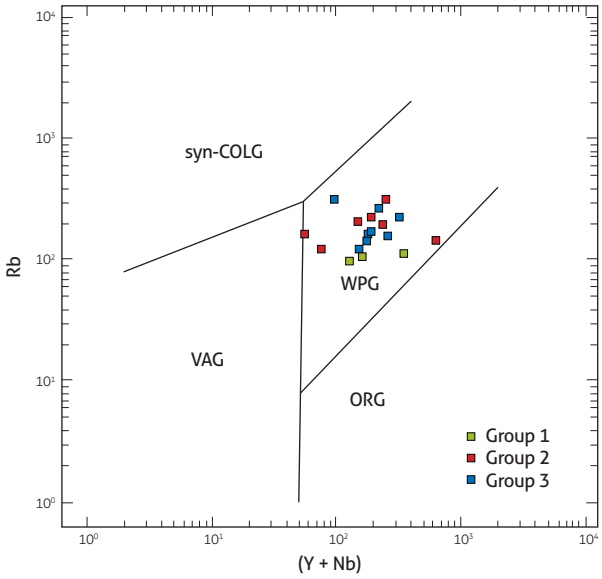

Figure 11. Tectonic discrimination diagram (Pearce et al., 1984) of the SJGS The samples belong to the field of within-plate granites (WPG)

4.4 Isotopes

The results from the Sm-Nd and Sr isotope analyses of two nepheline syenite (CAL-0014R, group 1, and JDB-0011R, group 2) and one syenogranite sample (JDB-0024R, Grupo 3) are outlined in Table 1. Based on geochronological data (Annex 3), a crystallization age of 604 Ma was used to calculate the $\varepsilon_{Nd}(T)$ and the initial $^{87}Sr/^{86}Sr$ ratio of the samples.

The samples have positive values of $\varepsilon_{Nd}(604)$, ranging from +0.8 to +1.8, with T_{DM} model ages ranging from 920 to 1000 Ma (Figure 13a). The ε_{Nd} values of the two nepheline syenite samples are very similar (+1.8 and +1.6) and slightly higher than that of the syenogranite sample (+0.6). In turn, the T_{DM} model ages of the nepheline syenite samples are consistent

Table 1. Sm-Nd and Sr isotopic data of the SJGS

Sample	Sm (ppm)	Nd (ppm)	$^{143}Nd/^{144}Nd$	$^{147}Sm/^{144}Nd$	ε_{Nd} (T)	T_{DM} (Ga)	Rb (ppm)	Sr (ppm)	$^{87}Sr/^{86}Sr$	$^{87}Rb/^{86}Sr$	$^{87}Sr/^{86}Sr_i$	T (Ga)
CAL 0014R	15.77	100.06	0.512320 (±13)	0.0952	+1.6	0.93	113.5	4710.0	0.70536 (±1)	0.0699	0.70477	0.604
JDB-0011R	5.17	32.86	0.512329 (±17)	0.0952	+1.8	0.92	149.5	1220.0	0.70836 (±1)	0.3556	0.70536	0.604
JDB-0024R	14.44	90.41	0.512272 (±16)	0.0966	+0.6	1.00	157.5	249.0	0.72218 (±5)	1.8378	0.70665	0.604

The uncertainties in the last two digits of the $^{143}Nd/^{144}Nd$ ratios and in the last digit of the $^{87}Sr/^{86}Sr$ ratio are 2σ. The values of the $^{143}Nd/^{144}Nd_{CHUR}$ and $^{147}Sm/^{144}Nd_{CHUR}$ ratios used in the calculations were 0.512638 and 0.1966, respectively (Jacobsen and Wasserburg, 1980, 1984). T_{DM} model ages according to the depleted mantle model of DePaolo (1981). The concentrations of Rb and Sr were determined by ICP-MS analysis (Annex 1). The $^{87}Rb/^{86}Sr$ ratio was calculated according to the procedure described by Faure and Mensing (2005).

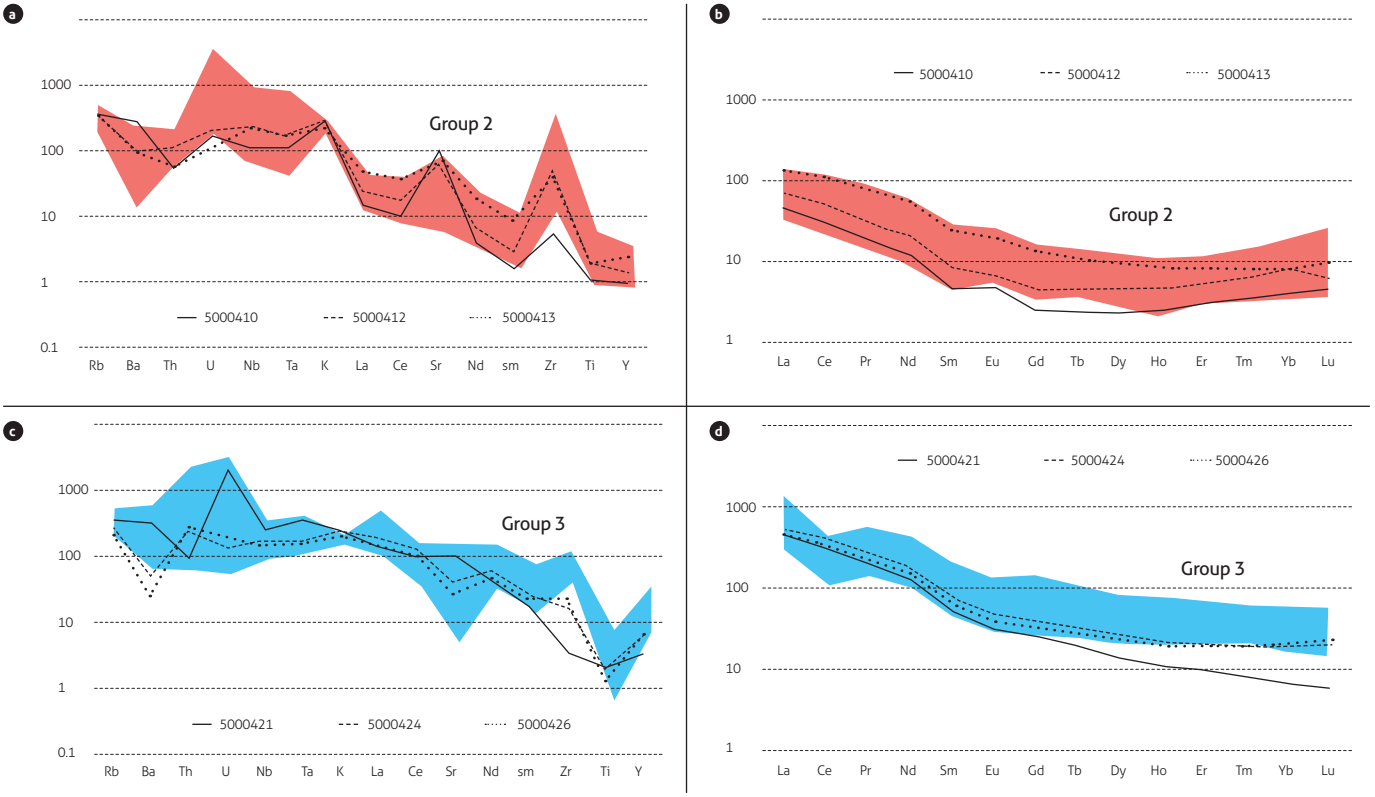

Figure 12. Primitive mantle- (McDonough et al., 1992) (a and b) and chondrite- (McDonough and Sun, 1995) (c and d) normalized multielement diagrams of northern (Arango et al., 2011, 2012) and southern SJGS rocks
The red and blue fields represent groups 2 and 3 defined in this study, respectively. The samples from the northern SJGS bodies are represented by lines.

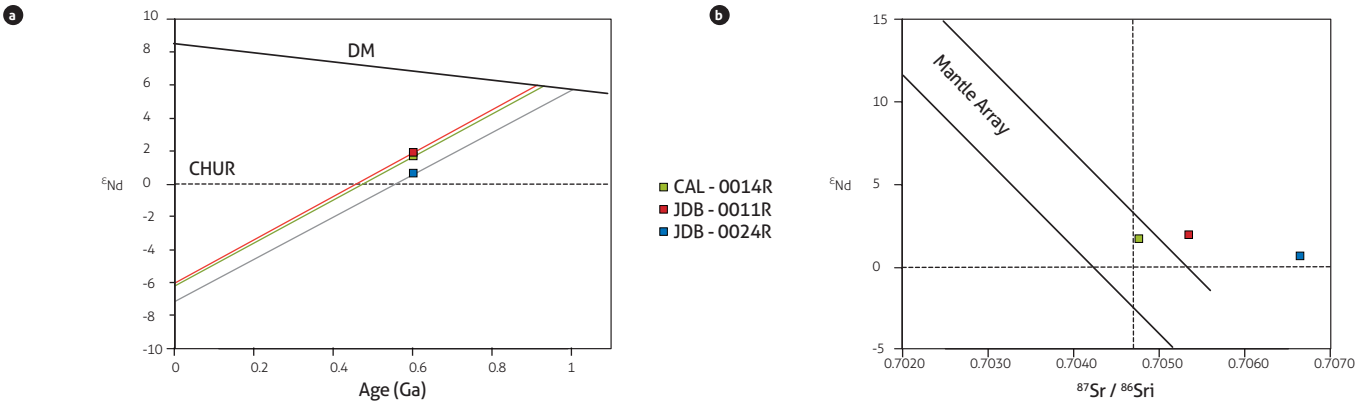

Figure 13. Isotope characteristics of the samples analyzed in this study
a) ε_{Nd} vs. age chart showing the mantle-derived character of the rocks, for a magmatic crystallization age of 604 Ma; b) ε_{Nd} vs. $^{87}Sr/^{86}Sr$ chart showing isotope signatures ranging from typical mantle values to decoupled values with high initial $^{87}Sr/^{86}Sr$ ratios. Depleted mantle (DM) curve according to the model by DePaolo (1981).

(0.92 and 0.93 Ga), whereas the model age of the syenogranite sample is slightly older (1.0 Ga). With initial $^{87}Sr/^{86}Sr$ ratios ranging from 0.7048 to 0.7067, the isotope signatures of these samples range from those of typical mantle-derived magmas within the mantle array region until reaching decoupled signatures to the right of this field, characterized by high initial ratios of $^{87}Sr/^{86}Sr$ (Figure 13b). The latter is the case for the syenogranite sample, which has an initial $^{87}Sr/^{86}Sr$ ratio of 0.7067, whereas the nepheline syenite samples have lower ratios of 0.7048 and 0.7054.

4.5 Geochronology

Geochronological analyses were performed using the LA ICP-MS U-Pb zircon method in two syenite samples (Annex 3), one located in the El Capricho body (JDB-0001R) and the other located in the Cerrito body (OPP-0074R) (Figure 14).

Authors such as Pinson et al. (1962), Arango et al. (2011, 2012), Franco et al. (2018), and Muñoz Rocha et al. (2019) have reported ages ranging from the Ordovician to the Neoproterozoic for syenite rocks, calculated using different methods (Table 2). By K-Ar and Rb-Sr isotope dating of biotites,

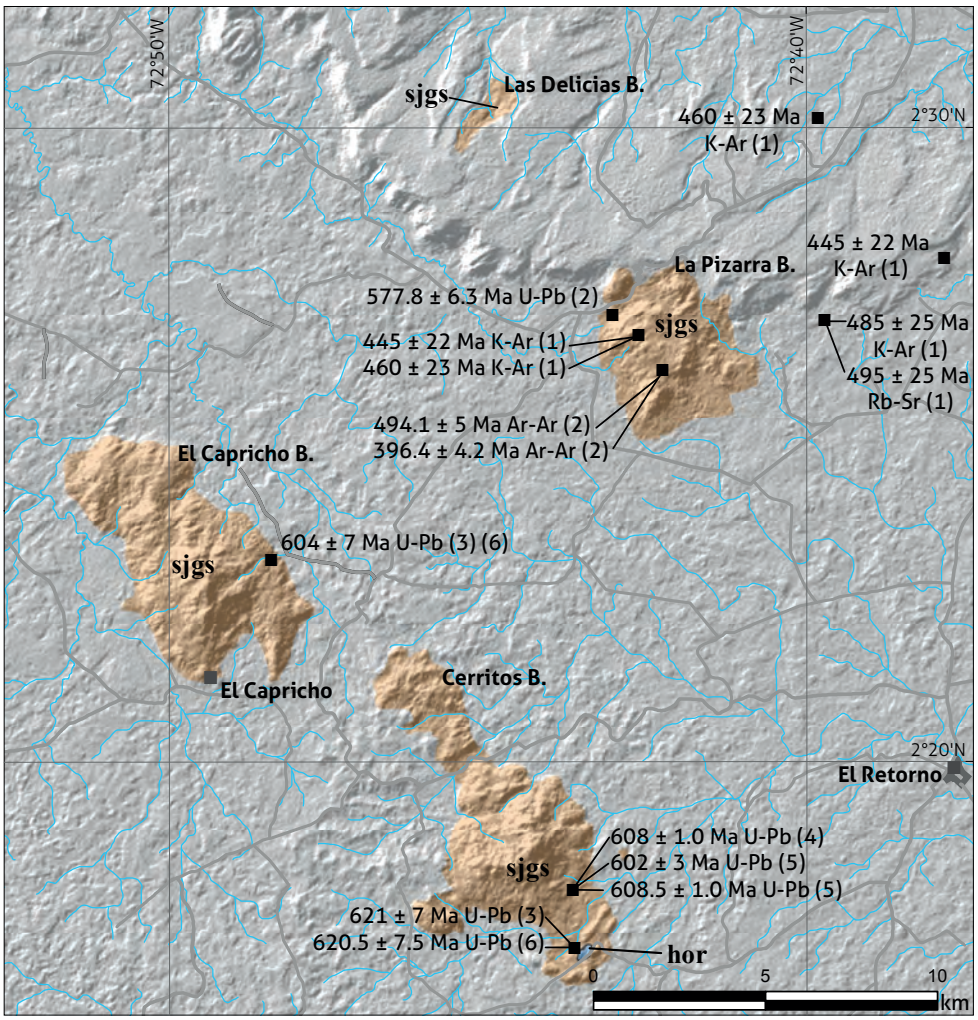

Figure 14. Ages of the different rock bodies that form the San José de Guaviare Syenite
Source: 1) Pinson et al. (1962); 2) Arango et al. (2011, 2012); 3) Maya et al. (2018); 4) Franco et al. (2018); 5) Muñoz Rocha et al. (2019); and 6) the present study.

Table 2. Ages of SJGS rocks assessed by different authors

Sample	Lithology	Reported age (Ma)	Recalculated age (Ma)	Method/material	Reference
B3592	Syenite	445 ± 22	457 ± 23	K-Ar/Biotite	(1) Pinson et al. (1962)
B3592	Syenite	460 ± 23	472 ± 24	K-Ar/biotite	(1) Pinson et al. (1962)
B3635	Syenite	445 ± 22	457 ± 23	K-Ar/biotite	(1) Pinson et al. (1962)
B3636	Syenite	460 ± 23	472 ± 24	K-Ar/biotite	(1) Pinson et al. (1962)
B3637	Syenite	485 ± 25	498 ± 26	K-Ar/biotite	(1) Pinson et al. (1962)
B3637	Syenite	495 ± 25	508 ± 26	Rb-Sr/biotite	(1) Pinson et al. (1962)
IGM500410	Nepheline syenite	494.1 ± 5		Ar-Ar/biotite	(2) Arango et al. (2011, 2012)
IGM500410	Nepheline syenite	396.4 ± 4.2		Ar-Ar/biotite	(2) Arango et al. (2011, 2012)
IGM500412	Nepheline syenite	577.8 ± 6.3		U-Pb/zircon	(2) Arango et al. (2012)
JDB-0001R (IGM5075537)	Nepheline syenite	604 ± 7		U-Pb/zircon	(3) Maya et al. (2018)
OPP-0074R (IGM5075695)	Syenite	621 ± 7		U-Pb/zircon	(3) Maya et al. (2018)
-	Nepheline syenite	608 ± 1		U-Pb/zircon	(4) Franco et al. (2018)
SNG-1	Nepheline syenite	602 ± 3		U-Pb/zircon	(5) Muñoz Rocha et al. (2019)
SNG-1	Nepheline syenite	608.5 ± 1.0		U-Pb/zircon	(5) Muñoz Rocha et al. (2019)
JDB-0001R (IGM5075537)	Nepheline syenite	604 ± 7		U-Pb/zircon	(6) Present study
OPP-0074R (IGM5075695)	Syenite	620.5 ± 7.5		U-Pb/zircon	(6) Present study

The ages calculated by Pinson et al. (1962) are corrected according to the constants of Steiger and Jager (1977) and to data published by Maya (1992).

Pinson et al. (1962) assessed ages ranging from 445 to 495 Ma for the La Pizarra body, which were considered ages of cooling by uplift followed by erosion or metamorphism, processes placed between the early and the Late Ordovician. A similar age of 494.1 ± 5 Ma, assessed in the same La Pizarra body using the $^{40}Ar/^{39}Ar$ biotite method, was reported by Arango et al. (2011, 2012). This age corresponds to the late Cambrian (Furongian) and was interpreted as a cooling age. Another age reported by Arango et al. (2011, 2012), using the U-Pb zircon method, is 577.8 ± 6.3-9 Ma (Ediacaran), which would be considered the age of crystallization. Other, more recent studies have yielded crystallization ages, assessed using the U-Pb zircon method, of 602 ± 3 and 608 ± 1 Ma (Ediacaran) for El Jordán syenite (Franco et al., 2018; Muñoz Rocha et al., 2019), which is found the southern section of the Cerritos body (Figure 14).

4.5.1 Nepheline syenite (JDB-0001R)

Zircons are in general anhedral and irregular, with a coarse concentric zoning of dark centers and lighter edges (Figure 15a, Annex 4). In dark zones, the uranium content is high, and the igneous fine oscillatory zoning is well defined. In contrast, in light zones, the uranium content is low, and the zoning is less perceptible or completely absent. The origin of this coarse zoning is not defined and could be associated with patchy zoning, attributed to local recrystallization along microfractures, according to Corfu et al. (2003). This characteristic is observed in one of the crystals with light veinlets that penetrate the dark zone

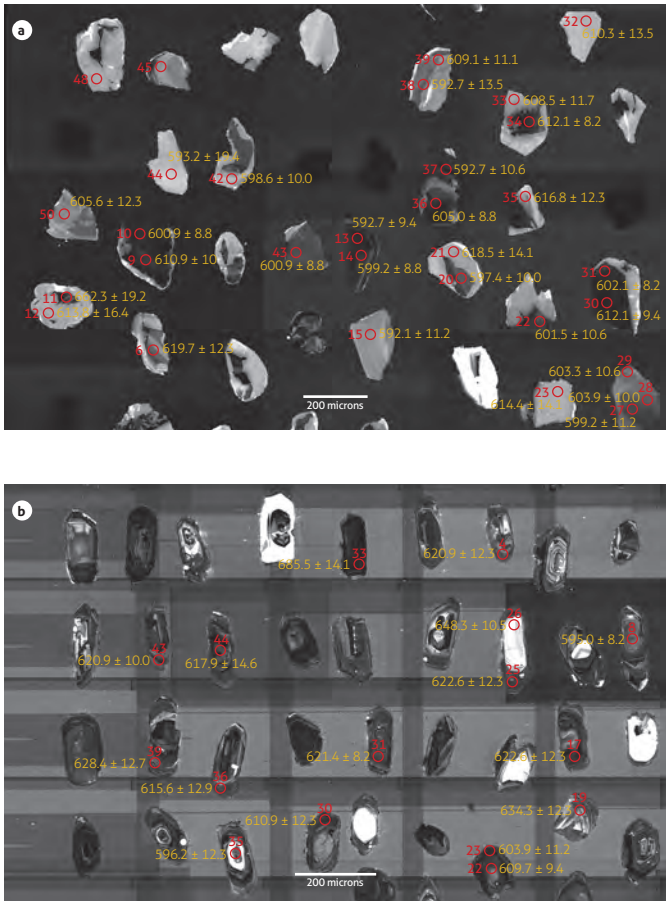

Figure 15. Cathodoluminescence images of SJGS zircons analyzed by LA-ICP-MS
a) Nepheline syenite (JDB-0001R); b) Syenite (OPP-0074R).

with good igneous fine zoning. The dark, uranium-rich areas may have begun to grow in a magma with a high content of this element, but the amount of uranium decreased due to assimilation of host rocks, as shown by the geochemical analysis.

The weighted-average $^{206}Pb/^{238}U$ age of this rock is 604.3 ± 2.2/7.0 Ma (2σ, n=45, MSWD=1.6), where the first level of uncertainty represents only internal analytical uncertainties, and the second level of uncertainty includes propagation from systematic and standard sources. This dating is interpreted as the age of the magmatic event (Figure 16a) and corresponds to the Ediacaran period of the Neoproterozoic. The $^{206}Pb/^{238}U$ age that should be cited is 604 ± 7 Ma because this value was calculated considering all sources of uncertainty, both internal and systematic, as well as standardization. Two (inherited) zircon xenocrysts yielded individual $^{206}Pb/^{238}U$ ages of 647 ± 14 and 662 ± 19 Ma (Figure 16b, blue ellipses), and their ages support the assumption of a lengthy magmatism because the area shows no known igneous or late Neoproterozoic metamorphic events.

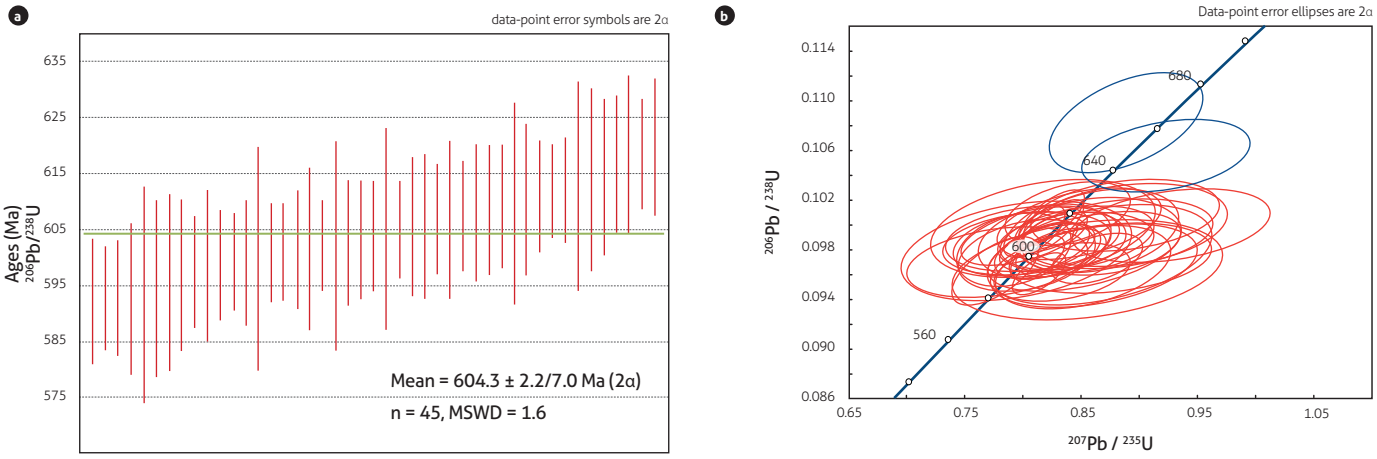

Figure 16. SJGS sample JDB-0001R
a) Diagram of mean $^{206}Pb/^{238}U$ ages; b) 'Wetherill' concordia curve. Blue ellipses: inherited zircon ages.

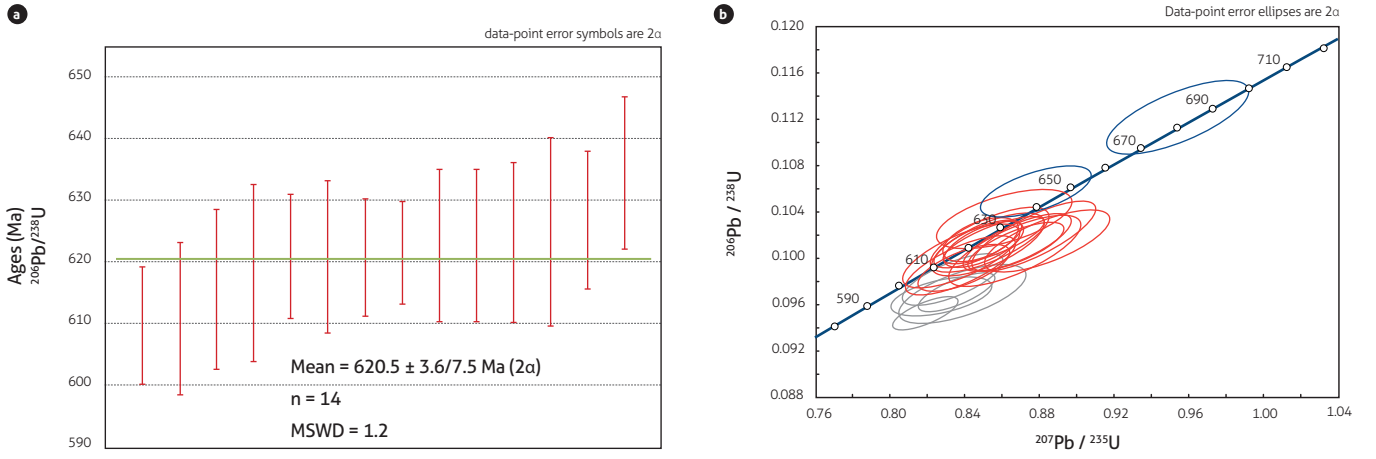

Figure 17. SJGS sample OPP-0074R
a) Diagram of mean $^{206}Pb/^{238}U$ ages; b) 'Wetherill' concordia curve. Blue ellipses: inherited zircons ages; gray ellipses: zircons with likely Pb loss.

4.5.2 Syenite (OPP-0074R)

The zircons in this sample are euhedral and prismatic, with well-defined igneous oscillatory zoning along the grain boundaries, whereas cores with concentric, sectorial, and chaotic zoning, homogeneous light and dark textures, and inclusions are observed at the center in some crystals (Figure 15b, Annex 5). Other zircons have radial fractures, which are attributed to marked differences in uranium content within the zircon, according to Corfu et al. (2003).

The weighted-average $^{206}Pb/^{238}U$ ages of this sample is 620.5 ± 3.6/7.5 Ma (2σ, n=14, MSWD=1.2), which is interpreted as the crystallization age of this intrusive body during the Ediacaran (Figure 17a). For sample JDB-0001R, the $^{206}Pb/^{238}U$ age that should be cited is 620.5 ± 7.5 Ma, which includes all sources of uncertainty. Besides the zircons from the magmatic event, two inherited zircons yielded older $^{206}Pb/^{238}U$ ages of 648 ± 10 and 685 ± 15 Ma (Figure 17b). Four analyses with apparently younger $^{206}Pb/^{238}U$ ages are clearly discordant (gray ellipses in Figure 17b); these values are affected by Pb loss and were therefore disregarded when calculating the crystallization age of this sample.

5. Discussion

The petrological evidence, the geochemical data, and the isotopic compositions of the nepheline syenite samples analyzed in this study (Figure 13b) indicate that the SJGS rocks derive from anorogenic and mantle-derived alkaline magmas subjected to magmatic differentiation and crustal assimilation.

Some of the magmas underwent fractional crystallization, resulting in Si-subsaturated compositions, which formed nepheline syenites. Others possibly reacted at the crustal level with the host rock, metamorphic rocks of the Guaviare Complex of varied compositions (Maya et al., 2018), producing some silica-saturated magmas, such as syenogranite. Such a contamination process is reflected in the isotope composition of a syenogranite sample, with an anomalously high initial $^{87}Sr/^{86}Sr$ ratio (0.7067, in contrast to the ratios of 0.7048 and 0.7054 of the nepheline syenite samples), which could have resulted from crustal assimilation of host rocks and/or rocks with low Rb/Sr ratios. Simultaneously, this contamination would also produce a lower ε_{Nd} value, assessed in syenogranite (+0.6), and an apparently older T_{DM} model age of 1000 Ma, in contrast to the model ages of 920 and 930 Ma assessed in the nepheline syenite samples. A similar origin has been suggested in other regions of the world where rocks are simultaneously subsaturated and saturated in silica (Foland et al., 1993; Zhu et al., 2016).

U-Pb zircon ages reported by different authors, such as Arango et al. (2012), Franco et al. (2018), and Muñoz Rocha et al. (2019), and those assessed in this study indicate that syenite was intruded in the Ediacaran period of the Neoproterozoic, in a magmatic age range of at least 30 Ma, between 621 – 7 and 577.8 + 6.3 Ma, which would indicate that the syenite magmas were not all intruded simultaneously but rather that multiple intrusions occurred during that period. The samples dated in this study contain inherited zircons with a minimum age of 662.3-19.2 Ma, that is, 643.1 Ma (Annex 3), and these zircons may be "antecrysts" formed in initial magma chambers of the syenites because no rocks of those ages are known in the area. Thus, the alkaline magmatism would have lasted approximately 59 million years. In the state of Bahia, Brazil, the alkaline magmatism associated with rifting lasted at least 58 million years (Rosa et al., 2007).

The Ar-Ar, K-Ar, and Rb-Sr biotite ages of intrusive rocks generally correspond to cooling ages. However, the large interval between the most recent U-Pb age (577.8 ± 6.3 Ma) and the oldest K-Ar age (508 ± 26 Ma) (Table 2) indicates a cooling age, below 300 °C, of 37 million years. Considering that hornfels were formed in the contact between syenite and regional metamorphic rocks, with injection migmatites, and not regional anatectic migmatites, the intrusion would have occurred at a depth of a few kilometers. Accordingly, cooling to 300 °C unlikely lasted 37 million years. Moreover, data presented by Arango et al. (2012) show that stepwise-extracted Ar fractions do not plateau well, which may result from excessive recoil during the $^{39}K(n,p)^{39}Ar$ reaction produced by irradiation, a complex thermal history, or the combination of both factors. The two possible events that may have generated a complex thermal history and that may have disturbed the $K\text{-}Ar/^{40}Ar\text{-}^{39}Ar$ systems are: 1) the Cambro-Ordovician sedimentary cover in the area may have been quite thick, which would have resulted in a complex cooling history of the syenites or allowed the syenites to reheat during tectonic burial; and 2) an important thermal event may have affected the western margin of the Amazonian Craton during the Cretaceous, as suggested by the presence of basaltic dikes dated at 102 Ma in the Araracuara region (Ibáñez-Mejía and Cordani, 2020). Although these rocks have not been reported in the Guaviare region, currently available data prevent us from ruling out the presence of a recent thermal event (for example, Cretaceous) in the area. Thus, the thermal and post-Ediacaran

tectonic burial history of the zone should be further studied to address these unanswered questions in the future.

The following model is proposed for the zone: At the end of the Neoproterozoic, a series of rifts enabled the disintegration of the Rodinia supercontinent into new continents. During this rifting period, at approximately 600 Ma, the northern zone of the Amazon was separated from Laurentia and Baltica, forming the Iapetus ocean (Condie, 2011; Cawood and Pisarevsky, 2017). Some of the rifts in the NW Amazon could have favored the intrusion of alkaline silica-subsaturated magmas, most likely generated by partial melting of mantle-derived igneous rocks during previous magmatic events, as indicated by the T_{DM} model ages of 920 and 930 Ma assessed in the nepheline syenite samples. These ages suggest that the source rocks of the SJGS magmas were likely formed during the Putumayo tectono-magmatic event, whose thermal and lithological record is common in several crustal segments of the northern Andes (Kroonenberg, 1982; Restrepo-Pace et al., 1997; Ramos, 2010; Cardona et al., 2010; Ibáñez-Mejía et al., 2011, 2015). Based on the isotope characteristics described in this study, an alternative origin of nepheline syenites related to juvenile mantle magmas (separated from the mantle at ~600 Ma) contaminated with older crust can also be ruled out; if such an origin were true, this contamination should have produced Si-saturated magmas, and therefore nepheline syenites would not have been formed in the first place, and their isotope signature would also be altered, moving away from the mantle array, as in the case of syenogranite.

Other authors have proposed different origins, such as crustal anatexis (Arango et al., 2011, 2012; Toussaint, 1993) or intraplate magmatism associated with Pan-African orogeny (Franco et al., 2018), which are not supported by isotope or regional geological data. Furthermore, Si-subsaturated magmas most likely cannot be derived from partial melting of common crustal rocks, which are typically saturated in quartz. Most data on alkaline magmatism reported in the literature indicate mantle sources with isotope signatures similar to those found in this study (Fitton and Upton, 1987; Winter, 2001).

6. Conclusions

U/Pb zircon dating of SJGS rocks places the unit in the Ediacaran, between 604 ± 7 and 620.5 ± 7.5 Ma. The SJGS derives from anorogenic magmatism in an intraplate setting, most likely resulting from rift-like stretching during the fragmentation of Rodinia at the end of the Neoproterozoic. The sources of the SJGS magmas would have been magmatic rocks directly formed by partial mantle melting during the Putumayo tectono-magmatic event.

The different syenite bodies consist of nepheline syenites, nepheline-bearing alkali-feldspar syenites, syenites, and syenogranites. The coexistence of nepheline- and quartz-bearing rocks could have resulted from the reaction between syenite magma and crustal rocks, which would have produced some silica-saturated magmas, such as the syenogranites that occur in southern SJGS bodies (El Capricho and Cerritos).

The southern SJGS syenite bodies tend to have broader compositions than the northern SJGS bodies, where the recorded rocks exclusively comprise nepheline syenites.

The SJGS is subdivided into three geochemical groups with contrasting characteristics that denote processes associated with the magmatic evolution of the igneous body, which include crustal differentiation and assimilation.

The intrusion of the SJGS generated a thermal metamorphism, in amphibolite and pyroxene-hornfels facies, in the host rocks of the Guaviare Complex, which allowed the recrystallization of minerals and the formation of hornfels and injection migmatites. A history of slow cooling, or a more recent thermal event not yet identified, affected the K-Ar/^{40}Ar-^{39}Ar systems of the syenites, yielding significantly younger ages than those assessed using the U-Pb zircon dating method.

Acknowledgements

This research summarizes and interprets part of the results from the project *Elaboración de la cartografía geológica en un conjunto de planchas a escala 1:100000 ubicadas en dos zonas del territorio colombiano, zona sur* [Geologic mapping of a set of plates at a 1:100 000 scale located in two zones of southern Colombia] of the Dirección de Geociencias Básicas del Servicio Geológico Colombiano (SGC), conducted by the geology team of the Serviminas company under contract No. 508 of 2017. Finally, the authors thank the anonymous reviewers for their valuable comments and suggestions, which helped to improve this manuscript.

Supplementary data

Supplementary data to this article can be found online at https://doi.org/10.32685/0120-1425/bol.geol.48.1.2021.503

References

Arango, M., Nivia, A., Zapata, G., Giraldo, M., Bermúdez, J., & Albarracín, H. (2011). *Geología y geoquímica de la Plancha 350 - San José del Guaviare. Memoria explicativa. Escala 1: 100.000*. Servicio Geológico Colombiano.

Arango, M., Zapata, G., & Martens, U. (2012). Caracterización petrográfica, geoquímica y edad de la Sienita Nefelínica de San José del Guaviare. *Boletín de Geología*, *34*(1), 15-26.

Bowie, S., & Simpson, P. (1977). Microscopy: reflected light. In J. Zussman (ed.), *Physical methods in determinative mineralogy* (2nd ed., pp. 109-165). Academic Press, Ltd.

Caicedo, J. C. (2003). *Toma de datos en la libreta de campo*. Ingeominas.

Cardona, A., Chew, D., Valencia, V., Bayona, G., Mišković, A., & Ibáñez-Mejía, M. (2010). Grenvillian remnants in the Northern Andes: Rodinian and phanerozoic paleogeographic perspectives. *Journal of South American Earth Sciences*, *29*(1), 92-104. https://doi.org/10.1016/j.jsames.2009.07.011

Cawood, P., & Pisarevsky, S. (2017). Laurentia-Baltica-Amazonia relations during Rodinia assembly. *Precambrian Research*, *292*, 386-397. https://doi.org/10.1016/j.precamres.2017.01.031

Condie, K. (2011). The Supercontinent Cycle. In *Earth as an Evolving Planetary System* (pp. 317-355). Academic Press. https://doi.org/10.1016/b978-0-12-385227-4.00003-1

Corfu, F., Hanchar, J., Hoskin, P., & Kinny, P. (2003). Atlas of zircon textures. *Reviews in Mineralogy and Geochemistry*, *53*(1), 469-500. https://doi.org/10.2113/0530469

Cox, K., Bell, J., & Pankhurst, R. (1979). *The interpretation of igneous rocks* (first ed.). Springer Science & Business Media. https://doi.org/10.1007/978-94-017-3373-1

DePaolo, D. (1981). A neodymium and strontium isotopic study of the mesozoic calc-alkaline granitic batholiths of the Sierra Nevada and Peninsular Ranges, California. *Journal of Geophysical Research*, *86*(B11), 10470-10488. https://doi.org/10.1029/JB086iB11p10470

Faure, G., & Mensing, T. (2005). *Isotopes: principles and applications* (Third). John Wiley & Sons, Inc.

Fitton, J., & Upton, B. (1987). Alkaline igneous rocks. *Geological Society Special Publication*, *30*, 1-568.

Foland, K., Landoll, J., Henderson, C., & Chen, J. (1993). Formation of cogenetic quartz and nepheline syenites. *Geochimica et Cosmochimica Acta*, *57*(3), 697-704. https://doi.org/10.1016/0016-7037(93)90380-F

Franco, J., Muñoz, J., Piraquive, A., Bonilla, A., Amaya, Z., Cramer, T., & Campos, H. (2018). *Geochronology of the Nepheline Syenite of el Jordán, Guaviare Colombia, evidences of neoproterozoic-cambrian intraplate magmatism and its implications during Pan-African tectonics in western Gondwana*. EGU General Assembly Conference Abstracts. 10861.

Galvis, J., Huguett, A., & Ruge, P. (1979). Geología de la Amazonia Colombiana. Informe No. 1792. *Boletín Geológico*, *22*(3), 1-153.

Gansser, A. (1954). The Guiana Shield (S. America). Geological observations. *Eclogae Geologicae Helvetiae*, *47*(1), 77-112.

Gehrels, G., Valencia, V., & Ruiz, J. (2008). Enhanced precision, accuracy, efficiency, and spatial resolution of U-Pb ages by laser ablation-multicollector-inductively coupled plasma-mass spectrometry. *Geochemistry, Geophysics, Geosystems*, *9*(3), 1-13. http://doi.org/10.1029/2007GC001805

Gioia, S., Hollanda, M., & Pimentel, M. (1999). *Uso de resinas RE-Spec e Sr-Spec em geoquímica isotópica.* Anais do V congresso de geoquímica dos países de língua portuguesa e VII Congresso Brasileiro de Geoquímica. 218.

Gioia, S., & Pimentel, M. (2000). The Sm-Nd isotopic method in the geochronology laboratory of the University of Brasília. *Anais da Academia Brasileira de Ciencias*, *72*(2), 219-245. https://doi.org/10.1590/s0001-37652000000200009

Hamilton, D., & Mackenzie, W. (1965). Phase-equilibrium studies in the system NaAlSiO4 (nepheline)-KAlSiO4 (kalsilite)-SiO2-H2O. *Mineralogical Magazine and Journal of the Mineralogical Society*, *34*(268), 214-231. https://doi.org/10.1180/minmag.1965.034.268.17

Heinrich, E. (1965). *Microscopic identification of minerals*. McGraw-Hill.

Ibáñez-Mejía, M., & Cordani, U. (2020). *Zircon U-Pb geochronology and Hf-Nd-O isotope geochemistry of the Paleo- to Mesoproterozoic basement in the westernmost Guiana Shield* (pp. 65-90). In Gómez, J. & Mateus-Zabala, D. (eds.), *The Geology of Colombia, Volume 1 Proterozoic - Paleozoic*. Publicaciones Geológicas Especiales 35, Servicio Geológico Colombiano. https://doi.org/10.32685/pub.esp.35.2019.04

Ibáñez-Mejía, M., Pullen, A., Arenstein, J., Gehrels, G., Valley, J., Ducea, M., Mora, A., Pecha, M., & Ruiz, J. (2015). Unraveling crustal growth and reworking processes in complex zircons from orogenic lower-crust: the proterozoic Putumayo Orogen of Amazonia. *Precambrian Research*, *267*, 285-310. https://doi.org/10.1016/j.precamres.2015.06.014

Ibáñez-Mejía, M., Ruiz, J., Valencia, V., Cardona, A., Gehrels, G., & Mora, A. (2011). The Putumayo Orogen of Amazonia and its implications for Rodinia reconstructions: new U-Pb geochronological insights into the proterozoic tectonic evolution of northwestern South America. *Precambrian Research*, *191*(1-2), 58-77. https://doi.org/10.1016/j.precamres.2011.09.005

Ibáñez-Mejía, M., & Tissot, F. (2019). Extreme Zr stable isotope fractionation during magmatic fractional crystallization. *Science Advances*, *5*(12), 1-14. http://doi.org/10.1126/sciadv.aax8648

Jacobsen, S., & Wasserburg, G. (1980). Sm-Nd isotopic evolution of chondrites. *Earth and Planetary Science Letters*, *50*(1), 139-155. https://doi.org/10.1016/0012-821X(80)90125-9

Jacobsen, S., & Wasserburg, G. (1984). Sm-Nd isotopic evolution of chondrites and achondrites, II. *Earth and Planetary Science Letters*, *67*(2), 137-150. https://doi.org/10.1016/0012-821X(84)90109-2

Kroonenberg, S. (1982). A grenvillian granulite belt in the Colombian Andes and its relation to the Guiana Shield. *Geologie en Mijnbouw*, *61*, 325-333.

Lugmair, G., & Marti, K. (1978). Lunar initial 143Nd/144Nd: differential evolution of the lunar crust and mantle. *Earth and Planetary Science Letters*, *39*(3), 349-357. https://doi.org/10.1016/0012-821X(78)90021-3

Maniar, P., & Piccoli, P. (1989). Tectonic discrimination of granitoids. *Geological Society of America Bulletin*, *101*(5), 635-643. https://doi.org/10.1130/0016-7606(1989)101<0635:TDOG>2.3.CO;2

Maya, M. (1992). Catalogo de dataciones isotopicas en Colombia. *Boletín Geológico*, *32*(1), 127-187.

Maya, M., Amaya, C., Gómez, J., Tabares, G., Palacio, A., García, J., Tabares, F., Camacho, J., Betancur, J., & Duque, J. (2019). *Guía para la elaboración de la libreta de campo de un proyecto de cartografía geológica*. Serviminas.

Maya, M., Amaya, C., Restrepo, J., Duque, J., Palacio, A., Gutiérrez, P., Pérez, O., Ríos, C., Arias, E., & Bedoya, J. (2018). *Memoria explicativa de la Plancha 372 – El Retorno. Escala 1: 100.000*. Servicio Geológico Colombiano.

McDonough, W., & Sun, S. (1995). The composition of the earth. *Chemical Geology*, *120*, 223-253.

McDonough, W., Sun, S., Ringwood, A., Jagoutz, E., & Hofmann, A. (1992). Potassium, rubidium, and cesium in the earth and moon and the evolution of the mantle of the earth. *Geochimica et Cosmochimica Acta*, *56*(3), 1001-1012. https://doi.org/10.1016/0016-7037(92)90043-I

Motoki, A., Sichel, S., Vargas, T., Aires, J., Iwanuch, W., Mello, S., Motoki, K., Silva, S., Balmant, A., & Gonçalves, J. (2010). Geochemical evolution of the felsic alkaline rocks of Tanguá and Rio Bonito intrusive bodies, State of Rio de Janeiro, Brazil. *Geociências*, *29*(3), 291-310.

Motoki, A., Sichel, S., Vargas, T., Melo, D., & Motoki, K. (2015). Geochemical behaviour of trace elements during fractional crystallization and crustal assimilation of the felsic alkaline magmas of the state of Rio de Janeiro, Brazil. *Anais da Academia Brasileira de Ciências*, *87*(4), 1959-1979. https://doi.org/10.1590/0001-3765201520130385

Muñoz Rocha, J., Piraquive, A., Franco, J., Bonilla, A., Peña, M., Cramer, T., Rayo, L., & Villamizar, N. (2019). Megacircones ediacáricos de la Sienita Nefelínica de San José del Guaviare y su potencial como material de referencia para datación U/Pb mediante LA-ICP-MS. *Boletín Geológico*, *45*, 5-22. https://doi.org/10.32685/0120-1425/boletingeo.45.2019.484

Nivia, A., Giraldo, M., Arango, M., Albarracín, H., Bermúdez, J. & Zapata, G. (2011). *Geología de la plancha 350 - San José del Guaviare - Mapa escala 1:100.000.* Servicio Geológico Colombiano.

Pearce, J., Harris, N., & Tindle, A. (1984). Trace element discrimination diagrams for the tectonic interpretation of granitic rocks. *Journal of Petrology*, *25*(4), 956-983. https://doi.org/10.1093/petrology/25.4.956

Pinson, W., Hurley, P., Mencher, E., & Fairbairn, H. (1962). K-Ar and Rb-Sr ages of biotites from Colombia, South America. *GSA Bulletin*, *73*(7), 907-910. https://doi.org/10.1130/0016-7606(1962)73[907:KARAOB]2.0.CO;2

Pullen, A., Ibáñez-Mejia, M., Gehrels, G., Giesler, D., & Pecha, M. (2018). Optimization of a laser ablation-single collector-inductively coupled plasma-mass spectrometer (thermo element 2) for accurate, precise, and efficient zircon U-Th-Pb geochronology. *Geochemistry, Geophysics, Geosystems*, *19*(10), 3689-3705. http://doi.org/10.1029/2018GC007889

Ramos, V. (2010). The Grenville-age basement of the Andes. *Journal of South American Earth Sciences*, *29*(1), 77-91. https://doi.org/10.1016/j.jsames.2009.09.004

Restrepo-Pace, P., Ruiz, J., Gehrels, G., & Cosca, M. (1997). Geochronology and Nd isotopic data of Grenville-age rocks in the Colombian Andes: new constraints for late proterozoic-early paleozoic paleocontinental reconstructions of the Americas. *Earth and Planetary Science Letters*, *150*(3-4), 427-441. https://doi.org/10.1016/s0012-821x(97)00091-5

Rosa, M., Conceição, H., Macambira, M., Galarza, M., Cunha, M., Menezes, R., Marinho, M., Filho, B., & Rios, D. (2007). Neoproterozoic anorogenic magmatism in the Southern Bahia Alkaline Province of NE Brazil: U-Pb and Pb-Pb ages of the blue sodalite syenites. *Lithos*, *97*(1-2), 88-97. https://doi.org/10.1016/j.lithos.2006.12.011

Sláma, J., Košler, J., Condon, D., Crowley, J., Gerdes, A., Hanchar, J., Horstwood, M., Morris, G., Nasdala, L., Norberg, N., Schaltegger, U., Schoene, B., Tubrett, M., & Whitehouse, M. (2008). Plešovice zircon - A new natural reference material for U-Pb and Hf isotopic microanalysis. *Chemical Geology*, *249*(1-2), 1-35. http://doi.org/10.1016/j.chemgeo.2007.11.005

Steiger, R., & Jager, E. (1977). Subcommission on geochronology: convention on the use of decay constants in geo- and cosmochronology. *Earth and Planetary Science Letters*, *36*(3), 359-362. https://doi.org/10.1016/0012-821X(77)90060-7

Storey, M., Wolff, J., Norry, M., & Marriner, G. (1989). Origin of hybrid lavas from Agua de Pau volcano, Sao Miguel, Azores. *Geological Society of London, Special Publication*, *42*, 161-180. https://doi.org/https://doi.org/10.1144/GSL.SP.1989.042.01.11

Streckeisen, A. (1976). To each plutonic rock its proper name. *Earth Science Reviews*, *12*(1), 1-33. https://doi.org/10.1016/0012-8252(76)90052-0

Toussaint, J. (1993). Introducción - Precámbrico. In *Evolución geológica de Colombia*. Universidad Nacional de Colombia.

Trumpy, D. (1943). Pre-Cretaceous of Colombia. *GSA Bulletin*, *54*(9), 1281-1304. https://doi.org/10.1130/GSAB-54-1281

Trumpy, D. (1944). *El Precretaceo de Colombia*. Bogotá.

Vesga, J., & Castillo, L. (1972). *Reconocimiento geológico y geoquímico preliminar del río Guaviare entre las confluencias con los ríos Ariari e Iteviare*. Ingeominas.

Whitney, D., & Evans, B. (2010). Abbreviations for names of rock-forming minerals. *American Mineralogist*, *95*(1), 185-187. https://doi.org/10.2138/am.2010.3371

Winter, J. (2001). *An introduction to igneous and metamorphic petrology*. Prentice-Hall Inc.

Wolff, J. (2017). On the syenite-trachyte problem. *Geology*, *45*(12), 1067-1070. https://doi.org/10.1130/G39415.1

Zhu, Y., Yang, J., Sun, J., Zhang, J., & Wu, F. (2016). Petrogenesis of coeval silica-saturated and silica-undersaturated alkaline rocks: mineralogical and geochemical evidence from the Saima alkaline complex, NE China. *Journal of Asian Earth Sciences*, *117*, 184-207. https://doi.org/10.1016/j.jseaes.2015.12.014

Annexes

Annex 1. Geochemical data for the San José del Guaviare syenite

	Group 1			Group 2					
Sample	**CAL-0013R**	**CAL-0014R**	**JDB-0002R**	**CAL-0017R**	**CAL-0019R**	**CAL-0023R**	**CAL-0024R**	**ENA-0036R**	**JDB-0011R**
IGM	**5075307**	**5075308**	**5075538**	**5075316**	**5075318**	**5075322**	**5075323**	**5075503**	**5075547**
					Oxide (%)				
SiO_2	55.40	53.58	55.03	58.69	57.00	57.16	60.03	56.35	56.79
TiO_2	0.72	1.54	0.71	0.24	0.46	0.20	0.52	0.24	1.30
Al_2O_3	22.80	20.81	22.08	21.87	22.23	22.76	19.04	22.67	19.26
Fe_2O_3	2.47	5.32	3.43	2.83	3.72	2.01	5.55	2.39	4.77
MnO	0.07	0.18	0.10	0.06	0.13	0.05	0.13	0.05	0.26
MgO	0.21	0.80	0.34	0.08	0.29	0.06	0.04	0.03	0.46
CaO	0.44	1.04	0.50	0.19	0.13	0.22	0.24	0.45	0.49
Na_2O	8.98	7.51	8.93	9.56	9.02	9.38	6.10	8.74	8.14
K_2O	6.87	6.78	6.15	4.68	5.92	6.08	7.55	7.34	5.28
BaO	0.10	0.32	0.20	0.02	0.03	0.05	0.11	0.05	0.17
SrO	0.20	0.49	0.21	0.02	0.02	0.13	0.18	0.13	0.12
ZrO2*	0.01	0.03	0.01	0.55	0.13	0.04	0.02	0.05	0.27
P_2O_5	0.01	0.02	0.04	<0.01	0.01	0.01	0.01	0.01	0.09
Cr_2O_3	0.02	<0.01	0.03	<0.01	0.04	0.04	<0.01	0.03	<0.01
LOI	0.85	0.69	0.63	0.50	0.58	1.34	0.31	1.05	0.67
Total	99.15	99.11	98.39	99.29	99.71	99.53	99.83	99.58	98.07
					Element (ppm)				
Ba	791.00	3110.00	1830.00	152.00	97.80	379.00	843.00	301.00	1670.00
Rb	110.00	113.50	98.70	198.00	309.00	222.00	211.00	126.50	149.50
Sr	1870.00	4710.00	1990.00	124.00	119.00	1255.00	1665.00	1260.00	1220.00
Cs	0.50	0.58	0.38	0.56	1.69	1.11	1.01	0.28	1.02
Ga	19.40	23.10	20.70	37.00	28.70	28.00	23.30	23.10	29.80
Ta	14.30	23.70	8.50	20.40	16.10	9.80	7.50	4.00	32.10
Nb	139.50	312.00	111.00	223.00	244.00	186.00	140.00	71.20	625.00
Hf	3.50	7.30	1.90	77.40	16.20	7.00	2.50	7.80	36.60
Zr	110.00	259.00	61.00	4070.00	933.00	267.00	134.00	384.00	1970.00
Y	20.50	38.90	16.20	9.70	5.40	5.00	7.40	4.20	15.60
Th	1.34	3.73	0.94	16.75	17.20	12.95	6.94	5.72	16.30
U	0.32	1.00	0.24	74.20	25.10	9.55	13.25	4.06	22.40
Cr	20.00	40.00	20.00	20.00	20.00	20.00	40.00	20.00	20.00
Ni	<1	2.00	1.00	<1	1.00	<1	<1	<1	<1
Co	<1	2.00	<1	1.00	2.00	<1	<1	<1	1.00
Sc	0.80	1.50	1.10	1.20	1.40	0.80	0.60	0.80	1.10
V	15.00	59.00	20.00	16.00	11.00	12.00	40.00	12.00	27.00
Cu	<1	2.00	2.00	7.00	1.00	1.00	1.00	3.00	<1
Pb	2.00	24.00	<2	25.00	13.00	8.00	9.00	12.00	9.00
Zn	46.00	107.00	72.00	56.00	106.00	43.00	104.00	36.00	139.00
Ti	0.18	0.18	0.15	0.49	0.72	0.50	0.16	0.24	0.17
Bi	<0.01	<0.01	<0.01	0.01	0.01	0.01	0.01	<0.01	0.01
Cd	<0.5	<0.5	<0.5	<0.5	<0.5	<0.5	<0.5	<0.5	<0.5
Sn	1.00	3.00	1.00	1.00	2.00	1.00	2.00	1.00	3.00
W	3.00	6.00	3.00	3.00	3.00	2.00	3.00	3.00	5.00
Li	<10	10.00	<10	10.00	20.00	10.00	10.00	<10	10.00
Mo	<1	<1	<1	<1	<1	<1	<1	<1	<1
Hg	0.02	0.02	0.03	0.01	0.06	0.03	<0.005	0.04	0.02
As	0.10	0.10	<0.1	0.20	0.20	0.20	0.50	0.30	0.20
Se	<0.2	<0.2	<0.2	<0.2	<0.2	<0.2	<0.2	<0.2	<0.2
Sb	<0.05	<0.05	<0.05	<0.05	<0.05	<0.05	<0.05	<0.05	<0.05

In	0.01	0.03	0.01	0.01	0.01	0.01	0.02	0.01	0.03
Te	0.02	0.01	0.03	0.03	0.05	0.03	<0.01	0.02	0.02
La	36.20	76.40	34.20	8.00	11.90	14.40	32.90	15.30	29.80
Ce	118.50	216.00	96.60	14.20	22.40	24.40	51.20	25.60	74.20
Pr	17.20	28.80	12.65	1.29	2.26	2.30	4.76	2.36	8.42
Nd	69.00	113.50	48.20	4.30	7.20	6.90	15.00	7.70	30.10
Sm	10.90	17.50	7.93	0.67	1.01	0.93	2.09	1.12	4.65
Eu	3.19	5.41	2.42	0.31	0.30	0.37	0.67	0.77	1.50
Gd	7.58	13.15	5.37	0.64	0.65	0.72	1.45	0.75	3.30
Tb	1.09	1.92	0.84	0.16	0.13	0.14	0.24	0.13	0.54
Dy	5.71	9.95	4.24	0.98	0.78	0.84	1.26	0.71	3.16
Ho	0.85	1.65	0.72	0.35	0.18	0.17	0.28	0.12	0.64
Er	2.12	4.09	1.66	1.59	0.63	0.57	0.83	0.52	1.91
Tm	0.24	0.50	0.20	0.36	0.14	0.11	0.12	0.08	0.36
Yb	1.24	2.71	1.00	3.08	1.09	0.75	0.78	0.56	2.20
Lu	0.15	0.32	0.11	0.65	0.19	0.15	0.10	0.09	0.43
	Group 2				**Group 3**				
Sample	**OPP-0064R**	**CAL-0008R**	**CMR-0013R**	**CMR-0027R-1**	**JDB-0024R**	**OPP-0061R**	**OPP-0065R**	**OPP-0073R-J**	**OPP-0074R**
IGM	**5075674**	**5075302**	**5075382**	**5075396**	**5075560**	**5075671**	**5075675**	**5075694**	**5075695**
					Oxide (%)				
SiO_2	63.86	59.14	56.31	61.25	66.07	67.68	69.70	74.20	64.09
TiO_2	0.18	0.99	1.35	0.85	0.63	0.55	0.49	0.13	0.85
Al_2O_3	18.53	18.53	17.12	17.22	16.75	15.18	14.42	12.63	16.38
Fe_2O_3	2.07	4.08	5.54	4.21	3.27	3.03	3.04	2.57	3.88
MnO	0.06	0.13	0.15	0.14	0.14	0.03	0.07	0.05	0.11
MgO	0.16	0.64	1.82	0.77	0.44	0.44	0.34	0.13	0.68
CaO	0.04	1.24	3.60	1.84	0.61	0.26	0.70	0.33	1.24
Na_2O	6.76	6.36	6.63	6.42	5.74	5.08	4.95	3.30	5.79
K_2O	6.47	5.95	4.40	5.58	6.03	5.50	5.40	5.44	5.82
BaO	0.10	0.26	0.39	0.11	0.15	0.05	0.09	0.07	0.10
SrO	0.07	0.18	0.33	0.09	0.03	0.03	0.05	0.01	0.06
ZrO2*	0.11	0.06	0.06	0.11	0.17	0.08	0.07	0.08	0.08
P_2O_5	0.01	0.15	0.53	0.17	0.10	0.10	0.09	0.02	0.16
Cr_2O_3	<0.01	<0.01	<0.01	<0.01	0.01	0.01	0.01	0.01	<0.01
LOI	0.27	0.69	1.13	0.11	0.60	0.43	0.26	0.46	0.31
Total	98.69	98.40	99.36	98.87	100.74	98.45	99.68	99.43	99.55
					Element (ppm)				
Ba	945.00	2270.00	3800.00	855.00	1185.00	439.00	744.00	529.00	713.00
Rb	166.50	163.00	122.00	173.00	157.50	278.00	146.00	322.00	229.00
Sr	644.00	1690.00	3100.00	752.00	249.00	306.00	472.00	115.00	474.00
Cs	0.42	1.09	1.50	0.50	0.38	2.19	0.55	1.46	1.57
Ga	30.40	20.90	23.80	25.50	22.90	25.70	19.90	21.90	23.10
Ta	1.70	10.60	6.40	9.90	4.50	14.00	9.90	5.70	16.90
Nb	46.60	147.50	112.50	152.50	114.00	185.50	128.00	67.10	219.00
Hf	15.50	7.50	9.60	16.30	26.70	14.70	12.00	21.70	14.70
Zr	798.00	416.00	457.00	821.00	1280.00	607.00	487.00	622.00	619.00
Y	8.90	34.30	44.40	38.70	141.00	31.50	45.90	31.40	102.00
Th	6.93	5.10	12.70	30.30	10.65	24.80	16.30	180.00	22.40
U	4.01	1.10	4.75	8.38	2.20	5.71	3.04	68.00	5.08
Cr	20.00	20.00	20.00	40.00	20.00	20.00	30.00	20.00	30.00
Ni	<1	<1	<1	<1	<1	<1	<1	1.00	3.00
Co	1.00	1.00	2.00	2.00	1.00	2.00	1.00	3.00	4.00
Sc	0.70	1.20	2.40	1.10	2.50	1.90	1.20	1.00	1.60
V	19.00	37.00	91.00	46.00	7.00	35.00	28.00	17.00	43.00
Cu	1.00	1.00	1.00	1.00	1.00	1.00	1.00	1.00	15.00
Pb	16.00	14.00	15.00	18.00	18.00	10.00	14.00	19.00	30.00

Zn	52.00	83.00	106.00	104.00	86.00	37.00	44.00	14.00	86.00
Ti	0.06	0.24	0.17	0.06	0.11	0.11	0.10	0.07	0.10
Bi	0.01	<0.01	0.02	0.02	0.01	0.06	0.02	0.14	0.08
Cd	<0.5	<0.5	<0.5	<0.5	<0.5	<0.5	<0.5	<0.5	<0.5
Sn	1.00	3.00	3.00	4.00	2.00	5.00	4.00	1.00	6.00
W	5.00	5.00	7.00	1.00	1.00	5.00	5.00	8.00	6.00
Li	<10	20.00	10.00	<10	10.00	20.00	<10	<10	20.00
Mo	<1	<1	2.00	<1	<1	3.00	3.00	1.00	2.00
Hg	0.01	0.02	0.01	<0.005	0.01	0.02	<0.005	0.01	0.01
As	0.20	<0.1	0.30	0.50	<0.1	<0.1	0.30	0.50	0.30
Se	<0.2	<0.2	<0.2	0.30	<0.2	<0.2	<0.2	<0.2	0.40
Sb	<0.05	<0.05	<0.05	<0.05	<0.05	<0.05	<0.05	0.09	<0.05
In	0.01	0.03	0.02	0.02	0.04	0.02	0.02	0.01	0.04
Te	<0.01	0.02	0.03	0.01	0.01	<0.01	0.02	0.02	0.02
La	33.10	99.10	144.00	122.00	326.00	70.70	73.10	71.00	175.50
Ce	49.30	209.00	275.00	220.00	195.50	225.00	186.00	61.30	269.00
Pr	4.70	23.70	29.90	22.90	53.20	18.00	18.10	13.10	41.30
Nd	14.40	84.20	108.00	78.10	200.00	58.80	62.20	44.00	146.50
Sm	1.86	12.40	16.50	11.40	30.60	8.97	9.93	6.39	23.10
Eu	0.69	3.42	5.30	2.57	7.13	1.55	1.95	1.67	4.13
Gd	1.45	9.00	11.65	8.75	28.60	5.80	7.73	5.10	18.35
Tb	0.24	1.33	1.65	1.31	3.76	0.97	1.29	0.86	2.77
Dy	1.35	7.25	8.96	6.82	20.50	5.79	7.77	4.89	15.85
Ho	0.31	1.35	1.59	1.37	4.19	1.16	1.53	1.06	3.20
Er	1.02	3.39	4.33	4.43	11.15	3.92	4.77	3.29	10.30
Tm	0.17	0.50	0.61	0.69	1.42	0.66	0.76	0.54	1.58
Yb	1.27	2.59	4.01	4.50	7.90	4.88	5.60	4.01	9.93
Lu	0.18	0.35	0.64	0.61	1.21	0.79	0.81	0.70	1.38

Annex 2. Modal composition of rocks of the San José del Guaviare syenite

Sample	IGM	Qz	Nph	Pl	Fsp	Px	Arf	Hbl	Bt	Ms	And	Opq	Zrn	Ttn	Cal	Ser	Ccn	Other	Petrographic classification	Subdivision
CAL-0008R	5075302		6.70	16.00	45.80				12.50			1.70	2.10	5.90	3.80	1.00	2.80	1.70	Nepheline-bearing alkali feldspar syenite	Cerritos
CAL-0011R	5075305		6.90	11.10	58.70	0.70			13.20			2.10	0.70	2.40	1.60	2.80		0.00	Nepheline-bearing alkali feldspar syenite	Cerritos
CAL-0013R	5075307		20.30	12.30	62.30				3.70			1.00		0.01	0.01	1.00	0.01	0.00	Nepheline monzosyenite	El Capricho
CAL-0014R	5075308		22.50	1.00	49.50				12.30			2.50	1.00	5.50	2.90	1.80	1.00	0.00	Nepheline syenite	El Capricho
CAL-0015R	5075309		15.70	4.00	70.30				4.00			1.70	0.30	3.00	1.00	0.01	0.01	0.00	Nepheline syenite	El Capricho
CAL-0017R	5075316		19.00	20.00	45.80				8.10			0.60	1.60		1.00	1.60	2.30	0.02	Nepheline syenite	Cerritos
CAL-0019R	5075318		28.30	11.00	54.30				4.70			1.70	0.01			0.01	0.01	0.01	Nepheline monzosyenite	Cerritos
CAL-0023R	5075322		23.60	1.30	43.90				12.90			0.30			2.60	6.40	9.00	0.00	Nepheline syenite	El Turpial
CAL-0024R	5075323		5.00	3.30	85.30				4.00			2.30	0.01		0.01	0.01	0.01	0.00	Nepheline-bearing alkali feldspar syenite	El Turpial
CMR-0013R	5075382		11.00	1.00	73.00				11.30			3.30	0.01		0.01	0.01	0.30	0.00	Nepheline syenite	Cerritos
CMR-0014R	5075383		17.90	0.70	58.90				8.40			4.90	0.70	0.01	1.10	3.20	4.20	0.00	Nepheline syenite	Cerritos
CMR-0015R	5075384		16.00	4.30	70.70				7.70			0.30			0.70	0.70	0.01	0.00	Nepheline syenite	Cerritos
CMR-0016R	5075385		18.70	3.00	70.90				5.70			1.70	0.01			0.01		0.00	Nepheline syenite	Cerritos
CMR-0028R	5075397		18.30	0.60	64.70				2.00			2.60	0.60		2.30	3.30	5.60	0.00	Nepheline syenite	Cerritos
ENA-0036R	5075503		22.30	3.00	72.00				1.00			1.30		0.01		0.01	0.01	0.02	Nepheline syenite	El Capricho
JDB-0001R	5075537		18.70	4.70	65.00				9.70			1.00	0.30	0.30	0.30	0.01	0.01	0.01	Nepheline syenite	El Capricho
JDB-0002R	5075538		25.20	2.00	58.60				4.00			3.00	0.40	0.30	3.00	1.70	1.80	0.00	Nepheline syenite	El Capricho
JDB-0003R	5075539		19.00	15.00	56.70				7.00			2.30	0.01		0.01	0.01	0.01	0.00	Nepheline monzosyenite	El Capricho
JDB-0011R	5075547		10.00	9.00	70.30				7.00			2.00	1.00	0.30	0.01	0.01	0.30	0.00	Nepheline-bearing alkali feldspar syenite	El Capricho
JDB-0013R	5075549		28.00	2.30	61.70				7.30			0.01			0.70	0.01	0.01	0.00	Nepheline syenite	El Capricho
OPP-0064R	5075674		3.30	3.00	92.00				1.30			0.30	0.01			0.01	0.01	0.00	Nepheline-bearing alkali feldspar syenite	Cerritos
CMR-0027R-1	5075396	3.30		13.00	62.80	0.01	4.30		14.30			0.30	0.01	2.00	0.01	0.01			Syenite	Cerritos
JDB-0024R	5075560	19.40		8.90	46.20		11.80		4.20			4.50	2.90	0.30		1.00		0.81	Syenogranite	El Capricho
OPP-0026R	5075632	9.30		10.30	66.30		7.70		4.00			2.30	0.01	0.01		0.01			Quartz-syenite	Cerritos
OPP-0058RD-1	5075668	68.90		15.20	11.10				1.90	0.40		0.90			0.40	1.20			Quartz-rich granitoid (silicification)	Cerritos
OPP-0061R	5075671	7.70		4.70	85.30				1.30			1.00	0.01			0.01		0.01	Quartz alkali feldspar syenite	Cerritos
OPP-0065R	5075675	20.00		19.70	48.30	1.70	5.30		1.30			1.70	0.01	2.00		0.01			Syenogranite	Cerritos
OPP-0073RG	5075691	37.70		13.70	44.70					3.70		0.30	0.01			0.01		0.01	Syenogranite	Cerritos
OPP-0073RJ	5075694	29.00		8.70	59.30				1.70	0.01		1.70	0.01			0.01			Syenogranite	Cerritos
OPP-0074R	5075695	4.70		11.10	67.60		2.90		3.60			2.90	0.30	4.90		1.30		0.70	Syenite	Cerritos
OPP-0058RA	5075665	40.00		22.00	4.30				31.30	1.00		1.30	0.01			0.01		0.01	Muscovite bearing feldspar-biotite-quartz hornfels	Pelitic
OPP-0058RC	5075667	0.40		60.60	3.20				13.80	2.80	2.50	3.90	0.01			11.70		1.12	Sillimanite-andalusite bearing biotite-feldspars hornfels	Pelitic
OPP-0073RA	5075685	46.30		8.00	4.00				39.70	0.01		2.00	0.01			0.01		0.01	Muscovite bearing feldspar-biotite-quartz hornfels	Pelitic
OPP-0058RB	5075666	17.70		3.00	8.00	14.30		54.70	0.01			0.01		2.30		0.01		0.00	Biotite bearing feldspars-diopside-quartz-hornblende hornfels	Mafic
OPP-0058RD-2	5075668	53.30		16.00	4.70	6.70		14.70	4.70	0.01		0.01			0.01	0.01		0.01	Diopside-hornblende-feldspars-quartz hornfels	Mafic
OPP-0073RC	5075687	10.00		12.70	16.00	25.00		22.30	12.00			0.01		2.00		0.01		0.00	Quartz-hornblende-diopside-feldspars and hornfels	Mafic
OPP-0073RB	5075686	13.70		57.40	9.10				13.00			3.90	0.01	0.01		0.01		2.92	Sillimanite bearing biotite-quartz-feldspar hornfels	Quartz – feldspathic
OPP-0073RD	5075688	22.90		54.30	4.90				11.30	0.70		3.20	0.01	0.01				2.70	Biotite-quartz-feldspar hornfels	Quartz – feldspathic
OPP-0073RE	5075689	29.00		31.00	29.90				6.00			2.00	0.01			0.01		2.30	Epidote bearing biotite-quartz-felspar hornfels	Quartz – feldspathic
OPP-0073RF	5075690	8.00		75.60	8.00				0.70	0.70		2.00	1.30	0.70	0.01	0.70		2.31	Quartz-feldspars hornfels	Quartz – feldspathic
OPP-0073RH	5075692	18.00		63.30	2.70				8.70	0.70		3.30	0.30	0.01	0.01	2.70		0.32	Sillimanite bearing biotite-quartz-feldspar hornfels	Quartz – feldspathic
OPP-0073RI	5075693	10.30		51.10	27.70				6.70	1.70		2.30	0.01		0.30	0.01		0.01	Muscovite bearing biotite-quartz-feldspar hornfels	Quartz – feldspathic

Qz: quartz; Nph: nepheline; Pl: plagioclase; Fsp: feldspar; Mc: Microcline; Px: pyroxene; Arf: arfvedsonite; Hbl: hornblende; Bt: biotite; Ms: muscovite; And: andalusite; Opq: opaque mineral; Zrn: zircon; Ttn: titanite; Cal: calcite; Ser: sericite; Ccn: cancrinite. Abbreviations according to Whitney and Evans (2010)

Annex 3. Analytical data for the U/Pb age of the San José del Guaviare Syenite

JDB-0001R (nepheline syenite)																
Analysis	Isotope ratio									Apparent age (Ma)						
	U	Th/U	206Pb*/	±	207Pb*/	±	206Pb*/	±	error	206Pb*/	±	207Pb*/	±	206Pb*/	±	Conc
	(ppm)		207Pb*	(%)	235U*	(%)	238U	(%)	corr.	238U*	(Ma)	235U	(Ma)	207Pb*	(Ma)	(%)
JDB_0001R_15	21	1.4	15.8983	5.4	0.8339	5.8	0.0962	2.0	0.34	592.1	11.2	615.8	26.6	704.9	115.1	84.0
JDB_0001R_13	246	0.2	16.2602	1.8	0.8162	2.4	0.0963	1.7	0.68	592.7	9.4	605.9	11.1	656.7	38.4	90.2
JDB_0001R_37	206	0.5	16.3399	2.1	0.8122	2.8	0.0963	1.9	0.66	592.7	10.6	603.7	12.9	646.3	45.7	91.7
JDB_0001R_38	45	0.9	17.0940	3.1	0.7764	3.9	0.0963	2.4	0.61	592.7	13.5	583.4	17.3	548.6	67.2	108.0
JDB_0001R_44	7	2.1	15.5280	10.6	0.8556	11.1	0.0964	3.4	0.31	593.3	19.4	627.7	52.0	754.8	223.4	78.6
JDB_0001R_24	14	1.2	15.5763	6.4	0.8547	7.0	0.0966	2.8	0.40	594.5	15.9	627.2	32.6	748.2	135.1	79.5
JDB_0001R_04	12	1.9	15.4799	7.9	0.8618	8.4	0.0968	2.8	0.33	595.6	15.9	631.1	39.4	761.3	166.7	78.2
JDB_0001R_47	12	1.7	17.1821	7.9	0.7780	8.3	0.0970	2.4	0.29	596.8	13.5	584.4	36.7	537.3	173.2	111.1
JDB_0001R_20	90	0.7	16.6667	3.0	0.8029	3.5	0.0971	1.8	0.50	597.4	10.0	598.5	15.7	603.6	64.9	99.0
JDB_0001R_17	8	1.6	15.3139	7.8	0.8757	8.2	0.0973	2.4	0.29	598.6	13.5	638.6	38.7	784.0	164.3	76.3
JDB_0001R_42	78	0.7	15.5039	3.3	0.8649	3.7	0.0973	1.7	0.47	598.6	10.0	632.8	17.4	758.0	68.7	79.0
JDB_0001R_14	181	0.5	15.8228	1.7	0.8484	2.3	0.0974	1.5	0.66	599.2	8.8	623.8	10.8	715.0	37.0	83.8
JDB_0001R_27	65	0.7	16.2075	2.9	0.8282	3.5	0.0974	2.0	0.56	599.2	11.2	612.6	16.1	663.7	62.5	90.3
JDB_0001R_16	8	2.0	15.5039	8.4	0.8667	9.1	0.0975	3.5	0.38	599.7	20.0	633.8	42.8	758.0	176.9	79.1
JDB_0001R_43	71	1.0	16.3132	3.3	0.8254	3.6	0.0977	1.5	0.43	600.9	8.8	611.1	16.6	649.8	70.1	92.5
JDB_0001R_10	256	0.4	16.4474	1.8	0.8187	2.4	0.0977	1.5	0.65	600.9	8.8	607.3	10.8	632.2	38.9	95.1
JDB_0001R_22	132	0.9	16.2602	2.4	0.8289	3.1	0.0978	1.8	0.60	601.5	10.6	613.0	14.1	656.7	52.3	91.6
JDB_0001R_18	15	1.4	16.6389	6.2	0.8101	6.7	0.0978	2.6	0.38	601.5	14.7	602.5	30.3	607.2	133.2	99.1
JDB_0001R_31	195	0.4	16.5017	1.8	0.8176	2.3	0.0979	1.4	0.62	602.1	8.2	606.7	10.6	625.0	39.1	96.3
JDB_0001R_48	7	2.0	16.9779	9.7	0.7947	10.2	0.0979	3.3	0.32	602.1	18.8	593.8	46.0	563.4	211.3	106.9
JDB_0001R_02	39	1.6	16.4474	4.1	0.8212	4.5	0.0980	1.9	0.43	602.7	11.2	608.7	20.8	632.2	88.6	95.3
JDB_0001R_29	33	1.1	16.7785	5.5	0.8058	5.8	0.0981	1.8	0.31	603.3	10.6	600.1	26.4	589.1	120.2	102.4
JDB_0001R_28	55	0.8	16.5289	3.5	0.8188	3.9	0.0982	1.7	0.45	603.9	10.0	607.4	17.7	621.5	74.9	97.2
JDB_0001R_05	10	1.7	16.1551	8.9	0.8394	9.4	0.0984	3.2	0.33	605.0	18.2	618.8	43.7	670.6	190.5	90.2
JDB_0001R_36	264	0.6	16.5837	2.0	0.8177	2.5	0.0984	1.5	0.61	605.0	8.8	606.8	11.5	614.3	43.0	98.5
JDB_0001R_50	18	1.5	15.5763	5.6	0.8715	6.0	0.0985	2.1	0.36	605.6	12.3	636.4	28.4	748.2	118.5	80.9
JDB_0001R_07	12	1.6	16.5017	8.7	0.8226	9.0	0.0985	2.2	0.25	605.6	12.9	609.5	41.4	625.0	188.9	96.9
JDB_0001R_03	30	1.1	16.3132	5.2	0.8338	5.5	0.0987	1.7	0.31	606.8	10.0	615.7	25.4	649.8	112.2	93.4
JDB_0001R_46	14	1.5	16.8350	6.4	0.8080	6.8	0.0987	2.4	0.36	606.8	14.1	601.3	31.1	581.8	139.1	104.3
JDB_0001R_01	43	1.6	17.3010	3.8	0.7870	4.2	0.0988	1.7	0.41	607.4	10.0	589.5	18.7	522.2	83.5	116.3
JDB_0001R_45	19	1.1	16.8634	7.3	0.8083	7.6	0.0989	2.1	0.28	608.0	12.3	601.5	34.3	578.1	157.8	105.2
JDB_0001R_33	19	1.2	15.9744	5.3	0.8541	5.6	0.0990	2.0	0.36	608.5	11.7	626.9	26.4	694.7	112.4	87.6
JDB_0001R_39	32	1.4	16.2602	4.1	0.8400	4.5	0.0991	1.9	0.43	609.1	11.1	619.1	20.8	656.7	87.2	92.7
JDB_0001R_08	11	1.7	16.1290	7.7	0.8476	8.3	0.0992	3.1	0.37	609.7	18.2	623.4	38.9	674.1	165.8	90.5
JDB_0001R_32	10	2.0	15.5039	7.1	0.8827	7.5	0.0993	2.3	0.31	610.3	13.5	642.4	35.7	758.0	150.6	80.5
JDB_0001R_09	169	0.5	16.9205	2.2	0.8096	2.8	0.0994	1.7	0.61	610.9	10.0	602.2	12.7	570.8	47.9	107.0
JDB_0001R_34	153	0.5	16.5837	2.3	0.8277	2.7	0.0996	1.4	0.52	612.1	8.2	612.3	12.5	614.3	50.2	99.6
JDB_0001R_30	316	0.3	16.7224	2.0	0.8209	2.6	0.0996	1.6	0.62	612.1	9.4	608.5	11.8	596.3	43.5	102.6
JDB_0001R_26	9	1.9	16.8067	9.1	0.8176	9.6	0.0997	3.2	0.33	612.7	18.8	606.7	44.0	585.5	197.3	104.6
JDB_0001R_12	9	1.9	15.6986	8.8	0.8770	9.2	0.0999	2.8	0.30	613.8	16.4	639.4	43.8	731.7	186.6	83.9
JDB_0001R_23	9	1.9	14.8588	7.1	0.9275	7.5	0.1000	2.4	0.32	614.4	14.1	666.3	36.8	847.1	148.5	72.5
JDB_0001R_35	34	1.5	16.0000	4.6	0.8648	5.1	0.1004	2.1	0.41	616.8	12.3	632.7	24.0	691.2	99.0	89.2
JDB_0001R_21	15	1.2	15.6495	7.2	0.8868	7.6	0.1007	2.4	0.31	618.5	14.1	644.7	36.2	738.3	152.5	83.8
JDB_0001R_40	135	0.7	16.7785	2.0	0.8271	2.6	0.1007	1.7	0.64	618.5	10.0	612.0	12.1	589.1	43.7	105.0
JDB_0001R_06	42	1.2	16.5837	4.8	0.8385	5.2	0.1009	2.1	0.40	619.7	12.3	618.3	24.3	614.3	103.9	100.9
JDB_0001R_25	15	2.2	15.7729	6.0	0.9227	6.4	0.1056	2.3	0.35	647.1	14.0	663.8	31.2	721.7	127.3	89.7
JDB_0001R_11	32	1.2	16.7785	5.2	0.8887	6.0	0.1082	3.0	0.51	662.3	19.2	645.7	28.8	589.1	112.9	112.4

OPP-0074R (syenite)																
Analysis	Isotope ratio									Apparent age (Ma)						
	U	Th/U	206Pb*/	±	207Pb*/	±	206Pb*/	±	error	206Pb*/	±	207Pb*/	±	206Pb*/	±	Conc
	(ppm)		207Pb*	(%)	235U*	(%)	238U	(%)	corr.	238U*	(Ma)	235U	(Ma)	207Pb*	(Ma)	(%)
OPP_0074R_11	599	1.3	16.0411	1.2	0.8188	1.8	0.0953	1.3	0.72	586.8	7.1	607.4	8.0	685.8	26.0	85.6
OPP_0074R_08	312	0.7	16.1031	2.3	0.8276	2.7	0.0967	1.4	0.54	595.0	8.2	612.3	12.3	677.6	48.2	87.8
OPP_0074R_35	190	1.0	15.9236	2.5	0.8387	3.3	0.0969	2.2	0.65	596.2	12.3	618.4	15.5	701.5	54.2	85.0
OPP_0074R_10	679	1.3	16.0154	1.4	0.8356	2.0	0.0971	1.4	0.72	597.4	8.2	616.7	9.3	689.2	29.7	86.7
OPP_0074R_23	699	1.4	16.2338	1.8	0.8337	2.6	0.0982	1.9	0.73	603.9	11.2	615.7	12.2	660.2	38.3	91.5
OPP_0074R_22	441	1.3	16.2866	1.8	0.8394	2.4	0.0992	1.6	0.67	609.7	9.4	618.8	11.2	653.3	38.5	93.3
OPP_0074R_30	473	1.4	16.3666	2.0	0.8370	2.9	0.0994	2.1	0.73	610.9	12.3	617.5	13.3	642.8	42.2	95.0
OPP_0074R_36	441	1.4	16.4745	2.1	0.8382	3.1	0.1002	2.2	0.72	615.6	12.9	618.2	14.2	628.6	46.1	97.9
OPP_0074R_44	522	1.3	16.0000	2.2	0.8665	3.3	0.1006	2.5	0.74	617.9	14.6	633.7	15.8	691.2	47.8	89.4
OPP_0074R_43	493	0.7	16.0514	1.6	0.8681	2.3	0.1011	1.7	0.72	620.9	10.0	634.5	11.0	684.4	34.3	90.7
OPP_0074R_04	242	2.1	16.3399	2.0	0.8527	2.9	0.1011	2.1	0.73	620.9	12.3	626.1	13.3	646.3	42.1	96.1
OPP_0074R_21	333	1.0	16.4935	1.6	0.8448	2.2	0.1011	1.6	0.71	620.9	9.4	621.8	10.4	626.1	34.1	99.2
OPP_0074R_31	415	1.3	16.4123	1.6	0.8498	2.1	0.1012	1.4	0.66	621.4	8.2	624.5	9.8	636.8	33.9	97.6
OPP_0074R_17	291	1.6	16.1031	1.8	0.8678	2.7	0.1014	2.1	0.76	622.6	12.3	634.4	12.9	677.6	37.8	91.9
OPP_0074R_25	290	1.2	16.3934	2.1	0.8525	3.0	0.1014	2.1	0.70	622.6	12.3	626.0	13.9	639.3	45.8	97.4
OPP_0074R_48	234	2.2	15.8228	2.2	0.8841	3.1	0.1015	2.2	0.70	623.2	12.9	643.2	14.8	715.0	47.1	87.2
OPP_0074R_02	430	1.2	16.0256	1.9	0.8755	3.2	0.1018	2.6	0.80	624.9	15.2	638.5	15.2	687.8	41.0	90.9
OPP_0074R_39	407	1.3	16.4204	2.0	0.8569	2.7	0.1021	1.9	0.69	626.7	11.1	628.4	12.7	635.7	42.4	98.6
OPP_0074R_19	121	1.2	16.5563	2.8	0.8607	3.5	0.1034	2.0	0.59	634.3	12.3	630.5	16.3	617.9	60.8	102.7
OPP_0074R_26	122	1.1	16.6113	2.2	0.8778	2.7	0.1058	1.7	0.62	648.3	10.5	639.8	13.0	610.7	46.7	106.1
OPP_0074R_33	405	1.3	16.2075	2.3	0.9541	3.2	0.1122	2.3	0.71	685.5	15.1	680.2	16.1	663.7	48.6	103.3

Annex 4.

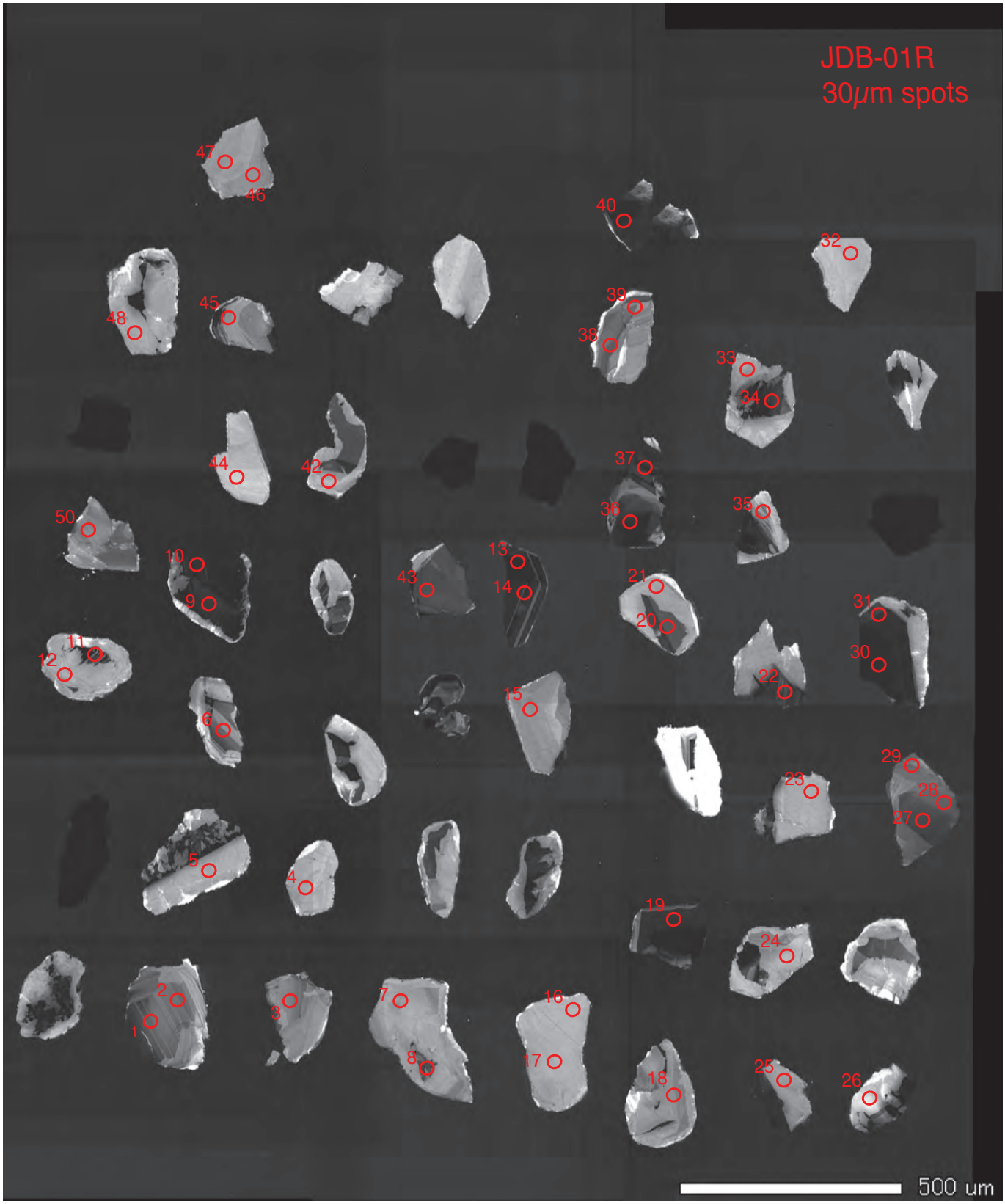
JDB-01R
30μm spots
47
46
40
32
48
45
39
38
33
34
44
42
37
36
35
50
13
10
43
14
21
9
20
31
11
12
30
22
15
6
29
23
28
27
5
4
19
24
2
3
7
16
1
8
17
18
25
26
500 um

Annex 5.

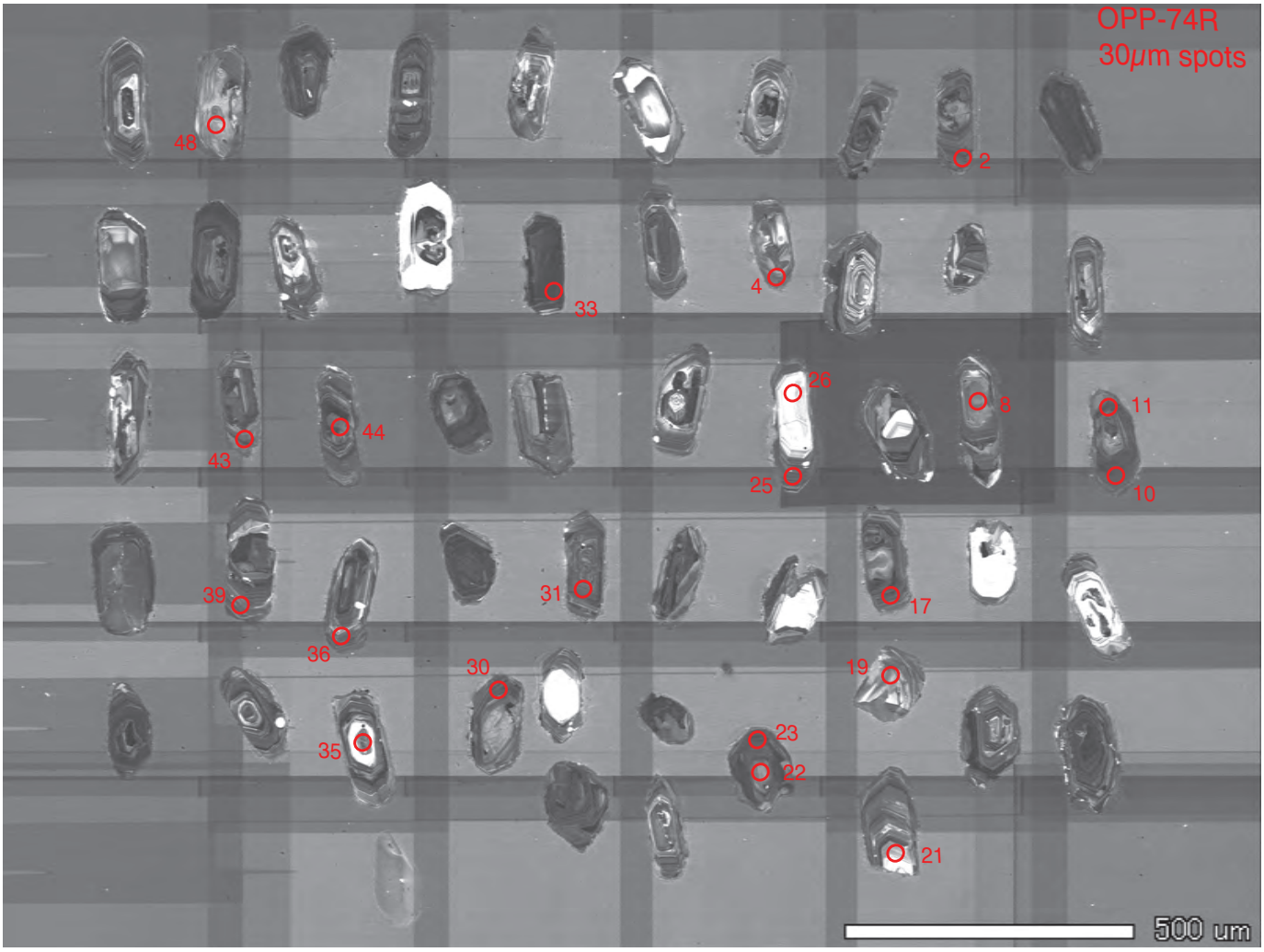
OPP-74R
30μm spots
48
2
4
33
26
8
11
44
43
25
10
39
31
17
36
30
19
23
35
22
21
500 um

Ultramylonite. Santa Fe de Antioquia Sector. Author: Julián López Isaza

Boletín Geológico

SERVICIO GEOLÓGICO COLOMBIANO

Boletín Geológico, 48(1), 81-122, 2021,
https://doi.org/10.32685/0120-1425/bol.geol.48.1.2021.524

© Author(s) 2021. This work is distributed under the Creative Commons Attribution 4.0 License.

Received: June 2, 2020

Revised: September 7, 2020

Accepted: February 15, 2021

Published online: July 12, 2021

Geological-structural mapping and geocronology of shear zones: A methodological proposal

Mapeo geológico-estructural y geocronología de zonas de cizalla: Una propuesta metodológica

Anny Julieth **Forero Ortega**[1], Julián Andrés **López Isaza**[1], Nelson Ricardo **López Herrera**[1], Mario Andrés **Cuéllar Cárdenas**[1], Lina Mara **Cetina Tarazona**[1], Luis Miguel **Aguirre Hoyos**[1]

1. Group of Tectonics, Dirección de Geociencias Básicas, Servicio Geológico Colombiano, Bogotá, Colombia
Corresponding author: Anny Julieth Forero, ajforte056@gmail.com

Abstract

The deformation registered in rocks in the field can be characterized based on the structures preserved in outcrops, which can related be to wide discontinuity zones named faults and shear zones. The geological-structural mapping and the geochronology of these tectonic structures are a topic of great interest not only for tectonic modeling but also for reconstruction of the geological evolution of the national territory. The methodology suggest for the analysis of faults and shear zones is based on eight steps, including: 1) definition of the geological context in which the structure was developed; 2) photointerpretation, image geoprocessing, and geological-structural mapping of the structural and lithological characteristics of the faults and shear zones; 3) petrographic analysis of field-oriented samples; 4) quantification of strain orientation and geometry through 3D finite strain analyses and quantification of non-coaxiliaty of deformation through vorticity analyses; 5) SEM-TEM-EBSD microanalysis; 6) quantification of the P-T conditions of deformation through phase-equilibria modeling or conventional geothermobarometry; 7) dating of syn-kinematic minerals phases and mylonitic rocks through Ar-Ar analyses, in order to determine the reactivation and deformation ages of the structure, respectively, as well as the implementation of the U-Pb technique in syn-kinematic calcite crystals developed in the fault planes; and 8) dating of geological elements adjacent to the structure, such as syn-kinematic intrusive bodies associated with the deformation event using zircon U-Pb dating, rocks hydrothermally altered through Ar-Ar method, and zircon and apatite fission-tracks dating of the blocks adjacent to the faults for determining exhumation ages.

Keywords: Shear zones, fault rocks, brittle regime, brittle-ductile transition, ductile regime, mapping, geochronology.

Resumen

La deformación registrada en las unidades geológicas en campo se puede caracterizar a partir de las estructuras encontradas en afloramientos, las cuales se relacionan, generalmente, con amplias zonas de discontinuidad denominadas *fallas* y *zonas de cizalla*.

Citation: Forero-Ortega, A. J., López-Isaza, J. A., López Herrera, N. R., Cuéllar-Cárdenas, M. A., Cetina Tarazona, L. M., & Aguirre Hoyos, L. M. (2021). Geological-structural mapping and geocronology of shear zones: A methodological proposal. *Boletín Geológico*, *48*(1), 81-122. https://doi.org/10.32685/0120-1425/bol.geol.48.1.2021.524

El mapeo geológico-estructural y la geocronología de estas estructuras tectónicas es un tema de gran interés, no solo para el modelamiento tectónico, sino para la reconstrucción de la evolución geológica de un territorio. Metodológicamente, para el mapeo geológico-estructural y la geocronología de fallas y zonas de cizalla se sugieren ocho fases, que incluyen: 1) definición del contexto geológico en el cual se desarrolló la estructura; 2) fotointerpretación, geoprocesamiento de imágenes y mapeo geológico-estructural de las características estructurales y litológicas de las fallas y zonas de cizalla; 3) análisis petrográfico de muestras orientadas en campo; 4) cuantificación de la orientación y geometría de deformación mediante análisis de deformación finita 3D y cuantificación de deformación no-coaxial por medio de análisis de vorticidad; 5) análisis submicroscópico SEM-TEM-EBSD; 6) cuantificación de condiciones de deformación P-T por medio de modelamiento de equilibrio de fases o geotermobarometría convencional; 7) datación de minerales sincinemáticos y rocas miloníticas por el método Ar-Ar, con el fin de determinar las edades de reactivación y deformación de la estructura, respectivamente, así como, la implementación de la técnica U-Pb en cristales sincinemáticos de calcita desarrollados en los planos de falla y en cristales de apatito con la finalidad de entender la evolución temporal de las zonas de cizalla; y finalmente, 8) fechamiento de elementos geológicos adyacentes a la estructura, tales como: intrusivos sincinemáticos asociados al evento deformacional por el método U-Pb en circón, rocas alteradas hidrotermalmente mediante el método Ar-Ar, y datación por trazas de fisión en circón y apatito de los bloques adyacentes a las fallas para determinar edades de exhumación.
Palabras clave: Zonas de cizalla, rocas de falla, régimen frágil, transición frágil-dúctil, régimen dúctil, mapeo, geocronología.

1. Introduction

The Geological-structural data acquisition for mapping of faults and shear zones is important as basic technical input in the formulation of engineering projects and territorial and national development plans, for the design and layout of road infrastructure with large civil works such as dams, viaducts and tunnels, among others, exploration of water, geothermal, mineral and hydrocarbon resources, for the reconstruction of the deformational evolution of an area, and for studies of regional tectonics (cf. Cox et al., 2001; Sausgruber and Brandner, 2001; Vega Granillo et al., 2009; Mejía et al., 2012; Jiang et al., 2020).

In this regard, it is necessary to develop a unified methodology facilitating fractal qualitative analysis of the pattern of the trace of the shear zone and segments of associated faults (cf. Turcotte, 1989, 1997; Cello, 1997; Park et al., 2010; Barão et al., 2018), from analysis on different scales by photointerpretation, mapping of outcroppings, hand samples and microscopy. This allows establishment of the structural level of the crust represented by the structures, the types of related fault rocks and their distribution, the amplitude over which the movement is distributed, geometry and its respective kinematics, the establishment of structural patterns, and the timing of the deformation.

A shear zone is defined as a high-deformation planar or curviplanar surface, along which the movement is distributed, it presents definite limits characterized by the presence of structures and fault rocks included in centimetric to kilometric areas, according to the scales of deformation (Ramsay, 1980 a, b; Rutter, 1986; Ramsay and Huber, 1987; Jiang and White, 1995; Fossen and Cavalcante, 2017). The shear zones focus the deformation heterogeneously (both coaxial and non-coaxial), arranged as subparallel or conjugate sets (anastomosed) in response to the rheology of rocks and minerals that they affect, and usually are surrounded by lithologies showing low deformation (Ramsay, 1980 a, b; Rutter, 1986; Ramsay and Huber, 1987; Jiang and White, 1995; Fossen and Cavalcante, 2017).

Considering that the deformation is heterogeneously distributed throughout the rock body (Ramsay, 1980 a, b; Ramsay and Huber, 1987; Fossen and Tikoff, 1997; Carreras et al., 2013), it is essential that interpretation of the timing of any deformative event and the analysis of the tectonic evolution of a shear zone is based not only on evaluation of the isotopic dating of the fault rocks (cf. Schneider et al., 2013), but also on the integration of cartography, microstructural analysis, ages of intrusion igneous bodies related to the shear zone, and ages of uplift and exhumation of blocks adjacent to the structure are integrated (cf. Oriolo et al., 2018).

This review presents a methodology for the identification, mapping and analysis of the nature of faults and shear zones. For this, it is suggested to characterize the structures and fault rocks, define the structural level observed, determine the movement's distribution and kinematics, and assign the relative

and absolute ages of deformation. In order to propose some minimum parameters necessary to perform geological-structural studies for acquiring basic information that aids understanding of the tectonic evolution.

2. Phases for geological-structural mapping of faults and shear zones

The characterization of geological-structural faults and shear zones, as first to measure, requires correct application of concepts and principles related to the study of faults and shear zones. Furthermore, as a second measure, one should be clear about the objective of the analysis, as well as the "for what?" the structural data are collected, which means being clear about what one will do with the data and how the subsequent analysis will be conducted. Finally, as a third measure, there must be broad and detailed knowledge of the methods of mapping, compilation of structural data, recognition of structures, field classification of fault rocks, collection of structural data with statistical representativeness, and determination of the distribution, kinematics (for which it is necessary to know the kinematic indicators) and geometry.

As a starting point, it is necessary to execute photointerpretation and geoprocessing analysis of satellite images with band compositions that highlight the structures. Such analysis should be complemented by geophysical inputs (e.g., maps of total magnetic intensity, total-field magnetic anomaly, analytical signal of the total-field magnetic anomaly, and complete Bouguer anomaly, among others) and an adequate map base (with drainage networks and contour lines). These allow identification and and definition of the preliminary outline of the structure (cf. Gunn et al., 1997; Betts et al., 2003; Grauch and Hudson, 2007; Aitken and Betts, 2009; Stewart et al., 2009; Stewart and Betts, 2010; Kadima et al., 2011; Blaikie et al., 2014; Armit et al., 2014; Blaikie et al., 2017). This implies the identification of geomorphological features that define the fault or shear zone and sites of interest for subsequent campaigns for field checking.

For mapping structures, it is recommended to perform a multiscale analysis of nature and the spatial distribution of structural elements in the central and marginal areas of the shear zone (Figure 1), in which one will observe the fractal distributions, considering similar arrangements of geological characteristics, independent of the scale of observation (Turcotte, 1989; 1997; Cello, 1997; Park et al., 2010; Fossen, 2013; Baron et al., 2018). This allows identification of the timing of the deformation events basen mainly on cross-cutting relationships. For this, it is suggested to do transects perpendicular to the strike of the structures that limit and constitute the shear zone (cf. Chetty, 2014; Choi et al., 2016), recording morphotectonic, geometric and kinematic characteristics, and acquiring structural data on the fabric developed in the main structure, as well as satellite faults, branches and other secondary structures (e.g., folds, tension gashes and foliations, among others), emphasizing the hierarchical structure of the structures.

Another relevant aspect in the mapping of this type of structure is a description of the associated fault rocks. These are a group of rocks developed in shear zones at different structural levels of the crust, which originate by heterogeneous deformation from cataclistic processes, intracrystalline plasticity or flow, depending on physical conditions of the deformation and the type of affected lithology (Sibson, 1977; 1983; Rutter, 1986; Ramsay and Huber, 1987). These are subdivided into non-cohesive rocks, mainly fault gouge and breccia, and cohesive rocks such as cataclasites and mylonite, which are the result of episodes of intense deformation, which reduce the grain size of the rocks, either by processes of abrasion or intracrystalline plasticity (Sibson, 1977; 1983; Killick, 2003), imprinting particular mechanical characteristics on the rocks (Sibson, 1977; Wise et al., 1984; Spray, 1995; Woodcock and Mort, 2008; Magloughlin, 2010).

The analysis of structural data acquired along fault planes and shear zones starts from the register of the orientation and direction of movement of the fault planes (cf. Petit, 1987; Hancock, 1985; Doblas, 1998). Moreover, it includes the categorization of structural data according to their quality determined in the field (supposed, probable or possible, and true) (Hardcastle, 1989; López-Isaza et al., 2021) and the cross-cutting relationship between the structures and geological units this affects (cf. Angelier, 1994; Sippel et al., 2009; Sperner et al., 1993; Tranos, 2009, 2011; Sperner and Zweigel, 2010). With the fault data, different inversion methods can be used to help determine the principal axes of deformation and stress, from kinematic and dynamic analyses, respectively (cf. Twiss and Unruh, 1998; Žalohar, 2014; Thakur et al., 2020).

The kinematic analysis involves plotting data on different diagrams, like the tangent-lineation (Twiss and Unruh, 1998) or Höeppener (1955), in order to display fault planes as poles, including the relative movement of blocks adjacent to the fault (Sperner and Zweigel, 2010). It is also recommended

to perform a kinematic compatibility analysis, which allows the establishment of compatible structures kinematically generated or activated under the same deformation event (e.g., Santamaría-Díaz et al., 2008). Furthermore, if possible, one should calculate the principal axes of elongation ε1, ε2 and ε3 (Sperner and Zweigel, 2010), and it is suggested to use the Linked Bingham method of distribution, which solves the axes of shortening and extension of a set of faults (Marrett and Allmendiger, 1990).

The dynamic analysis is performed based on classification of the subsets established in the kinematic analysis. With each subset, it is recommended to test the mechanical coherence of the data from their distribution on Morh's circle (cf. Velandia, 2017), followed by use of the inversion method of slickensides (Sperner and Ratschabacher 1994), to obtain the paleostress tensors. This method assumes that movement of the fault is controlled by a stress tensor and that the associated failures and slickensides were developed under the same deformation event. Therefore, the direction of the stress field can be determined from the preferential slips of the fault planes (Twiss and Unruh, 1998; Lacombe, 2012). This analysis is based on the following s assumptions: 1) the direction of movement is parallel to the maximum shear stress resolved on the plane (Wallace, 1951; Bott, 1959); 2) the rock behaves as a rheologically linear material (Srivastava et al., 1995); 3) the displacements on the fault planes are independent and small with respect to their lengths, and in them there is no rotation of the planes, obeying the Wallace-Bott criterion; 4) the stress field is homogeneous (Twiss and Unruh, 1998). The inversion method is calculated by graphical (right dihedral method) or mathematical solutions (numerical dynamic analysis), usually included in software of structural data processing (e.g, Wintensor 5.8, TectonicsFP 1.7.7).

On the other hand, considering that the data associated with slip faults may be heterogeneous, it is proposed to apply a genetic algorithm method (MGA, for its acronym in English). This allows direct estimation the states of paleostress from this type of data and does not require the separation of subsets of data (Thakur et al., 2020).

The right dihedral method developed by Angelier and Mecheler (1977) allows one to obtain an optimum orientation of stress fields from the directions and slip sense. It is based on graphing an auxiliary plane perpendicular to the slickensides, which divides the area around each fault plane into four quadrants that define compression and tension zones (Ortner et al., 2002). From the sum of the areas of solutions for each structural data is obtained the dihedrals resulting from distension and compression corresponding to the dataset, in which the common orientations correspond to the optimal positions of axes σ3 and σ1 in the dihedrals of extension and compression, respectively (Angelier, 1979, 1994; Sainz et al., 1990; Casas et al., 1990; Delvaux and Sperner, 2003; Delvaux, 2012; Delvaux et al., 2012).

2.1 Conceptualization and reference geological context

To do the geological-structural mapping it is necessary to have knowledge of the tectonic and geological context in which the structure developed. Moreover, one should previously consider the concept of shear zones, what characterizes them, their architecture, what their regimes are, and how they relate to depth. This is in order to have a theoretical approach to the depth position in a crustal cross-section or, in other words, the observed structural level of the crust.

On the surface, shear zones are characterized by morphotectonic features (Bull, 2007) that show the landscape forms produced specifically by tectonic processes, rather than by processes of sedimentation and erosion (Keller and Pinter, 2002; McCalpin, 2009; Burbank and Anderson, 2012). These types of features have been extensively documented in neotectonics studies. Among these features can be found mountain fronts with triangular facet, fault escarp, flexural escarp, sag pond, fault saddle, positive (pressure ridge) and negative (pull-apart basin) flower structures, shoulders, shutter ridge, and forebergs, in addition to the development of interference drains, which are very sensitive to changes in the surface, among others.

The identification of morphological and structural features associated with the development of shear zones have been widely characterized by aerial photograph analysis, satellite and radar images, during phases prior to field work, in order to identify the location and distribution of the landscape features, as well as the elevation of the terrain and its composition (Smith and Pain, 2009). These are characteristics that may not be directly recognizable in the field because of their scale.

In this sense, the photointerpretation is a fundamental part of any geological study that involves the recognition of morphological and structural features. Traditionally, aerial photographs have been used, which facilitate a perception of the terrain in 3D through stereoscopy, with vertical exaggera-

tion that makes it possible to estimate the slopes, stratification, and terrain configuration. However, given its optical character, its usefulness is restricted by cloudiness and thick vegetation cover, which prevent the assessment of the land (Mendivelso, 2008; Rampal, 1999).

During recent decades, great progress has been made in satellite and remote sensing technologies (Rao, 2002). The variety of available satellite images, with differing spatial, radiometric and temporal resolutions, allows their use in recognizing the composition of the earth's surface, its cover and temporal evolution. One can distinguish two major categories of satellite images: those from passive sensors (e.g., Landsat, Sentinel 1, Aster, SPOT, and others), and those from active sensors, commonly known as radar images (e.g., Sentinel 2, ALOS-PALSAR, GeoSAR, RADARSAT-1, and others). The latter have the advantage of allowing observation of the earth surface even in overcast conditions and at night. Additionally, some of them in the L band go beyond the vegetation cover and penetrate layers of soil, snow or ice (Paine and Kiser, 2003). They are therefore the most useful in geological and geomorphological studies.

Lidar (acronym for light detection and ranging) is another technology of the active type, like radar, which facilitates topographic data of high accuracy and density, so it supports the construction of digital elevation models with high spatial resolution. This technology can be implemented using unmanned aerial vehicles (UAV- drones), which enables the recognition of vast areas. Compared with traditional photogrammetry, Lidar provides data on terrain covered by vegetation (Paine and Kiser, 2003), as shown by the detection and characterization of active faults in wooded areas (e.g., Chen et al., 2015).

To facilitate the detection of fault zones and associated geomorphology features, various algorithms and processing techniques have been created, such as the application of spatial filters that highlight and automatically extract information from satellite imagery (e.g., Gannouni and Gabtni, 2015; Mallast et al., 2011). However, despite the quality and utility of remote sensing tools, field testing is always necessary (Marchionni and Cavayas, 2014) to fully recognize and characterize faults and shear zones.

The architecture, both longitudinal and transverse to the trace of the shear zones, is distributed in three main elements (Caine et al., 1996; Ganerød et al., 2008): *core, transition and damage zones* (Figure 1). The core corresponds to a zone parallel or semiparallel to the direction of the main fault and is a product of high strain and focused shear, accommodating displacement through one or more surfaces. It is made up of shear zones, sets of conjugate fractures with different orientations, geometry, and morphology (Caine et al., 1991; Caine et al., 1996; Gabrielsen and Braathen, 2014). It also includes lenses or areas of sheared rocks (e.g., foliate cataclasites and mylonites), locally fractured or crushed (e.g., ultracataclasites, breccia and fault gouge), with evidence of processes of precipitation and geochemical alteration (Sibson, 1977; Anderson et al., 1993; Chester and Logan, 1986; Childs et al., 1996; Wibberley et al., 2008; Gabrielsen et al., 2008; Bastesen and Braathen, 2010). Its width can vary from a few centimeters to hundreds of meters (Gabrielsen and Braathen, 2014).

The transitional zone is mainly composed of elongated fragments of protocataclasites and/or protobreccia (Lindanger et al., 2007; Gabrielsen and Braathen, 2014). It also includes fracture corridors, shear and gouge zones of minor faults, arranged in a subangular manner with respect to the general trend of the main fault plane, cross-cutting locally previously formed structures (Gabrielsen and Braathen, 2014). This zone also has of greater cohesion and is generally less affected by processes of hydrothermal alteration, as compared to the fault core (Berg and Skar, 2005; Faulkner et al., 2010; Gabrielsen and Braathen, 2014; Choi et al., 2016).

The damage zone, which surrounds the previous zones, corresponds to the volume of rock that is around the fault core and transitional zone, and preserves the original lithological properties of the deformed rocks (Chester et al., 1993; McGrath and Davinson, 1995; Beach et al., 1999; Storti et al., 2003; Billi et al., 2003; Chester et al., 2004; Berg and Skar, 2005; Johansen and Fossen, 2008; Mitchell and Faulkner, 2009; Gudmundsson et al., 2010; Riley et al., 2010; Hausegger and Kurz, 2013; Lin and Yamashita, 2013; Choi et al., 2016). The damage zone is characterized by thin bodies with rhombuses-shapes, with low deformation intensity (Gabrielsen and Braathen, 2014), as well as by structures of second order, synthetic and antithetic fractures, joints, veins and folds. These are related to the kinematics of the structure, being less representative in relation to increasing distance to the fault core (Chester and Logan, 1986; Smith et al., 1990; Berg and Skar, 2005; Faulkner et al., 2010; Gabrielsen and Braathen, 2014).

Inside the crust, the shear zones present structural levels characterized by the deformation regimes and structures produced in response to the distribution of the deformation, called *brittle*, *brittle-ductile* and *ductile* (Ramsay, 1980 a, b; Rutter,

1986; Ramsay and Huber, 1987; Fossen and Cavalcante, 2017). In conditions of average geothermal gradient (between 25 °C and 30 °C per kilometer), these structural levels are demarcated by limits depending on the rheological characteristics of quartz and the feldspar (Figure 1), which respond to fracturing deformation by abrasive processes (cataclastic) or flowing by accommodation processes (frictional sliding), respectively (Hills, 1972; Sibson, 1979; 1983; Knipe, 1989; Hatcher, 1995; Snoke et al., 1998; Blenkinsop, 2002).

In this regard, the brittle or elastic-frictional regime (Sibson, 1977; 1983; Ramsay, 1980 a, b; Rutter, 1986; Ramsay and Huber, 1987; Hanmer, 1988; Fossen and Cavalcante, 2017) is characterized by fault zones (Sibson, 1979; Chester et al., 1993; Chester and Chester, 1998; Kim et al., 2003; Chester et al., 2004; López et al., 2008; Hausegger and Kurz, 2013; Choi et al., 2016; Ostermeijer et al., 2020) and include interconnected and closely spaced subparallel structures that from fracturing, abrasion, grain-boundaries Sliding, pressure-dissolution and grain size decrease processes favor the development of breccia or gouge fault zones between them (Higgins, 1971; McClay, 1987; Davis and Reynolds, 1996). The fault zones include domains with different deformation intensity, distributed in the fault core and damage zone (Figure 1), characterized by structural elements defined by the variation in fracturing intensity. Furthermore, the development of fault rocks (fault gouge, breccia and cataclasites) and kinematic indicators (major fault -Y, -P shear, riedel shear R, conjugate riedel shear R', tensile fracture -T, crescentic marks, slickenside, congruous and incongruous steps, trailed material, asymmetric protruding grains, carrot-shape, trains of inclined planar structures, asymmetric elevations, mineralogical/crystallographic orientation, among others.) allows definition of the kinematics and type of structure, plus the associated stress field (cf. Hancock, 1985; Petit, 1987; Célérier, 1988; Doblas et al., 1997; Doblas, 1998; Fry, 2001).

Under conditions equivalent to the brittle-ductile regime or elastic-frictional/quasi-plastic transition, in a normal geother-

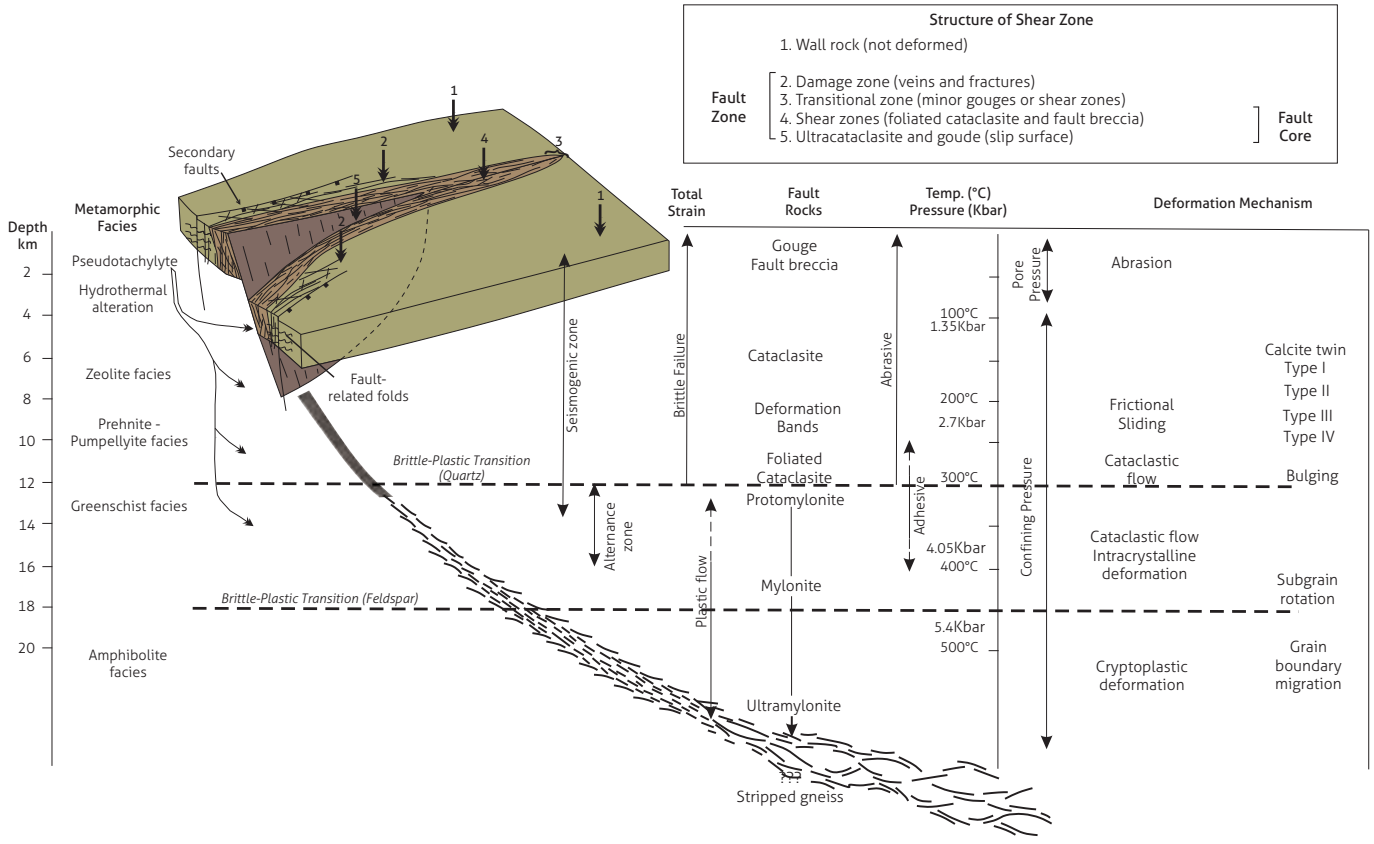

Figure 1. 3D architecture of shear zone, which includes transition from brittle, brittle-ductile and ductile deformation to depth, and their relationship with deformation mechanisms and associated fault rocks
Source: Constructed using information from Sibson (1979; 1983); Wise et al. (1984); Scholz (1988, 2006); Swanson (1992); Passchier and Trouw (2005); Chester et al. (2004); López et al. (2008), Fossen (2013), and Choi et al. (2016).

mal gradient (Sibson, 1977; 1983; Ramsay, 1980 a, b; Rutter, 1986; Ramsay and Huber, 1987; Hanmer, 1988; Scholz, 1988; Fossen and Cavalcante, 2017), rocks undergo a transition that is registered in the behavior of quartz, which goes from a brittle fracture mode to plastic flow (Rutter, 1986; Duba, 1990). Shear zones developed under this regime show a complex behavior related to processes of granular flow, cataclastic mechanisms and intracrystalline plastic deformations, which result in heterogeneous deformation of the rock with partition in stronger and weaker domains. Under these conditions, the behavior depends on temperature, pressure, rheology, previous anisotropies, and angular and linear geometric relationships in which the structure was generated (Sibson, 1977; Blenkinsop and Rutter, 1986; Scholz, 1988; Schmid and Handy, 1991; Babaie et al., 1991; Hadizadeh and Tullis, 1992; Passchier and Trouw, 2005; Balsamo et al., 2010; Fossen, 2013; Moreira and Dias, 2018; Kjenes, 2018; Nicchio et al., 2018; Barão et al., 2020). Moreover, it includes the development of fault rocks such as cataclasites S-C, phyllonites and protomylonites (Chester et al., 1985; Lin, 1999a; Passchier and Trouw, 2005; Passchier and Coelho, 2006; Trouw et al., 2010; Torgersen and Viola, 2014).

Another term commonly used for this deformation region is *semi-brittle* shear zones. These are areas of brittle shear influenced by mechanisms of plastic deformation, a situation in which the elements in the structure are intrisically brittle but mechanically resistant to stop the propagation of fractures (Gumbsch, 2001; Fossen, 2013). The fault rocks in semi-brittle shear zones show mineral fragments embedded in a fine matrix of crushed and fractured minerals, veins with mineral precipitation, and evidence of cataclastic flow product of hydrothermal processes, tension gashes, intergranular and transgranular microfractures domino type, and shear bands, the latter contribute to the development of intracrystalline plastic processes (Hodgson, 1989; McClay, 1991; Hadizadeh and Tullis, 1992; Babaie and La Tour, 1993; Gumbsch, 2001; Pec et al., 2012; Prigent et al., 2017; Papeschi et al., 2018; Reber and Pec, 2018; Barão et al., 2020).

In the ductile or quasi-plastic regime (Figure 1) with a normal geothermal gradient (Sibson, 1977; 1983; Ramsay, 1980 a, b; Rutter, 1986; Ramsay and Huber, 1987; Hanmer, 1988; Fossen and Cavalcante, 2017), shear zones are dominated by the mechanical response of feldspar and are generated at deeper levels in the crust, where metamorphic conditions prevail (Sibson, 1983; Riedmüller et al., 2001; Lopez et al., 2008). In these zones, the processes of plastic flow are distributed homogeneously and involving reduction of grain size. These zones are also characterized by the development of protomylonites, mylonites, ultramylonites, blastomylonites, ribbon mylonites, stripped gneiss, and mylonite gneiss (Sibson, 1980; White et al., 1980; Snoke et al., 1998; Killick, 2003; Passchier and Trouw, 2005; Trouw et al., 2010; Fossen, 2013).

2.1.1 Fault rocks

Initially, fault rocks were classified according to the level of primary cohesion and planar fabrics developed (Higgins, 1971; Hills, 1972; Sibson, 1977; Marshak and Mitra, 1988). However, this classification does not consider that under certain conditions cataclastic rocks can present foliation and that the deformation mechanisms that affect fault rocks can be different (cf. Bell and Etheridge, 1973; Ramsay and Huber, 1987; Lin, 1999a).

For the description of fault rocks, it is recommended to consider guidelines of the Subcomission on the Systematics of Metamorphic Rock (SCMR) of the International Union of Geological Sciences – IUGS (Brodie et al., 2007), supplemented by recent reviews that describe the characteristics of fault rocks and classify some of their types (cf. Woodcock and Mort, 2008; Magloughlin, 2010; Fossen and Cavalcante, 2017). The following describes fault rocks according according to the structural level they generate (cf. Figure 1), starting with the brittle regime and ending with the ductile regime. It should be noted that the type of fault rock generated inside the crust also depends on the prevailing geothermal gradient at the time of their formation, which is directly related to depth.

2.1.2 Fault breccia

This is a product of the brittle shear zones of the upper crust, and they are developed from the surface to a few kilometers deep in the crust (~0-6 km; cf. Sibson, 1977) and vary between non-cohesive and cohesive, foliated and non-foliated (Figure 2a) (Higgins, 1971; Sibson, 1977, 1986; Woodcock and Mort, 2008). Based on their cohesion, matrix or cement concentration, and clast size (> 2 mm), they are classified as: a) crackle breccia (75% to 100% of large clasts), with clasts with little rotation, separated by thin cement or matrix sutures; b) mosaic breccia (60% to 75% of large clasts) with adjacent clasts that fit together, but with more separation and rotation; c) chaotic breccia (30% to 60% of large clasts), with strongly rotated clasts and loss of geometric fit to each other (Woodcock and Mort, 2008; Magloughlin, 2010).

2.1.3 Fault gouge

This is a non-cohesive rock with less than 30% large clasts (> 2 mm), formed in the first kilometers of the upper crust (~0-4 km; cf. Sibson, 1977) from cataclassic processes dominated by fracturing and rotation of the rigid body of grains and fragments. It is restricted to shear fractures and slip planes in fault zones (Figure 2b) and it is composed by a material rich in clay, which can present foliation and plastic response in the presence of moisture (Higgins, 1971; Engelder, 1974; Wu, 1978; Chester et al., 1985; Scholz, 1987; 1988; Snoke et al., 1998; Killick, 2003; Vannucchi et al., 2003; Woodcock and Mort, 2008; Magloughlin, 2010; Haines et al., 2013; Vrolijk et al., 2018).

2.1.4 Cataclasite

This denomination classifies a cohesive rock with or without foliation (figure 2c), developed in the upper crust at depths shallower than those of the ductile-brittle transition (~4-1 0 km) (Figure 1). It is characterized by angular porphyroclasts in a fine-grained matrix of similar composition, which are deformed by mechanisms associated with processes of cataclastic and granular flow, fracturing, rotation and frictional sliding of particles (Higgins, 1971; Sibson, 1977; 1979; Scholz, 1988; Blenkinsop and Rutter, 1986; Babaie et al., 1991; Hadizadeh and Tullis, 1992; Snoke et al., 1998; Woodcock and Mort, 2008; Magloughlin, 2010; Balsamo et al., 2010; Moreira and Dias, 2018; Kjenes, 2018; Nicchio et al., 2018; Barão et al., 2020). According to the degree of proportion of the matrix (cf. Sibson, 1977; 1979; Snoke et al., 1998; Woodcock and Mort, 2008; Magloughlin, 2010), it is classified as: a) protoclasite, in the which the matrix makes up less than 50% of the rock volume; b) mesocataclasite, for which the matrix comprises more than 50% and less than 90 % of the rock volume; c) ultracataclasite, in which the rock volume consists of more than 90% matrix and is restricted to fault cores where the shear concentrates (Figure 1); d) S-C cataclasites, which are characterized by a shape orientation of some mineral phases (S planes) and the generation of micro-shear planes or shear bands (C planes), with quartz and feldspar crystals developing brittle deformative microstructures with no dynamically recrystallized grains in conditions of temperatures between 150 °C and 250 °C (Chester et al., 1985; Lin, 1999a).

2.1.5 Phyllonite

Cohesive rock with phyllitic appearance, formed by processes of aseismic creep (drag) (Higgins, 1971; Sibson, 1977; Passchier and Trouw, 2005; Trouw et al., 2010; Torgersen and Viola, 2014) or by syndeformational fluid circulation and flow during its generation (cf. Spruzeniece and Piazolo, 2015). It may be related to cataclasites and mylonites and develops transitional contacts with protomylonite in some shear zones, locally with complete lateral variation of the structure, or hosting quartz tension cracks (cf. Hippertt and Massucatto, 1998).

2.1.6 Mylonite

This designation includes cohesive rocks with mineral-stretching lineations (Figure 2d), strongly deformed in a ductile shear zone, surrounded by less deformed rocks, developed at depths equivalent to the middle-lower crust (Figure 1), under a normal geothermal gradient. It is characterized by two types of well-defined foliation, called S-C structures (Figure 2e), which result from a reduction in grain size from plastic processes. They are also constituted by lithic fragments or porphyrioclasts of type σ, δ, fish or sigmoidal, in addition to porphyroclastic systems with the development of mantle-core structures, quarter structures, reaction rings, and deformation shadows that, generally, have a composition similar to that of a fine-grained matrix (Bell and Etheridge, 1973; Lister and Snoke, 1984; Hooper and Hatcher, 1988; Hanmer, 1989; Ten Grotenhuis et al., 2003; Passchier and Trouw, 2005; Brodie et al., 2007; Trouw et al., 2010; Barão et al., 2020). Classification is based on the proportion of its original grains (size) and the recrystallized matrix (Sibson, 1977, 1979; Scholz, 1988; Snoke et al., 1998; Brodie et al., 2007; Woodcock and Mort, 2008; Magloughlin, 2010; Fossen and Cavalcante, 2017), and includes: a) protomylonite, in which less than 50% of the rock has been subjected to grain-size reduction processes and has greater development on C planes; b) (meso)mylonite, in which more than 50% and less than 90% of the rock shows grain-size reduction processes; c) ultramylonite (Figure 2f), in which more than 90% of the rock shows grain-size reduction; d) blastomylonite, corresponding to rocks that once deformation has ceased, increase the grain size due to processes associated with static recrystallization. However, this term is sometimes used to describe mylonites with a coarse-grained recrystallized matrix (Passchier and Trouw, 2005).

Besides the above descriptions of mylonites, other terms are also used, such as *augen mylonite*, used to describe rocks generated from a combination of cataclastic and crystalloblastic processes that show crystals or lithic fragments, generally of lenticular shape (larger than 0.5 mm), embedded in a

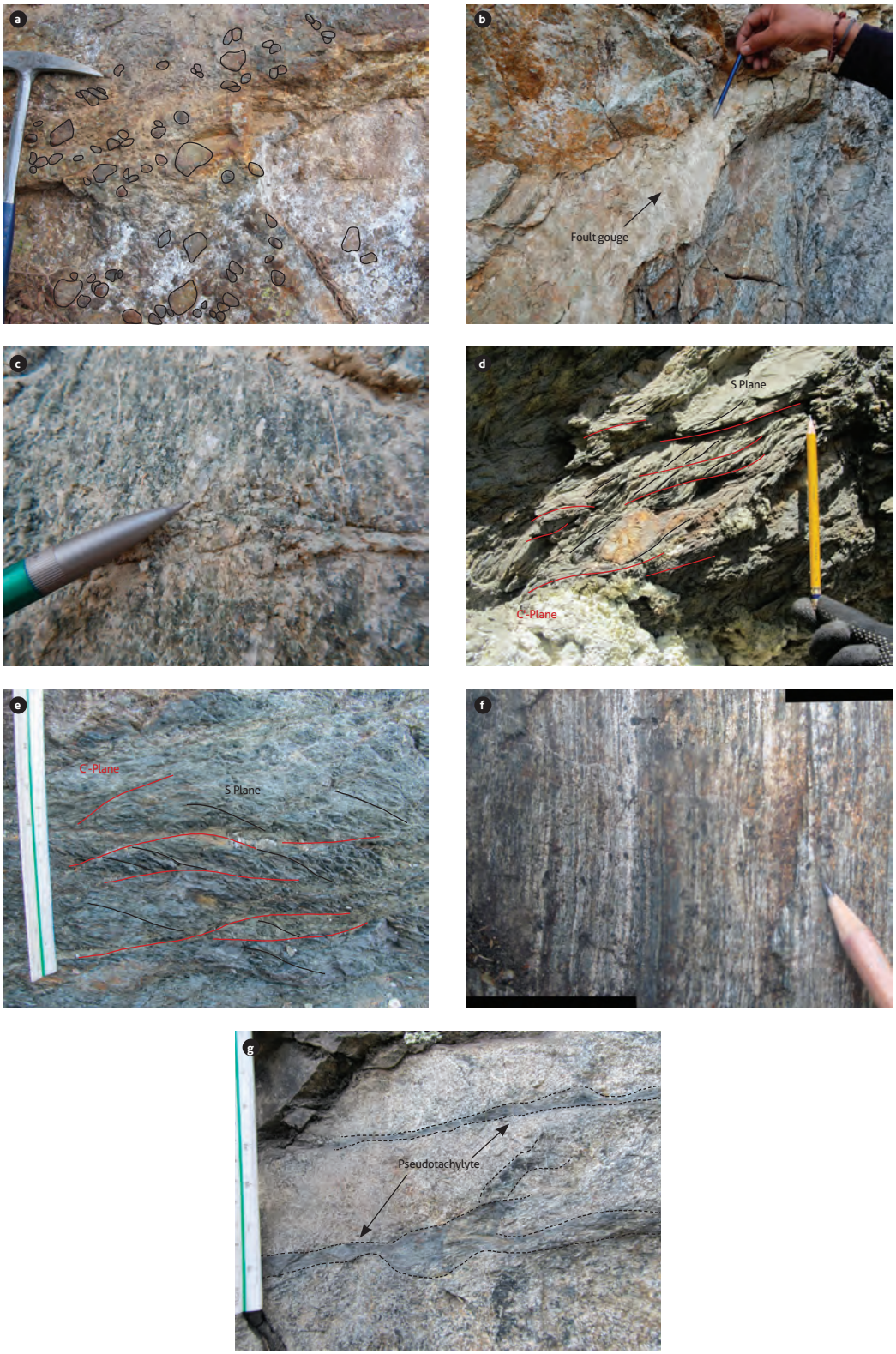

Figure 2. General appearance of a fault rock outcrop
a) Cohesive and non-foliated fault breccia; b) fault plane with fault gouge; c) foliated cataclasite; d) Mylonite with mineral orientation defined by the presence of milky quartz porphyroclasts; e) S-C structure characteristic of mylonites; f) ultramylonite with porphyroclasts of mafic minerals and oxides; g) pseudotachylite injection veins.

fine-grained matrix (recrystallized or neoformed), which shows deformation in solid state (Passchier and Trouw, 2005; Mukherjee, 2014). These rocks generally form symmetric or asymmetric anastomosed planar structures, consisting mainly of felsic minerals (Higgins, 1971; Brodie et al., 2007). The term *ribbon mylonite* is also used to describe strongly foliated rocks, mainly constituted by parallel monomineralic lenses (Passchier and Trouw, 2005; Trouw et al., 2010), common in high-grade shear zones that are transitional deformed to stripped gneisses. The *stripped gneisses* correspond to rocks interpreted as mylonites with gneissic structure defined by planar compositional, formed under high-grade metamorphism (Hippertt, Rocha et al., 2001; Passchier and Trouw, 2005; Trouw et al., 2010).

2.1.7 Pseudotachylites

These originate from (paleo)seismic movements producing melting during rapid frictional sliding and are mainly characterized by evidence of a a precursor melt phase (Magloughlin, 2010; Kirkpatrick and Rowe, 2013). The pseudotachylites occur as phases included within veinlets and veins with thicknesses from millimetric to centimetric (Figure 2g). They may consist of glass, devitrified glass, oxides, carbonates, chlorite and even epidote, as veins of the main fault plane, generation veins or injection veins, with sharp contacts, locally corroded, and cooling margins (cf. Lin, 2008; López et al., 2008; Magloughlin, 2010; Kirkpatrick and Rowe, 2013; Altenberger and López, 2014). They are constituted by fragments of broken crystals from host rock embedded in a matrix ranging from

Table 1. Recommended synoptic table for the textural classification of fault rocks

>30% visible fragments with >2 mm		Non-foliated → Foliated									
		Fault breccia Percentagem of large clasts >2 mm		crackle breccia 75 - 100%			Foliated fault breccia				
				mosaic breccia 60 - 75%							
				chaotic breccia 30 - 60%							
<30% visible fragments with > 2 mm	Incohesive		Fault gouge Visible fragments < 30%				Foliated fault gouge Visible fragments < 30%				
	Cohesive	Nature of the matrix and deformation					Phyllite appearance, mylonite rich in fine-grained micas	Phyllonite			
			Tectonic reduction in the size of grain and grain growth by recrystallization and neomineralization	Cataclasite series Fracturing processes and frictional sliding prevail, clasts <0.1 mm	Protocataclasite / Foliated protocataclasite		Mylonite series Plastic processes dominate in recrystallization of crystals, generation of sigmoids and development of S-C structures	Protomylonite	50%	Matrix percentage	
					Mesocataclasite / Foliated mesocataclasite			Mesomylonite	90%		
					Ultracataclasite / Foliated ultracataclasite			Ultramylonite			
			Glass or devitrified glass	Pseudotachylyte Present glass injections in its sidewalls			Foliated Pseudotachylyte				
Pronounced grain growth	Blastomylonite		Lenticular eye-shaped mineral in planar fabric		Augen mylonite	Lenses monophasic parallel. Rock strongly shear	Ribbon mylonite	Mylonite with gnesic structure and high grade of metamorphism	Stripped gneiss		

Source: Prepared with information from Sibson (1977; 1979); Scholz (1988), Snoke et al. (1998), Killick (2003), Woodcock and Mort (2008), and Magloughlin (2010).

cryptocrystalline to aphanitic, which develop structures due to flow, compositional banding, and spherulites caused by rapid cooling and devitrification (Philpotts, 1964; Sibson, 1975; Snoke et al., 1998; Lin, 1999b; 2008; Wenk et al., 2000; Winter, 2001; Passchier and Trouw, 2005; López et al., 2008; Magloughlin, 2010; Fossen, 2013; Kirkpatrick and Rowe, 2013; Altenberger and López, 2014).

2.1.8 Classification of fault rocks in the field

For fault rock classification in the field, it is suggested to use a tabular summary (Table 1) that synthesizes the previously described features, which includes the minimum classification parameters based on descriptions of the lithologic, physical, mineralogical, structural and textural characteristics of the rocks to be classified.

2.2 Petrography and microtectonics

Before performing the petrographic and microtectonic analyses, it is suggested to have control over the orientation of the sample collected in the field (Figure 3), indicating in the sample basic information related to the attitude of the plane, which should be orientated by specifying the strike of the reference surface according to the right-hand rule. It is also necessary to mark geographic North, the base (lower plane) and the top (upper plane), and the free faces of the sample (cf. Turner and Weiss, 1963; McClay, 1987; Passchier et al., 1990; Hopgood, 1999; Passchier and Trouw, 2005).

In the preparation of thin sections, one should consider that the tectonically deformed rocks can develop planar and linear fabrics, which are associated geometrically with the deformation ellipsoid, in which the greater mineral linetion is

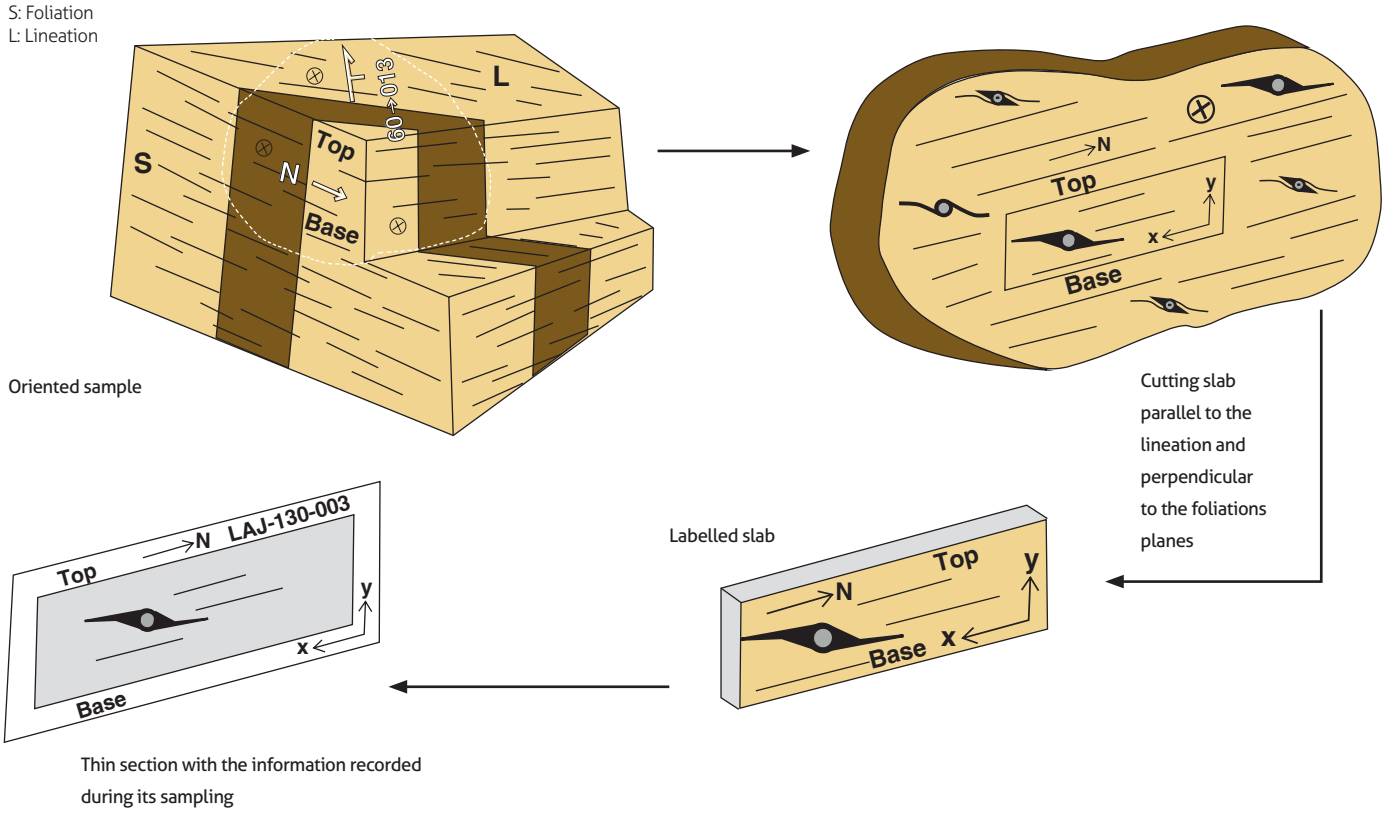

Figure 3. Schematic illustrating the orientation of the sample in the field
The direction of geographic North (→N), structural data, free face, and top and base are indicated. The cut oriented to obtain the labelled slab must be parallel to the mineral linetation and perpendicular to the foliation. Finally, on the thin section for petrographic and microtectonic analysis, the information recorded in the field is indicated as a reference for interpretation of the kinematics in relation to the sample orientation. Source: Prepared with information from Passchier and Trouw (2005), and García (2011).

generated along the X direction and the foliation correspond to the XY planes of the ellipsoid (Flinn, 1979; Ramsay and Huber, 1983; Passchier and Trouw, 2005; Fossen, 2013). To make a cut that reveals the greatest deformation, and additionally, the geometry and direction of movement registered by the kinematic indicators is observed, a section normal to the axis of deformation symmetry must be defined (XZ section of the deformation ellipsoid). This corresponds to the direction perpendicular to the foliation and parallel to the mineral lineation or direction of stretching of the linear fabric elements of interest (Figure 3) (Lister and Hobbs, 1980; Schmid and Casey, 1986; Law, 1990; Hippertt, Lana et al., 2001; Passchier and Trouw, 2005; Trouw et al., 2010; Rutter et al., 2011; Parsons et al., 2016; Goswami et al., 2018). A thin section normal to the mineral direction and parallel to the planes of foliation do not reflect the geometry of the kinematic indicators, because in this cut will be observed Φ and θ-type porphyroclasts and porphyroblasts. These do not exhibit deformation shadows, and thereforethey do not allow the establishment of a kinematic sense (Passchier and Trouw, 2005; Trouw et al., 2010; Davis et al., 2011). It is important also that the thin section replicates the information registered for the rock during sampling, i.e., which show the coordinate axes, geographic north and indications of top and base, among other aspects.

According to the mechanical response of the minerals, the conditions of pressure, temperature, differential stresses and deformation rate under the deformation occurs it is possible microscopically observe the following deformation mechanisms (Blenkinsop, 2002; Passchier and Trouw, 2005).

1. Brittle fracturing – a cataclastic flow, in which fragmentation, rotation and frictional sliding occurs between grain boundaries through inter and intragranular or transgranular microfractures, whether those microfractures are between the grains, affect one grain, or pass through several grains, respectively (Passchier and Trouw, 2005). This mechanism occurs mainly in brittle conditions of low temperature (~150 through ~400 °C) (Blenkinsop and Rutter, 1986; Hadizadeh and Tullis, 1992; Picazo et al., 2013; Baron et al., 2020) and high deformation rates.
2. Intragranular deformation, assisted by dissolution-precipitation processes, responsible for accommodating deformation along the contact surface between the grains or minerals, under semi-brittle regime and brittle-ductile transition conditions.
3. Intracrystalline deformation, which orders point defects and linear distortions along the lattice planes of the crystal, in conditions of brittle-ductile transition, developing deformation lamellae, twinning, undulatory extinction, and microkinks.
4. Processes of recovery and recrystallization, mechanism generating displacement and organization of dislocations, to be accumulated in the form of planes subsequently generate subgrain limits along the edges of larger crystals. One can identify three deformation mechanisms in dynamic recrystallization: *bulging* (*BLG*) (Figure 4a), *subgrain rotation* (*SGR*) (Figure 4b) and *grain boundary migration* (*GBM*) (Figure 4c), developed in ranges of deformation temperatures ~300-410 °C, 410-520 °C and > 520 °C, respectively (Zulauf, 2001; Stipp et al. 2002; Faleiros et al., 2010). At low temperatures (< 400 °C), the calcite is deformed by crystalloplastic processes along the twinning planes, called "e planes" (Despaigne and Caceres, 2009). According to the geometry in which the twinning planes develop, it is possible to estimate the deformation temperature conditions of the calcite crystals. These are classified as: a) *type I*, developed at temperatures of 170 °C (Burkhard, 1993; Passhier and Trouw, 2005; Despaigne and Caceres, 2009); b) *type II*, which occur at 150-300 °C (Ferrill, 1991; Ferrill et al., 2004; Despaigne and Caceres, 2009); c) *type III*, which develop at temperatures > 200 °C (Burkhard, 1993; Despaigne and Caceres, 2009), d) *type IV*, developed at temperatures > 250 °C (Burkhard, 1993; Ferrill et al., 2004; Despaigne and Cáceres, 2009).
5. Solid-state diffusion creep, which occurs mainly at high temperatures, and is related to the transfer of atoms along grain boundaries. It generates curved contacts and chemical zonations.

2.3 3D finite deformation and kinematic vorticity analysis

The 3D finite deformation analysis is based on the calculation of the deformation ellipsoid, which characterizes the planar and linear fabrics of the deformed rocks (corresponding to the XY planes and X axis of the finite deformation ellipsoid, respectively) (Passchier and Trouw, 2005) and quantifies its scalar parameters of magnitude and shape (T parameter, Jelinek, 1981; Flinn parameter or K value, Ramsay and Huber, 1983; degree of anisotropy, Ramsay and Huber, 1983; Borradaile and Werner, 1994; Lagroix and Borradaile, 2000; Nakamura

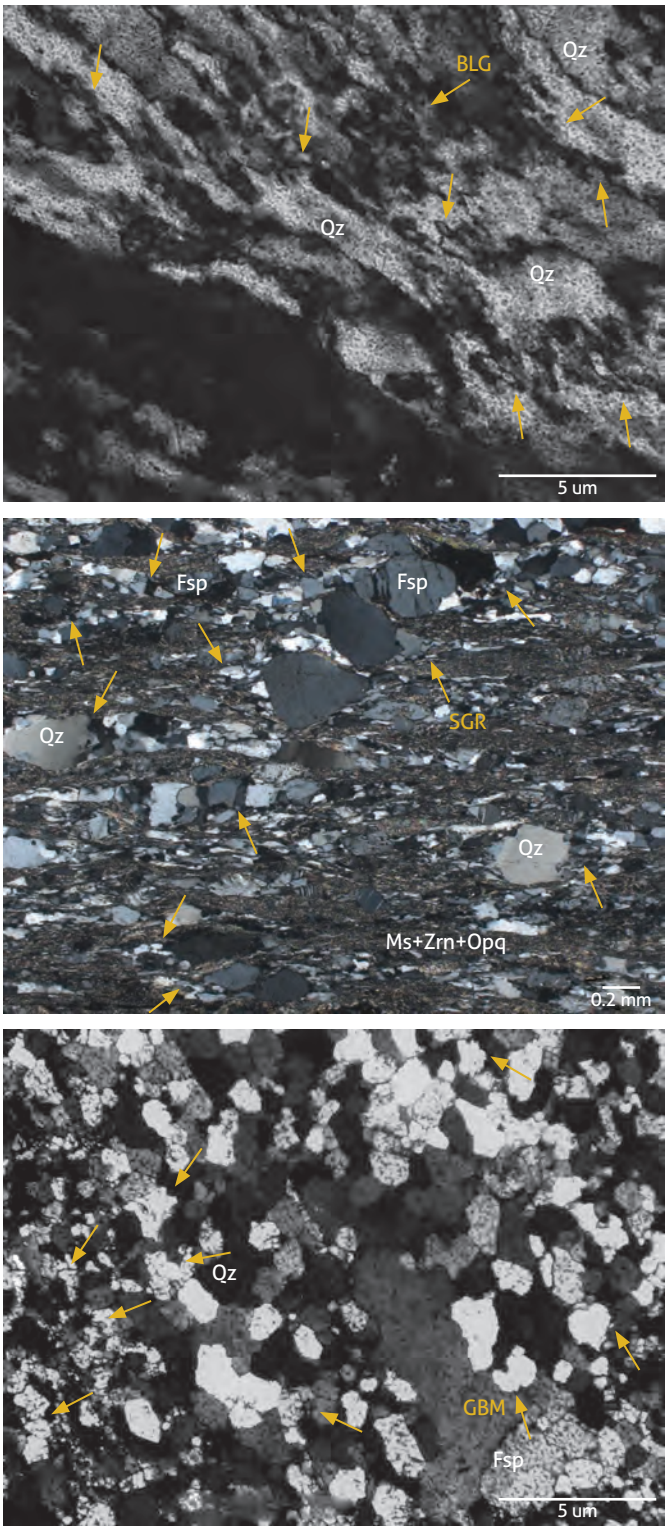

Figure 4. Microphotographs of samples showing intercrystalline plasticity processes evidenced by deformation mechanisms
a) ***Bulging***; b) ***Subgrain rotation***; c) ***Grain boundary migration***. Yellow arrows indicate sites where one observes the dynamic recrystallization previously described (see text).

and Borradaile, 2004). This analysis usually implements the inertial tensor (cf. Launeau and Cruden, 1998) and quadratic tensor (cf. Robin, 2002; Launeau and Robin, 2005) methods. It assumes that the deformation was homogeneous and that the crystals initially had equidimensional shapes. Therefore, the quantification of the geometric properties of the deformation ellipsoid and orientations of its main axes reflect the planar and linear structures developed in the rock body (Launeau and Robin, 2005; Passchier and Trouw, 2005). From the shape geometry and the orientation of the ellipsoid obtained, it is also possible to determine the nature of the deformation (coaxial vs. non-coaxial shear, and constructional vs. flattening deformation) and the stress regime under which the shear zone developed (transtension, transpression, shearing, tension and compression) (cf. Sanderson and Marchini, 1984; Fossen and Cavalcante, 2017; Riberio et al., 2019; Forero-Ortega et al., 2020).

The vorticity analysis determines and quantifies the kinematics of the flow in the shear zones (Xypolias, 2010). It focuses on the interpretation of structural fabrics in terms of the degree of noncoaxiality, i.e., evaluating the relationship between rotation and flow stretching components via numerical modeling (cf. McKenzie, 1979; Means et al., 1980; Lister and Williams, 1983), which quantifies the values of kinematic vorticity (W_k) (Truesdell, 1953), sectional kinematic vorticity (W_n) (Passchier, 1997), and mean kinematic vorticity (W_m). This analysis implements 2D methods on surfaces parallel to the XZ plane of the finite deformation ellipsoid, in order to estimate the spatial contribution of the simple and pure shear components in deformation zones in terms of W_m or W_n values, such as the distribution of linear materials (dikes or sets of deformed veins) (cf. Wallis, 1992; Kumerics et al., 2005; Short and Johnson, 2006), rotation of rigid objects (cf. Johnson et al., 2009; Langille et al., 2010, Thigpen et al., 2010; Forero-Ortega et al., 2020), inclusion patterns in porphyroblasts (cf. Beam and Fisher, 1999; Iacopini et al., 2007), R_{XZ}/β method (cf. Sarkarinejad et al., 2010; Law, 2010; Xypolias et al., 2010), δ/β method (cf. Xypolias, 2009; Ribeiro et al., 2019) and others (cf. Xypolias, 2010).

2.4 Submicroscopic SEM-TEM-EBSD analysis

The Scanning electron microscopy (SEM) and transmission electron microscopy (TEM) analyses with electron backs-cattering diffraction (EBSD) are performed to evaluate textures and compositions (number of phases), based on quantitative

microstructural analysis of crystallographic disorientation angles (characteristics of the boundary mineral) and the average shape and size distribution. These analyses also characterize crystallographic textures, intracrystalline deformation, dynamic recrystallization mechanism, and preferential crystallographic orientation (cf. Behrmann and Mainprice, 1987; Prior et al., 1999; Maitland and Sitzman, 2007; Mariani et al., 2008. Chen and Thomson, 2010; Kilian et al., 2011; Oliot et al., 2014; Platt, 2015; Desbois et al., 2016; Vrolijk et al., 2018; Cavalcante et al., 2018; Goswami et al., 2018; Scheiber et al., 2019; Bella et al., 2019; Ribeiro et al., 2019; Ault, 2020; Conte et al., 2020).

These analyses are carried out on fine-grained minerals in mylonites (mainly quartz and feldspar crystals), which define the transitions of structural levels and rheological conditions of the crust, as well as the location of deformation and development of the shear zone, depending on the prevailing geothermal gradient. These analyses are also performed on clay minerals in fault gouge and iron oxide precipitates developed along the sliding planes, for which it is not possible to easily observe the deformation mechanisms generated, the geometry, and the direction of movement registered by the kinematic indicators.

2.5 Geothermobarometry and thermodynamic modeling

Geothermobarometry has wide applications in the study of pressure and temperature conditions of the various phases and associations of mineral phases. These include establishing the emplacement depth of plutonic bodies (cf. Hammarstrom and Zen, 1986; Bohlen and Lindsley, 1987; Schmidt, 1992; Moazzen and Drop, 2005; Bernet et al., 2019; Cetina et al., 2020), determination of the metamorphic peak of metamorphic rocks, and definition of pressure-temperature-time path (cf. Bohlen and Lindsley, 1987; Essene, 1989; Spear, 1993). The objective of geothermobarometry is to infer the pressure and temperature conditions under which a sample has reached equilibrium (cf. Spear, 1993). The description of geothermometers and geobarometers, as well as the analytical methods used, is beyond the scope of this review, therefore, the interested reader can consult Essene (1989), Spear (1993), and Powell and Holland (1994, 2008) for the basis, and Moecher and Brearley (2004), Grujic et al. (2011), Cross et al. (2015) and Cao et al. (2017), among others, for specific applications to fault rocks.

Starting from petrographic and microtectonic analyses, the aspects that must be considered when conducting geothermobarometry studies in fault rocks involve: 1) recognition of the main deformation structures and kinematic indicators; 2) determination of the paragenesis and equilibrium mineral assemblage present in the rock related to the structures and kinematic indicators; 3) definition of minerals susceptible to microanalysis, in order to obtain compositional data for geothermometry (e.g., chlorite, quartz and mullite) and geobarometry (e.g., white mica or fengite, plagioclase + garnet); 4) calculation of pressures and temperatures.

It has been considered that the deformation in shear zones may affect the rates and mechanisms of chemical equilibrium in different mineral phases (cf. Steffen and Selverstone, 2006; Richard et al., 2014). The combination of metamorphism and deformation causes transient changes in the speed of the reactions and kinetic pathways that generate mineral associations in chemical equilibrium. These processes, therefore, affect the accuracy and uncertainty of results obtained from geothermobarometers analysis, thus evidencing the presence of heterogeneities or chemical imbalances (cf. Steffen and Selverstone, 2006).

To minimize uncertainties caused by chemical imbalances, another method used to obtain pressures and temperatures is thermodynamic modeling. This method allows the prediction of mineral phases in equilibrium within certain pressure and temperature ranges, based on a given chemical composition, and aims to understand the evolution of mineral associations (Spear, 1993). The diagrams that include mineral associations distributed in stability fields are called pseudosections, and correspond to maps or sections of phase diagrams that show the mineral equilibrium that can be used to predict the pressure-temperature conditions in which the major mineral associations are generated (Tinkham, 2007; Vernon and Clarke, 2008), from specific compositions of total rock (Powell et al., 1998; Zuluaga et al., 2006; Tinkham, 2007).

Starting from petrographic analysis, the aspects that must be considered to do thermodynamic modeling of fault rocks include: 1) defining the mineral phases to be modeled; 2) establishing the chemical components of the system; 3) determining the chemical system that defines the phase equilibrium (e.g., KFMASH, which corresponds to K_2O, FeO, MgO, Al_2O3, SiO_2, H_2O); 4) finding the intensive variables or degrees of freedom of the system to be modeled by application of the phase rule; 5) running the Gibbs free energy minimization routine (e.g., Perple_X); 6) constructing the P-T (pressure-temperature) pseudosection. Additionally, if geothermobarometry data are available, the P-T trajectories can be reconstructed.

Construction of a pseudosection is done using software, among which Thermocalc (Powell and Holland, 2001 and 2005; Zuluaga et al., 2006; Tinkham, 2007; https://hpxeosandthermocalc.org), Theriak Domino (De Capitani and Petrakakis, 2010; https://titan.minpet.unibas.ch/minpet/theriak/theruser.html), and Perple_X (Connolly, 2005; 2009; http://www.perplex.ethz.ch) stand out. The software description is beyond the scope of this review, so the reader is referred to the links cited above. Pseudosections are used in the modeling of faulting controlled by fluid infiltration in mylonites at different structural levels (cf. Selverstone et al., 2012; Précigout et al., 2017), of seismically coupled and uncoupled segments in subduction interfaces (cf. Angiboust et al., 2015) and the metamorphic rocks that host the shear zones (cf. Forero-Ortega et al., 2020). The pseudosections also demarcate deformation histories evidenced in most cases by prograde and retrograde segments of P-T paths owing to shear (cf. Steffen and Selverstone, 2006).

3. Estimation of the deformation age of faults and shear zones

Fault and shear zones control the distribution of deformation throughout the lithosphere and play a fundamental role in the emplacement of magmas and circulation of fluids (Ramsay, 1980b; Sibson, 1990; Brown and Solar, 1998; Micklethwaite et al., 2010; Vauchez et al., 2012; Clerc et al., 2015; Smeraglia et al., 2016; Précigout et al., 2017). Therefore, understanding of the timing of activity in the fault and shear zone is essential to comprehend the tectonic evolution in a specific geological context. For this, it is necessary to integrate the mapping and analysis of structures at macro and micro-scales, geochronological and thermochronological data that help determine directly and indirectly the thermal history of a shear zone over time, related to processes of exhumation, uplift and sedimentation associated with evolution of the structure (Bossi and Campal, 1992; Oyhantçabal et al., 1993; Oyhantçabal et al., 2001; Zwingmann and Mancktelow, 2004; van der Plujim et al., 2006; Löbens et al., 2011; Davids et al., 2013; Hnat and van der Pluijm, 2014; Viola et al., 2016; Oriolo et al., 2016 a, b; Ring et al., 2017; Süssenberger et al., 2017).

3.1 Geochronology of fault rocks

In order to delimit the deformation age in shear zones, determined in a relative way from field observations such as cross-cutting relationships between the structures and the geological units, generation of zones or surfaces erosion and discontinuities, among others, the use of geochronological and thermochronological methods is recommended for fault rocks or lithological units that constitute blocks adjacent to the shear zones (Table 2). The most relevant isotopic systems and dating methods for the study of shear zones are highlighted in certain reviews (cf. Ohtani et al., 2004; Oriolo et al., 2018; Hueck et al., 2020; and references cited therein). In brittle deformation conditions, methods such as K-Ar and Ar-Ar in neoformed phyllosilicates, such as chlorite, white mica, sericite, muscovite and illite have been implemented (cf. Crone, 1996; Chan et al., 2000; Jefferies et al., 2006; McWilliams et al., 2007; Vinasco, 2001; Löbens et al., 2011; Oyhantçabal et al., 2012; Wang et al., 2016), in fault gouge (cf. Vrolijk and van der Plujim, 1999; van der Pluijm et al., 2001; Zwingmann and Mancktelow, 2004; Haines and van der Plujim, 2008; Duvall et al., 2011; Fitz-Díaz and van der Plujim, 2013; Viola et al., 2016; Scheiber et al., 2019) and in the pseudotachylite matrix (cf. Crone and Omdahl, 1987; Sherlock and Hetzel, 2001; Magloughlin et al., 2001; Streepey et al., 2002; Cosca et al., 2005; Reiners and Brandon, 2006; Whitmeyer, 2008; Cassata et al., 2009; Sherlock et al., 2009; Wolff et al., 2012; Di Vincenzo et al., 2013; Bense et al., 2014; Viola et al., 2016; Süssenberger et al., 2017, Vrolijk et al., 2018). Likewise, U-Pb and U-Th analyses in veins and fibres of calcite and opal precipitated on the fault planes have been performed (cf. Verhaert et al., 2003; Uysal et al., 2007;

Table 2. Synthesis of materials and methods proposed to establish the age under different thermal conditions present in the shear zones, and the probable interpretation of these data

Deformation conditions	Material for dating	Proposed dating methods	Probable interpretation
Brittle	Quartz grains that constitute the fault gouge	Electron spin resonance (ESR)	Reactivation age of fault zone
Brittle	Hematite, magnetite and goethite precipitate	(U-Th)/He and fission track	Reactivation age of fault zone
Brittle	Veins and fibers of calcite in fault planes	U-Pb	Reactivation age of fault zone or syntectonic precipitation
Brittle	Neoformed micas	Ar-Ar/K-Ar	Reactivation age of fault zone
Brittle/Brittle-ductile	Neoformed micas, fault gouge, and pseudotaquilite matrix	Ar-Ar/K-Ar	Reactivation age of fault zone
Ductile	Neoformed micas in mylonites	Ar-Ar	Reactivation age, cooling or isotopic resetting of shear zone
Ductile	Pre and synkinematic minerals in mylonites	U-Th-Pb	Deformation age in shear zone

Watanabe et al., 2008; Nuriel et al., 2011, 2017, 2019; Roberts and Walker, 2016; Pagel et al., 2018), in order to establish the age of reactivation of the shear zones (Kelley, 2002).

The U-Pb geochronology in calcite is proposed because calcite can register a rapid deformation event at low temperature in the upper crust, process that would be difficult to dated radiometrically with other minerals, since they do not have the time necessary to crystallize and record deformation under these conditions. Therefore, calcite constitutes an effective chronometer that relates deformation processes (development of faults and folds) and hydrothermal mineralization (cf. Roberts and Walker, 2016; Goodfellow et al., 2017; Mottram et al., 2018, Beaudoin et al., 2018; Roberts et al., 2020a). The main objective is the U-Pb dating of calcite crystals in mineralized fault planes that show textures filled by fracturing and sealing (crack-seal) (Nuriel et al., 2011; Robert and Walker, 2016). Likewise, the material to be dated must be present in syntectonic structures upon the brittle deformational event, either as tension gashes or fault-gouge injection veins, and displaying some of the following characteristics (Nuriel et al., 2011; Dressel et al., 2018; Miranda et al., 2020; Roberts et al., 2020b): 1) crack seal textures with sliding in micro pull-apart structures; 2) crack seal textures with growth fiber lineation; 3) crack seal textures within implosion breccia structures; 4) sigmoidal, in echelon, and pocket-type shapes with normal kinematics, the latter associated with discontinuous veins, massive internal textures, brechoid or sheared.

To guarantee the simultaneity of the calcite and deformational event that gave rise to its precipitation, i.e., the temporal relationship between the fault, fracturing, fluid circulation, and the process of precipitation and growth of calcite (Ramsay, 1980; Barker et al., 2006; Nuriel et al., 2011), geochemical, microstructural and petrographic analyses should be integrated into the U-Pb geochronology of calcite minerals (cf. Nuriel et al., 2011; Miranda et al., 2020).

Low-temperature thermochronometers ((U-Th)/He and fission track) (Table 2) have been used in fault zones that show fluid circulation along the damage zones and in the core of the structure, these generally synkinematic upon the deformational event and characterized by the precipitation of hematite, magnetite and goethite in veins, breccias, and as patina along the sliding planes (cf. Tagami and Murakami, 2007; Wolfler et al., 2010; Gorynski et al., 2014; Hickey et al., 2014; Reiner et al., 2014; MacNamee and Stockli, 2015; Ault et al., 2016; Louis et al., 2019; Tagami, 2019). Under these conditions, the occurrence of iron oxides is the deformation dating target, these also record the temperatures in which the displacement of the structure was induced (cf. Wernicke and Lippolt, 1997; Shuster et al., 2005; Blackburn et al., 2007; Farley and Flowers, 2012; Evenson et al., 2014; Monteiro et al., 2014; Farley and McKeon, 2015; Ault et al., 2015, 2016; Cooperdock and Stockli, 2016; Miller et al., 2017; McDermott et al., 2017; Moser et al., 2017; García et al., 2018; Calzolari et al., 2018; Ault, 2020).

Other techniques applied to fault zones that present fluid circulation and that host mineralizations are dating of U-Th-Pb in hydrothermal monazite (cf. Bergemann et al., 2017, 2018; Ricchi, Bergemann et al., 2020; Ricchi, Gnos et al., 2020; Prent et al., 2020), Rb-Sr in feldspar crystals (cf. Tillberg et al., 2017; Tillberg et al., 2020), and Re-Os in hydrothermal sulfides (Vernon et al., 2014; Lawley et al., 2013; Dichiarante et al., 2016).

For fault gouge, the method of dating by electron spin resonance (ESR) has been used for quartz grains that make up this non-cohesive rock (Table 2) (cf. Ikeya et al. 1982; Ikeya, 1993; Lee and Schwarcz, 1994; Lee and Yang, 2007). The technique is based on the ability to analyze damage caused by natural radiation in geological and biological materials such as shells, corals, bones and fossilized teeth, by detecting alpha, beta and gamma radioactivity from the sample and its environment (Duval et al., 2011; Duval, 2018). This radiation produces defects in the crystal lattice that can trap electrical charges that eventually form a "paramagnetic center" that produces a detectable signal in ESR spectrometry. The height (intensity) of the spectrum obtained is proportional to the number of electrons trapped in each paramagnetic center, the radiation dose and its duration (Ikeya et al., 1982; Ikeya, 1993, Grün, 1989; Lee and Schawarcz, 1994; Lee and Yang, 2007; Qju et al., 2018; Duval, 2018).

In shear zones that exhibit deformations of the brittle-ductile transition, which include associations of cataclasites, phyllonites, protomylonites and pseudotaquilites (Sibson, 1983; Simpson, 1986), as well as mineral reactions and fluids, the Ar-Ar isotopic system in micas and the pseudotaquilite matrix is the most widely used tool for absolute dating of deformational activity (Crone, 1996; Vinasco, 2001; Oyhantçabal et al., 2012; Bense et al., 2014; Süssenberger et al., 2017). This is because of substantial retentiveness of Ar in the structure of neoformed minerals (closed isotopic system) (Purdy and Jäger, 1976; Reddy and Potts, 1999; Harrison et al., 2009) in intervals of low-to-medium temperature, conditions in which the reactivation of structures normally occurs (Grégoire et al., 2009; Webb et al., 2010; Bonamici et al., 2004; Oriolo et al., 2016a). When

pseudotaquilites are processed, it is recommended to exclude clasts present in the matrix, since they can contribute foreign Ar derived from preexistent rock, which can yield ages without geological sense (Di Vincenzo et al., 2004).

The deformation age under middle crust conditions, mainly affected by the ductile regime, is traditionally determined by fine muscovites and neoformed biotites (cf. Freeman et al., 1998; Fossen and Dunlap; 1998; Müller et al., 2000; Vinasco, 2001; Whitmeyer, 2008, Vinasco and Cordani, 2012), and recrystallized minerals (cf. Kligfield et al., 1986; Oriolo et al., 2015, 2016b) (Table 2), which provide information on tectonic activation from cooling ages or isotopic resetting, given the low closure temperature of these isotopic systems (cf. van der Pluijm et al., 1994).

Nevertheless, there are debates about the meaning of the geochronological data of these isotopic methods when diffusion, dissolution and precipitation processes by creep processes and fluid-assisted recrystallization have developed in the fault rocks. This is because the age intervals obtained would be related to cooling processes of the system and not be directly related to the deformation timing (cf. Harrison et al., 1985; Jenkin, 1997; Carreras et al., 2013; Eberlei et al., 2015; Vissers et al., 2016; Druguet et al., 2018). For these conditions, in order to constrain the thermal history in the shear zone, *in-situ* Rb-Sr and Ar-Ar micas and U-Th-Pb zircon, monazite, titanite, rutile and apatite have been integrated. The latter are resistant to physical and chemical alterations of the system, and in which the reported ages are related to crystallographic deformation process@, since the migration and formation of crystalline faces are subject to development without incorporation of radiogenic Pb in the crystal lattice (Dahl, 1997; Lee et al., 1997; Cherniak and Watson, 2000; Santos et al., 2003; Cherniak et al., 2004; Cocherie et al., 2005; Dahl et al., 2005; Harley et al., 2007; Reddy et al., 2007; Timms et al., 2011; Oyhantçabal et al., 2012; Bonamici et al., 2015; Erickson et al., 2015; Oriolo et al., 2016a; Kirkland et al., 2018 a, b; Giraldo et al., 2019; Odlum and Stockli, 2020; Ribeiro et al., 2020 a, b; Van Daele et al., 2020).

3.1.1 Considerations for mineral dating of fault rocks

For analysis and application of different isotopic systems is necessary to consider the closure temperatures of the minerals. This is because once the isotopic system has reached a specific temperature range, the host mineral does not exchange isotopes with the system (a closed isotopic system), so negligible diffusion rates are obtained, as therefore precise chronological information on the deformation event (cf. Dodson, 1973; Villa, 2002; Braun et al., 2006). Closure temperatures depend on physical factors such as grain size, mineral composition, cooling rate, and pressure, among others (cf. Dodson, 1973; Hames and Bowring, 1994; Grove and Harrison, 1996; Cherniak, 1995; Farley, 2000; Jenkin et al., 2001; Braun et al., 2006; Harrison et al., 2009). For this reason, to date fault rocks, it is necessary to rely on the reconstruction of geothermobarometric diagrams (P-T-t), geochemical analysis, thermodynamic modeling, and microstructural studies (cf. van der Plujim et al., 1994; Stönitz, 1998; Steffen and Selverstone, 2006; Villa et al., 2014; Odlum and Stockli, 2020; Ribeiro et al., 2020 a, b).

The temperature reached during the deformation process must be less than or equal to the closure temperature of the isotopic system of the geochronological method used. Otherwise, the age obtained will be a cooling age of the isotopic system and not of the deformation (Vinasco, 2001). This is because dynamic recrystallization, neo-crystallization, metamorphic reactions and fluid circulation (dissolution-precipitation processes) take place during deformation, which modify the physical properties (reset) of the isotopic system of minerals in fault rocks (cf. Dunlap, 1997; Villa, 2002; Mulch et al., 2002; Mulch and Cosca, 2004; Harley et al., 2007; Cosca et al., 2011; Tagami, 2012; Harlov, 2015; Oriolo et al., 2016a).

In the case of U-Pb dating of carbonates (e.g., calcite), once the event of interest has been identified through field observations, petrography, cathodoluminescence and electron microscopy, one should confirm that: 1) the carbonate is contemporary or synchronous, or very close, to the geological event of interest; 2) the carbonate formed rapidly and under conditions that allowed enrichment in U and exclusion of Pb; 3) there is no evidence of dissolution,recrystallization, or alteration (e.g., diagenetic); 4) there are no different generations of carbonate; 5) there are optimal concentrations of U in the mineral to ensure accurate dating, which can be determined by compositional maps (cf. Rasbury and Cole, 2009; Roberts and Walker, 2016; Roberts, 2019; Roberts et al., 2020a).

3.2 Radiometric dating of geological features adjacent to shear zones

Given the different geological processes (deformation, metamorphism, and fluid-rock interaction) related to the evolution of a shear zone, it is necessary to integrate geochronological and thermochronological studies of syntectonic elements of the structure, in order to constrain the age of deformation in

shear zones (Fossen and Tikoff, 1997; Xypolias and Kokkalas, 2006; Vitale and Mazzoli, 2008; Carreras et al., 2013; Pennacchioni and Zucchi, 2013; Ribeiro et al., 2020b). These studies include:

a) Intrusive synkinematic (Table 3), which correspond to igneous bodies emplaced during reactivation episodes of fault systems, in which magmatic units are transported through the crust by shear zones that behave as channels connecting magma generation areas with the upper crust (D'Lemos et al., 1992; Reavy, 1989; Clemens and Mawer, 1992; Rosenberg, 2004). The emplacement of granitoids thus marks a direct relationship between tectonic deformation and magmatic bodies (D'Lemos et al., 1992; Druguet and Hutton, 1998; Brown and Solar, 1999; Grocott and Taylor, 2002; Vinasco and Cordani, 2012; Ávila et al., 2019) and delimits strongly deformed areas in which igneous bodies fill open spaces within brittle-ductile transition zones, mainly associated with transtensional deformations and limited by the traces of regional faults. To date these intrusives, it is necessary to perform a priori detailed analysis of magmatic fabrics (cf. Romn-Berdiel et al., 1997; Blumenfeld and Bouchez, 1988; Paterson et al., 1989; Bouchez et al., 1992; Paterson and Vernon, 1995; Paterson et al., 1998), in order to discriminate between pre-, syn- and postkinematic igneous bodies (Steenken et al., 2000; Rosenberg, 2004; Siegesmund et al., 2004; Wang et al., 2009; Oyhantçabal et al., 2009). Once determined from the magmatic fabric that the igneous body is synkinematic, the igneous units are dated by U-Pb dating of zircon, in order to obtain the age of emplacement of the igneous body, information directly related to reactivation periods of the shear zone.
b) Hydrothermally altered rocks related to shear zone activity (Table 3), for which the Ar-Ar dating method is mainly used for neoformed white micas, which provide information on tectonic reactivations, because they are related to fluids generated during deformational events in the shear zones (Vinasco, 2001; Vinasco and Cordani, 2012).
c) Blocks adjacent to the structure (Table 3) in which the exhumation ages are related to periods of deformation or reactivation of the fault zone, because low-temperature thermochronology dates the cooling ages, which in shear zone contexts are widely related to timing of the fault slip (cf. van der Pluijm et al., 1994; Stockli et al., 2002; Wells et al., 2000; Echler and Farley, 2003; Colgan et al., 2008; Bidgoli et al., 2015; Curry et al., 2016; Oriolo et al., 2016b; Abbey and Niemi, 2018; Collett et al., 2019; Heineke et al., 2019; Amaya-Ferreira et al., 2020). Exhumation ages are determined using low-temperature thermochronology methods (surface conditions of the lithosphere at ~10-km depth, for a normal geothermal gradient), including thermochronometers such as apatite fission track (AFT) and zircon fission track (ZFT), which give closing temperatures between ~110-120 °C and ~230-240 °C, respectively, under conditions of constant cooling and relatively rapid exhumation (Zaun and Wagner, 1985; Hurford, 1986; Laslett et al., 1987; Brandon and Vance, 1992, Ketcham et al., 1999; Bernet et al., 2002; Bernet et al., 2019).

4. Conclusions and recommendations

For geological-structural mapping of shear zones, it is suggested to perform an analysis of photointerpretation and geoprocessing of images in which the trace of the structure is preliminarily delimited. Once defined, field transects must be made perpendicular to the strike of the deformed area in order to collect structural data with statistical representativeness and determine the distribution, kinematics and geometry of the central and marginal areas of the principal structure in the shear zone, as well as of satellite faults, branches and secondary structures, in order to define the timing of deformation events and rank the developed structures.

To classify fault rocks in the field, it is recommended to adopt the modified proposal of Sibson (1977; 1979), Scholz (1988), Snoke et al. (1998), Killick (2003), Woodcock and Mort (2008) and Magloughlin (2010), which differentiated between cohesive and non-cohesive rocks, categorizes the rocks

Table 3. Synthesis of the material and proposed method for dating geological elements adjacent to the shear zone, as well as the information obtained thereby

Material for dating	Proposed methods for dating	Informaction obtained
Zircons of synkinematic intrusive	U-Pb	Age of emplacement
Neoformed micas of hydrothermally altered rocks	Ar-Ar	Age of reactivation of shear zone, cooling or isotopic resetting
Fission tracks in apatite and zircon of blocks adjacent to the structure	AFT and ZFT	Exhumation ages

according to the percentage of original and matrix grains, and describes the characteristics and deformation mechanisms developed during the deformation event.

The proposed methodology to determine and constrain the period of deformation in shear zones uses technical differences according to the deformational regime in which the fault rocks were generated, implements materials and methods of geological elements adjacent to the shear zone, and it is constituted by the following activities: 1) submicroscopic analysis of minerals; 2) dating of neoformed micas, fault gouge, and pseudotakylite matrix by the Ar-Ar method, and of calcite fibers and iron precipitates by the U-Pb and (U-Th)/He systems, respectively, under conditions of brittle/brittle-ductile deformation; 3) *in-situ* K-Ar dating of micas and U-Th-Pb of pre- and synkinematic minerals in mylonite rocks; 4) dating of synkinematic intrusives, adjacent blocks, and hydrothermally altered rocks by the U-Pb, AFT/ZFT and Ar-Ar methods, respectively.

The minerals that make up fault rocks are formed in the presence of fluids and conditions of varying pressure and temperature, and can be isotopic resetting during the evolutionary history of shear zones. Considering that the dating of fault rocks depends on the deformation temperature, it is suggested to establish the temperature from geothermometers and microscopic analysis of the microstructures. However, the presence of retrograde, recrystallization or dissolution-precipitation processes must be determined, since these processes substantially affect the closure temperature of the minerals used in the geochronological and thermochronological methods implemented and do not guarantee a closed isotopic system with negligible diffusion rates.

Acknowledgements

This contribution was made in the framework of the Tectonic Model project of Colombia, of the Tectonic Group of the Dirección de Geociencias Básicas of the Servicio Geológico Colombiano, in compliance with its mission related to comprehensive management of geoscientific knowledge. The authors thank the Geodynamics Research Group of the Tectonics Group and geologists Jairo Alonso Osorio, Yadira Rodríguez, Edward Salazar Ortiz and Ana Milena Suárez for their suggestions, as well as the anonymous reviewers for their technical contributions and constructive feedback.

References

Abbey, A. L., & Niemi, N. A. (2018). Low-temperature thermochronometric constraints on fault initiation and growth in the northern Rio Grande rift, upper Arkansas River valley, Colorado, USA. *Geology*, *46*(7), 627-630. https://doi.org/10.1130/G40232.1

Aitken, A. R. A., & Betts, P. G. (2009). Multi-scale integrated structural and aeromagnetic analysis to guide tectonic models: An example from the eastern Musgrave Province, Central Australia. *Tectonophysics*, *476*(3-4), 418-435. https://doi.org/10.1016/j.tecto.2009.07.007

Altenberger, U., & López I., J. A. (2014). Evidence of frictional melts in weak carbonate rocks: Examples from the Cuisa Fault, alta Guajira/Northern Colombia. *Geología Colombiana*, *37*, 5-14.

Amaya-Ferreira, S., Zuluaga, C. A., & Bernet, M. (2020). Different levels of exhumation across the Bucaramanga Fault in the Cepitá area of the southwestern Santander Massif, Colombia: Implications for the tectonic evolution of the northern Andes in northwestern South America. In J. Gómez & D. Mateus Zabala (eds.), *The geology of Colombia. Vol. 3: Paleogene-Neogene*. Publicaciones Geológicas Especiales, 37. Servicio Geológico Colombiano. https://doi.org/10.32685/pub.esp.37.2019.17

Anderson, L. J., Osborne, R. H., & Palmer, D. F. (1993). Cataclastic rocks of the San Gabriel Fault: An expression of deformation at deeper crustal levels in the San Andreas fault zones. *Tectonophysics*, *98*(3-4), 209-251. https://doi.org/10.1016/0040-1951(83)90296-2

Angelier, J. (1979). Determination of the mean principal directions of stresses for a given fault population. *Tectonophysics*, *56*(3-4), 17-26. https://doi.org/10.1016/0040-1951(79)90081-7

Angelier, J. (1994). Fault slip analysis and palaeostress reconstruction. In P. L. Hancock (ed.), *Continental deformation* (pp. 53-100). Pergamon Press.

Angelier, J. T., & Mechler, P. (1977). Sur une méthode graphique de recherche des contraintes principales également utilisables en tectonique et en séismologie: La méthode des dièdres droits. *Bulletin de la Société Géologique de France*, *7*(6), 1309-1318.

Angiboust, S., Kirsch, J., Oncken, O., Glodny, J., Monié, P., & Rybacki, E. (2015). Probing the transition between seismically coupled and decoupled segments along an ancient subduc-

tion interface. *Geochemistry, Geophysics, Geosystems*, *16*(6), 1905-1922. https://doi.org/10.1002/2015GC005776

Armit, R. J., Ailleres, L., Betts, P. G., Schaefer, B. F., & Blaikie, T. N. (2014). High-heat geodynamic setting during the Paleozoic evolution of the Mount Painter Province, SA, Australia: Evidence from combined field structural geology and potential-field inversions. *Geophysical Journal International*, *199*(1), 253-275. https://doi.org/10.1093/gji/ggu263

Ault, A. K. (2020). Hematite fault rock thermochronometry and textures inform fault zone processes. *Journal of Structural Geology*, *133*, 104002. https://doi.org/10.1016/j.jsg.2020.104002

Ault, A. K., Frenzel, M., Reiners, P. W., Woodcock, N. H., & Thomson, S. N. (2016). Record of paleofluid circulation in faults revealed by hematite (U-Th)/He and apatite fission-track dating: An example from Gower Peninsula fault fissures, Wales. *Lithosphere*, *8*(4), 379-385. https://doi.org/10.1130/L522.1

Ault, A. K., Reiners, P. W., Evans, J. P., & Thomson, S. N. (2015). Linking hematite (U-Th)/He Utah, USA. *Geology*, *43*(9), 771-774. https://doi.org/10.1130/G36897.1

Ávila, C., Archanjo, C., Fossen, H., & Hollanda, M. H. (2019). Zippered shear zone model for interacting shear zones in the Borborema Province, Brazil, as constrained by U-Pb dating. *Tectonics*, *38*(10). https://doi.org/10.1029/2019TC005547

Babaie, H. A., Babaei, A., & Hadizadeh, J. (1991). Initiation of cataclastic flow and development of cataclastic foliation in nonporous quartzites from a natural fault zone. *Tectonophysics*, *200*(1-3), 67-77. https://doi.org/10.1016/0040-1951(91)90006-e

Babaie, H. A., & La Tour, T. E. (1993). Semibrittle and cataclastic deformation of hornblende-quartz rocks in a ductile shear zone. *Tectonophysics*, *229*(1-2), 19-30. https://doi.org/10.1016/0040-1951(94)90003-5

Balsamo, F., Storti, F., Salvini, F., Silva, A. T., & Lima, C. C. (2010). Structural and petrophysical evolution of extensional fault zones in low-porosity, poorly lithified sandstones of the Barreiras Formation, NE Brazil. *Journal of Structural Geology*, *32*(11), 1806-1826. https://doi.org/10.1016/j.jsg.2009.10.010

Barão, L. M., Trzaskos, B., Angulo, R. J., & De Souza, M. C. (2018). Análise qualitative fractal das estruturas nas Ilhas Belmonte e Challenger e sua relação com a estruturação local: Arquipélago de São Pedro e São Paulo. In J. E. Lins Oliveira, D. de L. Viana, M. A. Carvalho de Sousa (eds.), *Arquipélago de São Pedro e São Paulo: 20 anos de pesquisa* (pp. 221-224). Via Design Publicações.

Barão, L. M., Trzaskos, B., Angulo, R. J., & De Souza, M. C. (2020). Deformation and structural evolution of mantle peridotites during exhumation on transform faults: A forced transition from ductile to brittle regime. *Journal of Structural Geology*, *133*, 103981. https://doi.org/10.1016/j.jsg.2020.103981

Barker, S. L. L., Cox, S. F., Eggins, S. M., & Gagan, M. K. (2006). Microchemical evidence for episodic growth of antitaxial veins during fracture-controlled fluid flow. *Earth and Planetary Science Letters*, *250*(1-2), 331-344. https://doi.org/10.1016/j.epsl.2006.07.051

Bastesen, E., & Braathen, A. (2010). Extensional faults in fine grained carbonates: Analysis of fault core lithology and thickness-displacement relationships. *Journal of Structural Geology*, *32*(11), 1609-1628. https://doi.org/10.1016/j.jsg.2010.09.008

Beach, A., Welbon, A. I., Brockbank, P. J., & McCallum, J. E. (1999). Reservoir damage around faults: Outcrop examples from the Suez Rift. *Petroleum Geoscience*, *5*(2), 109-116. https://doi.org/10.1144/petgeo.5.2.109

Beam, E. C., & Fisher, D. M. (1999). An estimate of kinematic vorticity from rotated elongate porphyroblasts. *Journal of Structural Geology*, *21*(11), 1553-1559. https://doi.org/10.1016/S0191-8141(99)00110-8

Beaudoin, N., Lacombe, O., Roberts, N. M., & Koehn, D. (2018). U-Pb dating of calcite veins reveals complex stress evolution and thrust sequence in the Bighorn Basin, Wyoming, USA. *Geology*, *46*(11), 1015-1018. https://doi.org/10.1130/G45379.1

Behrmann, J. H., & Mainprice, D. (1987). Deformation mechanisms in a high-temperature quartz-feldspar mylonite: Evidence for superplastic flow in the lower continental crust. *Tectonophysics*, *140*(2-4), 297-305. https://doi.org/10.1016/0040-1951(87)90236-8

Bell, T. H., & Etheridge, M. A. (1973). Microstructure of mylonites and their descriptive terminology. *Lithos*, *6*(4), 337-348. https://doi.org/10.1016/0024-4937(73)90052-2

Bella, B. E. N., Njanko, T., & Tchakounte, J. (2019). CPO and kinematic analysis of the Bitou S-tectonites (Central Camerrom shear zone): AMS and EBSD investigations. *Journal of Earth System Science*, *128*(231), 1-14. https://doi.org/10.1007/s12040-019-1264-9

Bense, F. A., Wemmer, K., Löbens, S., & Siegesmund, S. (2014). Fault gouge analyses: K-Ar illite dating, clay mineralogy and tectonic significance: a study from the Sierras Pampeanas, Argentina. *International Journal of Earth Sciences*, *103*, 189-218. https://doi.org/10.1007/s00531-013-0956-7

Berg, S. S., & Skar, T. (2005). Controls on damage zone asymmetry of a normal fault zone: Outcrop analyses of a segment of the Moab fault, SE Utah. *Journal of Structural Geology*, *27*(10), 1803-1822. https://doi.org/10.1016/j.jsg.2005.04.012

Bergemann, C. A., Gnos, E., Berger, A., Whitehouse, M. J., Mullis, J., Wehrens, P., Pettke, T., & Janots, E. (2017). Th-Pb ion probe dating of zoned hydrothermal monazite and its implications for repeated shear zone activity: An example from the Central Alps, Switzerland. *Tectonics*, *36*(4), 671-689. https://doi.org/10.1002/2016TC004407

Bergemann, C. A., Gnos, E., Berger, A., Whitehouse, M. J., Mullis, J., Walter, F., & Bojar, H. P. (2018). Constraining long-term fault activity in the brittle domain through in situ dating of hydrothermal monazite. *Terra Nova*, *30*(6), 440-446. https://doi.org/10.1111/ter.12360

Bernet, M., Brandon, M. T., Garver, J. I., Reiners, P. W., & Fitzgerald, P. G. (2002). Determining the zircon fission-track closure temperature. GSA Cordilleran Section, 98th annual meeting, Abstract with Programs (34), 18.

Bernet, M., Piraquive, A., Urueña, C., López-Isaza, J., Bermúdez, M., Zuluaga, C., Amaya, S., & Villamizar, N. (2019). Multidisciplinary petro-geo-thermochronological approach to ore deposit exploration. *Ore Geology Reviews*, *112*, 103017. https://doi.org/10.1016/j.oregeorev.2019.103017

Betts, P. G., Valenta, R. K., & Finlay, J. (2003). Evolution of the Mount Woods Inlier, northern Gawler Craton, Southern Australia: An integrated structural and aeromagnetic analysis. *Tectonophysics*, *366*(1-2), 83-111. https://doi.org/10.1016/S0040-1951(03)00062-3

Bidgoli, T. S., Stockli, D. F., & Walker, J. D. (2015). Low-temperature thermochronologic constraints on the kinematic histories of the Castle Cliffs, Tule Springs, and Mormon Peak detachments, southwestern Utah and southeastern Nevada. *Geosphere*, *11*(3), 850-867. https://doi.org/10.1130/GES01083.1

Billi, A., Salvini, F., & Storti, F. (2003). The damage zone-fault core transition in carbonate rocks: Implications for fault growth, structure and permeability. *Journal of Structural Geology*, *25*(11), 1779-1794. https://doi.org/10.1016/S0191-8141(03)00037-3

Blackburn, T. J., Stockli, D. F., & Walker, J. D. (2007). Magnetite (U-Th)/He dating and its application to the geochronology of intermediate to mafic volcanic rocks. *Earth and Planetary Science Letters*, *259*(3-4), 360-371. https://doi.org/10.1016/j.epsl.2007.04.044

Blaikie, T. N., Ailleres, L., Betts, P. G., & Cas, R. A. F. (2014). Interpreting subsurface volcanic structures using geologically constrained 3-D gravity inversions: Examples of maar-diatremes, Newer Volcanics Province, southeastern Australia. *Journal of Geophysical Research: Solid Earth*, *119*(4), 3857-3878. https://doi.org/10.1002/2013JB010751

Blaikie, T. N., Betts, P. G., Armit, R. J., & Ailleres, L. (2017). The ca. 1740-1710 Ma Leichhardt Event: Inversion of a continental rift and revision of the tectonic evolution of the North Australian Craton. *Precambrian Research*, *292*, 75-92. https://doi.org/10.1016/j.precamres.2017.02.003

Blenkinsop, T. (2002). *Deformation microstructures and mechanism in mineral and rocks*. Klewer Academic Publishers.

Blenkinsop, T., & Rutter, E. (1986). Cataclastic deformation of quartzite in the moine thrust zone. *Journal of Structural Geology*, *8*(6), 669-681. https://doi.org/10.1016/0191-8141(86)90072-6

Blumenfeld, P., & Bouchez, J. L. (1988). Shear criteria in granite and migmatite deformed in the magmatic and solid states. *Journal of Structural Geology*, *10*(4), 361-312. https://doi.org/https://doi.org/10.1016/0191-8141(88)90014-4

Bohlen, S. R., & Lindsley, D. H. (1987). Thermobarometry and barometry of igneous and metamorphic rocks. *Annual Reviews in Earth and Planetary Sciences*, *15*, 397-420.

Bonamici, C. E., Fanning, C. M., Kozdon, R., Fournelle, J. H., & Valley, J. W. (2015). Combined oxygen-isotope and U-Pb zoning studies of titanite: New criteria for age preservation. *Chemical Geology*, *398*, 70-84. https://doi.org/10.1016/j.chemgeo.2015.02.002

Bonamici, C. E., Kozdon, R., Ushikubo, T., & Valley, J. W. (2014). Intragrain oxygen isotope zoning in titanite by SIMS: Cooling rates and fluid infiltration along the CarthageColton Mylonite Zone, Adirondack Mountains, NY, USA. *Journal of Metamorphic Geology*, *32*(1), 71-92. https://doi.org/10.1111/jmg.12059

Borradaile, G. J., & Werner, T. (1994). Magnetic anisotropy of some phyllosilicates. *Tectonophysics*, *235*(3), 223-248. https://doi.org/10.1016/0040-1951(94)90196-1

Bossi, J., & Campal, N. (1992). Magmatismo y tectónica transcurrente durante el Paleozoico inferior del Uruguay. In

J. Gutiérrez, J. Saavedr, & I. Rábano (eds.), *Paleozoico Inferior de Ibero-América* (pp. 343-356). Universidad de Extremadura, Alicante.

Bott, M. (1959). The mechanics of oblique slip faulting. *Geological Magazine*, *96*(2), 109. https://doi.org/10.1017/S0016756800059987

Bouchez, J. L., Delas, C., Gleizes, G., & Nédélec, A. (1992) Submagmatic microfractures in granites. *Geology*, *20*(1), 35-38. https://doi.org/10.1130/0091-7613(1992)020<0035:SMIG>2.3.CO;2

Brandon, M. T., & Vance, J. A. (1992). Tectonic evolution of the Cenozoic Olympic subduction complex, Washington State, as deduced from fission track ages for detrital zircons. *American Journal of Science*, *292*(8), 565-636.

Brodie, K., Fettes, D., Harte, B., & Schmid, R. (2007). *Structural terms including fault rock terms.* From IUGS Subcomission on the Systematics of Metamorphic Rocks (SCMR).

Brown, M., & Solar, G. S. (1998). Shear-zone systems and melts: Feedback relations and self-organization in orogenic belts. *Journal of Structural Geology*, *20*(2-3), 211-227. https://doi.org/10.1016/S0191-8141(97)00068-0

Brown, M., & Solar, G. S. (1999). The mechanism of ascent and emplacement of granite magma during transpression: A syntectonic paradigm. *Tectonophysics*, *312*(1), 1-33. https://doi.org/10.1016/S0040-1951(99)00169-9

Bull, W. B. (2007). *Tectonic geomorphology of mountains: A new approach to paleoseismology*. Blackwell Publishing. https://doi.org/10.1016/S0040-1951(99)00169-9

Burkhard, M. (1993). Calcite twin, their geometry, appearance and significance as strain-stress markers and indicators of tectonic regime: A review. *Journal of Structural Geology*, *15*(3-5), 351-368. https://doi.org/10.1016/0191-8141(93)90132-T

Burrbank, D. W., & Anderson, R. S. (2011). *Tectonic geomorphology* (2nd ed.). Wiley-Blackwell.

Caine, J. S., Coates, D. R., Timoffeef, N. P., & Davis, W. D. (1991). Hydrogeology of the Northern Shawangunk Mountains. *New York State Open-File Report* 1, 806.

Caine, J. S., Evans, J. P., & Forster, C. B. (1996). Fault zone architecture and permeability structure. *Geology*, *24*(11), 1025-1028. https://doi.org/10.1130/0091-7613(1996)024<1025:FZAAPS>2.3.CO;2

Calzolari, G., Rossetti, F., Ault, A. K., Lucci, F., Olivetti, V., & Nozaem, R. (2018). Hematite (U-Th)/He thermochronometry constrains strike-slip faulting on the Kuh-e-Faghan fault, central Iran. *Tectonophysics*, *728-729*, 41-54. https://doi.org/10.1016/j.tecto.2018.01.023

Cao, S., Neubauer, F., Liu, J., Bernroider, M., Cheng, X., Li, J., Yu, Z., & Genser, J. (2017). Rheological weakening of high-grade mylonites during low-temperature retrogression: The exhumed continental Ailao Shan-Red River fault zone, SE Asia. *Journal of Earth Sciences*, *139*, 40-60. https://doi.org/10.1016/j.jseaes.2016.10.002

Carreras, J., Cosgrove, J. W., & Druguet, E. (2013). Strain partitioning in banded and/or anisotropic rocks: Implications for inferring tectonic regimes. *Journal of Structural Geology*, *50*, 7-21. https://doi.org/10.1016/j.jsg.2012.12.003

Casas, A., Peña, I., & Simón, J. (1990). Los métodos de análisis de paleoesfuerzos a partir de poblaciones de fallas: Sistemática y técnicas de aplicación. *Estudios Geológicos*, *46*(5-6), 385-398. https://doi.org/10.3989/egeol.90465-6469

Cassata, W. S., Renne, P. R., & Shuster, D. L. (2009). Argon diffusion in plagioclase and implications for thermochronometry: A case of study from the Bushveld Complex, South Africa. *Geochimica et Cosmochimica Acta*, *73*(21), 6600-6612. https://doi.org/10.1016/j.gca.2009.07.017

Cavalcante, C., Lagoeiro, L., Fossen, H., Egydio Silva, M., Morales, L. F. G., Ferrerira, F., & Conte, T. (2018). Temperature constraints on microfabric patterns in quartz-ofeldsphatic mylonites, Ribeira belt (SE Brazi). *Journal of Structural Geology*, *115*, 243-262. https://doi.org/10.1016/j.jsg.2018.07.013

Célérier, B. (1988). How much does slip on a reactived fault plane constrain the stress tensor? *Tectonics*, *7*(6), 1257-1278. https://doi.org/10.1029/TC007i006p01257

Cello, G. (1997). Fractal analysis of a Quaternary fault array in the central Apennines, Italy. *Journal of Structural Geology*, *19*(7), 945-953. https://doi.org/10.1016/s0191-8141(97)00024-2

Chan, Y.-C., Crespi, J. M., & Hodges, K. V. (2000). Dating cleavage formation in slates and phyllites with the $^{40}Ar/^{39}Ar$ laser microprobe: An example from the western New England Appalachians, USA. *Terra Nova*, *12*(6), 264-271. https://doi.org/10.1046/j.1365-3121.2000.00308.x

Chen, C.-L., & Thomson, R. C. (2010). The combined use of EBSD and EDX analyses for the identification of complex intermetallic phases in multicomponent Al-Si piston alloys. *Journal of Alloys and Compounds*, *490*(1-2), 293-300. https://doi.org/10.1016/j.jallcom.2009.09.181

Chen, R.-F., Lin, C.-W., Chen, Y.-H., He, T.-C., & Fei, L.-Y. (2015). Detecting and characterizing active thrust fault and deep-seated landslides in dense forest areas of southern Taiwan using airborne LiDAR DEM. *Remote Sensing*, *7*(11), 15443-15466. https://doi.org/10.3390/rs71115443

Cherniak, D. J. (1995). Diffusion of lead in plagioclase and K-feldspar: An investigation using Rutherford backscattering and resonant nuclear reaction analysis. *Contributions to Mineralogy and Petrology*, *120*, 358-371. https://doi.org/10.1007/BF00306513

Cherniak, D. J., & Watson, E. B. (2000). Pb diffusion in zircon. *Chemical Geology*, *172*(1-2), 5-24. https://doi.org/10.1016/S0009-2541(00)00233-3

Cherniak, D. J., Watson, E. B., Grove, M., & Harrison, T. M. (2004). Pb diffusion in monazite: A combined RBS/SIMS study. *Geochimica et Cosmochimica Acta*, *68*(4), 829-840. https://doi.org/10.1016/j.gca.2003.07.012

Chester, F. M., & Chester, J. S. (1998). Ultracataclasite structure and friction processes of the Punchbowl fault, San Andreas system, California. *Tectonophysics 295*(1-2), 199-221. https://doi.org/10.1016/S0040-1951(98)00121-8

Chester, F. M., Chester, J. S., Kirschner, D. L., Schulz, S. E., & Evans, J. P. (2004). Structure of large-displacement, strike-slip fault zones in the brittle continental crust. In G. D. Karner, B. Taylor, N. W. Driscoll, & D. L. Kohlstedt (eds.), *Rheology and deformation in the lithosphere at continental margins*. Columbia University Press.

Chester, F. M., Evans, J. P., & Biegel, R. L. (1993). Internal structure and weakening mechanisms of the San Andreas fault. *Journal of Geophysical Research*, *98*(B1), 771-786. https://doi.org/10.1029/92JB01866

Chester, F. M., Friedman, M., & Logan, J. M. (1985). Foliated cataclasites. *Tectonophysics*, *111*(1-2), 139-146. https://doi.org/10.1016/0040-1951(85)90071-X

Chester, F. M., & Logan, J. M. (1986). Composite planar fabric of gouge from the Punchbowl fault zone, California. *Journal of Structural Geology*, *9*(5-6), 621-634. https://doi.org/10.1016/0191-8141(87)90147-7

Chetty, T. R. K. (2014). Deep crustal shear zones in the Eastern Ghats Mobile Belt, India: Gondwana correlations. *The Journal Indian Geophysical Union*, *18*(1), 19-56.

Childs, C., Nicol, A., Walsh, J. J., & Watterson, J. (1996). Growth of vertically segmented normal faults. *Journal of Structural Geology*, *18*(12), 1389-1397. https://doi.org/10.1016/S0191-8141(96)00060-0

Choi, J., Edwards, P., Ko, K., & Kim, Y. (2016). Definition and classification of fault damage zones: A review and a new methodological approach. *Earth-Science Reviews*, *152*, 70-87. https://doi.org/10.1016/j.earscirev.2015.11.006

Clemens, J. D., & Mawer, C. K. (1992). Granitic magma transport by fracture propagation. *Tectonophysics*, *204*(3-4), 339-360. https://doi.org/10.1016/0040-1951(92)90316-X

Clerc, C., Jolivet, L., & Ringenbach, J.-C. (2015). Ductile extensional shear zones in the lower crust of a passive margin. *Earth and Planetary Science Letters*, *431*, 1-7. https://doi.org/10.1016/j.epsl.2015.08.038

Cocherie, A., Be Mezeme, E., Legendre, O., Fanning, C. M., Faure, M., & Rossi, P. (2005). Electron-microprobe dating as a tool for determining the closure of Th-U-Pb systems in migmatitic monazites. *American Mineralogist*, *90*(4), 607-618. https://doi.org/10.2138/am.2005.1303

Colgan, J. P., Shuster, D. L., & Reiners, P. W. (2008). Two-phase Neogene extension in the northwestern basin and range recorded in a single thermochronology sample. *Geology*, *36*(8), 631-634. https://doi.org/10.1130/G24897A.1

Collett, C. M., Duvall, A. R., Flowers, R. M., Tucker, G. E., & Upton, P. (2019). The timing and style of oblique deformation within New Zealand's Kaikōura ranges and Marlborough fault system based on low-temperature thermochronology. *Tectonics*, *38*(4), 1250-1272. https://doi.org/10.1029/2018TC005268

Conte, T., Cavalcante, C., Lagoeiro, L. E., Fossen, H., & Silveira, C. S. (2020). Quartz textural analysis from an anastomosing shear zone system: Implications for the tectonic evolution of the Ribeira belt, Brazil. *Journal of South American Earth Sciences*, *103*, 102750. https://doi.org/10.1016/j.jsames.2020.102750

Connolly, J. A. D. (2005). Computation of phase equilibria by linear programming: A tool for geodynamic modeling and its application to subduction zone decarbonation. *Earth and Planetary Science Letters*, *236*(1-2), 524-541. https://doi.org/10.1016/j.epsl.2005.04.033

Connolly, J. A. D. (2009). The geodynamic equation of state: What and how. *Geochemistry, Geophysics, Geosystems*, *10*(10). https://doi.org/10.1029/2009GC002540

Cooperdock, E. H., & Stockli, D. F. (2016). Unraveling alterations histories in serpentinites and associated ultramafic rocks with magnetite (U-Th)/He geochronology. *Geology*, *44*(11), 967-970. https://doi.org/10.1130/G38587.1

Cosca, M., Stünitz, H., Bourgeix, A.-L., & Lee, J. P. (2011). Ar* loss in experimentally deformed muscovite and biotite with implications for $^{40}Ar/^{39}Ar$ geochronology of naturally deformed rocks. *Geochimica et Cosmochimica Acta*, *75*(24), 7759-7778. https://doi.org/10.1016/j.gca.2011.10.012

Cosca, M. A., Caby, P., & Bussya, F. (2005). Geochemistry and $^{40}Ar/^{39}Ar$ geochronology of pseudotachylite associated with UHP whiteschists from the Dora Maira massif, Italy. *Tectonophysics*, *402*(1-2), 93-110. https://doi.org/10.1016/j.tecto.2004.12.033

Cox, S. F., Knackstedt, M. A., & Braun, J. (2001). Principles of structural control on permeability and fluid flow in hydrothermal systems. In J. P. Richards, & R. M. Tosdal (eds.), *Reviews in Economic Geology*, *vol. 14, Structural controls on ore genesis*. Society of Economic Geologists. https://doi.org/10.5382/Rev.14.01

Crone, A. J., & Omdahl, E. M. (1987). *Directions in Paleoseismology*. U. S. Geological Survey, New Mexico.

Cross, A. J., Kidder, S., & Prior, D. J. (2015). Using microstructures and TitaniQ thermobarometry of quartz sheared around garnet porphyroclasts to evaluate microstructural evolution and constrain an Alpine fault zone geotherm. *Journal of Structural Geology*, *75*, 17-31. https://doi.org/10.1016/j.jsg.2015.02.012

Curry, M. A. E., Barnes, J. B., & Colgan, J. P. (2016). Testing fault growth models with low-temperature thermochronology in the northwest basin and range, USA. *Tectonics*, *35*(10), 2467-2492. https://doi.org/10.1002/2016TC004211

D'Lemos, R. S., Brown, M., & Strachan R. A. (1992). Granite magma generation, ascent and emplacement with a transpresional orogen. *Journal of the Geological Society*, *149*(4), 487-490. https://doi.org/10.1144/gsjgs.149.4.0487

Dahl, P. S. (1997). A crystal-chemical basis for Pb retention and fission-track annealing systematics in U-bearing minerals, with implications for geochronology. *Earth and Planetary Science Letters*, *150*(3-4), 277-290. https://doi.org/10.1016/S0012-821X(97)00108-8

Dahl, P. S., Terry, M. P., Jercinovic, M. J., Williams, M. L., Hamilton, M. A., Foland, K. A., Clement, S. M., & Friberg, L. M. (2005). Electron probe (ultrachron) micronometry of metamorphic monazite: Unraveling the timing of polyphase thermotectonism in the easternmost Wyoming craton (Black Hills, South Dakota). *American Mineralogist*, *90*(11-12), 1712-1728. https://doi.org/10.2138/am.2005.2002

Davids, C., Wemmer, K., Zwingmann, H., Kohlmann, F., Jacobs, J., & Bergh, S. G. (2013). K-Ar illite and apatite fission track constraints on brittle faulting and the evolution of the northern Norwegian passive margin. *Tectonophysics*, *608*, 196-211. https://doi.org/10.1016/j.tecto.2013.09.035

Davis, G. H., & Reynolds, S. J. (1996). *Structural Geology of Rocks and Regions* (2nd ed.). Wiley.

Davis, G. H., Reynolds, S. J., & Kluth, C. F. (2011). *Structural Geology of rocks and regions* (3rd ed). Jhon Wiley & Sons, INC.

De Capitani, C., & Petrakakis, K. (2010). The computation of equilibrium assemblage diagrams with Theriak/Domino software. *American Mineralogist*, *95*(7), 1006-1016. https://doi.org/10.2138/am.2010.3354

Delvaux, D. (2012). Release of program Win-Tensor 4.0 for tectonic stress inversión: statistical expression of stress parameters. EGU General Assembly, Vienna. *Geophysical Research Abstracts*, *14*, EGU2012-5899.

Delvaux, D., Kervyn, F., Macheyeki, A. S., & Temu, E. B. (2012). Geodynamic significance of the TRM segment in the East African Rift (W-Tanzania): Active tectonics and paleostress in the Ufipa plateau and Rukwa basin. *Journal of Structural Geology*, *37*, 161-180. https://doi.org/10.1016/j.jsg.2012.01.008

Delvaux, D., & Sperner, B. (2003). *New aspects of tectonic stress inversion with reference to the Tensor program* (pp. 75-100). Special Publications vol. 212. Geological Society of London. https://doi.org/10.1144/GSL.SP.2003.212.01.06

Desbois, G., Hemes, S., Laurich, B., Houben, M., Klaver, J., Hohne, N., Urai, J. L., VIggiani, G., & Bésuelle, P. (2016). Investigation of microstructures in naturally and experimentally deformed reference clay rocks using innovative methods in scanning electron microscopy. *The Clay Minerals Society Workshop Lectures Series, 21*(1), 1-14. https://doi.org/10.1346/CMS-WLS-21.1

Despaigne Díaz, A. I., & Cáceres, D. G. (2009). Las maclas de calcita en los metacarbonatos: Significado tectónico y su empleo para la determinación de temperaturas de deformación. *Minería y Geología*, *25*(2), 1-31.

Dichiarante, A. M., Holdsworth, R. E., Dempsey, E. D., Selby, D., McCaffrey, K. J. W., Michie, U. M., Morgan, G., & Bonniface, J. (2016). New structural and Re-Os geochronological evidence constraining the age of faulting and associated mineralization in the Devonian Orcadian basin, Scotland. *Journal of the Geological Society*, *173*(3), 457-473. https://doi.org/10.1144/jgs2015-118

Di Vincenzo, G., Rocchi, S., Rossetti, F., & Storti, F. (2004). ^{40}Ar-^{39}Ar dating of pseudotachylytes: the effect of clast-hosted extraneous argon in Cenozoic fault-generated friction melts from the West Antarctic Rift System. *Earth and Planetary Science Letters*, *223*(3-4), 349-364. https://doi.org/10.1016/j.epsl.2004.04.042

Di Vincenzo, G., Rossetti, F., Viti, C., & Balsamo, F. (2013). Constraining the timing of fault reactivation: Eocene coseismic slip along a Late Ordovician ductile shear zone (northern Victoria Land, Antarctica). *Geological Society of America Bulletin*, *125*(3-4), 609-624. https://doi.org/10.1130/B30670.1

Doblas, M. (1998). Slickenside kinematic indicators. *Tectonophysics*, *295*(1-2), 187-197. https://doi.org/10.1016/S0040-1951(98)00120-6

Doblas, M., Mahecha, V., Hoyos, M., & López Ruiz, J. (1997). Slickenside and fault surface kinematic indicators on active normal faults of the Alpine Betic cordilleras, Granada, southern Spain. *Journal of Structural Geology*, *19*(2), 159-170. https://doi.org/10.1016/S0191-8141(96)00086-7

Dressel, B. C., Chauvet, A., Trzaskos, B., Biondi, J. C., Bruguier, O., Monié, P., Villavona, S. N., & Newton, J. B. (2018). The Passa Três lode gold deposit (Paraná State, Brazil): An example of structurally-controlled mineralization formed during magmatic-hydrothermal transition and hosted within granite. *Ore Geology Reviews*, *102*, 701-727. https://doi.org/10.1016/j.oregeorev.2018.09.007

Druguet, E., Carreras, J., & Mezger, J. E. (2018). Discussion on 'Middle Jurassic shear zones at Cap de Creus (eastern Pyrenees, Spain): a record of pre-drift extension of the Piemonte-Ligurian Ocean?' Journal of the Geological Society, London, 174, 289-300. *Journal of the Geological Society*, *175*(1), 187-188. https://doi.org/10.1144/jgs2017-042

Druguet, E., & Hutton, D. (1998). Syntectonic anatexis and magmatism in a mid-crustal transpresional shear zone: An example from the Hercynian rocks of the eastern Pyrenees. *Journal of Structural Geology*, *20*(7), 905-916. https://doi.org/10.1016/S0191-8141(98)00017-0

Duba, A. G., Durham, W. B., Handin, J. W., & Wang, H. F. (1990). *The brittle-ductile transition in rocks*. Geophysical Monograph Series 56. https://doi.org/10.1029/GM056

Dunlap, W. J. (1997). Neocrystallization or cooling? $^{40}Ar/^{39}Ar$ ages of white micas from low-grade mylonites. *Chemical Geology*, *143*(3-4), 181-203. https://doi.org/10.1016/S0009-2541(97)00113-7

Duval, M. (2018). Sobre el potencial de la resonancia paramagnética electrónica como herramienta geocronológica en contextos geoarqueológicos: Un resumen de 30 años de investigación en la península ibérica. *Boletín Geológico y Minero*, *1129*(1-2), 35-57. https://doi.org/10.21701/bolgeomin.129.1.002

Duval, M., Moreno, D., Shao, Q., Voinchet, P., Falguères, C., Bahain, J. J., García, T., García, J., & Martínez, K. (2011). Datación por ESR del yacimiento arqueológico del Pleistoceno inferior de Vallparadís (Terrassa, Cataluña, España). *Trabajos de Prehistoria*, *68*(1), 7-24. https://doi.org/10.3989/tp.2011.11056

Duvall, A. R., Clark, M. K., Van del Plujim, B. A., & Li, C. (2011). Direct dating of Eocene reverse faulting in northeastern Tibet using Ar-dating of fault clays and low-temperature thermochronometry. *Earth and Planetary Science Letters*, *304*(3-4), 520-526. https://doi.org/10.1016/j.epsl.2011.02.028

Eberlei, T., Habler, G., Wegner, W., Schuster, R., Körner, W., Thöni, M., & Abart, R. (2015). Rb/Sr isotopic and compositional retentivity of muscovite during deformation. *Lithos*, *227*, 161-178. https://doi.org/10.1016/j.lithos.2015.04.007

Ehlers, T. A., & Farley, K. A. (2003). Apatite (U-Th)/He thermochronometry: Methods and applications to problems in tectonics and surface processes. *Earth and Planetary Science Letters*, *206*(1-2), 1-14. https://doi.org/10.1016/S0012-821X(02)01069-5

Engelder, J. T. (1974). Cataclasis and the generation of fault gouge. *GSA Bulletin*, *85*(10), 1515-1522. https://doi.org/10.1130/0016-7606(1974)85<1515:CATGOF>2.0.CO;2

Erickson, T. M., Pearce, M. A., Taylor, R. J. M., Timms, N. E., Clark, C., Reddy, S. M., & Buick, I. S. (2015). Deformed monazite yields high-temperature tectonic ages. *Geology*, *43*(5), 383-386. https://doi.org/10.1130/G36533.1

Essene, E. J. (1989). The current status of thermobarometry in metamorphic rocks. In J. S. Daly, R. A. Cliff, & B. W. D. Yardley (eds.). *Evolution of metamorphic belts* (pp. 1-44.). Special Publication, vol. 43. Geological Society of London. https://doi.org/10.1144/GSL.SP.1989.043.01.02

Evenson, N. S., Reiners, P. W., Spencer, J., & Shuster, D. L. (2014). Hematite and Mn oxide (U-Th)/He dates from the Buckskin-Rawhide detachment system, western Arizona: Constraining the timing of mineralization and hematite (U-Th)/He systematics. *American Journal of Science*, *314*(10), 1373-1435. https://doi.org/10.2475/10.2014.01

Faleiros, F. M., Campanha, G. A. C., Bello, R. M. S., & Fuzikawa, K. (2010). Quartz recrystallization regimes, c-axis texture transitions and fluid inclusion reequilibration in a prograde greenschist to amphibolite facies mylonite zone (Ribeira Shear Zone, SE Brazil). *Tectonophysics*, *485*(1-4), 193-214. https://doi.org/10.1016/j.tecto.2009.12.014

Farley, K. A. (2000). Helium diffusion from apatite: General behavior as illustrated by Durango fluorapatite. *Journal Geophysical Research*, *105*(B2), 2903-2914. https://doi.org/10.1029/1999JB900348

Farley, K. A., & Flowers, R. M. (2012). (U-Th)/Ne and multidomain (U-Th)/He systematics of a hydrothermal hematite from eastern Grand Canyon. *Earth and Planetary Science Letters*, *359-360*, 131-140. https://doi.org/10.1016/j.epsl.2012.10.010

Farley, K. A., & McKeon, R. E. (2015). Radiometic dating and temperature history of banded iron formation-associated hematite, Gogebic iron range, Michigan, USA. *Geology*, *43*(12), 1083-1086. https://doi.org/10.1130/G37190.1

Faulkner, D. R., Jackson, C. A. L., Lunn, R. J., Schlische, R. W., Shipton, Z. K., Wibberley, C. A. J., & Withjack, M. O. (2010). A review of recent developments concerning the structure, mechanics and fluid flow properties of fault zones. *Journal Structural Geology*, *32*(11), 1557-1575. https://doi.org/10.1016/j.jsg.2010.06.009

Ferrill, D. A. (1991). Calcite twin widths and intensities as metamorphic indicators in natural low temperature deformation in limestone. *Journal of Structural Geology*, *13*(6), 667-675. https://doi.org/10.1016/0191-8141(91)90029-I

Ferrill, D. A., Morris, A. P., Evans, M. A., Burkhard, M., Groshong, R. H., & Onasch, C. M. (2004). Calcite twin morphology: A low temperature deformation geothermometer. *Journal of Structural Geology*, *26*(8), 1521-1529. https://doi.org/10.1016/j.jsg.2003.11.028

Fitz-Díaz, E., & van der Plujim, B. (2013). Fold dating: A new Ar/Ar illite dating application to constrain the age of deformation in shallow crustal rocks. *Journal of Structural Geology*, *54*, 174-179. https://doi.org/10.1016/j.jsg.2013.05.011

Flinn, D. (1979). The deformation matrix and the deformation ellipsoid. *Journal of Structural Geology*, *1*(4), 299-307. https://doi.org/10.1016/0191-8141(79)90004-X

Forero-Ortega, A. J., Campanha, G. A. C., Faleiros, F. M., & Yogi, M. T. A. G. (2020). Pure shear-dominated transpression and vertical extrusion in a strike-slip fault splay from the Itapirapuã Shear Zone, Ribeira Belt, Brazil. *Tectonophysics*, *786*, 228455. https://doi.org/10.1016/j.tecto.2020.228455

Fossen, H. (2013). *Structural geology*. Cambridge University Press.

Fossen, H., & Cavalcante, G. C. G. (2017). Shear zones: A review. *Earth-Science Reviews*, *171*, 434-455. https://doi.org/10.1016/j.earscirev.2017.05.002

Fossen, H., & Dunlap, W. J. (1998). Timing and kinematics of Caledonian thrusting and extensional collapse, southern Norway: evidence from 40Ar/39Ar thermochronology. *Journal of Structural Geology*, *20*(6), 765-781. https://doi.org/10.1016/S0191-8141(98)00007-8

Fossen, H., & Tikoff, B. (1997). Forward modeling of non-steady-state deformations and the "minimum strain path". *Journal of Structural Geology*, *19*(7), 987-996. https://doi.org/10.1016/S0191-8141(97)00021-7

Freeman, S. B., Butler, R. W. H., Cliff, R. A., & Rex, D. C. (1998). Direct dating of mylonite evolution: A multi-disciplinary geochronological study from the Moine thrust zone, NW Scotland. *Journal of the Geological Society*, *155*(5), 745-758. https://doi.org/10.1144/gsjgs.155.5.0745

Fry, N. (2001). Stress space: Striated fault, deformation twins and their constraints on paleostress. *Journal of Structural Geology*, *23*(1), 1-9. https://doi.org/10.1016/S0191-8141(00)00136-X

Gabrielsen, R. H., & Braathen, A. (2014). Models of fracture lineaments: Joints swarms, fracture corridor and faults in crystalline rocks, and their generic relations. *Tectonophysics*, *628*, 26-44. https://doi.org/10.1016/j.tecto.2014.04.022

Gabrielsen, R. H., Braathen, A., & Ganerød, M. (2008). *A reactivated fault system of southern Norway: How far east did the Mesozoic extension reach?* International Geological Congress, Oslo, 4-15 August. Key note lecture, 33.

Gannouni, S., & Gabtni, H. (2015). Structural interpretation of lineaments by satellite image processing (Landsat TM) in the region of Zahret Medien (Northern Tunisia). *Journal of Geographic Information System*, *7*(2), 119-127. https://doi.org/10.4236/jgis.2015.72011

García, D. A. C. (2011). *Caracterización de la deformación y metamorfismo de los esquistos de Sabaletas, parte norte de la cordillera Central de Colombia* (Master thesis). Universidad Nacional de Colombia, Medellín.

García, V. H., Reiners, P. W., Shuster, D. L., Idleman, B. D., & Zeitler, P. K. (2018). Thermochronology of sandstone-hosted secondary Fe- and Mn-oxides near Moab, Utah: Record of paleo-fluid flow along a fault. *GSA Bulletin*, *130*(1-2), 93-113. https://doi.org/10.1130/B31627.1

Giraldo, S. J., Trouw, R. A. J., Duffles, P., Vinagre, R., Mejía, M. I., & Marimon, R. S. (2019). Structural analysis combined with new geothermobarometric and geochronological results of the Além Paraíba shear zone, between Três Rios and Bananal, Ribeira Orogen, SE Brazil. *Journal of South American Earth Sciences*, *90*, 118-136. https://doi.org/10.1016/j.jsames.2018.11.018

Goodfellow, B. W., Viola, G., Bingen, B., Nuriel, P., & Kylander Clark, A. R. (2017). Paleocene faulting in SE Sweden from U-Pb dating of slickenfibre calcite, *Terra Nova*, *29*(5), 321-328, 2017. https://doi.org/10.1111/ter.12280

Gorynski, K. E., Walker, J. D., Stockli, D. F., & Sabin, A. (2014). Apatite (U-Th)/He thermochronometry as an innovative geothermal exploration tool: A case study from the southern Wassuk range, Nevada. *Journal of Volcanology and Geothermal Research*, *270*, 99-114. https://doi.org/10.1016/j.jvolgeores.2013.11.018

Goswami, S., Mamtani, M. A., & Rana, V. (2018). Quartz CPO and kinematic analysis in deformed rocks devoid of visible stretching lineations: An integrated AMS and EBSD investigation. *Journal of Structural Geology*, *115*, 270-283. https://doi.org/10.1016/j.jsg.2018.04.008

Grauch, V., & Hudson, M. R. (2007). Guides to understanding the aeromagnetic expression of faults in sedimentary basins: Lessons learned from the central Rio Grande rift, New Mexico. *Geophere*, *3*(6), 596-623. https://doi.org/10.1130/GES00128.1

Grégoire, V., Nédélec, A., Monié, P., Montel, J.-M., Ganne, J., & Ralison, B. (2009). Structural reworking and heat transfer related to the late-Panafrican Angavo shear zone of Madagascar. *Tectonophysics*, *477*(3-4), 197-216. https://doi.org/10.1016/j.tecto.2009.03.009

Grocott, J., & Taylor, G. K. (2002). Magmatic arc fault systems, deformation partitioning and emplacement of granitic complexes in the Coastal Cordillera, north Chilean Andes (25° 30' S to 27°00' S). *Journal of the Geological Society*, *159*(4), 425-442. https://doi.org/10.1144/0016-764901-124

Grujic, D., Stipp, M., & Wooden, J. L. (2011). Thermometry of quartz mylonites: Importance of dynamic recrystallization on Ti-in-quartz reequilibration. *Geochemistry, Geophysics, Geosystems*, *12*(6), Q06012. https://doi.org/10.1029/2010GC003368

Grün, R. (1989). Electron spin resonance (ESR) dating. *Quaternary International*, *1*, 65-109. https://doi.org/10.1016/1040-6182(89)90010-4

Gudmundsson, A., Simmenes, T. H., Larsen, B., & Philipp, S. L. (2010). Effects of internal structure and local stresses on fracture propagation, deflection, and arrest in Fault zones. *Journal Structural Geology*, *32*(11), 1643-1655. https://doi.org/10.1016/j.jsg.2009.08.013

Gumbsch, P. (2001). Modelling brittle and semi-brittle fracture processes. *Materials Science and Engineering*, *A*(319-321), 1-7. https://doi.org/10.1016/S0921-5093(01)01062-0

Gunn, P., Maidment D., & Milligan. P. (1997). Interpreting aeromagnetic data in areas of limited outcrop. *AGSO Journal of Australian Geology and Geophysics*, *17*(2), 175-186.

Hadizadeh, J., & Tullis, J. (1992). Cataclastic flow and semi-brittle deformation of anorthosite. *Journal of Structural Geology*, *14*(1), 57-63. https://doi.org/10.1016/0191-8141(92)

Haines, S., & van der Pluijm, B. (2008). Clay quantification and Ar-Ar dating of synthetic and natural gouge: Application to the Miocene Sierra Mazatán detachment fault, Sonora, Mexico. *Journal of Structural Geology*, *30*(4), 525-538. https://doi.org/10.1016/j.jsg.2007.11.012

Haines, S. H., Kaproth, B., Marone, C., Saffer, D., & van der Pluijm, B. (2013). Shear zones in clay-rich fault gouge: A laboratory study of fabric development and evolution. *Journal of Structural Geology*, *51*, 206-225. https://doi.org/10.1016/j.jsg.2013.01.002

Hammarstrom, J. M., & Zen, E. A. (1986). Aluminum in hornblende: An empirical geobarometer. *American Mineralogist*, *71*(11-12), 1297-1313.

Hames, W. E., & Bowring, S. A. (1994). An empirical evaluation of the Ar diffusion geometry in muscovite. *Earth and Planetary Science Letters*, *124*(1-4), 161-167. https://doi.org/10.1016/0012-821X(94)00079-4

Hancock, P. L. (1985). Brittle microtectonics Principles and practice. *Journal of Structural Geology*, *7*(3-4), 437-457. https://doi.org/10.1016/0191-8141(85)90048-3

Hanmer, S. (1988). Great Slave Lake shear zone, Canadian Shield: Reconstructed vertical profile of a crustal-scale fault zone. *Tectonophysics*, *149*(3-4), 245-264. https://doi.org/10.1016/0040-1951(88)90176-X

Hanmer, S. (1989). Initiation of cataclastic flow in a mylonite zone. *Journal of Structural Geology*, *11*(6), 751-762. https://doi.org/10.1016/0191-8141(89)90009-6

Hardcastle, K. C. (1989). Possible paleostress tensor configurations derived from fault-slip data in eastern Vermont and western New Hampshire. *Tectonics*, *8*(2), 265-284. https://doi.org/10.1029/TC008i002p0026

Harley, S. L., Kelly, N. M., & Möller, A. (2007). Zircon behavior and the thermal histories of mountain chains. *Elements*, *3*(1), 25-30. https://doi.org/10.2113/gselements.3.1.25

Harlov, D. (2015). Fluids and geochronometers: Charting and dating mass transfer during metasomatism and metamorphism. *Journal of Indian Institute of Science*, *95*(2), 109-123.

Harrison, T. M., Célérier, J., Aikman, A. B., Hermann, J., & Heizler, M. T. (2009). Diffusion of ^{40}Ar in muscovite. *Geochimica et Cosmochimica Acta*, *73*(4), 1039-1051. https://doi.org/10.1016/j.gca.2008.09.038

Hatcher, R. D. (1995). *Structural Geology: Principles, concepts, and problems*. Prentice Hall.

Hausegger, S., & Kurz, W. (2013). Cataclastic faults along the SEMP fault system (Eastern Alps, Austria): A contribution to fault zone evolution, internal structure and paleo-stresses. *Tectonophysics*, *608*, 237-251. https://doi.org/10.1016/j.tecto.2013.09.032

Heineke, C., Hetzel, R., Nilius, N. P., Zwingmann, H., Todd, A., Mulch, A., Wölfler, A., Glotzbach, C., Akal, C., & Dunkl, I. (2019). Detachment faulting in a divergent core complex constrained by fault gouge dating and low-temperature thermochronology. *Journal of Structural Geology*, *127*, 103865. https://doi.org/10.1016/j.jsg.2019.103865

Hickey, K. A., Barker, S. L. L., Dipple, G. M., Arehart, G. B., & Donelick, R. A. (2014). The brevity of hydrothermal fluid flow revealed by thermal halos around giant gold deposits: Implications for Carlin-type gold systems. *Economic Geology*, *109*(5), 1461-1487. https://doi.org/10.2113/econgeo.109.5.1461

Higgins, M. W. (1971). *Cataclastic rocks*. Geological Survey Professional Paper, 687. United States Government Printing Office. Library of Congress catalog-card No. 71-611932. Washington.

Hills, S. (1972). *Elements of structural geology*. Chapman and Hall Ltd. https://doi.org/10.1007/978-94-009-5843-2

Hippertt, J., Lana, C., & Takeshita, T. (2001). Deformation partitioning during folding of banded iron formation. *Journal of Structural Geology*, *23*(5), 819-834. https://doi.org/10.1016/S0191-8141(00)00128-0

Hippertt, J., Rocha, A., Lana, C., Egydio Silva, M., & Takeshita, T. (2001). Quartz plastic segregation and ribbon development in high-grade stripped gneisses. *Journal of Structural Geology*, *23*(1), 67-80. https://doi.org/10.1016/S0191-8141(00)00129-2

Hippertt, J. F., & Massucatto, A. J. (1998). Phyllonitization and development of kilometer-size extension gashes in a continental-scale strike-slip shear zone, north Goiás, central Brazil. *Journal of Structural Geology*, *20*(4), 433-445. https://doi.org/10.1016/S0191-8141(97)00106-5

Hnat, J. S., & van der Pluijm, B. A. (2014). Fault gouge dating in the Southern Appalachians, USA. *GSA Bulletin*, *126*(5-6), 639-651. https://doi.org/10.1130/B30905.1

Hodgson, C. J. (1989). The structure of shear-related, vein-type gold deposits: A review. *Ore Geology Reviews*, *4*(3), 231-273. https://doi.org/10.1016/0169-1368(89)90019-X

Hooper, R. J., & Hatcher, R. D. (1988). Mylonite from the Towaliga fault zone, central Georgia: Products of heterogeneous non-coaxial deformation. *Tectonophysics*, *152*(1-2), 1-17. https://doi.org/10.1016/0040-1951(88)90026-1

Hopgood, A. M. (1999). *Determination of structural successions in migmatites and gneisses*. Springer Science + Busines Media, B. V. https://doi.org/10.1007/978-94-011-4427-8

Höeppener, R. (1955). Tektonik im Schiefergebirge. *Geologische Rundschau*, *44*, 26-58. https://doi.org/10.1007/BF01802903

Hueck, M., Wemmer, K., Basei, M. A. S., Philipp, R. P., Oriolo, S., Heidelbach, F., Oyhantçabal, P., & Siegesmund, S. (2020). Dating recurrent shear zone activity and the transition from ductile to brittle deformation: White mica geochronology applied to the Neoproterozoic Dom Feliciano Belt in Sourh Brazil. *Journal of Structural Geology*, *141*, 104-199. https://doi.org/10.1016/j.jsg.2020.104199

Hurford, A. J. (1986). Cooling and uplift patterns in the Lepontine Alps, South Central Switzerland and an age of vertical movement on the Insubric fault line. *Contributions to Mineralogy and Petrology*, *92*, 413-427. https://doi.org/10.1007/BF00374424

Iacopini, D., Passchier, C. W., Koehn, D., & Carosi, R. (2007). Fabric attractors in general triclinic flow systems and their application to high strain shear zones: A dynamical system approach. *Journal of Structural Geology*, *29*(2), 298-317. https://doi.org/10.1016/j.jsg.2006.10.002

Ikeya, M. (ed.). (1993). *New applications of electron spin resonance*. World Scientific. https://doi.org/10.1142/1854

Ikeya, M., Miki, T., & Tanaka, K. (1982). Dating of a fault by electron spin resonance on intrafault materials. *Science*, *215*(4538), 1392-1393. https://doi.org/10.1126/science.215.4538.1392

Jefferies, S. P., Holdsworth, R. E., Wibberley, C. A. J., Shimamoto, T., Spiers, C. J., Niemeijer, A. R., & Lloyd, G. E. (2006).

The nature and importance of phyllonite development in crustal-scale fault cores: an example form the Median Tectonic Line, Japan. *Journal of Structural Geology*, *28*(2), 220-235. https://doi.org/10.1016/j.jsg.2005.10.008

Jelinek, V. (1981). Characterization of the magnetic fabric of rocks. *Tectonophysics*, *79*(3-4), 63-67. https://doi.org/10.1016/0040-1951(81)90110-4

Jenkin, G. R. T. (1997). Mode effects on cooling rate estimates from Rb-Sr data. *Geology*, *25*, 907-910.

Jenkin, G. R. T., Ellam, R. M., Rogers, G., & Stuart, F. M. (2001). An investigation of closure temperature of the biotite Rb-Sr system: The importance of cation exchange. *Geochimica et Cosmochimica Acta*, *65*(7), 1141-1160. https://doi.org/10.1016/S0016-7037(00)00560-3

Jiang, D., & White, J. C. (1995). Kinematic of rock flow and the interpretation of geological structures, with particular reference to shear zones. *Journal of Structural Gelogy*, *17*(9), 1249-1265. https://doi.org/10.1016/0191-8141(95)00026-A

Jiang, Y., Zhao, K., Imber, J., Chen, L., & Hu, H. (2020). Recognizing the internal structure of normal faults in clastic rocks and its impact on hydrocarbon migration: A case study from Nanpu Depression in the Bohai Bay Basin, China. *Journal of Petroleum Science and Engineering*, *184*, 106492. https://doi.org/10.1016/j.petrol.2019.106492

Johansen, S. E., & Fossen, H. (2008). Internal geometry of fault damage zones in interbedded siliciclastic sediments. In W. Kurz, C. A. J. Wibberley, J. Imber, C. Collettini, & R. E. Holdsworth (eds), *The Internal Structure of Fault Zones: Implications for Mechanical and Fluid-Flow Properties* (pp. 35-56), Special Publications vol. 299. Geological Society of London. https://doi.org/10.1144/SP299.3

Johnson, S. E., Lenferink, H. J., Price, N. A., Marsh, J. H., Koons, P. O., West Jr., D. P., & Beane, R. (2009). Clast-based kinematic vorticity gauges: The effects of slip at matrix/clast interfaces. *Journal of Structural Geology*, *31*(11), 1322-1339. https://doi.org/10.1016/j.jsg.2009.07.008

Kadima, E., Delvaux, D., Sebagenzi, S., Tack, L., & Kabeya, S. (2011). Structure and geological history of the Congo Basin: An integrated interpretation of gravity, magnetic and reflection seismic data. *Basin Research*, *23*(5), 499-527. https://doi.org/10.1111/j.1365-2117.2011.00500.x

Keller, E. A., & Pinter, N. (2002). *Active tectonics, earthquakes, uplift and landscape* (2nd ed.), Prentice Hall, Upper Saddle River.

Kelley, S. (2002). K-Ar and Ar-Ar Dating. *Reviews in Mineralogy and Geochemistry*, *47*(1), 785-818. https://doi.org/10.2138/rmg.2002.47.17

Ketcham, R. A., Donelick, R. A., & Carlson, W. D. (1999). Variability of apatite fission-track annealing kinetics. III: Extrapolation to geological time scales. *American Mineralogist*, *84*(9), 1235-1255. https://doi.org/https://doi.org/10.2138/am-1999-0903

Kilian, R., Heilbronner, R., & Stünitz, H. (2011). Quartz grain size reduction in a granitoid rock and the transition from dislocation to diffusion creep. *Journal of Structural Geology*, *33*(8), 1265-1284. https://doi.org/10.1016/j.jsg.2011.05.004

Killick, A. M. (2003). Fault rock classification: An aid to structural interpretation in mine and exploration geology. *South African Journal of Geology*, *106*(4), 394-402. https://doi.org/10.2113/106.4.395

Kim, Y. S., Peacock, D. C. P., & Sanderson, D. J. (2003). Mesoscale strike-slip faults and damage zones at Marsalforn, Gozo Island, Malta. *Journal of Structural Geology*, *25*(5), 793-812. https://doi.org/10.1016/S0191-8141(02)00200-6

Kirkland, C. L., Fougerouse, D., Reddy, S. M., Hollis, J., & Saxey, D. W. (2018a). Assessing the mechanisms of common Pb incorporation into titanite. *Chemical Geology*, *483*, 558-566. https://doi.org/10.1016/j.chemgeo.2018.03.026

Kirkland, C. L., Yakymchuk, C., Szilas, K., Evans, N., Hollis, J., McDonald, B., & Gardiner, N. J. (2018b). Apatite: A U-Pb thermochronometer or geochronometer? *Lithos*, *318-319*, 143-157. https://doi.org/10.1016/j.lithos.2018.08.007

Kirkpatrick, J. D., & Rowe, C. D. (2013). Disappearing ink: How pseudotachylytes are lost from the rock record. *Journal of Structural Geology*, *52*, 183-198. https://doi.org/10.1016/j.jsg.2013.03.003

Kjenes, M. (2018). *The geometry and evolution of deformation bands in volcaniclastic rocks: Insights from Eastern Tawan* (Master thesis). Departamento de Ciencias de la Tierra. Universidad de Bergen.

Kligfield, R., Hunziker, J., Dallmeyer, R. D., & Schamel, S. (1986). Dating of deformation phases using K-Ar and Ar/Ar techniques: Results from the Northern Apennines. *Journal of Structural Geology*, *8*(7), 791-798. https://doi.org/10.1016/0191-8141(86)90025-8

Knipe, R. J. (1989). Deformation mechanisms: Recognition from natural tectonites. *Journal of Structural Geology*, *11*(1-2), 127-146. https://doi.org/10.1016/0191-8141(89)90039-4

Kumerics, C., Ring, U., Brichau, S., Glodny, J., & Monié, P. (2005). The extensional Messaria shear zone and associated brittle detachment faults, Aegean Sea, Greece. *Journal of the Geological Society*, *162*(4), 701-721. https://doi.org/10.1144/0016-764904-041

Lacombe, O. (2012). Do fault slip data inversions actually yield "paleostresses" that can be compared with contemporary stresses? A critical discussion. *Compter Rendus Geoscience*, *344*(3-4), 159-173. https://doi.org/10.1016/j.crte.2012.01.006

Lagroix, F., & Borradaile, G. J. (2000). Magnetic fabric interpretation complicated by inclusions in mafic silicates. *Tectonophysics*, *325*(3-4), 207-255. https://doi.org/10.1016/S0040-1951(00)00125-6

Langille, L., Jessup, M. J., Cottle, J. M., Newell, D., & Seward, G. (2010). Kinematic evolution of the Ama Drime detachment: Insights into orogen-parallel extension and exhumation of the Ama Drime Massif, Tibet-Nepal. *Journal of Structural Geology*, *32*(7), 900-919. https://doi.org/10.1016/j.jsg.2010.04.005

Laslett, G. M., Green, P. F., Duddy, I. R., & Gleadow, A. J. W. (1987). Thermal annealing of fission tracks in apatite. 2. A quantitative analysis. *Chemical Geology*, *65*(1), 1-13. https://doi.org/10.1016/0168-9622(87)90057-1

Launeau, P., & Cruden A. R. (1998). Magmatic fabric acquisition mechanisms in a syenite: Results of a combined anisotropy of magnetic susceptibility and image analysis study. *Journal of Geophysical Research*, *103*(B3), 5067-5089. https://doi.org/10.1029/97JB02670

Launeau, P., & Robin, P. Y. (2005). Determination of fabric and strain ellipsoids from measured sectional ellipses: Implementations and applications. *Journal of Structural Geology*, *27*(12), 2223-2233. https://doi.org/10.1016/j.jsg.2005.08.003

Law, R. D. (1990). Crystallographic fabrics: a selective review of their applications to research in structural geology. In R. J. Knipe, & E. H. Rutter (eds.), *Deformation mechanisms, rheology and tectonics* (pp. 335-352). Special Publication vol. 54. Geological Society of London. https://doi.org/10.1144/GSL.SP.1990.054.01.30

Law, R. D. (2010). Moine thrust zone mylonites at the Stack of Glencoul: II e results of vorticity analyses and their tectonic significance. In R. D. Law, R. W. H. Butler, R. E. Holdsworth, M. Krabbendam, & R. A. Strachan (eds.), *Continental tectonics and mountain building: The Legacy of Peach and Horne* (pp. 579-602). Special Publications vol. 335. Geological Society of London.

Lawley, C. J. M., Selby, D., & Imber, J. (2013). Re-Os molybdenite, pyrite, and chalcopyrite geochronology, Lupa Goldfield, Southwestern Tanzania: Tracing metallogenic time scales at midcrustal shear zones hosting orogenic Au deposits. *Economic Geology*, *108*(7), 1591-1613. https://doi.org/10.2113/econgeo.108.7.1591

Lee, H. K., & Schwarcz, H. P. (1994). ESR plateau dating of fault gouge. *Quaternary Science Reviews*, *13*(5-7), 629-634. https://doi.org/10.1016/0277-3791(94)90090-6

Lee, H. K., & Yang, J. S. (2007). ESR dating of the Eupchon fault, South Korea. *Quaternary Geochronology*, *2*(1-4), 392-397. https://doi.org/10.1016/j.quageo.2006.04.009

Lee, J. K. W., Williams, I. S., & Ellis, D. J. (1997). Pb, U and Th diffusion in natural zircon. *Nature*, *390*(6656), 159-162. https://doi.org/10.1038/36554

Lin, A. (1999a). S-C cataclasite in granitic rock. *Tectonophysics*, *304*(3), 257-273. https://doi.org/10.1016/S0040-1951(99)00026-8

Lin, A. (1999b). Roundness of clast in pseudotachylytes and cataclastic rocks as an indicator of frictional melting. *Journal of Structural Geology*, *21*(5), 473-478. https://doi.org/10.1016/S0191-8141(99)00030-9

Lin, A. (2008). *Fossil earthquakes: The formation and preservation of pseudotachylytes*. Lecture notes in Earth Sciences. Springer. Springer-Verlag.

Lin, A., & Yamashita, K. (2013). Spatial variations in damage zone width along strike-slip faults: An example from active faults in southwest Japan. *Journal of Structural Geology*, *57*, 1-15. https://doi.org/10.1016/j.jsg.2013.10.006

Lindanger, M., Gabrielsen, R. H., & Braathen, A. (2007). Analysis of rock lenses in extensional faults. *NorwegianzJournal Geology*, 87(4), 361-372.

Lister, G. S., & Hobbs, B. E. (1980). The simulation of fabric development during plastic deformation and its application to quartzite: the influence of deformation history. *Journal of Structural Geology*, *2*(3), 355-370. https://doi.org/10.1016/0191-8141(80)90023-1

Lister, G. S., & Snoke, A. W. (1984). S-C mylonites. *Journal of Structural Geology*, *6*(6), 616-638. https://doi.org/10.1016/0191-8141(84)90001-4

Lister, G. S., & Williams, P. F. (1983). The partitioning of deformation in flowing rock masses. *Tectonophysics*, *92*(1-3), 1-33. https://doi.org/10.1016/0040-1951(83)90083-5

Löbens, S., Bense, F. A., Wemmer, K., Dunkl, I., Costa, C. H., Layer, P., & Siegesmund, S. (2011). Exhumation and uplift of the Sierras Pampeanas: Preliminary implications from K-Ar fault gouge dating and low-T thermochronology in the Sierra de Comechingones (Argentina). *International Journal of Earth Science*, *100*, 671-694. https://doi.org/10.1007/s00531-010-0608-0

López-Isaza, J. A., Cuéllar Cárdenas, M. A., Osorio N., J. A. N., Bernal V., L. E. V., & Cortés, E. C. (2008). Pseudotaquilitas y el carácter paleosísmico de un segmento del Sistema de Fallas de Bucaramanga (SFB), noreste del municipio Pailitas, departamento del Cesar, Colombia. *Boletín de Geología*, *30*(2), 79-92.

López-Isaza, J. A., Cuéllar-Cárdenas, M. A., Cetina Tarazona, L. A. T., Forero-Ortega, A. J., Suárez Arias, A. M., Muñoz Rodríguez, O. F., Aguirre, L. M., & Gutiérrez López, M. J. (2020). *Representación gráfica de datos estructurales en campo: Una propuesta metodológica para su aplicación en terrenos deformados.* Informe interno. Servicio Geológico Colombiano.

Louis, S., Luijendijk, E., Dunkl, I., & Person, M. (2019). Episodic fluid flow in an active fault. *Geology*, *47*(10), 938-942. https://doi.org/10.1130/G46254.1

MacNamee, A., & Stockli, D. F. (2015). Constraining age and locations of active and paleofluid flow systems in Dixie Valley, Nevada, with Apatite (U-Th)/He thermochronometry, AGU fall meeting abstracts, San Francisco, CA, December 2015, Abstract V51H-06.

Magloughlin, J. F. (2010). Discussion of "Classification of fault breccias and related fault rocks", by Woodcock & Mort: The particular problem of pseudotachylyte. *Geological Magazine*, *147*(6), 971-973. https://doi.org/10.1017/S0016756810000166

Magloughlin, J. F., Hall, C. M., & van der Pluijm, B. A. (2001). ^{40}Ar-^{39}Ar geochronometry of pseydotachylytes by vacuum encapsulation: North Cascade Mountains, Washington, USA. *Geology*, *29*(1), 51-54. https://doi.org/10.1130/0091-7613(2001)029<0051:AAGOPB>2.0.CO;2

Maitland, T., & Sitzman, S. (2007). Electron backscatter diffraction (EBSD) technique and materials characterization examples. In W. Zhou, & Z. L. Wang, *Scanning microscopy for nanotechnology: Techniques and applications* (pp. 41-75). Springer.

Mallast, U., Gloaguen, R., Geyer, S., Rödiger, T., & Siebert, C. (2011). Derivation of groundwater flow-paths based on semi-automatic extraction of lineaments from remote sensing data. *Hydrology and Earth System Sciences*, *15*(1), 2665-2678. https://doi.org/10.5194/hessd-8-1399-2011

Marchionni, D. S., & Cavayas, F. (2014). La teledetección por radar como fuente de información litológica y estructural. Análisis espacial de imágenes SAR de RADARSAT-1. *Geoacta*, *39*(1), 62-89.

Mariani, E., Prior, D. J., McNamara, D., Pearce, M. A., Seaton, N., Seward, G., Tatham, D., & Wheeler, J. (2008). Electron backscatter diffraction (EBSD) in the SEM: Applications to microstructures in minerals and rocks and recent technological advancements. *Seminarios de la Sociedad Española de Mineralogía* (5), 7-19.

Marrett, R., & Allmendinger, R. W. (1990). Kinematic analysis of fault-slip data: *Journal of Structural Geology*, *12*(8), 973-986. https://doi.org/10.1016/0191-8141(90)90093-E

Marshak, S., & Mitra, G. (1988). *Basic methods of structural geology*. Prentice Hall.

McCalpin, J. P. (2009). *Paleoseismology* (2nd ed.). International Geophysics Series, vol. 95. Elsevier.

McClay, K. (1987). *The mapping of geological structures*. John Wiley and Sons.

McDermott, R. G., Ault, A. K., Evans, J. P., & Reiners, P. W. (2017). Thermochronometric and mirrors, Wasatch fault zone, UT, USA. *Earth and Planetary Science Letters*, *471*, 85-93. https://doi.org/10.1016/j.epsl.2017.04.020

McGrath, A. G., & Davison, I. (1995). Damage zone geometry around fault tips. *Journal of Structural Geology*, *17*(7), 1011-1024. https://doi.org/10.1016/0191-8141(94)00116-H

McKenzie, D. (1979). Finite deformation during fluid flow. *Geophysical Journal of the Royal Astronomical Society*, *58*(3), 689-715. https://doi.org/10.1111/j.1365-246X.1979.tb04803.x

McWilliams, C. K., Wintsch, R. P., & Kunk, M. J. (2007). Scales of equilibrium and disequilibrium during cleavage formation in chlorite and biotite-grade phyllites, SE Vermont. *Journal of Metamorphic Geology*, *25*(8), 895-913. https://doi.org/10.1111/j.1525-1314.2007.00734.x

Means, W. D., Hobbs, B. E., Lister, G. S., & Williams, P. F. (1980). Vorticity and non-coaxiality in progressive deformations. *Journal of Structural Geology*, *2*(3), 371-378. https://doi.org/10.1016/0191-8141(80)90024-3

Mejía, E. L., Velandia, F., Zuluaga, C. A., López, J. A., & Cramer, T. (2012). Análisis estructural al noreste del volcán Nevado del Ruiz, Colombia: Aporte a la exploración geotérmica. *Boletín de Geología*, *14*(1), 27-21.

Mendivelso, D. L. (2008). *Curso de fotogeología, geomorfología y aplicaciones de la percepción remota: Metodología para los levantamientos fotogeológicos*. http://recordcenter.sgc.gov.co/B12/23008002524448/documento/pdf/2105244481103000.PDF

Micklethwaite, S., Sheldon, H. A., & Baker, T. (2010). Active fault and shear processes and their implications for mineral deposit formation and discovery. *Journal of Structural Geology*, *32*(2), 151-165. https://doi.org/10.1016/j.jsg.2009.10.009

Miller, H. B. D., Vasconcelos, P. M., Eiler, J. M., & Farley, K. A. (2017). A Cenozoic terrestrial paleoclimate record from He dating and stable isotope geochemistry of goethite from Western Australia. *Geology*, *45*(10), 895-898. https://doi.org/10.1130/G38989.1

Miranda, T. S., Neves, S. P., Celestino, M. A. L., & Roberts, N. M. W. (2020). Structural evolution of the Cruzeiro do Nordeste shear zone (NE Brazil): Brasiliano-Pan-African-ductile-to-brittle transition and Cretaceous brittle reactivation. *Journal of Structural Geology*, *141*, 104203. https://doi.org/10.1016/j.jsg.2020.104203

Mitchell, T. M., & Faulkner, D. R. (2009). The nature and origin of off-fault damage surrounding strike-slip fault zones with a wide range of displacements: a field study from the Atacama fault system, northern Chile. *Journal of Structural Geology*, *31*(8), 802-816. https://doi.org/10.1016/j.jsg.2009.05.002

Moazzen, M., & Drop, G. T. R. (2005). Application of mineral thermometers and barometers to granitoid igneous rocks: The Etive Complex, W Scotland. *Mineralogy and Petrology*, *83*(1), 27-53. https://doi.org/10.1007/s00710-004-0059-z

Moecher, D. P., & Brearley, A. J. (2004). Mineralogy and petrology of a mullite-bearing pseudotachylyte: Constraints on the temperature of coseismic frictional fusion. *American Mineralogist*, *89*(10), 1486-1495. https://doi.org/10.2138/am-2004-1017

Monteiro, H., Vasconcelos, P. M., Farley, K. A., Spier, C. A., & Mello, C. L. (2014). (U-Th)/He geochronology of goethtite and the origin and evolution of cangas. *Geochimica et Cosmochimica Acta*, *131*, 267-289. https://doi.org/10.1016/j.gca.2014.01.036

Moreira, N., & Dias, R. (2018). Domino structures evolution in strike-slip shear zones: The importance of the cataclastic flow. *Journal of Structural Geology*, *110*, 187-201. https://doi.org/10.1016/j.jsg.2018.01.010

Moser, A. C., Evans, J. P., Ault, A. K., Janecke, S. U., & Bradbury, K. K. (2017). (U-Th)/He thermochronometry reveals Pleistocene punctuated deformation and synkinematic hematite minarlization in the Mecca Hills, southernmost San Andreas Fault zone. *Earth and Planetary Science Letters*, *476*, 87-99. https://doi.org/10.1016/j.epsl.2017.07.039

Mottram, C., Grujic, D., & Coutand, I. (2018). Using U-Pb calcite dating to directly-date continental-scale faults. *Geophysical Research Abstracts*, *20*, EGU2018-14685.

Mukherjee, S. (2014). *Atlas of shear zone structures in Meso-scale*. Springer Science and Business Media.

Mulch, A., & Cosca, M. A. (2004). Recrystallization or cooling ages: In situ UV-laser $^{40}Ar/^{39}Ar$ geochronology of muscovite in mylonitic rocks. *Journal of Geological Society*, *161*(4), 573-582. https://doi.org/10.1144/0016-764903-110

Mulch, A., Cosca, M. A., & Handy, M. R. (2002). In-situ UV-laser $^{40}Ar/^{39}Ar$ geochronology of a micaceous mylonite: An example of defect-enhanced argon loss. *Contributions to Mineralogy and Petrology*, *142*, 738-752. https://doi.org/10.1007/s00410-001-0325-6

Müller, W., Mancktelow, N. S., & Meier, M. (2000). Rb-Sr microchrons of synkinematic mica in mylonites: An example from the DAV fault of the Eastern Alps. *Earth and Planetary Science Letter*, *180*(3-4), 385-397. https://doi.org/10.1016/S0012-821X(00)00167-9

Nakamura, N., & Borradaile, G. (2004). Metamorphic control of magnetic susceptibility and magnetic fabrics: a 3-D projection. In F. Martín Hernández, C. M. Luneburg, C. Aubourg, & M. Jackson (eds.), *Magnetic fabric: methods and applications – an introduction*. Special Publications vol. 238. Geological Society of London. https://doi.org/10.1144/GSL.SP.2004.238.01.01

Nicchio, M. A., Nogueira, F. C. C., Balsamo, F., Souza, J. A. B., Carvalho, B. R. B. M., & Bezerra, F. H. R. (2018). Development of cataclastic foliation in deformation bands in feldspar-rich conglomerates of the Rio do Peixe Basin, NE Brazil. *Journal of Structural Geology*, *107*, 132-141. https://doi.org/10.1016/j.jsg.2017.12.013

Nuriel, P., Miller, D. M., Schmidt, K. M., Coble, M. A., & Maher, K. (2019). Ten-million years of activity within the Eastern California shear zone from U-Pb dating of fault-zone opal. *Earth and Planetary Science Letters*, *521*, 37-45. https://doi.org/10.1016/j.epsl.2019.05.047

Nuriel, P., Rosenbaum, G., Uysal, T. I., Zhao, J., Golding, S. D., Weinberger, R., Karabacak, V., & Avni, Y. (2011). For-

mation of fault-related calcite precipitates and their implications for dating fault activity in the East Anatolian and Dead Sea fault zones. In A. Fagereng, V. G. Toy, & J. V. Rowland (eds.), *Geology of the earthquake source: A volume in honour of Rick Sibson* (pp. 229-248). Special Publications vol. 359. Geological Society of London. https://doi.org/10.1144/SP359.13

Nuriel, P., Weinberger, R., Kylander Clark, A. R. C., Hacker, B. R., & Craddock, J. P. (2017). The onset of the Dead Sea transform based on calcite age-strain analyses. *Geology*, *45*(7), 587-590. https://doi.org/10.1130/G38903.1

Ohtani, T., Shigematsu, N., Fujimoto, K., Tomita, T., & Iwano, H. (2004). Grochronological constraint on the brittle-plastic deformation along the Hatagawa fault zone, NE Japan. *Earth Planets Space*, *56*(Suppl. 12), 1201-1027. https://doi.org/10.1186/BF03353341

Oliot, E., Gonçalves, P., Schulmann, K., Marquer, D., & Lexa, O. (2014). Mid-crustal shear zone formation in granitic rocks: Constraints from quantitative textural and crystallographic preferred orientations analyses. *Tectonophysics*, *612-613*, 63-80. https://doi.org/10.1016/j.tecto.2013.11.032

Oriolo, S., Oyhantçabal, P., Heidelbach, F., Wemmer, K., & Siegesmund, S. (2015). Structural evolution of the Sarandí del Yí shear zone: Kinematics, deformation conditions and tectonic significance. *International Journal Earth Science*, *104*(7), 1759-1777. https://doi.org/10.1007/s00531-015-1166-2

Oriolo, S., Oyhantçabal, P., Wemmer, K., Basei, M. A. S., Benowitz, J., Pfänder, J., Hannich, F., & Siegesmund, S. (2016a). Timing of deformation in the Sarandí del Yí shear zone, Uruguay: Implications for the amalgamation of Western Gondwana during the Neoproterozoic Brasiliano-Pan-African Orogeny. *Tectonics*, *35*(3), 754-771. https://doi.org/10.1002/2015TC004052

Oriolo, S., Oyhantçabal, P., Wemmer, K., Heidelbach, F., Pfänder, J., Basei, M. A. S., Hueck, M., Hannich, F., Sperner, B., & Siegesmund, S. (2016b). Shear zone evolution and timing of deformation in the Neoproterozoic transpressional Dom Feliciano Belt, Uruguay. *Journal Structural Geology*, *92*, 59-78. https://doi.org/10.1016/j.jsg.2016.09.010

Oriolo, S., Wemmer, K., Oyhantçabal, P., Fossen, H., Schulz, B., & Siegesmund, S. (2018). Geochronology of shear zones: A review. *Earth-Science Reviews*, *185*, 665-683. https://doi.org/10.1016/j.earscirev.2018.07.007

Ortner, H., Reiter, F., & Acs, P. (2002). Easy handling of tectonic data: The programs TectonicVP for Mac and TectonicsFP for Windows. *Computers & Geosciences*, *28*(10), 1193-1200. https://doi.org/10.1016/S0098-3004(02)00038-9

Ostermeijer, G. A., Mitchell, T. M., Aben, F. M., Dorsey, M. T., Browning, J., Rockwell, T. K., Fletcher, J. M., & Ostermeijer, F. (2020). Damage zone heterogeneity on seismogenic faults in crystalline rock; a field study of the Borrego Fault, Baja California. *Journal of Structural Geology*, *137*, 104016. https://doi.org/10.1016/j.jsg.2020.104016

Oyhantçabal, P., Heimann, A., & Miranda, S. (2001). Measurement and interpretation of strain in the syntectonic Solís de Mataojo Granitic Complex, Uruguay. *Journal of Structural Geology*, *23*(5), 807-817. https://doi.org/10.1016/S0191-8141(00)00152-8

Oyhantçabal, P., Muzio, R., & de Souza, S. (1993). Geología y aspectos estructurales del borde orogénico en el extremo sur del cinturón Dom Feliciano. *Revista Brasileira de Geociências*, *23*(3), 296-300. https://doi.org/10.25249/0375-7536.1993233296300

Oyhantçabal, P., Siegesmund, S., Wemmer, K., & Layer, P. (2009). The Sierra Ballena shear zone in the southernmost Dom Feliciano Belt (Uruguay): Evolution, kinematics, and deformation conditions. *International Journal of Earth Sciences*, *99*, 1227-1246. https://doi.org/10.1007/s00531-009-0453-1

Oyhantçabal, P., Wegner Eimer, M., Wemmer, K., Schulz, B., Frei, R., & Siegesmund, S. (2012). Paleo- and Neoproterozoic magmatic and tectonometamorphic evolution of the Isla Cristalina de Rivera (Nico Pérez Terrane, Uruguay). *International Journal of Earth Sciences*, *101*, 1745-1762. https://doi.org/10.1007/s00531-012-0757-4

Pagel, M., Bonifacie, M., Schneider, D. A., Gautheron, C., Brigaud, B., Calmels, D., Cros, A., Saint-Bezar, B., Landrein, P., & Sutcliffe, C. (2018). Improving paleohydrological and diagenetic reconstructions in calcite veins and breccia of a sedimentary basin by combining Δ47 temperature, δ18Owater and U-Pb age. *Chemical Geology*, *481*, 1-17. https://doi.org/10.1016/j.chemgeo.2017.12.026

Paine, D. P., & Kiser, J. D. (2003). *Aerial photography and image interpretation* (2nd ed.). Wiley.

Papeschi, S., Musumeci, G., & Mazzarini, F. (2018). Evolution of shear zones through the brittle-ductile transition: The Calamita Schists (Elba Island, Italy). *Journal of Structural Geology*, *113*, 100-114. https://doi.org/10.1016/j.jsg.2018.05.023

Park, S., Kim, Y., Ryoo, C., & Sanderson, D. J. (2010). Fractal analysis of the evolution of a racture network in a granite outcrop, SE Korea. *Geosciences Journal*, *14*, 201-215. https://doi.org/10.1007/s12303-010-0019-z

Parsons, A. J., Ferré, E. C., Law, R. D., Lloyd, G. E., Phillips, R. J., & Searle, M. P. (2016). Orogen-parallel deformation of the Himalayan midcrust: Insights from structural and magnetic fabric analyses of the Greater Himalayan Sequence, Annapurna-Dhaulagiri Himalaya, central Nepal. *Tectonics*, *35*(11), 2515-2537. https://doi.org/10.1002/2016TC004244

Passchier, C. W. (1997). The fabric attractor. *Journal of Structural Geology*, *19*(1), 113-127. https://doi.org/10.1016/S0191-8141(96)00077-6

Passchier, C. W., & Coelho, S. (2006). An outline of shear-sense analysis in high-grade rocks. *Gondwana Research*, *10*(1), 66-76. https://doi.org/10.1016/j.gr.2005.11.016

Passchier, C. W., Myers, J. S., & Kröner, A. (1990). *Field geology of high-grade gneiss terrains*. Springer-Verlag. https://doi.org/10.1007/978-3-642-76013-6

Passchier, C. W., & Trouw, R. A. J. (2005). *Microtectonics*. Springer Science and Business Media. https://doi.org/10.1007/3-540-29359-0

Paterson, S. R., & Vernon, R. H. (1995). Bursting the bubble of ballooning plutons: A return to nested diapirs emplaced by multiple processes. *GSA Bulletin*, *107*(11), 1356-1380. https://doi.org/10.1130/0016-7606(1995)107<1356:BTBOBP>2.3.CO;2

Paterson, S. R., Fowler, T. K. J., Schmidt, K. L., Yoshinobu, A. S., Yuan, E. S., & Miller, R. B. (1998). Interpreting magmatic fabric patterns in plutons. *Lithos*, *44*(1-2), 53-82. https://doi.org/10.1016/S0024-4937(98)00022-X

Paterson, S. R., Vernon, R. H., & Tobisch, O. T. (1989). A review of criteria for the identification of magmatic and tectonic foliations in granitoids. *Journal of Structural Geology*, *11*(3), 349-363. https://doi.org/10.1016/0191-8141(89)90074-6

Pec, M., Stünitz, H., & Heilbronner, R. (2012). Semi-brittle deformation of granitoid gouges in shear experiments at elevated pressures and temperatures. *Journal of Structural Geology*, *38*, 200-221. https://doi.org/10.1016/j.jsg.2011.09.001

Pennacchioni, G., & Zucchi, E. (2013). High temperature fracturing and ductile deformation during cooling of a pluton: the Lake Edison granodiorite (Sierra Nevada batholith, California). *Journal Structural Geology*, *50*, 54-81. https://doi.org/10.1016/j.jsg.2012.06.001

Petit, J. P. (1987). Criteria for the sense of movement on fault surfaces in brittle rocks. *Journal of Structural Geology*, *9*(5-6), 597-608. https://doi.org/10.1016/0191-8141(87)90145-3

Philpotts, A. R. (1964). Origin of pseudotachylytes. *American Journal of Science*, *262*(8), 1008-1035. https://doi.org/10.2475/ajs.262.8.1008

Picazo, S., Manatschal, G., Cannat, M., & Andréani, M. (2013). Lithos deformation associated to exhumation of serpentinized mantle rocks in a fossil Ocean Continent transition: The Totalp unit in SE Switzerland. *Lithos*, *175-176*, 255-271. https://doi.org/10.1016/j.lithos.2013.05.010

Platt, J. P. (2015). Rheology of two-phase systems: A microphysical and observational approach. *Journal of Structuctural Geology*, *77*, 213-227. https://doi.org/10.1016/j.jsg.2015.05.003

Powell, R., & Holland, T. J. B. (1994). Optimal geothermometry and geobarometry. *American Mineralogist*, *79*(1-2), pp. 120-133.

Powell, R., & Holland, T. J. B. (2001). Course Notes for "Thermocalc Workshop 2001: Calculating Metamorphic Phase Equilibria".

Powell, R., & Holland, T. J. B. (2008). On thermobarometry. *Journal of Metamorphic Geology*, *26*(2), pp. 155-179. https://doi.org/10.1111/j.1525-1314.2007.00756.x

Powell, R., Holland, T. J. B., & Worley, B. (1998). Calculating phase diagrams involving solid solutions via non-linear equations, with examples using Thermocalc. *Journal of Metamorphic Geology*, *16*(4), 577-588. https://doi.org/10.1111/j.1525-1314.1998.00157.x

Prent, A. M., Beinlich, A., Raimondo, T., Kirkland, C. L., Evans, N. J., & Putnis, A. (2020). Apatite and monazite: An effective duo to unravel superimposed fluid-flow and deformation events in reactivated shear zones. *Lithos*, *376-377*, 105752. https://doi.org/10.1016/j.lithos.2020.105752

Précigout, J., Prigent, C., Palasse, L., & Pochon, A. (2017). Water pumping in mantle shear zones. *Nature Commununications*, *8*, 15736. https://doi.org/10.1038/ncomms15736

Prigent, C., Warren, J., Kohli, A., & Teyssier, C. (2017). *The semi-brittle to ductile transition in oceanic faults in peridotite: Mechanisms and P-T conditions*. In AGU Fall Meeting 2017, 1-2, Nueva Orleáns.

Prior, D. J., Boyle, A. P., Brenker, F., Cheadle, M.C., Day, A., Lopez, G., Peruzzo, L., Potts, G. J., Reddy, S., Spiess, R., Timms, N. E., Trimby, P., Wheeler, J., & Zetterstrom, L. (1999). The application of electron backscatter diffraction and orientation contrast imaging in the SEM to textural problems

in rocks. *American Mineralogist*, *84*(11-12), 1741-1759. https://doi.org/10.2138/am-1999-11-1204

Purdy, J. W., & Jäger, E. (1976). K-Ar ages on rock-forming minerals from the Central Alps. *Memorie degli Istituti di geologia e mineralogia dell'Università di Padova*, 30, 3-31.

Qju, D., Liu, Q., Yun, J., Jin, Z., Zhu, D., Li, T., & Sun, D. (2018). Electron spin resonance (ESR) dating of pre-Quaternary faults in the Sichuan basin, SW China. *Journal of Asian Earth Sciences*, *163*, 142-151. https://doi.org/10.1016/j.jseaes.2018.06.011

Rampal, K. K. (1999). *Handbook of aerial photography and interpretation*. Concept Publishing Company. https://books.google.com.co/books?id=rmiPV3ABi9EC

Ramsay, J. G., & Huber, M. I. (1983). *The techniques of modern structural geology*. Vol. 1: *Strain analysis*. Academic Press.

Ramsay, J. G. (1980a). The crack-seal mechanism of rock deformation. *Nature*, *284*(5752), 135-139. https://doi.org/10.1038/284135a0

Ramsay, J. G. (1980b). Shear zone geometry: A review. *Journal of Structural Geology*, *2*(1-2), 83-99. https://doi.org/10.1016/0191-8141(80)90038-3

Ramsay, J. G., & Huber, M. I. (1987). *The techniques of modern structural geology. Vol. 2: Folds and fractures*. Academic Press.

Rao, D. P. (2002). Remote sensing application in geomorphology. *Tropical Ecology*, *43*(1), 49-59.

Rasbury, E. T., & Cole, J. M. (2009). Directly dating geologic events: U-Pb dating of carbonates. *Reviews of Geophysics*, *47*(3), RG3001. https://doi.org/10.1029/2007RG000246

Reavy, R. (1989). Structural controls on metamorphism and syntectonic magmatism: The Portuguese Hercyan collision belt. *Journal of the Geological Society*, *146*(4), 649-657. https://doi.org/10.1144/gsjgs.146.4.0649

Reber, J. E., & Pec, M. (2018). Comparison of brittle and viscous creep in quartzites: Implications for semi-brittle flow of rocks. *Journal of Structural Geology*, *113*, 90-99. https://doi.org/10.1016/j.jsg.2018.05.022

Reddy, S., & Potts, G. (1999). Deformation mechanisms and Ar isotope systematics. In Micas: Implications for absolute deformation ages. *Journal of Conference Abstracts*, *4*(1), 830 p. Cambridge Publications. Cambridge, United Kingdom.

Reddy, S. M., Timms, N. E., Pantleon, W., & Trimby, P. (2007). Quantitative characterization of plastic deformation of zircon and geological implications. *Contributions to Mineralogy and Petrology*, *153*(6), 625-645. https://doi.org/10.1007/s00410-006-0174-4

Reiners, P. W., & Brandon, M. T. (2006). Using thermochronology to understand orogenic erosion. *Annual Reviews or Earth and Planetary Sciences*, *34*(1), 419-466. https://doi.org/10.1146/annurev.earth.34.031405.125202

Ribeiro, B. V., Faleiros, F. M., Campanha, G. A. C., Lagoeiro, L., Weinberg, R. F., & Hunter, N. J. R. (2019). Kinematics, deformational conditions and tectonic setting of the Taxaquara shear zone, a major transpressional zone of the Ribeira Belt (SE Brazil). *Tectonophysics*, *751*, 83-108. https://doi.org/10.1016/j.tecto.2018.12.025

Ribeiro, B. V., Lagoeiro, L., Faleiros, F. M., Hunter, N. J. R., Queiroga, G., Raveggi, M., Cawood, P. A., Finch, M., & Campanha, G. A. C. (2020a). Strain localization and fluid-assited deformation in apatite and its influence on trace elements and U-Pb systematics. *Earth and Planetary Science Letters*, *542*, 116421. https://doi.org/10.1016/j.epsl.2020.116421

Ribeiro, B. V., Mulder, J. A., Faleiros, F. M., Kirkland, C. L., Cawood, P. A., O'Sullivan, G., Campanha, G. A. C., Finch, M. A., Weinberg, R. F., & Nebel, O. (2020b). Using apatite to resolve the age and protoliths of mid-crustal shear zones: A case study from the Taxaquara shear zone, SE Brazil. *Lithos*, *378-379*, 105817. https://doi.org/10.1016/j.lithos.2020.105817

Richard, J., Gratier, J. P., Doan, M. L., Boullier, A. M., & Renard, F. (2014). Rock and mineral transformations in a fault zone leading to permanent creep: Interactions between brittle and viscous mechanisms in the San Andreas Fault. *Journal of Geophysical Research: Solid Earth*, *119*(11), 8132-8153. https://doi.org/10.1002/2014JB011489

Ricchi, E., Bergemann, C. A., Gnos, E., Berger, A., Rubatto, D., Whitehouse, M. J., & Walter, F. (2020). Cenozoic deformation in the Tauern Window (Eastern Alps) constrained by in situ Th-Pb dating of fissure monazite. *Solid Earth*, *11*(2), 437-467. https://doi.org/10.5194/se-11-437-2020

Ricchi, E., Gnos, E., Rubatto, D., Whitehouse, M. J., & Pettke, T. (2020). Ion microprobe dating of fissure monazite in the Western Alps: Insights from the Argentera Massif and the Piemontais and Briançonnais Zones. *Swiss Journal of Geosciences*, *113*(1), 1-27. https://doi.org/10.1186/s00015-020-00365-3

Riedmüller, G., Brosch, F. J., Klima, K., & Medley, E. W. (2001). Engineering geological characterization of brittle faults and classification of fault rocks. *Felsbau*, *19*(4), 13-19.

Riley, P. R., Goodwin, L. B., & Lewis, C. J. (2010). Controls on fault damage zone width, structure, and symmetry in the Bandelier Tuff, New Mexico. *Journal of Structural Geology*, *32*(6), 766-780. https://doi.org/10.1016/j.jsg.2010.05.005

Ring, U., Uysal, I. T., Glodny, J., Cox, S. C., Little, T., Thomson, S. N., Stübner, K., & Bozkaya, Ö. (2017). Fault-gouge dating in the Southern Alps, New Zealand. *Tectonophysics*, *717*, 321-338. https://doi.org/10.1016/j.tecto.2017.08.007

Roberts, N. M. W. (2019). *Mind over methods: Dating deformation with U-Pb carbonate geochronology*. EGU Blogs, Divisions, Tectonics and Structural Geology. https://blogs.egu.eu/divisions/ts/2019/08/16/minds-over-methods-dating-deformation-with-u-pb-carbonate-geochronology/

Roberts, N. M. W., & Walker, R. (2016). U-Pb geochronology of calcite-mineralized faults: Absolute timing of rift-related fault events on the northeast Atlantic margin. *Geology*, *44*(7), 531-534. https://doi.org/10.1130/G37868.1

Roberts, N. M. W., Drost, K., Horstwood, M. S. A., Condon, D. J., Chew, D., Drake, H., Milodowski, A. E., McLean, N. M., Smye, A. J., Walker, R. J., Haslam, R., Hodson, K., Imber, J., Beaudoin, N., & Lee, J. K. (2020a). Laser ablation inductively coupled plasma mass spectrometry (LA-ICP-MS) U-Pb carbonate geochronology: Strategies, progress, and limitations. *Geochronology*, *2*, 33-61. https://doi.org/10.5194/gchron-2-33-2020

Roberts, N. M. W., Lee, J. K., Holdsworth, R. E., Jeans, C., Farrant, A. R., & Haslam, R. (2020b). Near-surface Paleocene fluid flow, mineralization and faulting at Flamborough Head, UK: New field observations and U-Pb calcite dating constraints. *Solid Earth*, *11*(5), 1931-1945. https://doi.org/10.5194/se-11-1931-2020

Robin, P. Y. F. (2002). Determination of fabric and strain ellipsoids from measured sectional ellipses-theory. *Journal Structural Geology*, *24*(3), 531-544. https://doi.org/10.1016/S0191-8141(01)00081-5

Romn-Berdiel, T., Gapais, D., & Brun, J. P. (1997). Granite intrusion along strike slip zones in experiment and nature. *American Journal of Science*, *297*(6), 651-678. https://doi.org/10.2475/ajs.297.6.651

Rosenberg, C. L. (2004). Shear zones and magma ascent: A model based on a review of the Tertiary magmatism in the Alps. *Tectonics*, *23*(3), TC3002. https://doi.org/10.1029/2003TC001526

Rutter, E. H., Mecklenburgh, J., & Brodie, K. H. (2011). Rock mechanics constraints on mid-crustal, low-viscosity flow beneath Tibet. In D. J. Prior, E. H. Rutter, & D. J. Tatham (eds.), *Deformation mechanisms, rheology and tectonics: Microstructures, mechanics and anisotropy* (pp. 329-336). Special Publications vol. 360. Geological Society of London. https://doi.org/10.1144/SP360.19

Rutter, E. H. (1986). On the nomenclature of mode of failure transitions in rocks. *Tectonophysics*, *122*(3-4), 381-387. https://doi.org/10.1016/0040-1951(86)90153-8

Sainz, A. C., Peña, I. G., & Gómez, J. S. (1990). Los métodos de análisis de paleoesfuerzos a partir de poblaciones de fallas: Sistemática y técnicas de aplicación. *Estudios Geológicos*, *46*(5-6), 385-398. https://doi.org/10.3989/egeol.90465-6469

Sanderson, S., & Marchini, O. (1984). Transpression. *Journal of Structural Geology*, *6*(5), 449-458. https://doi.org/10.1016/0191-8141(84)90058-0

Santamaría-Díaz, A., Alaniz-Álvarez, S. A., & Nieto-Samaniego, A. F. (2008). Deformaciones cenozoicas en la cobertura de la falla Caltepec en la región de Tamazulapam, sur de México. *Revista Mexicana de Ciencias Geológicas*, *25*(3), 494-516.

Santos, J. O. S., Hartmann, L. A., Bossi, J., Campal, N., Schipilov, A., Piñeyro, D., & McNaughton, N. J. (2003). Duration of the Trans-Amazonian cycle and its correlation within South America based on U-Pb Shrimp Geochronology of the La Plata Craton, Uruguay. *International Geology Review*, *45*(3), 27-48. https://doi.org/10.2747/0020-6814.45.1.27

Sarkarinejad, K., Heyhat, M., Faghih, A., & Kusky, T. (2010). Heterogeneous ductile deformation and quartz c-axis fabric development within the HP-LT Sanandaj-Sirjan Metamorphic Belt, Iran. *Tectonophysics*, *485*(1-4), 283-289. https://doi.org/10.1016/j.tecto.2010.01.006

Sausgruber, T., & Brandner, R. (2001). The relevance of brittle fault zones in tunnel construction: Lower inn valley feeder line north of the Brenner base tunnel, Tyrol, Austria. Mitt. *Österreichische Geologische Gesellschaft*, *94*, 157-172.

Scheiber, T., Viola, G., Van der Lelij, R., Margreth, A., & Schönenberger, J. (2019). Microstructurally-constrained versus bulk fault gouge K-Ar dating. *Journal of Structural Geology*, *127*, 103868. https://doi.org/10.1016/j.jsg.2019.103868

Schmidt, M. W. (1992). Amphibole composition in tonalite as a function of pressure: An experimental calibration of the Al-in-hornblende barometer. *Contributions to Mineralogy and Petrology*, *110*(2-3), 304-310. https://doi.org/10.1007/bf00310745

Schmid, S. M., & Casey, M. (1986). Complete fabric analysis of some commonly observed quartz c-axis patterns. In *Mineral and Rock Deformation: Laboratory Studies*, vol. 36 *American Geophysical Union*. https://doi.org/10.1029/GM036p0263

Schmid, S. M., & Handy, M. R. (1991). Towards a genetic classification of fault rocks: Geological usage and tectonophysical implication. In D. W. Müller, J. A. McKenzie, & H. Weissert, *Controversies in modern geology: Evolution of geological theories in sedimentology, earth history and tectonics*. Academic Press.

Schneider, S., Hammerschmidt, K., & Rosenberg, C. L. (2013). Dating the longevity of shear zones: Insight from $^{40}Ar/^{39}Ar$ in situ analysis. *Earth and Planetary Science Letters*, *369-370*, 43-58. https://doi.org/10.1016/j.epsl.2013.03.002

Schoene, B. (2014). U-Th-Pb geochronology. In R. L. Rudnick (ed). *Treatise on geochemistry: The crust* (pp. 341-378). Elsevier, 4.

Scholz, C. H. (1987). Wear and gouge formation in brittle faulting. *Geology*, *15*(6), 493-495. https://doi.org/10.1130/0091-7613(1987)15<493:WAGFIB>2.0.CO

Scholz, C. H. (1988). The brittle-plastic transition and the depth of seismic faulting: *Geologische Rundschau*, *77*(1), 319-328. https://doi.org/10.1007/BF01848693

Scholz, C. H. (2006). *The mechanics of Earthquakes and faulting* (2nd ed.). Cambridge University Press. https://doi.org/10.1017/9781316681473

Selverstone, J., Axen, G. J., & Luther, A. (2012). Fault localization controlled by fluid infiltration into mylonites: Formation and strength of low-angle normal faults in the midcrustal brittle-plastic transition. *Journal of Geophysical Research: Solid Earth*, *117*(B6), B06210. https://doi.org/10.1029/2012JB009171

Sherlock, S. C., & Hetzel, R. (2001). A laser-probe $^{40}Ar/^{39}Ar$ study of pseudotachylite from the Tambach Fault Zone, Kenya: Direct isotopic dating of brittle faults. *Journal Structural Geology*, *23*(1), 33-44. https://doi.org/10.1016/S0191-8141(00)00082-1

Sherlock, S. C., Strachan, R. A., & Jones, K. A. (2009). High spatial resolution $^{40}Ar/^{39}Ar$ dating of pseudotachylites: Geochronological evidence for multiple phases of faulting within basement gneisses of the Outer Hebrides (UK). *Journal of the Geological Society of London*, *166*(6), 1049-1059. https://doi.org/10.1144/0016-76492008-125

Short, H. A., & Johnson, S. E. (2006). Estimation of vorticity from fibrous calcite veins, central Maine, USA. *Journal of Structural Geology*, *28*(7), 1167-1182. https://doi.org/10.1016/j.jsg.2006.03.024

Shuster, D. L., Vasconcelos, P. M., Heim, J. A., & Farley, K. A. (2005). Weathering geochronology by (U-Th)/He dating of goethite. *Geochimica et Cosmochimica Acta*, *69*(3), 659-673. https://doi.org/10.1016/j.gca.2004.07.028

Sibson, R. H. (1975). Generation of pseudotachylite by ancient seismic faulting. *Geophysical Journal International*, *43*(3), 775-794. https://doi.org/10.1111/j.1365-246X.1975.tb06195.x

Sibson, R. H. (1983). Continental fault structure and the shallow earthquake source. *Journal of the Geological Society*, *140*(5), 741-767. https://doi.org/10.1144/gsjgs.140.5.0741

Sibson, R. H. (1977). Fault rocks and fault mechanisms. *Journal of the Geological Society*, *133*(3), 191-213. https://doi.org/10.1144/gsjgs.133.3.0191

Sibson, R. H. (1979). Fault rocks and structure as indicators of shallow earthquake source processes. *U.S. Geological Survey Open-File Report* (79), 1239. Proceedings of conference VIII - Analysis of actual fault zones in bedrock.

Sibson, R. H. (1980). Transient discontinuities in ductile shear zones. *Journal of Structural Geology*, *2*(1-2), 165-171. https://doi.org/10.1016/0191-8141(80)90047-4

Sibson, R. H. (1990). Conditions for fault-valve behaviour. In R. J. Knipe, & E. H. Rutter (eds.), *Deformation mechanisms, rheology and tectonics* (pp. 15-28). Special Publications vol. 54. Geological Society of London. https://doi.org/10.1144/GSL.SP.1990.054.01.02

Siegesmund, S., Steenken, A., López, M. G. L., Wemmer, K., Hoffman, A., & Mosh, S. (2004). The Las Chacras-Potrerillo batholith (Pampean Ranges, Argentina): Structural evidences, emplacement and timing of the intrusion. *International Journal Earth Science*, *93*(1), 23-43. https://doi.org/10.1007/s00531-003-0363-6

Simpson, C. (1986). Fabric development in brittle-to-ductile shear zones. *Pure and Applied Geophysics*, *124*(1-2), 269-288. https://doi.org/10.1007/BF00875728

Sippel, J., Scheck-Wenderoth, M., Reicherter, K., & Stanislaw Mazur, S. (2009). Paleostress states at the south-western margin of the Central European Basin System-application of fault-slip analysis to unravel a polyphase deformation pattern. *Tectonophysics*, *470*(1-2), 129-146. https://doi.org/10.1016/j.tecto.2008.04.010

Smeraglia, L., Berra, F., Billi, A., Boschi, C., Carminati, E., & Doglioni, C. (2016). Origin and role of fluids involved in the seismic cycle of extensional faults in carbonate rocks. *Earth and Planetary Science Letters*, *450*, 292-305. https://doi.org/10.1016/j.epsl.2016.06.042

Smith, L., Porster, C. B., & Evans, J. P. (1990). Interaction of faults zones, fluid flow, and heat transfer at the basin scale. En: *Hydrogeology of permeability environments*. (pp. 41-67). Vol. 2. International Association of Hydrogeologists.

Smith, M. J., & Pain, C. F. (2009). Applications of remote sensing in geomorphology. *Progress in Physical Geography: Earth and Environment*, *33*(4), 568-582. https://doi.org/10.1177/0309133309346648

Snoke, A. W., Tullis, J., & Todd, V. R. (1998). *Fault related rocks: A photographic atlas*. Princeton University Press.

Spear, F. S. (1993). *Metamorphic phase equilibria and pressure-temperature-time paths*. Monograph Series, Mineralogical Society of America, D.C.

Sperner, B., & Ratschbacher, L. (1994). A Turbo Pascal program package for graphical presentation and stress analysis of calcite deformation. *Zeitschrift der Deutschen Geologischen Gesellschaft*, *145*, 414-423.

Sperner, B., Ratschbacher, L., & Ott, R. (1993). Fault-striae analysis: a Turbo Pascal program package for graphical presentation and reduced stress tensor calculation. *Computers & Geosciences*, *19*(9), 1361-1388. https://doi.org/10.1016/0098-3004(93)90035-4

Sperner, B., & Zweigel, P. (2010). A plea for more caution in fault-slip analysis. *Tectonophysics*, *482*(1-4), 29-41. https://doi.org/10.1016/j.tecto.2009.07.019

Spray, J. G. (1995). Pseudotachylyte controversy: Fact or friction? *Geology*, *23*(12), 1119-1122. https://doi.org/10.1130/0091-7613(1995)023<1119:PCFOF>2.3.CO;2

Spruzeniece, L., & Piazolo, S. (2015). Strain localization in brittle-ductile shear zones: Fluid-abundant vs. fluid-limited conditions (an example from Wyangala area, Australia). *Solid Earth Discussions*, *7*(2), 1399-1446. https://doi.org/10.5194/sed-7-1399-2015

Srivastava, D. C., Lisle, R. J., & Vandycke, S. (1995). Shear zones as a new type of paleostress indicator. *Journal of Structural Geology*, *17*(5), 663-673. https://doi.org/10.1016/0191-8141(94)00084-D

Steenken, A., Siegesmund, S., & Heinrichs, T. (2000). The emplacement of the Rieserferner Pluton (Eastern Alps, Tyrol): Constraints from field observations, magnetic fabrics and microstructures. *Journal Structural Geology*, *22*(11-12), 1855-1873. https://doi.org/10.1016/S0191-8141(00)00071-7

Steffen, K. J., & Selverstone, J. (2006). Retrieval of P-T information from shear zones: Thermobarometric consequences of changes in plagioclase deformation mechanisms. *Contributions to Mineralogy and Petrology*, *151*, 600. https://doi.org/10.1007/s00410-006-0073-8

Stewart, J. R., & Betts, P. G. (2010). Late Paleo-Mesoproterozoic plate margin deformation in the southern Gawler Craton: Insights from structural and aeromagnetic analysis. *Precambrian Research, 177*(1-2), 55-72. https://doi.org/10.1016/j.precamres.2009.11.004

Stewart, J. R., Betts, P. G., Collins, A. S., & Schaefer, B. F. (2009). Multi-scale analysis of Proterozoic shear zones: An integrated structural and geophysical study. *Journal of Structural Geology*, *31*(10), 1238-1254. https://doi.org/10.1016/j.jsg.2009.07.002

Stipp, M., Stünitz, H., Heilbronner, R., & Schmid, S. M. (2002). Dynamic recrystallization of quartz: Correlation between natural and experimental conditions. In S. De Meer, M. R. Drury, J. H. P. De Bresser, & G. M. Pennock (eds.), *Deformation mechanisms, rheology and tectonics: Current status and future perspectives* (pp. 171-190). Special Publication vol. 200. Geological Society of London.

Stockli, D. F., Surpless, B. E., Dumitru, T. A., & Farley, K. A. (2002). Thermocrhonological constraints on the timing and magnitude of Miocene and Pliocene extension in the central Wassuk Range, western Nevada. *Tectonics*, *21*(4), 10-28. https://doi.org/10.1029/2001TC001295

Storti, F., Holdsworth, R. E., & Salvini, F. (2003). Intraplate strike-slip deformation belts. In F. Storti, R. E. Holdsworth, & F. Salvini (eds.), *Intraplate strike-slip deformation belts* (pp. 1-14). Special Publication vol. 210. Geologicas Society of London

Stünitz, H. (1998). Syndeformational recrystallization: Dynamic or compositionally induced? *Contribution to Mineralogy and Petrology*, *131*, 219-236. https://doi.org/10.1007/s004100050390

Süssenberger, A., Schmidt, S. T., Wemmer, K., Baumgartner, L. P., & Grobéty, B. (2017). Timing and thermal evolution of fold-and-thrust belt formation in the Última Esperanza District, 51° S Chile: Constraints from K-Ar dating and illite characterization. *GSA Bulletin*, *130*(5), 975- 998. https://doi.org/10.1130/B31766.1

Swanson, M. T. (1992). Fault structure, wear mechanisms and rupture processes in pseudotachylyte generation. *Tectonophysics*, *204*(3-4), 223-242. https://doi.org/10.1016/0040-1951(92)90309-T

Tagami, T. (2012). Thermochronological investigation of fault zones. *Tectonophysics*, *538-540*, 67-85. https://doi.org/10.1016/j.tecto.2012.01.032

Tagami, T. (2019). Application of fission-track thermochronology to understand fault zones (pp. 221-233). In M. Malusà, & P. Fitzgerald (eds.). *Fission-track thermochronology and its application to geology*. Springer. https://doi.org/10.1007/978-3-319-89421-8_12

Tagami, T., & Murakami, T. (2007). Probing fault zone heterogeneity on the Nojima fault: Constraints from zircon fission-track analysis of borefole samples. *Tectonophysics*, *443*(3-4), 139-152. https://doi.org/10.1016/j.tecto.2007.01.013

Ten Grotenhuis, S. M., Trouw, R. A. J., & Passchier, C. W. (2003). Evolution of mica fish in mylonitic rocks. *Tectonophysics*, *372*(1-2), 1-21. https://doi.org/10.1016/S0040-1951(03)00231-2

Thakur, P., Srivastava, D. C., & Gupta, P. K. (2020). HGA: A genetic algorithm method for direct estimation of paleostress states from heterogeneous fault-slip data. *Journal of Structural Geology*, *138*, 104084. https://doi.org/10.1016/j.jsg.2020.104084

Thigpen, J. R., Law, R. D., Lloyd, G. E., & Brown, S. J. (2010). Deformation temperatures, vorticity of flow, and strain in the Moine thrust zone and Moine nappe: Reassessing the tectonic evolution of the Scandian foreland-hinterland transition zone. *Journal of Structural Geology*, *32*(7), 920-940. https://doi.org/10.1016/j.jsg.2010.05.001

Tillberg, M., Drake, H., Zack, T., Hogmalm, J., & Astrom, M. (2017). In situ Rb-Sr dating of fine-grained vein mineralizations using LA-ICP-MS. *Procedia Earth and Planetary Science*, *17*, 464-467. https://doi.org/10.1016/j.proeps.2016.12.117

Tillberg, M., Drake, H., Zack, T., Kooijman, E., Whitehouse, M. J., & Åström, M. E. (2020). In situ Rb-Sr dating of slickenfibres in deep crystalline basement faults. *Scientific Reports*, *10*, 1-13, 2020. https://doi.org/10.1038/s41598-019-57262-5

Timms, N. E., Kinny, P. D., Reddy, S. M., Evans, K., Clark, C., & Healy, D. (2011). Relationship among titanium, rare Earth elements, U-Pb ages and deformation microstructures in zircon: Implications for Ti-in-zircon thermometry. *Chemical Geology*, *280*(1-2), 33-46. https://doi.org/10.1016/j.chemgeo.2010.10.005

Tinkham, D. K. (2007). *Metamorphic phase equilibria modeling: Techniques and programs. An informal short course manual*. The University of Alabama. Metamorphic Studies Group. October 22-24.

Torgersen, E., & Viola, G. (2014). Structural and temporal evolution of a reactivated brittle-ductile fault. Part I: Fault architecture, strain localization mechanisms and deformation history. *Earth and Planetary Science Letters*, *407*, 205-220. https://doi.org/10.1016/j.epsl.2014.09.019

Tranos, M. D. (2009). Faulting of Lemnos Island: A mirror of faulting of the North Aegean Trough (Northern Greece). *Tectonophysics*, *467*(1-4), 72-88. https://doi.org/10.1016/j.tecto.2008.12.018

Tranos, M. D. (2011). Strymon and Strymonikos Gulf basins (Northern Greece): Implications on their formation and evolution from faulting. *Journal of Geodynamics*, *51*(4), 285-305. https://doi.org/10.1016/j.jog.2010.10.002

Trouw, R. A. J., Passhier, C. W., & Wiersma, D. R. (2010). *Atlas of mylonites, and related microstructures* (2nd ed.). Springer Science and Business Media. https://doi.org/10.1007/978-3-642-03608-8

Truesdell, C. (1953). Two measures of vorticity. *Journal of Rational Mechanics Analysis*, 2, 173-217. https://www.jstor.org/stable/24900328

Turcotte, D. L. (1989). Fractals in geology and geophysics. *Pure and Applied Geophysics*, *131*(1-2), 171-196. https://doi.org/10.1007/bf00874486

Turcotte, D. L. (1997). *Fractals and chaos in geology and geophysics* (2nd ed.). Cambridge University Press. https://doi.org/10.1017/CBO9781139174695

Turner, F. J., & Weiss, L. E. (1963). *Structural analysis of metamorphic tectonites*. McGraw-Hill Book Company, Inc.

Twiss, R. J., & Unruh, J. R. (1998). Analysis of fault slip inversions: Do they constrain stress or strain rate? *Journal of Geophysical Research: Solid Earth*, *103*(B6), 12205-12222. https://doi.org/10.1029/98JB00612

Uysal, T. I., Feng, Y., Zhao, J.-X., Altunel, E., Weatherley, D., Karabacak, V., Cengiz, O., Golding, S. D., Lawrence, M. G., & Collerson, K. D. (2007). U-series dating and geochemical tracing of late Quaternary travertine in co-seismic fissures. *Earth and Planetary Science Letters*, *257*(3-4), 450-462. https://doi.org/10.1016/j.epsl.2007.03.004

Van Daele, J., Dewaele, S., Melcher, F., Onuk, P., Spikings, R., Glorie, S., Jepson, G., & Muchez, P. (2020). Geochronology of metamorphism, deformation and fluid circulation: A comparison between and Ar-Ar phyllosilicate and U-Pb apatite systematics in the Karagwe-Ankole Belt (Central Africa). *Gondwana Research*, *83*, 279-297. https://doi.org/10.1016/j.gr.2020.02.008

Van der Pluijm, B. A., Hall, C. M., Vrolijk, Pevear, D. R., & Covey, M. C. (2001). The Dating of shallow faults in the Earth's crust. *Nature*, *412*(6843), 172-5. https://doi.org/10.1038/35084053

Van der Pluijm, B. A., Vrolijk, P. J., Pevear, D. R., Hall, C. M., & Solum, J. (2006). Fault dating in the Canadian Rocky Mountains: Evidence for late Cretaceous and early Eocene orogenic pulses. *Geology*, *34*(10), 837-840. https://doi.org/10.1130/G22610.1

Van der Pluijm, V. A., Mezger, K., Cosca, M. A., & Essene, E. J. (1994). Determining the significance of high-grade shear zones by using temperature-time paths, with examples from the Grenville orogen. *Geology*, *22*(8), 743-746. https://doi.org/10.1130/0091-7613(1994)022<0743:DTSOHG>2.3.CO;2

Vannucchi, P., Maltman, A., Bettelli, G., & Clennell, B. (2003). On the nature of scaly fabric and scaly clay. *Journal of Structural Geology*, *25*(5), 673-688. https://doi.org/10.1016/S0191-8141(02)00066-4

Vauchez, A., Tommasi, A., & Mainprice, D. (2012). Fault (shear zones) in the Earth's mantle. *Tectonophysics*, *558-559*, 1-27. https://doi.org/10.1016/j.tecto.2012.06.006

Vega Granillo, R., Calmus, T., Meza Figueroa, D., Ruiz, J., Talavera Mendoza, O., & López Martínez, M. (2009). Structural and tectonic evolution of the Acatlán Complex, Southern Mexico: Its role in the collisional history of Laurentia and Gondwana. *Tectonics*, *28*(4), TC4008. https://doi.org/10.1029/2007TC002159

Velandia, F. A. P. (2017). *Cinemática de las fallas mayores del macizo de Santander: Énfasis en el modelo estructural y temporalidad al sur de la falla de Bucaramanga* (Ph.D. thesis), Universidad Nacional de Colombia, Bogotá.

Verhaert, G., Muchez, P., Sintubin, M., Similox Tohon, D., Vandycke, S., & Waelkens, M. (2003). Reconstruction of neotectonic activity using carbonate precipitates: A case study from northwestern extremity of the Isparta Angle (SW Turkey). *Journal of Geochemical Exploration*, *78-79*, 197-201. https://doi.org/10.1016/S0375-6742(03)00070-0

Vernon, R. H., & Clarke, G. L. (2008). *Principles of metamorphic petrology*. Cambridge University Press.

Vernon, R. H, Holdswoth, R. E., Selby, D., Dempsey, E., Finlay, A. J., & Fallick, A. E. (2014). Structural characteristics and Re-Os dating of quartz-pyrite veins in the Lewisian Gneiss Complex, NW Scotland: Evidence of an Early Paleoproterozoic hydrothermal regime during terrane amalgamation. *Precambrian Research*, *246*, 256-267. https://doi.org/10.1016/j.precamres.2014.03.007

Ganerød, G. V., Braathen, A., & Willemoes Wissing, B. (2008). Predictive permeability model of extensional faults in crystalline and metamorphic rocks; verification by pre-grouting in sub-sea tunnels in Norway. *Journal of Structural Geology*, *30*(8), 993-1004. https://doi.org/10.1016/j.jsg.2008.04.001

Villa, I. (2002). Isotopic closure. *Terra Nova*, *10*(1), 42-47. https://doi.org/10.1046/j.1365-3121.1998.00156.x

Villa, I. M., Bucher, S., Bousquet, R., Kleinhanns, I. C., & Schmid, S. M. (2014). Dating polygenetic metamorphic assemblages along a transect across the Western Alps. *Journal of Petrology*, *55*(4), 803-830. https://doi.org/10.1093/petrology/egu007

Vinasco, C., & Cordani, U. (2012). Reactivation episodes of the Romeral Fault System in the northwestern part of Central Andes, Colombia, through ^{39}Ar-^{40}Ar and K-Ar results. *Boletín Ciencias de la Tierra*, *32*, 111-124.

Vinasco, C. J. (2001). *A utilização da metodologia 40Ar-39Ar para o estudo de reativações tectônicas em zonas de cisalhamentos. Paradigma, O Falhamento de Romeral nos Andes Centrais de Colômbia* (Master thesis). Universidade de São Paulo.

Viola, G., Scheiber, T., Fredin, O., Zwingmann, H., Margreth, A., & Knies, J. (2016). Deconvoluting complex structural histories archived in brittle fault zones. *Nature Communications*, *7*, 13448. https://doi.org/10.1038/ncomms13448

Vissers, R. L. M., Van Hinsbergen, D. J. J., Wilkinson, C. M., & Ganerød, M. (2016). Middle Jurassic shear zones at Cap de Creus (eastern Pyrenees, Spain): A record of pre-drift extension of the Piemonte-Ligurian Ocean? *Journal of the Geological Society*, *174*(2), 289-300. https://doi.org/10.1144/jgs2016-014

Vitale, S., & Mazzoli, S. (2008). Heterogeneous shear zone evolution: The role of shear strain hardening/softening. *Journal Structural Geology*, *30*(11), 1383-1395. https://doi.org/10.1016/j.jsg.2008.07.006

Vrolijk, P., Pevear, D., Covey, M., & La Riviere, A. (2018). Fault gouge dating: History and evolution. *Clay Minerals*, *53*(3), 305-324. https://doi.org/10.1180/clm.2018.22

Vrolijk, P., & van der Plujim, B. A. (1999). Clay gouge. *Journal of Structural Geology*, *21*(8-9), 1039-1048. https://doi.org/10.1016/S0191-8141(99)00103-0

Wallace, R. (1951). Geometry of shearing stress and relation to faulting. *The Journal of Geology*, *59*(2), 118-130. https://doi.org/10.1086/625831

Wallis, S. R. (1992). Vorticity analysis in a metachert from the Sanbagawa belt, SW Japan. *Journal of Structural Geology*, *14*(3), 271-280. https://doi.org/10.1016/0191-8141(92)90085-B

Wang, B., Cluzel, D., Shu, L., Faure, M., Charvet, J., Chen, Y., Meffre, S., & Jong, K. (2009). Evolution of calc-alkaline to alkaline magmatism through Carboniferous convergence to Permian transcurrent tectonics, western Chinese Tianshan. *International Journal of Earth Sciences*, *98*(6), 1275. https://doi.org/10.1007/s00531-008-0408-y

Wang, Y., Zwingmann, H., Zhou, L., Lo, C., Viola, G., & Hao, J. (2016). Direct dating of folding events by $^{40}Ar/^{39}Ar$ analysis of synkinematic muscovite from flexural-slip planes. *Journal Structural Geology*, *83*, 46-59. https://doi.org/10.1016/j.jsg.2015.12.003

Watanabe, Y., Nakai, S. I., & Lin, A. (2008). Attempt to determine U-Th ages of calcite veins in the Nojima fault zone, Japan. *Geochemical Journal*, *42*(6), 507-513. https://doi.org/0.2343/geochemj.42.507

Webb, L. E., Johnson, C. L., & Minjin, C. (2010). Late Triassic sinistral shear in the East Gobi Fault Zone, Mongolia. *Tectonophysics*, *495*(3-4), 246-255. https://doi.org/10.1016/j.tecto.2010.09.033

Wells, M. L., Snee, L. W., & Blythe, A. E. (2000). Dating of major normal fault systems using western United States. *Journal of Geophysical Research: Solid Earth*, *105*(B7), 16303-16327. https://doi.org/10.1029/2000JB900094

Wenk, H. R., Johnson, L. R., & Ratschbacher, L. (2000). Pseudotachylytes in the Eastern Peninsular Ridges of California. *Tectonophysics*, *321*(2), 253-277. https://doi.org/10.1016/S0040-1951(00)00064-0

Wernicke, R. S., & Lippolt, H. J. (1997). (U+Th)-He evidence of Jurassic continuous hydrothermal activity in the Schwarzwald basement, Germany. *Chemical Geology*, *138*(3-4), 273-285. https://doi.org/10.1016/S0009-2541(97)00020-X

White, S. H., Burrows, S. E., Carreras, J., Shaw, N. D., & Humphreys, F. J. (1980). On mylonites in ductile shear zones. *Journal of Structural Geology*, *2*(1-2), 175-187. https://doi.org/https://doi.org/10.1016/0191-8141(80)90048-6

Whitmeyer, S. J. (2008). Dating fault fabrics using modern techniques of $^{40}Ar/^{39}Ar$ thermochronology: Evidence for Paleozoic deformation in the Eastern Sierras Pampeanas, Argentina. *Journal of the Virtual Explorer*, *30*. https://doi.org/10.3809/jvirtex.2008.00207

Wibberley, C. A. J., Yielding, G., & Di Toro, G. (2008). Recent advances in the under-standing of fault zone internal structure: A review. In C. A. J. Wibberley, W. Kurz, J. Imber, R. E. Holdsworth, & C. Collettini (eds.), *The internal structure of fault zones: Implications for mechanical and fluid-flow properties* (pp. 5-33). Special Publication vol. 299. Geological Society of London. https://doi.org/10.1144/SP299.2

Winter, J. D. (2001). *An introduction to igneous and metamorphic petrology*. Prentice Hall.

Wise, D. U., Dunn, D. E., Engelder, J. T., Gieser, P. A., Hatcher, R. D., Kish, S. A., Odom, A. L., & Schamel, S. (1984). Fault-related rocks: Suggestions for terminology. *Geology*, *12*(7), 391-394. https://doi.org/10.1130/0091-7613(1984)12<391:FRSFT>2.0.CO;2

Wolff, R., Dunkl, I., Kiesselbach, G., Wemmer, K., & Siegesmund, S. (2012). Thermochronological constraints on the multiphase exhumation history of the IvreaVerbano Zone of the Southern Alps. *Tectonophysics*, *579*, 104-117. https://doi.org/10.1016/j.tecto.2012.03.019

Wolfler, A., Kurz, W., Danisik, M., & Rabitsch, R. (2010). Dating of fault zone activity by apatite fission track and apatite (U-Th)/He thermochronometry: A case study from the Lavanttal fault system (Eastern Alps). *Terra Nova*, *22*(4), 274-282. https://doi.org/10.1111/j.1365-3121.2010.00943.x

Woodcock, N. H., & Mort, K. (2008). Classification of fault breccias and related fault rocks. *Geological Magazine*, *145*(3), 435-440. https://doi.org/10.1017/S0016756808004883

Wu, F. T. (1978). Mineralogy and physical nature of clay gouge. *Pure and Applied Geophysics*, *116*(4-5), 655-689. https://doi.org/10.1007/BF00876531

Xypolias, P. (2009). Some new aspects of kinematic vorticity analysis in naturally deformed quartzites. *Journal of Structural Geology*, *31*(1), 3-10. https://doi.org/10.1016/j.jsg.2008.09.009

Xypolias, P. (2010). Vorticity analysis in shear zones: A review of methods and applications. *Journal of Structur-*

al Geology, *32*(12), 2072-2092. https://doi.org/10.1016/j.jsg.2010.08.009

Xypolias, P., Spanos, D., Chatzaras, V., Kokkalas, S., & Koukouvelas, I. (2010). Vorticity of flow in ductile thrust zones: Examples from the Attico-Cycladic Massif (Internal Hellenides, Greece). In R. D. Law, R. W. H. Butler, R. E. Holdsworth, M. Krabbendam, & R. A. Strachan (eds.), *Continental tectonics and mountain building: The legacy of Peach and Horne* (pp. 687-714). Special Publications vol. 335. Geological Society of London. https://doi.org/10.1144/SP335.28

Xypolias, P., & Kokkalas, S. (2006). *Heterogeneous ductile deformation along a mid-crustal extruding shear zone: An example from the External Hellenides (Greece)* (pp. 497-516). Special Publications vol. 268. Geological Society of London. https://doi.org/10.1144/GSL.SP.2006.268.01.23

Žalohar, J. (2014). *T-Tecto Studio X5. Integrated software for structural analysis of earthquake focal-machanism and fault-slip data. Introductory tutorial.*

Zaun, P. E., & Wagner G. A. (1985). Fission-track stability in zircons under geological conditions. *Nuclear Tracks and Radiation Measurements*, *10*(3), 303-307. https://doi.org/10.1016/0735-245X(85)90119-X

Zulauf, G. (2001). Structural style, deformation mechanisms and paleodifferential stress along an exposed crustal section: Constraints on the rheology of quartzofeldspathic rocks at supra- and infrastructural levels (Bohemian Massif). *Tectonophysics*, *332*(1-2), 211-237. https://doi.org/10.1016/S0040-1951(00)00258-4

Zuluaga, C., Stowell, H., & Tinkham, D. (2006). *Thermodynamic modeling: A tool for understanding phase equilibria & metamorphic processes. A workshop manual.*

Zwingmann, H., & Mancktelow, N. S. (2004). Timing of Alpine fault gouges. *Earth and Planetary Science Letters*, *223*(3-4), 415-425. https://doi.org/10.1016/j.epsl.2004.04.041

Boletín Geológico

SERVICIO GEOLÓGICO COLOMBIANO

Boletín Geológico, 48(1), 123-97, 2021,
https://doi.org/10.32685/0120-1425/bol.geol.48.1.2021.504

© Author(s) 2021. This work is distributed under the Creative Commons Attribution 4.0 License.

Received: May 15, 2020

Revised: August 14, 2020

Accepted: March 2, 2021

Published online: July 12, 2021

Graphical representation of structural data in the field: A methodological proposal for application in deformed areas

Representación gráfica de datos estructurales en campo: Una propuesta metodológica para su aplicación en áreas deformadas

Julián Andrés **López Isaza**[1], Mario Andrés **Cuéllar Cárdenas**[1], Lina María **Cetina Tarazona**[1], Anny Julieth **Forero Ortega**[1], Ana Milena **Suárez Arias**[1], Óscar Freddy **Muñoz Rodríguez**[1], Luis Miguel **Aguirre Hoyos**[1], María Juliana **Gutiérrez López**

1 Dirección de Geociencias Básicas, Servicio Geológico Colombiano, Bogotá, Colombia.
Corresponding author: Julián Andrés López, jlopez@sgc.gov.co

Abstract

The description of the fabric elements represented by the linear and planar structures present at different scales is a key component of fieldwork. A scheme is proposed for the systematic registration of planes and lineations, coded as S (planar surfaces), F (folds), and L (lineations), among others, that allows for the orderly storage of the measurements taken. This scheme includes information related to the kinematics, the kinematic indicators, and the certainty or reliability ascribed to the assigned movement. In the fieldwork, the graphic representation of the structural measures in modified projection nets includes concentric circles for each dip. Direct drawing of the outcrop data is undertaken, dispensing with the use of tracing or transparent paper. The stereograms resulting from the graphic representation in the modified Wulff stereographic projection net, and the modified Schmidt equal-area net, can be complemented by rose diagrams for visualization of the spatial ordering. During field campaigns in the outcrops, it is essential to visualize the spatial orientation of the data in the diagrams to determine the main structural trends, the vergence, the kinematic nature of faults and shear zones, paleo-stress tensors, and to differentiate structural domains, among others. This information supports the reconstruction of geological and tectonic history and the establishment of relationships between the different geological processes.

Keywords: Structural analysis, structural data, stereographic projection, equal-area projection, rose diagram, fabric elements.

Citation: López Isaza, J. A., Cuéllar Cárdenas, M. A., Cetina Tarazona, L. M., Forero Ortega, A. J., Suárez Arias, A. M. Muñoz Rodríguez, O. F., Muñoz Rodríguez, O. F., Aguirre Hoyos, L. M., & Gutiérrez López, M. J. (2021). Graphical representation of structural data in the field: A methodological proposal for its application in deformed areas. *Boletín Geológico, 48*(1), 123-139. https://doi.org/10.32685/0120-1425/bol.geol.48.1.2021.504

Resumen

La descripción de los elementos de fábrica representados por las estructuras lineales y planares presentes a diferentes escalas es uno de los aspectos más relevantes del trabajo de campo. Así, para el registro sistemático de planos y lineaciones, codificados como S (superficies planas), F (pliegues), L (lineamientos), entre otros, se propone un esquema que permite el almacenamiento ordenado de las mediciones realizadas. Este esquema incluye información relacionada con la cinemática, los indicadores cinemáticos y la certeza o confiabilidad que se otorga al movimiento asignado. Durante el trabajo de campo, la representación gráfica de las mediciones estructurales se realiza en redes de proyección modificadas que incluyen círculos concéntricos para cada buzamiento, y permiten dibujar al trazo los datos estructurales en el afloramiento, prescindiendo del uso de papel de calco o transparente. Como tal, los estereogramas resultantes de la representación gráfica en la red de proyección estereográfica de Wulff modificada, y la red de igual área de Schmidt modificada, deben complementarse con diagramas rosa para la visualización del ordenamiento espacial. Durante las campañas de campo, en los afloramientos es fundamental visualizar la orientación espacial de los datos en los diagramas para determinar las principales tendencias estructurales, la vergencia, el sentido cinemático de fallas y zonas de cizallamiento, los tensores de paleo-esfuerzo, y diferenciar dominios estructurales, entre otros factores. Esta información apoya la reconstrucción de la historia geológica y tectónica y el establecimiento de las relaciones entre los diferentes procesos geológicos.

Palabras clave: Registro de datos estructurales, red de proyección modificada, proyección estereográfica, proyección de igual área, diagrama rosa, elementos de fábrica.

1. Introduction

Analysis of the spatial location of geological structures acquired in the field using graphical techniques during mapping campaigns is of vital importance for determining the direction of tectonic drag, the kinematics of shear zones and paleostress tensors, and axes of elongation and shortening; and to define the deformation phases recorded by lithological units. This makes it possible to reconstruct geological and tectonic history as well as establish relationships between different geological processes (Turner and Weiss, 1963; McClay, 1987; Passchier et al., 1990; Hatcher, 1995; Hopgood, 1999; Passchier and Trouw, 2005; Babín and Gómez, 2010a; Fossen, 2010; López and Zuluaga, 2012; Compton, 2016; Fossen et al., 2019; Fossen, 2019). Traditionally, to determine the spatial orientation of fabric elements, the horizontal and vertical angular relationships of geological structures are measured using analog geological compasses, and the data thus acquired are recorded in field notebooks.

The acquisition and storage of structural data is possible with the use of different mobile devices subject to connection availability, through the implementation of applications (apps) such as *Stereonet Mobile, eGEO Compass Pro*, *GeoClino for iPhone*, *Geological Compass Full*, *Lambert*, and *Structural Compass*. This makes it possible to obtain a quick record of the orientation of geological structures and to evaluate the uncertainty, from the visualization of the spatial distribution of the data in stereograms. It is also possible to obtain the location of the points or stations where the structural data are taken on digital map platforms, by means of positioning systems included in mobile devices, and their visualization is possible in viewers, such as *Google Earth*, or apps compatible with geographic information systems, such as *Mobile Data Collection*, *CartoDruid*, *MAPit*, *Nextgis* and *Qfield for Qgis*, and *ArcGIS Explorer* and *Collector for ArcGIS*. Describing each of the aforementioned applications is beyond the scope of this article, but the interested reader is referred to Allmendinger et al. (2017), Novakova and Pavlis (2017), Lee et al. (2018), and Whitmeyer et al. (2019), among others, as well as the respective descriptions provided by the developers.

For the discrimination, recording, and description of data pertaining to different structures, basic concepts are used and applied from different structural geology texts (Hills, 1972; Hobbs et al., 1976; Blés, 1977; Bartlett et al., 1981; Hancock, 1985; McClay, 1987; Marshak and Mitra, 1988; Price and Cosgrove, 1990; Hatcher, 1995; Ragan, 2009; Babín and Gómez, 2010b and c; Allmendinger, 2019). However, it is important to keep in mind the methodical and orderly recording of the data acquired in the field, since, particularly when they are not measured with mobile devices (which by default integrate the data in tables), they should allow differentiating the types of data and structures measured (e.g., foliation, cleavage, fault

plane, mineral lineation, striation, and fold axes), as well as including parameters for rating certainty or reliability (quantitative or qualitative) vis-à-vis kinematics of faults and shear zones. Whether and the extent to which data logging is undertaken appropriately depends on the nature and extent of the geologist´s experience as well as the complexity of the task. If it is assumed that the data will be analyzed using some specialized software (such as Tectonics FP written and developed by Reiter, F. and Acs, P. http://www.tectonicsfp.com, Ortner et al. (2002); TectonicVB written and developed by Ortner, H. https://www.uibk.ac.at/geologie/tvb/front.html, Ortner et al. (2002); Stereonet written and developed by Allmendinger, R. https://www.rickallmendinger.net, Allmendinger et al. (2012) and Cardozo and Allmendinger (2013); GEOrient written and developed by Holcombe, R. https://www.holcombe.net.au/software/georient.html, Holcombe (2015); Faultkin written and developed by Allmendinger, R. https://www.rickallmendinger.net, Marrett and Allmendinger (1990) and Allmendinger et al. (2012); Win-Tensor written and developed by Delvaux, D. http://damiendelvaux.be/Tensor/WinTensor/win-tensor.html, Delvaux and Sperner (2003); and T-Tecto written and developed by Žalohar, J. https://quantectum.com/t-tecto/, Žalohar and Vrabec (2007)), then parameters for assigning certainty to kinematics must be taken into account.

There are different notations and conventions for the recording of structural data taken in the field (McClay, 1987), among which the azimuthal conventions or azimuth of dip, right hand rule, quadrants, and the convention given by dip (inclination of the plane)®azimuth of dip (direction of inclination) or dip direction stand out. Additionally, to gauge the representativeness of the structural data acquired in the field, the following should be described: the types of structures investigated, the shear relationships between them, the lithology analyzed, and the uncertainties generated by the surface irregularities of the structure planes. Some questions that are very common among students, researchers, and other professionals faced with carrying out work with emphasis on structural geology, especially at sites where it is not possible to use mobile devices, are as follows. What structural variables should be measured? How should data be recorded during a field campaign? How much data should be acquired on average? To answer some of these questions, in this paper we present a proposal for the rapid recording and graphical visualization of structural data acquired in the field directly in the outcrop. To this end, we propose a scheme (either by means of analog compasses or with mobile devices to complement the information) that allows their arrangement by type of fabric element (planar or linear), including a qualitative rating of the certainty or reliability of the kinematics assigned to the direction of movement of shear zones (Delvaux and Sperner, 2003; Žalohar, 2020).

In addition, during the field campaign, spatial visualization of strike-dip relationships of geological structures directly in outcrops is realized by plotting structural data from the application of conventional methods facilitated by stereographic projection grids, as a graphical alternative to represent three-dimensional data in a two-dimensional way (Bucher, 1944; Ramsay, 1967; Sander, 1970; Chica, 1984). This implies the dedication of time in the field to obtain a sufficiently representative amount of data for the stereograms. A stereographic projection network allows representing orientations of planes and lines with respect to the center of a sphere on an equatorial projection plane, combining spherical and azimuthal projections (Phillips, 1973; Lisle and Leyshon, 2004; Babín and Gómez, 2010a).

For conventional graphical representation of structural data in the field, especially in areas where it is not possible to use mobile devices for data visualization purposes, it is necessary to have a stereographic grid at hand (available in many structural geology textbooks) and paper (transparent or tracing) which is rotated over the fixed grid to plot the data (Phillips, 1973; Allmendinger, 2019). This process can be streamlined by using a modified stereographic template that allows the data to be plotted directly, i.e., dispensing with paper that must be rotated over the stereographic template. Taking into account the need to ensure that the graphical representation of structural data directly in the outcrop is done effectively and efficiently, in this article we propose the use of a modified stereographic projection grid that facilitates the direct plotting of the data, dispensing with the use of transparent / tracing paper. This is complemented with the elaboration of rose diagrams or histograms of circular frequencies that allow visualizing the main trends of the structures in the field. This makes it possible to establish the direction of tectonic drag (among other important considerations for accurate interpretation in the field), to formulate hypotheses, and to have a general understanding of the paleo-stress field.

2. Recording of data acquired in the field

Structural characterization in deformed areas includes the study of fabric elements represented by linear structures (e.g., mineral lineations, axial axes of folds or microfolds, and slickenside linea-

tions or slickenlines) and planar structures (e.g., stratification, joints, cleavages, and fault planes), which are described during fieldwork, in addition to the establishment of the relationships between them, the mechanics of the deformation, their temporalities, and the structural level of the crust in which they developed (Turner and Weiss, 1963; Roberts, 1982; Wilson, 1982; Passchier *et al*., 1990; Price and Cosgrove, 1990; Hatcher, 1995; Hopgood, 1999; Van der Pluijm and Marshak, 2004; Fossen, 2010). A fact of particular importance for descriptions of geologic structures is that one should have control, as far as possible, of the three-dimensional layout of the structure. The most accepted convention for the recording of structures generated from progressive deformation, deformation phases, and superposition of deformation events classifies structures by type, discriminating the fabric elements (planes and lineations) including the relative temporal order of the formation of the structures (Turner and Weiss, 1963; Marshak and Mitra, 1988; Passchier and Trouw, 2005).

In this sense, the fabric elements are distinguished as 'S' for planar surfaces, 'F' for folding, 'L' for lineations, 'J' for joints, 'V' for veins and veinlets, 'D' for deformations, and 'M' for metamorphic events (Sander, 1911; Turner and Weiss, 1963; McClay, 1987; Marshak and Mitra, 1988; Passchier and Trouw, 2005). The temporal order between the developed structures is defined according to their shear relationships, and in this sense, they are recorded from oldest to most recent, as $_{-0}$ (when the structure is primary) to -n (Turner and Weiss, 1963; Passchier and Trouw, 2005). Planar structures are denoted S_0 when they correspond to layering, and S_1 to S_n when they are overlapping planes and include foliations, whereas folds, lineations, joints, veins and veinlets, deformations, and metamorphic events range from $_{-1}$ to $_{-n}$ (cf. McClay, 1987; Marshak and Mitra, 1988; Price and Cosgrove, 1990; Passchier and Trouw, 2005).

Since exact determination of structure types is fundamental for the visualization of the structural data in the field, a scheme for recording the different fabric elements, planar or linear, is proposed, so that the information can be properly ordered (Table 1). This scheme considers the ordered recording of the planar and linear fabric elements, differentiating the main data groups, which include the different types of planar structures and lineations. The proposed model includes two columns for recording planar structures and lineations, one for the structural data, regardless of the notation used, and another for the type of structure, either planar or lineation. It is suggested that, where required, the recording of lineations should always be undertaken in front of the datum of the plane containing them, which is essential when recording striations that demarcate the direction of displacement (e.g., slickenside lineations or slickenlines) associated with fault planes, or when recording lineations associated with foliations (e.g., mineral lineation). On the other hand, it is also important, as far as possible, to specify the frequency, intensity, and spacing between fault planes. Additionally, for faults, it is necessary to include the data corresponding to the kinematics or direction of movement, including the indicators that support the kinematics, and an assessment of the certainty or reliability of the kinematics assigned to the direction of movement.

Among the fabric elements, planes (or planar surfaces) include layering (S_0), cleavage (S1 - S_n), compaction cleavage, dissolution pressure (stylolites and slickolites), disjunctive, pencil, slate, hinge or axial plane, phyllitic, crenulation, as well as other types of foliations (S_{n+1} - S_{n+n}), such as schistosity, gneissic foliation, banding, transposition and/or mylonitic foliation, shear band cleavage (C), deformation bands, joints (J), magmatic or flow foliation, shears and fault planes, friction or slickensides, contacts, and veins and dykes. Lineations (L) can be discrete structural or stretching (oriented pebbles, ooids, fossils, and alteration spots), constrained structural (intersections, charnels, boudins, mullions, and slip), or polycrystalline mineral lineations (rods, mineral aggregates, mineral slickenlines, and non-fibrous overgrowth), and grain or monomineral (acicular habit, elongation, and mineral fibers), among others.

For the recording of structural data of faults and shear zones, different considerations must be taken into account, including the type of shear (fault planes), the determination of the kinematics or direction of movement, with their respective indicators, and the assignment of the level of certainty or reliability of the kinematics. The latter is of particular importance for subsequent data processing in specialized software. The shear types (and failure planes) included in brittle shear zones can be described as *principal shears* (Y), which accommodate most of the displacement and are parallel to the main direction of motion in a shear zone, synthetic Riedel shears (R) oriented with angles equivalent to half the angle of internal friction, antithetic Riedel shears (R') oriented with angles equal to the difference of the subtraction of 90° and half the angle of internal friction, tension fractures (T) oriented with angles of 45° with respect to the main direction of motion, and synthetic (P) and antithetic (P' or X) post-Riedel shears (Figure 1). On the other hand, the development of step veins (*en echelon*), kink bands, and antifractures is also common in shear zones; and in ductile shear zones the limits of the shear zone and the foliations contained in them are recorded.

Table 1. Proposed data recording scheme for measurements undertaken on planar and linear fabric elements during field campaigns.

Plane		Lineation		Movement direction and Sense of shear	
Structural data	**Planar type[1]**	**Structural data**	**Lineation type**	**Kinematic**	**Assurance level**
	Planar fabric elements				
	S_0		Linear fabric elements		
	$S_1 - S_n$		Mineral lineation		
	$S_{n+1} - S_{n+n}$		Hinge line of folds		
	Axial surface or hinge plane		Crenulation		
Dip Direction (*Dip→Dir*)[2]	Veins		Intersection lineation		
Quadrants	Contacts	Plunge → Az. Plunge[2]			
Right hand rule	Joints (J)	Pitch or Rake and pitching sense		Right lateral or dextral	Low (Kinematic: supposed)
Strike Azimuth	Slickenside plane or fault plane		Slickenline	Left lateral or sinistral	Medium (Kinematic: Possible or Probable)
	Riedel shear type (Y, R, R', P, T, X)		Slickenside-related features	Normal	High (Kinematic: True)
			Striations	Reverse Thrust	
				Oblique	
				Kinematic indicators[3]	

1 Includes the designation of the type of plane, i.e., Sn - foliation

2 Notation taken from McClay (1987)

3 The kinematic indicators by which the kinematics or direction of motion is determined should be recorded.

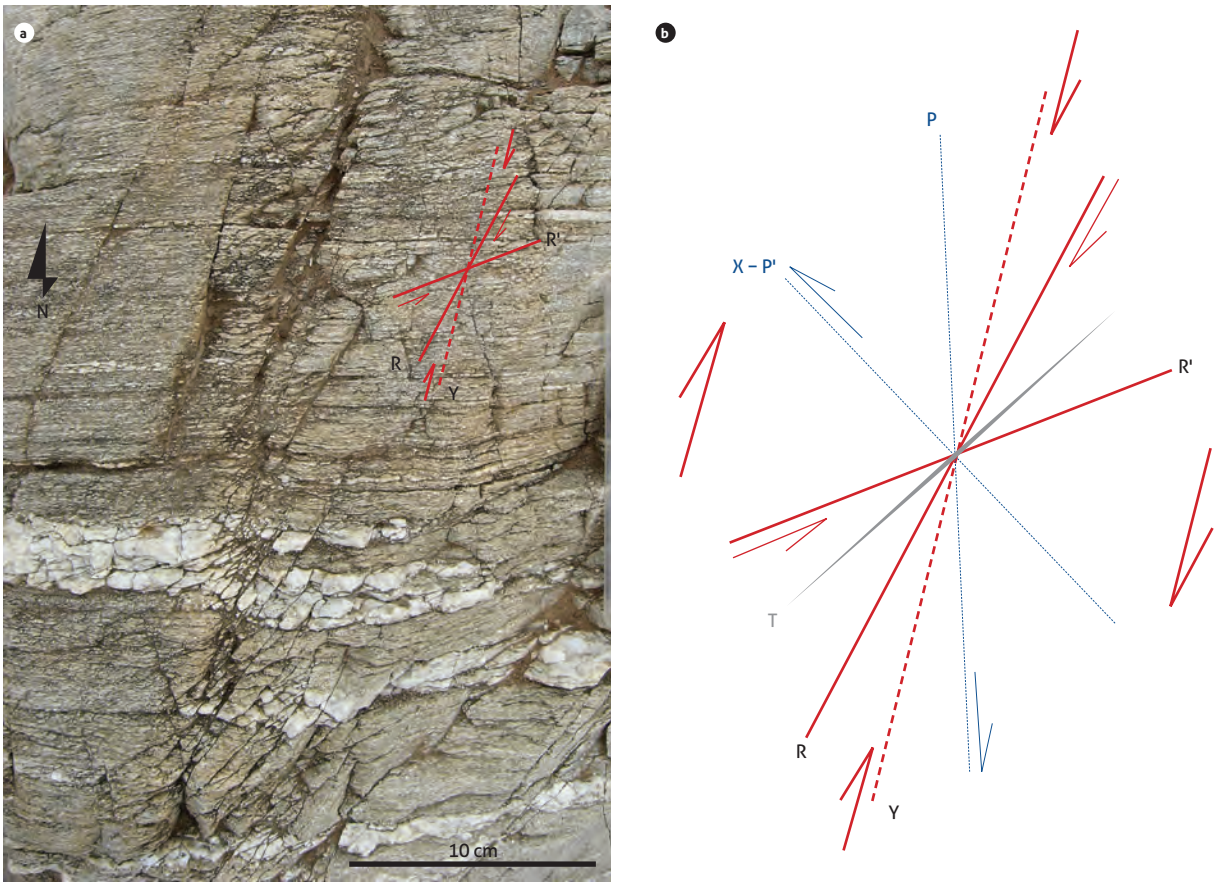

Figure 1. Interpretation of Riedel shears in outcrop
a) Distribution of synthetic and staggered antithetic Riedel shears in amphibolite outcrops belonging to the Neis de Macuira, Serranía de Simarúa, Alta Guajira. b) Schematic representation of the distribution of conjugate Riedel shears, which may be associated. R, synthetic Riedel shears. R', antithetic Riedel shears. Y, principal shears. T, tension fractures. P, post-Riedel synthetic shears. P' or X, antithetic post-Riedel shears.

In faults and shear zones, the direction of movement or kinematics can be defined as normal, reverse, strike or transcurrent, and oblique, and can be determined from kinematic or shear direction indicators on the friction or fault plane, or in sections perpendicular to the friction plane (Simpson and Schmid, 1983; Doblas, 1987; 1998; Hanmer and Passchier, 1991; Mawer, 1992; Passchier and Trouw, 2005). Accordingly, kinematic indicators are structures that allow determining the direction of movement or flow of one rock mass relative to another, both in brittle and ductile shear zones (Petit et al., 1983; Sugden, 1987; Petit, 1987; Doblas, 1987; 1998; Doblas et al., 1997 a and b; Passchier and Coelho, 2006). The most common kinematic indicators in faults and brittle shear zones that have developed on the fault plane are fault grooves, tectonic channels, slickenlines, congruent and incongruent steps, growth fibers, 'V' or crescentic markings, trails, rolling grooves, spurs, notches and normal and reverse microfractures, among others (Figure 2). On the other hand, in sections perpendicular to the friction plane, Riedel shears (T, R, and P criteria), congruent and incongruent starting steps, crystallization steps, accretion steps, tension cracks, normal and inverse microfractures, fault-produced schistosities and spurs, among others, can be differentiated. The most common kinematic indicators in ductile shear zones include shear bands and S-C-C' structures, boudinage, objects (porphyroclasts and porphyroblasts) of mantle, sigmoids, pressure shadows, flanking structures, tension veins, and folds, among others (Figure 2). However, describing the full array of kinematic indicators is beyond the scope of this paper, so the reader is referred to review the foregoing references.

Qualitative assessment of the certainty or reliability of the kinematics assigned to the direction of movement of faults and shear zones depends on kinematic indicators, which in some cases can be ambiguous, or, in other words, not all indicators are reliable, which is why it is necessary to correctly describe the observed indicators (on types of indicators and their interpretation, see Doblas, 1998). Therefore, robust indicators, such as steps with crystal fiber development, tension cracks, hybrid fractures, Riedel (synthetic and conjugated antithetic), or slickensides, associated with slickenlines, allow for obtaining a reliable sense of movement. On the other hand, kinematic indicators, such as V-shaped notches, congruent and incongruent starting steps, accretionary steps, isolated synthetic or antithetic microfractures, transposed previous foliations, and the inclination of microfractures, can lead to ambiguous or erroneous interpretations, and result in an unreliable sense of motion. Similarly, a combination of reliable and unreliable indicators results in interpretations in which a moderately reliable sense of motion is obtained, and, therefore, a medium level of certainty. Accordingly, we propose that the kinematics in the data recording table should be qualitatively ascribed as true, when the level of certainty is high; probable or possible, when the level of certainty is moderate or the indicators taken into account for the definition of the kinematics are ambiguous; and assumed, when the level of certainty is low. However, we consider that the way in which the level of certainty is designated and recorded depends to a large extent on the user's preference for particular software, since numerical or alphabetical codes may be required. On the other hand, although it is not always possible, certainty or reliability should ideally be determined from the identification of an association of different kinematic indicators that confirm the assigned direction of movement, so it is necessary to identify both those that are on the friction or failure plane, as well as those that occur in sections perpendicular to the friction plane.

3. Graphical representation of planar and linear data: Modified stereographic projection grid

To dispense with the use of transparent / tracing paper during the graphical representation of structural data in the field, the stereographic projection grid (Figure 3) has been modified to facilitate the direct plotting of structural data. More specifically, for the graphical representation of planar and linear data in the field, the Wulff (Figure 3a) and Schmidt (Figure 3b) grids were modified, including concentric circles for each inclination value (of 10°) inside the stereographic projection grid, which allows for direct plotting without rotations; in this way, visualization of the data in the outcrop is possible. This methodology simplifies the process that has traditionally been followed, in which the plotting of structural data is performed on a stereographic projection grid involving the use of tracing or transparent paper, and the plotting of the data is undertaken by rotating the paper on the stereographic projection grid (Figure 4) (Lisle and Leyshon, 2004; Ghosh, 2013).

Geometrically, stereographic grids represent the equatorial plane of a sphere viewed from the zenith. These grids are constituted by major circles, which correspond to north-south planes with different angles of inclination, passing exactly through the center of the sphere containing the equatorial plane, and by

Figure 2. Kinematic indicators of brittle and ductile shear zones
a) Fault or friction plane developed in the Santa Barbára Monzogranite, Los Curos-Guaca road, La Judia creek sector. b) Detail of fault plane with development of fault grooves (*s*). The white line is arranged parallel to the direction of the fault grooves, oblique dextral kinematics. c) Slickenlines and step-steps, Perchiquez river fault, oblique dextral kinematics. d) Beheaded folds (*p*) with boudinized flanks and development of *pinch and swell* structures (*b*) parallel to the transposition foliation, as evidence of ductile shearing, Neis de Bucaramanga, Rio de Oro sector, Cesar.

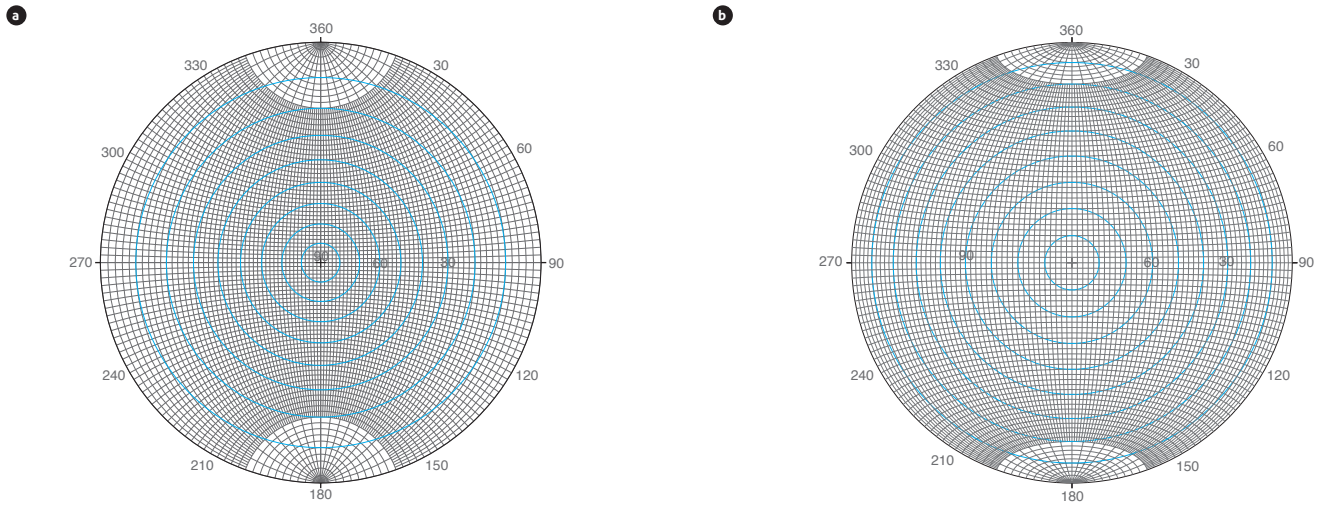

Figure 3. a) Modified Wulff stereographic projection grid, including concentric guiding circles (blue) for dip measurement and great circle plotting. b) Modified Schmidt equal-area projection grid, including concentric guiding circles (blue) for dip measurement and major circle plotting. c) Modified Schmidt equal-area projection grid, including concentric guiding circles (blue) for dip measurement and major circle plotting.

minor circles, which correspond to vertical planes that, in general, do not pass through the center of the sphere containing the equatorial plane, and form circles with increasing radius; the maximum radius constitutes the center of the sphere, or east-west line (Phillips, 1973). The intersection between the arcs representing the major circles and the arcs representing the minor circles gives rise to what is known as the *stereographic network* (Phillips, 1973). Starting from the construction of the stereographic net, minor circles parallel to the equatorial plane, projected from the nadir and similar to a polar stereographic net, can be included on the equatorial plane (Phillips, 1973). These circles are at a tangent to the major and minor circles defining the stereographic grid (Figure 3), and indicate a given inclination, which in the case of the modified stereographic grid represent divisions between 0° and 90°. Thus, any major circle arc of random bearing with defined inclination can be plotted tangentially to the equivalent concentric minor circle (Figure 4).

The procedure followed for graphically visualizing the spatial orientation of structural data acquired in the field depends on the convention or structural notation used for recording data during fieldwork (McClay, 1987). Relevant instructions for the stereographic projection of structural data are taken into account (Phillips, 1973; Marshak and Mitra, 1988; Lisle and Leyshon, 2004), which, in general terms, places the direction of the dip azimuth on the outer circle, and the dip or inclination on the inner circles, increasing the inclination from the edge towards the center. This facilitates the graphical representation of structural data acquired under the convention or notation of quadrants, strike azimuth, right hand rule, and dip azimuth or dip direction.

3.1 Procedures for graphical representation of data

1. The orientation is measured on the outer circle of the grid for modified stereographic projection. The circle can be divided into quadrants (northeast, northwest, southeast, and southwest), or it can be read in azimuth (0 to 360°). Each major division equals 10°.
2. The dip (inclination of the plane) is read on the inner circles, taking into account that it increases towards the center; that is, the lowest inclinations would be located on the outer edge, and the highest towards the center.
3. Quadrants. As an example, the notation N 58° E/70 °NW will be plotted. On the modified stereographic projection grid the location of the northwest (NW) quadrant is identified and the bearing is located by counting 58° from north to west on the outer circle. At 90° from the point where the bearing was found, in the northeast (NE) quadrant, the dip is measured on the inner circles towards the center, locating the circle equivalent to 70°. An arc (or cyclographic trace) is drawn which joins the notch of the bearing on the outer circle and the point corresponding to the dip on the appropriate inner circle (Figure 5a), to represent the spatial orientation of the plane.

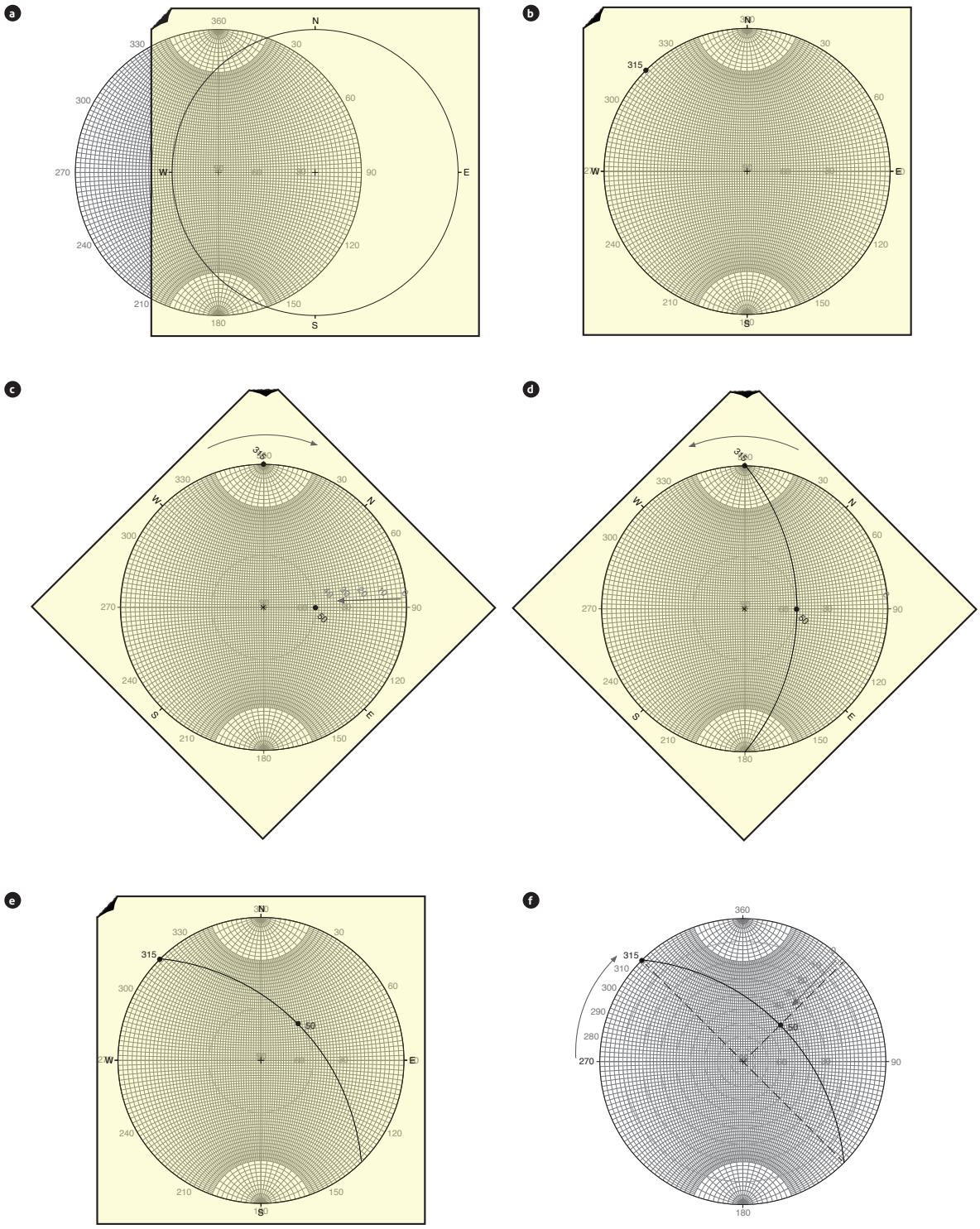

Figure 4. Traditional graphical representation of field-acquired structural data compared to the modified Wulff stereographic projection graph
a) Wulff stereographic projection grid and paper on which the structural datum 315/50 will be plotted. b) Location of the plane heading datum (315) in azimuth on the outer circle. c) Right turn of the paper until the plane heading (located on the outer circle) coincides with the north-south line of the projection grid or with the notch of 360°. d) Measurement of the dip or inclination of the plane from the outer circle inward to the notch indicating 50. e) Measurement of the dip or inclination of the plane from the outer circle inward to the notch indicating 50. f) Measurement of the plane heading (315) in azimuth on the outer circle to the notch indicating 50. Measurement of the dip or inclination of the plane from the outer circle to the inner circle, up to the notch indicating 50°. d) Trace the cyclograph along the major circle of the stereographic grid. e) Left turn of the paper to the starting point. f) Modified Wulff equal-area projection grid, in which the cyclographic trace and the pole of the cross-sectioned plane are shown directly; the cyclograph is tangent to the circle representing the 50° inclination.

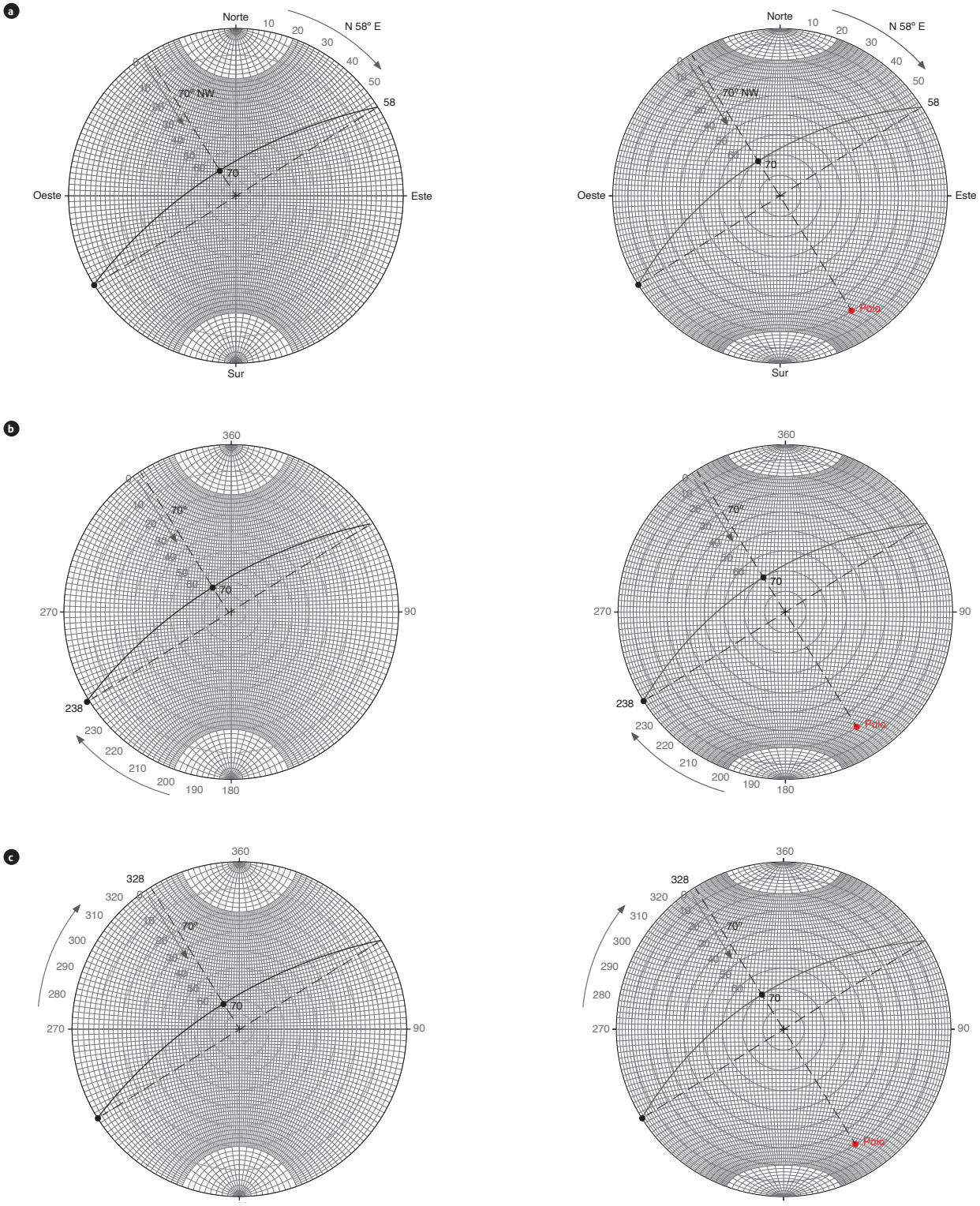

Figure 5. a) Graphical representation of structural data acquired in the field and recorded as quadrants on the modified stereographic projection grid. Left: modified Wulff stereographic projection grid. Right: modified Schmidt equal-area projection grid, showing the cyclographic trace and the plane pole. b) Graphical representation of structural data acquired in the field and recorded as heading azimuth over the modified stereographic projection grid. Left: modified Wulff stereographic projection grid. Right: modified Schmidt equal-area projection grid showing the cyclographic trace and plane pole. c) Graphical representation of structural data acquired in the field and recorded as Dip Direction (dip→dir) azimuth over the modified stereographic projection grid. Left: modified Wulff stereographic projection grid. Right: modified Schmidt equal-area projection grid, showing the cyclographic trace and the pole of the plane.

4. Azimuth of bearing (right hand ruler). As an example, the notation 238°/70° will be plotted. On the modified stereographic projection grid, the location of the bearing azimuth of 238° of a plane on the outer circle is identified. At 90 °and to the right of the point where the bearing was found, the dip is measured on the inner circles towards the center, locating the circle equivalent to 70°. An arc (or cyclographic trace) is drawn which joins the notch of the bearing on the outer circle and the point corresponding to the dip on the appropriate inner circle (Figure 5b), to represent the spatial orientation of the plane.
5. Dip direction azimuth. As an example, the notation 70°→328*° will be plotted. In the modified stereographic projection network, the location of the dip azimuth of 328° of a plane on the outer circle is identified. From this point the dip is measured on the inner circles towards the center, locating the circle equivalent to 70°. An arc (or cyclographic trace) is drawn which joins the point corresponding to the dip on the appropriate inner circle with the notch of the bearing on the outer circle (Figure 5c), to represent the spatial orientation of the plane. It should be noted that at 90°, counterclockwise and clockwise, and from the dip azimuth notch, notches can be located that would represent the strike of the plane on the outer circle.

4. Statistical determination of main structural data trends and their graphical representation

A rose plot, also known as a polar histogram, is a circular histogram of frequencies (Mardia, 1972; Davis, 2002; Borradaile, 2003; McKillup and Dyar, 2010; Singhal and Gupta, 2010; Davis et al. 2012; Sanderson and Peacock, 2020). It allows for a quick angular graphical display of the data (Marshak and Mitra, 1988; Kutty and Parthasarathi, 1992; Robson, 1994; Twiss and Moores, 2007) in areas where clarity is needed vis-à-vis the predominant principal structural trend of the fabric element of interest. This diagram is constituted by a radial distribution of lines dividing intervals of ranges of 10°, and concentric circles representing a percentage of data included in the ranges, which from the inside increase every 10 % up to the outer circle, which corresponds to 100 % (Figure 6). In such diagrams, the data are grouped into frequency intervals, converted to percentages and plotted as shaded wedge-shaped zones, called *petals*, in which the radius corresponds to the percentage value, and their orientation represents the predominant trend of orientation of the geological structures, which are directly related to the amount of data.

Preferential trends of planes and lines, such as families of joints, and structural trends of planes of different types, such as

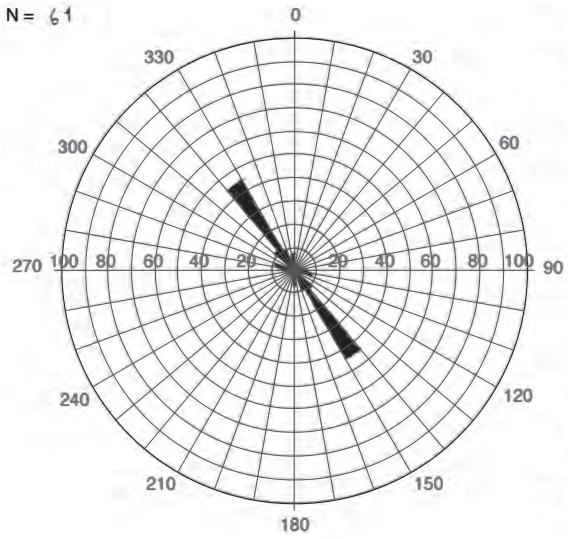

Data table for graphical representation in the strike

Total number of data (N): 61

Az. Range of Dip		Az. Range of Strike		Quadrants	Data	%
0-9	180-189	90-99	270-279	N 81-90 W	= 3	5 %
10-19	190-199	100-109	280-289	N 71-80 W	= 5	8 %
20-29	200-209	110-119	290-299	N 61-70 W		
30-39	210-219	120-129	300-309	N 51-60 W		
40-49	220-229	130-139	310-319	N 41-50 W	= 7	11 %
50-59	230-239	140-149	320-329	N 31-40 W	= 27	44 %
60-69	240-249	150-159	330-339	N 21-30 W	= 10	10 %
70-79	250-259	160-169	340-349	N 11-20 W		
80-89	260-269	170-179	350-359	N 01-10 W	= 4	7 %
90-99	270-279	0-9	180-189	N 00-09 E		
100-109	280-289	10-19	190-199	N 10-19 E		
110-119	290-299	20-29	200-209	N 20-29 E		
120-129	300-309	30-39	210-219	N 30-39 E		
130-139	310-319	40-49	220-229	N 40-49 E		
140-149	320-329	50-59	230-239	N 50-59 E		
150-159	330-339	60-69	240-249	N 60-69 E	= 1	1 %
160-169	340-349	70-79	250-259	N 70-79 E	= 1	1 %
170-179	350-359	80-89	260-269	N 80-89 E	= 3	5 %

Figure 6. Template for the graphical representation of structural data in a rose diagram, and an example of a table for the determination of the amount of data per class or interval, for its schematization by percentage
The structural data are grouped based on 10° intervals, corresponding to dip azimuth (Az. Dip Range), heading azimuth (Az. Heading Range), each with two columns of data between 0 °and 179°, and 180° and 359°, respectively, and quadrant. The data are grouped by classes in the "Data" column. In the final column, the percentage (%) is calculated by dividing the amount of data in the class by the total amount of data and then multiplying the result by 100.

S_0, S_1 to S_n, and S_{n+1} to S_{n+n}, as well as dikes, veins, and so on can be plotted on a rose diagram, and can also be used for the graphical representation of the preferential orientation of lineaments in remote sensing images. The rose diagram should be plotted by structural data type (S_0, S_1, S_n, or S_{n+n}) and include the amount of structural data represented in the plot. Traditionally, the construction of rose diagrams is performed using specialized software and mobile device applications for structural geology, such as Stereonet (Allmendinger, https://www.rickallmendinger.net). During fieldwork, it is crucial to visualize the main trends in strike and/or dip of the geological structure data so as to have control of the regional spatial distribution of the analyzed structures among the different rock bodies. Hence why it is important to construct this type of graph directly in the outcrop, as a complement to the construction of graphs by means of the modified stereographic projection network. For this purpose, a methodology is presented that facilitates the realization of this type of graph in the field, from structural data that are recorded by any of the structural notations.

According to the foregoing, the fieldwork prior to the elaboration of rose diagrams begins by grouping the structural data in classes measured in the outcrop, where the classes, for practical purposes, correspond to 10° intervals. Thus, the data are organized by classes in a table in which all possible data ranges included in the rose plot are included. The data ranges are included in three groups, which correspond to the structural notations of data measurement, and which in the table are equivalent to the dip azimuth (Az. Dip Range) and heading azimuth (Az. Heading Range) ranges, each with two columns with data between 0° and 179°, and between 180° and 359°, respectively, along with quadrants in which the data are organized in a single column (Figure 6). This grouping is arranged in such a way as to allow direct visualization of the equivalence between the types of structural notations, while favoring the grouping of axial data in 180° modes (Sanderson and Peacock, 2020). Once the data are grouped by classes in the "Data" column, the percentage (%) value is calculated by dividing the amount of data in the class by the total amount of data and multiplying the result by 100.

To construct the graph, the corresponding ranges are plotted and shaded in the rose diagram, with their respective percentages. For this, from the columns in the table that make up the heading azimuth range (Az. Heading Range), each of the classes with a percentage value is selected and associated with its respective 10° interval from the outer circle of the graph. Once this is done, the percentage value is plotted from the center to the edge within each interval, thus forming the wedges that correspond to the petals (Figure 6). One way to validate the diagram is to sum the plotted percentages, which should correspond to a total of 100. The rose diagram results in the graphical representation of the orientation, in which the petal with the highest percentage corresponds to the range that includes the preferential direction of the data, and shows trends with random distributions or with uniform directions. This diagram allows regional comparisons of the preferential orientation of different data set distributions (Sanderson and Peacock, 2020).

5. Discussion

The description and interpretation of all the fabric elements or structures present, at all scales, is one of the main inputs for the reconstruction of the geological and tectonic history of an area. In this sense, the mapping of structures directly in the field is conducive to the correct discrimination of the different fabric elements, either planar or linear, in addition to their measurement (either by using analog compasses or mobile devices) and visualization. When regional surveys are undertaken using analog compasses or mobile devices, the visualization of the data directly in the outcrop is fundamental for differentiating structural domains, validating tectonic drag directions, paleocurrent directions and structural trends, among others (Potter and Pettijohn, 1963; Nemec, 1988; Hatcher, 1995; Gabrielsen and Braathen, 2014; Abdunaser, 2015; Ahmadirouhani et al., 2017; Han et al., 2018; Rajasekhar et al., 2018). Considering that it is vital to know the arrangement of geological structures in an area by outcrop or station, the methodological implementation of the modified stereographic network approach presented herein constitutes a practical and innovative solution for the graphical representation of structural data when mapping in areas with broken, canyoned, or difficult to access topography, where there is no signal for the use of mobile devices to generate stereograms directly using apps. Also, the use of the proposed modified stereographic network allows the inclusion of stereograms and rose diagrams directly in the field notebook (e.g., if printed on sheets of adhesive paper) and simplifies the use of tracing paper, tables, stereographic projection diagrams and thumbtacks, which tend to be cumbersome and even impractical particularly when inclement weather prevails.

The use of analog compasses involves carefully obtaining readings and approximating each reading to the nearest degree

(Ragan, 2009). The accuracy of the readings depends on the location of the compasses in the correct position to perform the measurement on a surface, and on systematic errors, which can be induced by the use of erroneous angles for the correction of the data with respect to the magnetic declination, the presence of magnetic materials near or on the reading surface, or due to the presence of induced electromagnetic fields (Ragan, 2009). From the orderly and methodical recording of data it is possible to construct stereograms to verify the accuracy of the measurements made, mainly when developing data surveys of lineations related to planes, as is the case with structural data of slickenlines in faults or brittle shear zones, although there is software that allows minimizing the error by approximation to the nearest degree in office data processing, as is the case of Tectonics. The use of mobile devices with different operating systems (iOS or Android) for structural data acquisition facilitates the recording and visualization of orientation measurements of geological structures (Allmendinger et al., 2017; Novakova and Pavlis, 2017; Lee et al., 2018; Whitmeyer et al., 2019), and additionally allows many measurements to be taken quickly (Allmendinger, 2017; 2019). In some cases, these devices offer additional advantages in terms of accuracy in gauging the structural data and identifying the locations of field stations where the structural data measurements are taken using the positioning systems included in mobile devices which can be visualized on digital mapping platforms (e.g., Google Earth). Whether using analog compasses or mobile devices, a recording scheme is proposed that facilitates the direct association between plans and lineaments contained in them, from the incorporation of the data in a table, in which the planar surfaces and lineations will be distributed in adjacent columns, including the data and type of structure. This allows standardizing the data recording in an orderly and methodical way (see Table 1), especially when annotations of the measurements are made in notebooks.

Where measurements are taken using mobile devices or analog compasses, the graphical representation of the spatial orientation of structures is made on stereographic (Wulff) or equal-area (Schmidt) grids, using the projection on the lower hemisphere, which means that the observations are projected to the horizontal plane passing through the center of the sphere (Allmendinger, 2019). Visualization on stereograms is not only a good, but a necessary, practice when performing work involving the comparison of spatial orientations of structures between stations for the definition of structural domains or the direction of tectonic drag, among other factors. As already mentioned, the use of mobile devices has facilitated the graphic visualization of structural data. However, it is not always possible to use these devices in the field, which forces individuals to resort to manual construction of conventional graphic representations on tracing or transparent paper, although this is imprecise, and in many cases cumbersome and frustrating. The use of the stereographic or equal-area projection for the graphic representation of the spatial orientation of structures is determined by the data set; that is, if the densities of the plotted directions are important for the determination and analysis of preferred orientations, the equal-area projection should be used, since such a projection does not show the effect of area distortion (Lisle and Leyshon, 2004). However, the use of one or the other for the realization of geometric constructions is irrelevant, although the Wulff grid is more useful for graphical representations involving the cyclographic trace, and is used to determine the geometric relationships of structures (Phillips, 1973; Babín and Gómez, 2010d). Another form of two-dimensional visualization that complements the applications of stereograms for structural analysis is the representation of strike trends in structural data via rose diagrams, which, in the case of joints, for example, is important because of its relation to the orientation of the stress field.

The use of a modified network for the direct graphical representation of structural data in an outcrop, which allows dispensing with tracing or transparent paper, is a simple, efficient, and effective alternative solution to visualize the geometric relationships of fabric elements (planar and linear) during structural surveys involving comparisons of the spatial orientations of structures between stations or outcrops, in areas where it is not possible to use mobile devices for this purpose. The procedure proposed here to perform the graphical representation in the field is useful and innovative, can be applied with any type of structural notation, and serves as a complement to field studies in which it is necessary to differentiate structural domains, the direction of tectonic drag, the presence of local and regional folds, or the preliminary structural analysis, in which the stress field relationship is identified, among other aspects. For the visualization of data to determine the geometrical relationship between fabric elements, the Wulff stereographic network has been modified, while for the visualization of data involving the determination of preferential directions and their relationship to the stress field, the Schmidt network has been modified. Both graphical representations can be used to perform geometrical constructions and can be complemented with the representation of orientations in rose diagrams.

6. Conclusions

This article proposes a scheme for recording data acquired in the field in a table, which allows sorting by type of fabric element (planar or linear), and the recording of the lineations always in front of the plane that contains them. In addition, the recording scheme includes the data corresponding to the kinematics or direction of movement of faults and shear zones, the indicators that support the kinematics, and a qualitative assessment of the certainty or reliability of the kinematics assigned to the direction of movement of shear zones; this is essential for determining paleostress tensors through the application of software. This logging scheme constitutes a standard that can be implemented by students, researchers, and other professionals in geosciences, and has applications in structural analysis that, depending on the purpose, can be complemented with data specific to the objective, whether cartographic, geomechanical, geotechnical, or mining, among others.

The direct graphical representation of geological structure data in the field is realized by a fast method to visualize the data on modified Wulff and Schmidt grids, which allow the structural data to be plotted in the outcrop, dispensing with the use of tracing or transparent paper, regardless of the structural notation used. The visualization of the spatial orientation of planar and linear structures in modified stereographic projection diagrams is complemented with rose diagrams, to reveal and understand the probable relationships between the structures, and to facilitate understanding of the different phases of deformation recorded by the lithological units analyzed.

The use of the methodology proposed herein during field campaigns, can minimize human errors at the time of recording and manipulating data in the outcrops. The correct, methodical, and orderly implementation of data recording of the measurements made concerning the fabric elements (planar and linear) in the proposed table, whether obtained by using mobile devices or analog geological compasses, is fundamental for the analysis of the spatial distribution of the data directly in the outcrops. Further, implementation of the modified network for direct graphical representation and visualization of data in the field is innovative, and simplifies the use of tracing paper, making this process more effective and efficient. The use of stereographic or equal-area projection diagrams allows determining key structural trends and differentiating between structural domains, as well as determining the direction of tectonic drag, kinematics of faults and shear zones, and paleostress tensors, among other considerations, to support the reconstruction of the geologic and tectonic history of an area and the establishment of the relationships between different geologic processes.

Acknowledgments

This work was completed within the framework of the Tectonic Group, Dirección de Geociencias Básicas, Servicio Geológico Colombiano. The authors are grateful to the anonymous reviewers whose comments and suggestions helped to improve the manuscript. We also extend our gratitude to Sergio Adrián López Isaza and Luis Fernando Páez Sinuco for fruitful discussions concerning the practical implications of this technique.

References

Abdunaser, K. M. (2015). Satellite imagery for structural geological interpretation in Western Sirt Basin, Libya: Implication for petroleum exploration. *Geosciences*, *5*(1), 8-25.

Allmendinger, R. W. (2017). *Stereonet mobile for iOS v 3.0*. http://www.geo.cornell.edu/geology/faculty/RWA/programs/stereonet-mobile.html

Allmendinger, R. W. (2019). *Modern structural practice: A structural geology laboratory manual for the 21st Century*. http://www.geo.cornell.edu/geology/faculty/RWA/structure-lab-manual/

Allmendinger, R. W., Cardozo, N., & Fisher, D. (2012). *Structural geology algorithms: Vectors and tensors*. Cambridge University Press.

Allmendinger, R. W., Siron, C. R., & Scott, C. P. (2017). Structural data collection with mobile devices: Accuracy, redundancy, and best practices. *Journal of Structural Geology*, *102*, 98-112. https://doi.org/10.1016/j.jsg.2017.07.011

Ahmadirouhani, R., Rahimi, B., Karimpour, M. H., Malekzadeh S., A., Afshar N., S., & Pour, A. B. (2017). Fracture mapping of lineaments and recognizing their tectonic significance using SPOT-5 satellite data: A case study from the Bajestan area, Lut Block, east of Iran. *Journal of African Earth Sciences*, *134*, 600-612. https://doi.org/10.1016/j.jafrearsci.2017.07.027

Babín V., R. S., & Gómez O., D. (2010a). Problemas de geología estructural. 1. Conceptos generales. *Reduca (Geología), Serie Geología Estructural*, *2*(1), 1-10.

Babín V., R. S., & Gómez O., D. (2010b). Problemas de geología estructural. 2. Orientación y proyección de planos en el espacio. *Reduca (Geología), Serie Geología Estructural*, *2*(1), 11-23.

Babín V., R. S., & Gómez O., D. (2010c). Problemas de geología estructural. 3. Orientación y proyección de líneas en el espacio. *Reduca (Geología), Serie Geología Estructural*, *2*(1), 24-40.

Babín V., R. S., & Gómez O., D. (2010d). Problemas de geología estructural. 9. Análisis estructural mediante diagramas de contornos. *Reduca (Geología), Serie Geología Estructural*, *2*(1), 148-192.

Bartlett, W. L., Friedman, M., & Logan, J. M. (1981). Experimental folding and faulting of rocks under confining pressure. Part IX: Wrench faults in limestone layers. *Tectonophysics*, *79*(3-4), 255-277.

Blés, J. L. (1977). *La fracturation des roches. 2eme partie: Observation et interprétation des fractures naturelles*. Bureau de Recherches Géologiques et Minières, Service Géologique National, France.

Borradaile, G. (2003). *Statistics of earth science data*. Springer.

Bucher, W. H. (1944). Studies for students: The stereographic projection, a handy tool for the practical geologist. *The Journal of Geology*, *52*(3), 191-212. https://doi.org/10.1086/625206

Cardozo, N., & Allmendinger, R. W. (2013). Spherical projections with OSXStereonet. *Computers & Geosciences*, *51*, 193-205. https://doi.org/10.1016/j.cageo.2012.07.021

Chica S., A. (1984). *Análisis de estructuras geológicas*. Universidad Nacional de Colombia

Compton, R. R. (2016). *Geology in the field*. Earthspun Books.

Davis, J. C. (2002). *Statistics and data analysis in geology*. John Wiley & Sons Inc.

Davis, G. H., Reynolds, S. J., & Kluth, C. F. (2012). *Structural geology of rocks and regions*. John Wiley & Sons, Inc.

Delvaux, D., & Sperner, B. (2003). New aspects of tectonic stress inversion with reference to the Tensor program. In D. A. Nieuwland (ed.), *New insights into structural interpretation and modelling*. Special Publications, vol. 212. Geological Society of London. https://doi.org/10.1144/GSL.SP.2003.212

Doblas, M. (1987). Criterios del sentido de movimiento en espejos de fricción: Clasificación y aplicación a los granitos cizallados de la sierra de San Vicente (sierra de Gredos). *Estudios Geológicos*, *43*(1-2), 47-55.

Doblas, M. (1998). Slickenside kinematic indicators. *Tectonophysics*, *295*(1-2), 187-197. https://doi.org/10.1016/S0040-1951(98)00120-6

Doblas, M., Mahecha, V., Hoyos, M., & López Ruiz, J. (1997a). Slickenside and fault Surface kinematic indicators on active normal faults of the Alpine Betic cordilleras, Granada, southern Spain. *Journal of Structural Geology*, *19*(2), 159-170. https://doi.org/10.1016/S0191-8141(96)00086-7

Doblas, M., Faulkner, D., Mahecha, V., Aparicio, A., López Ruiz, J., & Hoyos, M. (1997b). Morphologically ductile criteria for the sense of movement on slickensides from an extensional detachment fault in southern Spain. *Journal of Structural Geology*, *19*(8), 1045-1054. https://doi.org/10.1016/S0191-8141(97)00032-1

Fossen, H. (2010). *Structural geology*. Cambridge University Press.

Fossen, H. (2019). Writing papers with an emphasis on structural geology and tectonics: advices and warnings. *Brazilian Journal of Geology*, *49*(4). https://doi.org/10.1590/2317-4889201920190109

Fossen, H., Cavalcante, G. C. G., Pinheiro, R. V. L., & Archanjo, C. J. (2019). Deformation: progressive or multiphase? *Journal of Structural Geology*, *125*, 82-99. https://doi.org/10.1016/j.jsg.2018.05.006

Gabrielsen, R. H., & Braathen, A. (2014). Models of fracture lineaments: joint swarms, fracture corridors and faults in crystalline rocks, and their genetic relationships. *Tectonophysics*, *628*, 26-44. https://doi.org/10.1016/j.tecto.2014.04.022

Ghosh, S. K. (2013). *Structural geology: fundamentals and modern developments*. Pergamon Press.

Han, L., Liu, Z., Ning, Y., & Zhao, Z. (2018). Extraction and analysis of geological lineaments combining a DEM and remote sensing images from the northern Baoji loess area. *Advances in Space Research*, *62*(9), 2480-2493. https://doi.org/10.1016/j.asr.2018.07.030

Hancock, P. L. (1985). Brittle microtectonics: Principles and practice. *Journal of Structural Geology*, *7*(3-4), 437-457. https://doi.org/10.1016/0191-8141(85)90048-3

Hanmer, S., & Passchier, C. (1991). *Shear-sense indicators: A review*. Geological Survey of Canada, Paper 90-17.

Hatcher, R. D. Jr. (1995). *Structural geology: Principle, concepts and problems*. Prentice Hall.

Hills, E. S. (1972). *Elements of structural geology* (2nd ed.). Chapman and Hall, Ltd.

Holcombe, R. J. (2015). GEOrient v.9.5.1. Department of Earth Sciences, University of Queensland, Australia. http://www.holcombe.net.au/software/

Hopgood, A. M. (1999). *Determination of structural successions in migmatites and gneisses*. Springer Science + Busines Media, B. V. https://doi.org/10.1007/978-94-011-4427-8

Hobbs, B. E., Means, W. D., & William, P. E. (1976). *An outline of structural geology*. John Wiley & Sons, Inc.

Kutty, T. S., & Parthasarathi, G. (1992). Rose.C- A program in "C" for producing high-quality rose diagrams. *Computers & Geosciences, 18*(9), 1195-1211. https://doi.org/10.1016/0098-3004(92)90040-X

Lisle, R. J., & Leyshon, P. R. (2004). *Stereographic projection techniques for geologist and civil engineers*. Cambridge University Press. https://doi.org/10.1017/CBO9781139171366

Lee, S., Suh, J., & Choi, Y. (2018). Review of smartphone applications for geoscience: Current status, limitations, and future perspectives. *Earth Science Informatics*, 11, 463-486. https://doi.org/10.1007/s12145-018-0343-9

López I., J. A., & Zuluaga C., C. A. (2012). Neis de Macuira: Evolución tectónica de las rocas metamórficas paleozoicas de la alta Guajira, Colombia. *Boletín de Geología*, *34*(2), 15-36.

Mardia, K. V. (1972). *Statistics of directional data*. Academic Press, Inc.

Marrett, R. A., & Allmendinger, R. W. (1990). Kinematic analysis of fault-slip data. *Journal of Structural Geology*, *12*(8), 973-986. https://doi.org/10.1016/0191-8141(90)90093-E

Marshak, S., & Mitra, G. (1988). *Basic methods of structural geology*. Prentice Hall.

Mawer, C. K. (1992). Kinematic indicators in shear zones. In M. J. Bartholomew, D. W. Hyndman, D. W. Mogk, and R. Mason (eds.), *Basement tectonics 8: Characterization and comparison of ancient and Mesozoic continental margins: Proceedings of the 8th International Conference on Basement Tectonics (Butte, Montana, 1988)*. Kluwer Academic Publishers. https://doi.org/10.1007/978-94-011-1614-5

McClay, K. R. (1987). *The mapping of geological structures*. John Wiley & Sons.

McKillup, S., & Dyar, M. D. (2010). *Geostatistics explained: An introductory guide for earth scienctists*. Cambridge University Press. https://doi.org/10.1017/CBO9780511807558

Nemec, W. (1988). The shape of the rose. *Sedimentary Geology*, *59*(1-2), 149-152.

Novakova, L., & Pavlis, T. L. (2017). Assessment of the accuracy of smart phones and tablets for measurement of planar orientations: A case study. *Journal of Structural Geology*, 97, 93-103. https://doi.org/10.1016/j.jsg.2017.02.015

Ortner, H., Reiter, F., & Acs, P. (2002). Easy handling of tectonic data: The programs TectonicVB for Mac and TectonicsFP for Windows™. *Computers & Geosciences, 28(10)*, 1193-1200. https://doi.org/10.1016/s0098-3004(02)00038-9

Passchier, C. W., & Trouw, R. A. J. (2005). *Microtectonics*. Springer Science and Business Media. https://doi.org/10.1007/3-540-29359-0

Passchier, C. W., & Coelho, S. (2006). An outline of shear-sense analysis in high-grade. *Gondwana Research*, *10*(1-2), 66-76. https://doi.org/10.1016/j.gr.2005.11.016

Passchier, C. W., Myers, J. S., & Kröner, A. (1990). *Field geology of high-grade gneiss terrains*. Springer-Verlag. https://doi.org/10.1007/978-3-642-76013-6

Petit, J. P. (1987). Criteria for the sense of movement on fault surfaces in brittle rocks. *Journal of Structural Geology*, *9*(5-6), 597-608. https://doi.org/10.1016/0191-8141(87)90145-3

Petit, J. P., Proust, F., & Tapponnier, P. (1983). Critèriesde sens de movement sur les miroirs de failles en roches non calcaires. *Bulletin de la Société Ggéologique de France*, *XXV*(4), 589-608. https://doi.org/10.2113/gssgfbull.S7-XXV.4.589

Phillips, F. C. (1973). *La aplicación de la proyección estereográfica en geología estructural.* Trans.: C. M. Escorza (1975). Blume.

Potter, P. E., & Pettijohn, F. J. (1963). *Statistics of directional data*. Academic Press.

Price, N. J., & Cosgrove, J. W. (1990). *Analysis of geological structures*. Cambridge University Press.

Ragan, D. M. (2009). *Structural geology: An introduction to geometrical techniques*. Cambridge University Press.

Rajasekhar, M., Sudarsana R., G., Siddi R., R., Ramachandra, M., & Pradeep K., B. (2018). Data on comparative studies of lineaments extraction from ASTER DEM, SRTM, and Cartosat for Jilledubanderu River basin, Anantapur district, A. P, India by using remote sensing and GIS. *Data in Brief*, 20, 1676-1682. https://doi.org/10.1016/j.dib.2018.09.023

Ramsay, J. G. (1967). *Folding and fracturing of rocks*. McGraw-Hill Book Company.

Roberts, J. L. (1982). *Introduction to geological maps and structures*. Pergamon Press.

Robson, R. M. (1994). A multi-component rose diagram. *Journal of Structural Geology*, *16*(7), 1039-1040. https://doi.org/10.1016/0191-8141(94)90086-8

Sander, B. X. (1911). Über Zusammenhänge zwischen Teilbewegung und Gefüge in Gesteinen. *Tschermaks Mineralogische und Petrographische Mitteilungen*, 30, 281-314. https://doi.org/10.1007/BF02994467

Sander, B. (1970). *An introduction to the study of fabrics of geological bodies*. Pergamon Press.

Sanderson, D. J., & Peacock, D. C. P. (2020). Making rose diagrams fit-for-purpose. *Earth-Science Reviews*, 201, 103055. https://doi.org/10.1016/j.earscirev.2019.103055

Simpson, C., & Schmid, S. M. (1983). An evaluation of criteria to deduce the sense of movement in sheared rocks. *GSA Bulletin*, *94*(11), 1281-1288. https://doi.org/10.1130/0016-7606(1983)94<1281:AEOCTD>2.0.CO;2

Singhal, B. B. S., & Gupta, R. P. (2010). *Applied hydrogeology of fractured rocks*. Springer. https://doi.org/10.1007/978-90-481-8799-7

Sugden, T. (1987). Kinematic indicators: Structures that record the sense of movement in mountain chains. *Geology Today*, *3*(3-4), 93-99. https://doi.org/10.1111/j.1365-2451.1987.tb00496.x

Turner, F. J., & Weiss, L. E. (1963). *Structural analysis of metamorphic tectonites*. McGraw-Hill Book Company, Inc.

Twiss, R. J., & Moores, E. M. (2007). *Structural geology*. W. H. Freeman and Company.

Wilson, G. (1982). *Introduction to small-scale geological structures*. George Allen & Unwin. https://doi.org/10.1007/978-94-011-6838-0

Whitmeyer, S. J., Pyle, E. J., Pavlis, T. L., Swanger, W., & Roberts, L. (2019). Modern approaches to field data collection and mapping: Digital methods, crowdsourcing, and the future of statistical analyses. *Journal of Structural Geology*, *125*, 29-40. https://doi.org/10.1016/j.jsg.2018.06.023

Van der Pluijm, B. A., & Marshak, S. (2004). *Earth Structure: An introduction to structural geology and tectonics*. W. W. Norton & Company.

Žalohar, J. (2020). *T-Tecto Studio X5. Integrated software for structural analysis of earthquake focal-machanism and fault-slip data*. Introductory tutorial. Quantectum.

Žalohar, J., & Vrabec, M. (2007). Paleostress analysis of heterogeneous fault-slip data: The Gauss method. *Journal of Structural Geology, 29*(11), 1798-1810. https://doi.org/10.1016/j.jsg.2007.06.009

Pseudotachylite veins. Santa Fé de Antioquia sector, Author: Julián Andrés López Isaza

Boletín Geológico

SERVICIO GEOLÓGICO COLOMBIANO

Boletín Geológico, 48(1), 141-156, 2021,
https://doi.org/10.32685/0120-1425/bol.geol.48.1.2021.529

© Author(s) 2021. This work is distributed under the Creative Commons Attribution 4.0 License.

Received: June 10, 2020

Revised: September 24, 2020

Accepted: December 2, 2020

Published online: July 12, 2021

Possible hydrogeological and thermal conditions of the Quilmes Tectonic Trough (Buenos Aires Province, Argentina): a working hypothesis

Posibles condiciones hidrogeológico-termales de la fosa de Quilmes (Provincia de Buenos Aires, Argentina): una hipótesis de trabajo

Eduardo A. **Rossello**[1], Gerardo **Veroslavsky**[2], Jorge N. **Santa Cruz**[3]

1. CONICET-IGEBA, Universidad de Buenos Aires. Facultad de Ciencias Exactas y Naturales, Buenos Aires, Argentina
2. Facultad de Ciencias, Universidad de la República, Montevideo, Uruguay
3. Centro de Estudios Transdisciplinarios del Agua –CETA–, Universidad de Buenos Aires –UBA–, Buenos Aires, Argentina
Corresponding author: Eduardo Rossello, ea_rossello@yahoo.com.ar

Abstract

The proposal of the Quilmes Tectonic Trough (*Fosa tectónica de Quilmes* – FQ) as the extension of the southern end of the Santa Lucía basin in Uruguay and its connection to the Salado basin in Argentina suggest the existence of a large sedimentary volume capable of housing a new aquifer on the La Plata River coast. However, the sedimentary volumes that form the FQ are hidden under a thick, recently deposited cover, and thus, there is a lack of studies on the nature of this formation. Nevertheless, the Uruguayan section of the Meso-Cenozoic depocenter of the Santa Lucía basin has been more thoroughly studied for hydrocarbon exploration, which enabled us to estimate the equivalent tectosedimentary characteristics in the FQ. In the Uruguayan territory, three aquifer systems of the Santa Lucía basin are exploited: the Raigón (Plio-Pleistocene) aquifer, which is the most important source of groundwater for various uses in the south-central region of Uruguay, and the Mercedes (Upper Cretaceous) and Migues (Lower Cretaceous) aquifers, which are also used, albeit to a lesser extent, for drinking water, irrigation, and industrial purposes. The Migues aquifer, the least known of the three, shows a variable depth ranging from 100 to 1500 m and considerable stratigraphic sequences of porous and permeable sandstones. These sandstones provide the aquifer with very good qualities as a reservoir rock; as such, the Migues aquifer has been studied for its potential natural gas reserves and geothermal and water resources. Accordingly, if the same sequences with equivalent sedimentary and hydrogeological qualities are present in the FQ, similar aquifers with interesting properties may remain unidentified along the Buenos Aires coast beneath the intensely explored Puelches, Pampeano and Paraná aquifers. In conclusion, specific exploratory activities may prove the existence and quality of these hydrogeological

Citation: Rossello, E. A., Veroslavsky, G., & Santa Cruz, J. N. (2021). Possible hydrogeological and thermal conditions of the Quilmes Tectonic Trough (Buenos Aires Province, Argentina): a working hypothesis. *Boletín Geológico, 48*(1), 141-156. https://doi.org/10.32685/0120-1425/bol.geol.48.1.2021.529

resources, the regional slope toward the southwest from the Uruguayan outcrops, upwelling or semiupwelling conditions and even geothermal energy associated with the deepest cretaceous aquifers.
Keywords: Hydrogeological resources, Quilmes tectonic trough, Buenos Aires Province, Argentina.

Resumen

A partir de la propuesta de la fosa tectónica de Quilmes (FQ) como extensión de la prolongación austral de la cuenca Santa Lucía de Uruguay, y su conexión con la cuenca del Salado, de Argentina, se puede considerar como hipótesis de trabajo la existencia de un gran volumen sedimentario, capaz de albergar un nuevo acuífero sobre el litoral rioplatense. Los volúmenes sedimentarios que constituyen la FQ están ocultos debajo de una potente cubierta moderna, por esta razón la falta de estudios de superficie específicos no permite conocer su verdadera naturaleza. Dado que la continuación uruguaya del depocentro meso-cenozoico de la cuenca Santa Lucía está mejor estudiada, a partir de la exploración de hidrocarburos, se pueden estimar características tectosedimentarias equivalentes en la fosa de Quilmes. En el territorio uruguayo se explotan tres sistemas acuíferos que se desarrollan en la cuenca Santa Lucía: el acuífero Raigón (Plio-Pleistoceno), que constituye la fuente de agua subterránea más importante de la región centro-sur de Uruguay, destinada a diversos usos, y los acuíferos cretácicos Mercedes (Cretácico Superior) y Migues (Cretácico Inferior), que también son usados, en menor medida, para el suministro de agua potable, riego y usos industriales. El acuífero Migues es el menos conocido y se desarrolla a profundidades variables (100 a 1500 m), donde exhibe considerables sucesiones de areniscas porosas y permeables que le confieren muy buenas cualidades como roca reservorio, y es objeto de estudio con fines de almacenamiento de gas, recursos geotermales e hídricos. Por esta razón, si las mismas secuencias con cualidades sedimentarias e hidrogeológicas equivalentes están presentes en la fosa de Quilmes, se podría esperar el hallazgo de interesantes acuíferos relacionados, aún desconocidos en el litoral bonaerense, por debajo de los tradicionales Puelches, Pampeano y Paraná. De comprobarse la existencia y calidad de estos recursos hidrogeológicos a partir de la realización de actividades exploratorias específicas, la pendiente-gradiente regional hacia el sudoeste desde los afloramientos de Uruguay, se podrían esperar condiciones de surgencia o semisurgencia natural, e incluso geotermalismo asociado a los acuíferos cretácicos más profundos.
Palabras clave: Recursos hidrogeológicos, fosa tectónica de Quilmes, Provincia de Buenos Aires, Argentina.

1. Introduction

The identification and interpretation of the Quilmes Tectonic Trough (*Fosa Tectónica de Quilmes* – FQ) as the southern extension of the Santa Lucía basin in Uruguay and its connection to the Salado basin in Argentina (Rossello et al., 2011) suggest the existence of a large sedimentary volume capable of housing several unknown aquifer systems on the La Plata River coast (Santa Cruz, 1972; Sala and Hernández, 1993; Santa Cruz et al., 1997; Auge, 2005; Amato and Silva Busso, 2006), which is the working hypothesis of this study.

The area of the western extension of the Santa Lucía basin (De Santa Ana et al., 1994) remains uncertain due to its location on the international boundary between Argentina and Uruguay and a general lack of data (Figure **1**). Nevertheless, through joint interpretations, studies from both countries have identified evidence of Meso-Cenozoic infills on the northern coast of the Buenos Aires province (the FQ), which are considered the extension of the Santa Lucía basin into the Argentinian territory (Rossello et al., 2017, 2018).

Rossello et al. (2017, 2018) provided potential arguments that weaken the hypothesis of a first-order tectonic boundary, originally proposed by the geologist Alberto Mingramm in *Umbral de Martín García* [Martin García Swell] (Zambrano, 1974). Since then, most researchers have continued to support this interpretation, designating the structure as Martin García High (*Alto de Martín García*), based on a lack of data for the Santa Lucía basin in the Argentine territory. This tectonic feature was assumed to be an uplifted sector of the crystalline basement from the projection of Martín García Island, the outline of which is located in the La Plata River and almost matches the international boundary between Argentina and Uruguay. Thus, the Martin García High became a physical western boundary in the Mesozoic records of the Santa Lucía basin and was even projected onto the Atlantic continental shelf as the La Plata River High (*Alto del Plata*).

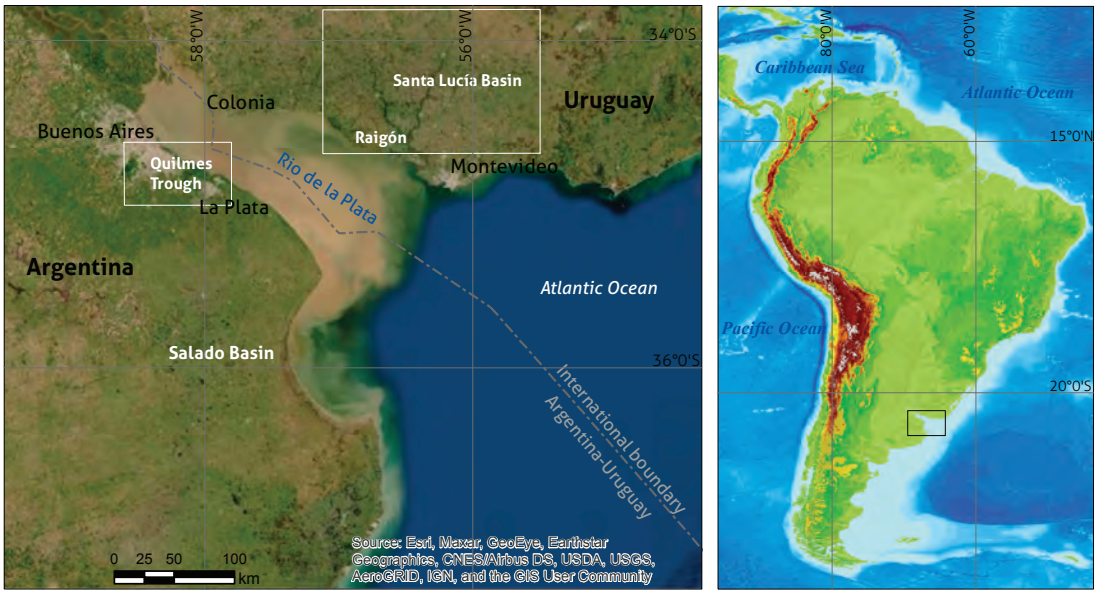

Figure 1. Regional location of the study sector on a satellite image of the La Plata River (left) and on a map of South America (right)
Source: Earth Sciences and Image Analysis Laboratory, NASA - https://eol.jsc.nasa.gov/

However, the true nature of the sedimentary volumes that form the FQ and that may eventually become suitable aquifers for various uses (drinking water, agricultural-industrial uses, geothermal purposes and fluid storage) is poorly known due to the current lack of specific subsurface studies (Rossello et al., 2017, 2018). This region lacks detailed geophysical surveys and sufficiently deep exploratory wells because the potential exploration targets are hidden under a deep and modern cover. For this reason, in this study, assuming that the FQ is the extension of the depocenter of the Santa Lucía basin into the territory of Buenos Aires, the possibility of examining and analyzing the existence of large aquifers located in Cretaceous continental siliciclastic sequences is proposed as a working hypothesis.

Thus, the main objective of this study is to propose a working hypothesis that will generate interest in promoting exploration activities and basic research to confirm or reject this new hydrogeological potential located at greater depths and beneath the structure commonly known as the Puelches aquifer.

2. Method

The geological arguments that support the hypothesis that new deeper aquifers may be found in the FQ based on gravimetric and shallow well data available in the literature are summarized in this study.

To compare the possible sedimentological, petrophysical and hydrogeological characteristics of the deepest aquifers in the FQ, a general tectono-stratigraphic correlation is performed between the Santa Lucía basin to the east (Veroslavsky, 1999; Rossello et al., 2011; Rodríguez et al., 2020) and the Salado basin to the west (Yrigoyen, 1975; Tavella and Wright 1996; Yrigoyen, 1999; Tavella, 2005; Raggio et al., 2012).

A review of the sedimentological, petrophysical and hydrogeological characteristics of different aquifers located in the sedimentary infill and basement of the Santa Lucía basin provides the expected data for the FQ.

The regional structural deepening trend of sedimentary sequences capable of supporting upwelling aquifers and the observed geothermal capacity from Uruguay to the Salado basin is established based on simplified schemes.

3. Regional geological framework

The waters of the La Plata River divide the Argentinian and Uruguayan territories, the coasts of which are characterized by extensive plains covered by recent sediments that have been partly or fully deposited on pediment areas of the Precambrian basement, constituents of the La Plata River Craton and the Mesozoic depocenters of the Salado and Santa Lucía basins (Rossello et al., 2017, 2018). In the Argentinian territory, excluding

the outcrops of the Tandilia Mountain Ranges, the only inlier of this basement on the Martín García Island consists of amphibolites, gneisses and schists, which indicates a sedimentary protolith with a greater overall planar anisotropy in the NE direction (Dalla Salda, 1981), in line with observations for the southeastern Uruguayan basement (Oyhantçabal et al., 2011).

3.1 Quilmes tectonic trough

Based on a limited number of old wells in Buenos Aires, the province basement has been located at varying subsurface depths (Figures 2 and 4), which according to the data available at the time, were quite shallow (Artaza, 1943; Groeber, 1945). For example, drilling at La Piedad church (located along the current streets of Bartolomé Mitre and Paraná in Buenos Aires) revealed lithologies attributed to the crystalline basement 283 m below the wellhead (m.b.w.h.) (Figure 2). In the city of Olivos, Buenos Aires Province, the same lithologies were found at 245 and 401 (when drilling at La Noria Bridge (Groeber, 1945). Farther south, at Vucetich Park, in the city of La Plata, Groeber (1945) mentioned in a profile of San Nicolás - Monte Veloz that the basement was found 485.35 m.b.w.h. and included a well in Hudson (10.25 m above sea level (m.a.s.l.)); below approximately 200 m of sediment, gneissic material was identified at 369.95 m.b.w.h.; further, this formation was originally described as *el Rojo Mesopotámico inferior* [Red Lower Mesopotamic] and subsequently termed the Olivos Formation (Oligocene-Lower Miocene, continental), the *Verde Mesopotámico superior* [Green Upper Mesopotamic] and the Paraná Formation (Upper Miocene, marine) and was ultimately overlain with the Puelches and Pampeano aquifers and had good hydrogeological conditions (González Bonorino, 1965; Santa Cruz et al., 1997).

The Hudson well is located on the central axis of the proposed FQ (Figure 2). As in other wells drilled at that time

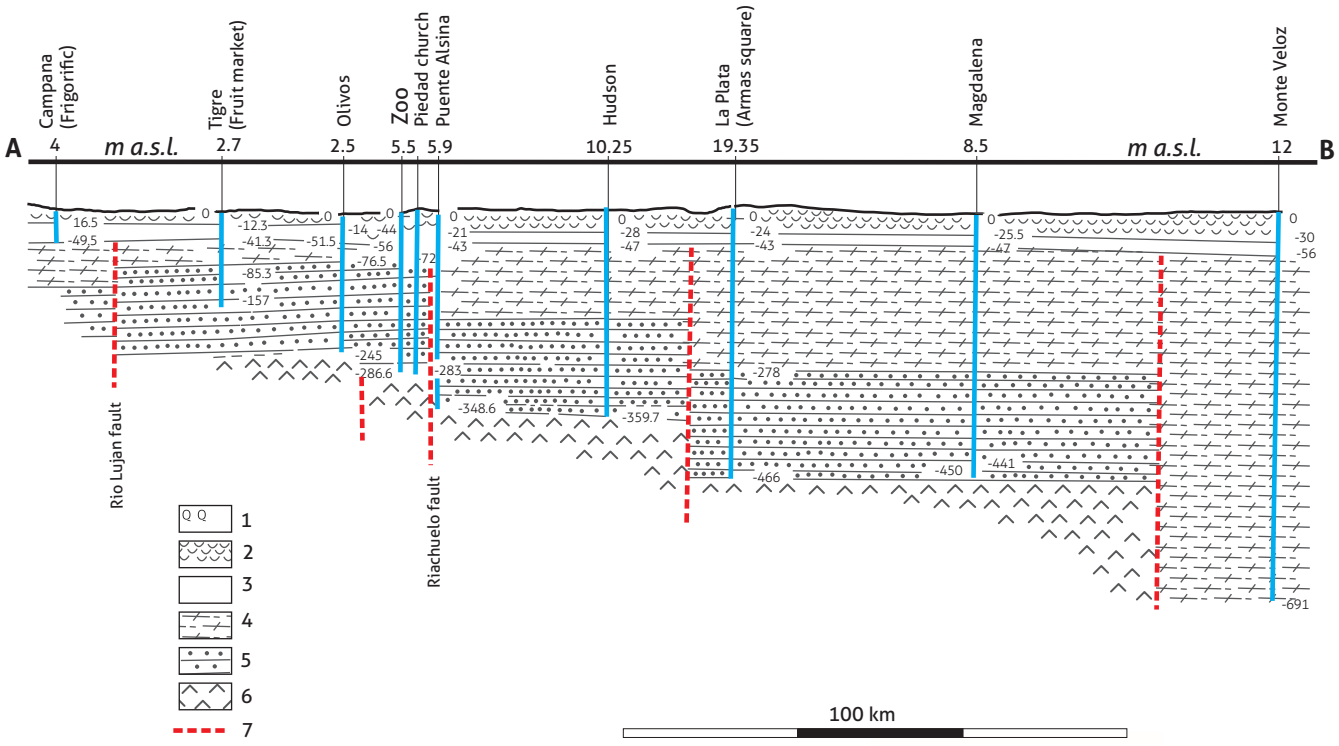

Figure 2. Reproduction of the San Nicolás - Monte Veloz profile along the Buenos Aires coast of the La Plata River (see the location in Figure 4)
Location and depth in meters and lithologies crossed by wells drilled in the 1940s to provide drinking water. 1: Querandino; 2: Pampeano; 3: Puelches; 4: Verde Mesopotámico superior"; 5: "Rojo Mesopotámico inferior"; 6: basement; 7: fault. Source: retrieved from Groeber (1945).

(Artaza, 1943), the Hudson well ends at the point when the drill cuttings generated by percussion drilling methods in the typical crystalline basement lithologies (gneisses, granites and amphibolites) are recovered. However, these drill cuttings, presumably derived from the tops of the basement blocks, could have also been generated by intercalations of conglomeratic levels formed by granitic clasts. Levels with these petrographic characteristics form the outcrops of the Cañada Solís and Migues formations in the western region of Minas and the exploratory wells of the Santa Lucía basin (Veroslavsky et al., 2004). Thus, considering the last alternative, these findings match the interpretation supported by gravimetry, which suggests a much deeper sedimentary infill than that supplied by the Hudson well (Rossello et al., 2011; Rodríguez et al., 2020). In turn, Perdomo et al. (2017) performed vertical electrical sounding, measured gravity values in the Buenos Aires partido [county] of La Plata and assessed depth variations of up to 200 m in the basement proposed for the Vucetich Park well (Figure 2), with a block morphology delimited by extensional faults arranged in a NE-SW direction.

Although neither seismic data nor sufficiently deep wells are available yet in this riparian sector of the La Plata River, in the province of Buenos Aires, gravimetric data and regional correlations suggest that the FQ is the western extension of the Santa Lucía basin into Argentinean territory (Rossello et al., 2011, 2017). Based on the available tectosedimentary data, the sedimentary infill has an average depth of approximately 200 m and essentially consists of continental Cretaceous sequences that merge from the Santa Lucía basin directly into the Salado basin and are then covered by a Cenozoic sedimentary cover (Figure 3).

Based on gravimetric data acquired on the NE coast of Buenos Aires and between Buenos Aires and Magdalena (Gianibelli and Ríos, 1989; Gianibelli et al., 1989; Cabassi et al., 1996) and combined with other data from the geodetic bases of the Argentinean National Geographic Institute (*Instituto Geográfico Nacional de la República Argentina* – IGN), new gravimetric models were generated and processed using the GM-SYS software. These models made it possible to identify a depocenter occupying approximately 20000 km^2 under the

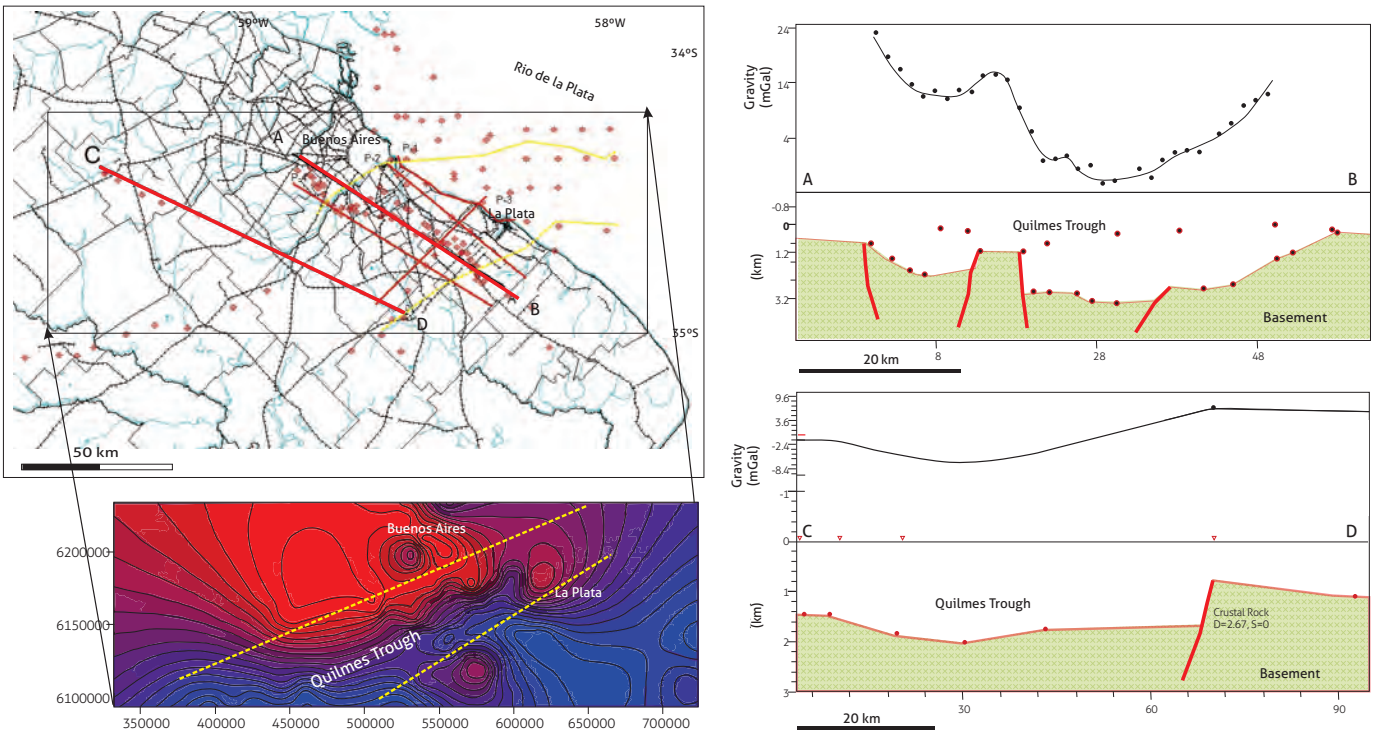

Figure 3. Bouguer anomaly map of the province of Buenos Aires and gravity cross-sections obtained using data from the Military Geographic Institute (*Instituto Geográfico Militar* – IGM) collected on the Buenos Aires shore of the La Plata River and from the GM-SYS model
Source: retrieved from Rossello et al. (2011)

recent sedimentary cover of the continental and fluvial Buenos Aires territories. Rossello et al. (2011) identified first-order structural features with subparallel highs and lows and matching general ENE-WSW directions in the basement, similar to those in the Santa Lucía basin, and with extensional tectonics related to the Gondwana breakup and the early opening of the Atlantic Ocean (Figure 3). This structuring is considered to be one of the factors responsible for the 3.8-degree earthquake recorded approximately 20 km south of Buenos Aires on November 30, 2018, with an estimated epicenter of approximately 4.5 km (Rossello et al., 2020).

3.2 The Santa Lucía basin

The Santa Lucía basin (CSL, for its acronym in Spanish) covers an area of nearly 6000 km^2 in the Uruguayan territory, has a slightly triangular geometry and is filled with almost 2500 m of sequences from the Jurassic to the present day. These sequences most likely continue in equivalent units in the FQ (Figure 4).

The CSL derives from an intracratonic pull-apart depocenter (Veroslavsky, 1999; Rossello et al., 2001) that is spread through the main zones of crustal weakness in the crystalline basement, particularly those that determine the main boundaries of the sedimentary infills and internal highs arranged in E-NE directions.

As shown by subsurface surveying for hydrocarbon exploration involving gravimetric and 2D seismic surveys with wellhead control, the Santa Lucía basin has a morphostructural conformation typical of a pull-apart rift generated by dextral transpression, with uplifted basement blocks and intermediate troughs with syn-sedimentary infills (Rossello et al., 2001). The Santa Lucía basin shows an asymmetric profile generated by a conjugated system of synthetic and antithetic listric normal faults defining successive grabens and horsts of different scales (Figure 5). This arrangement highlights two subbasins separated by the crystalline Santa Rosa High (*Alto de Santa Rosa*) (Veroslavsky et al., 2004).

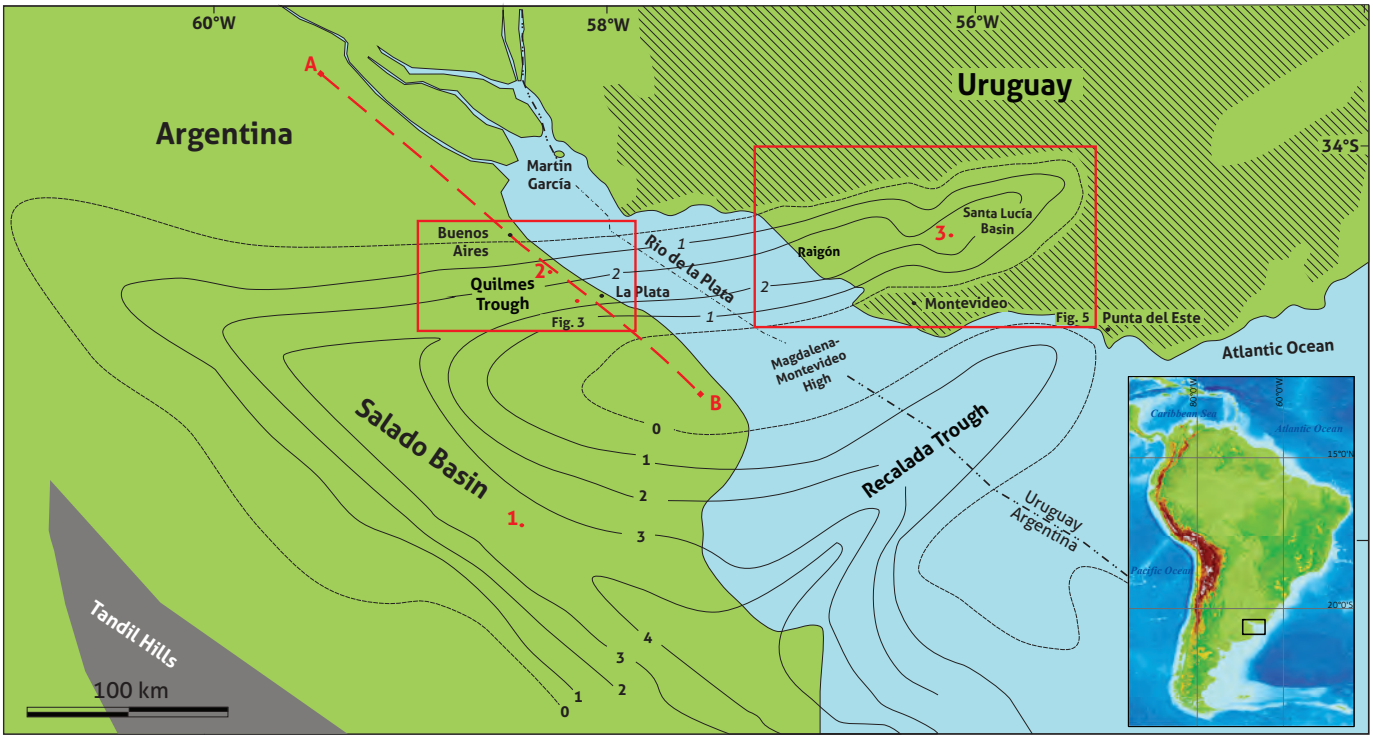

Figure 4. Schematic isopach map of Meso-Cenozoic sedimentary records showing the location of the FQ and the Recalada trough and their relationships with the Salado and Santa Lucía basins
The striped sectors correspond to crystalline basement outcrops. The red dashed A-B line indicates the approximate position of the profile in Figure 2. The red circles indicate the positions of the 1) General Belgrano, 2) Hudson and 3) Sauce wells. Source: retrieved from Rossello et al. (2017).

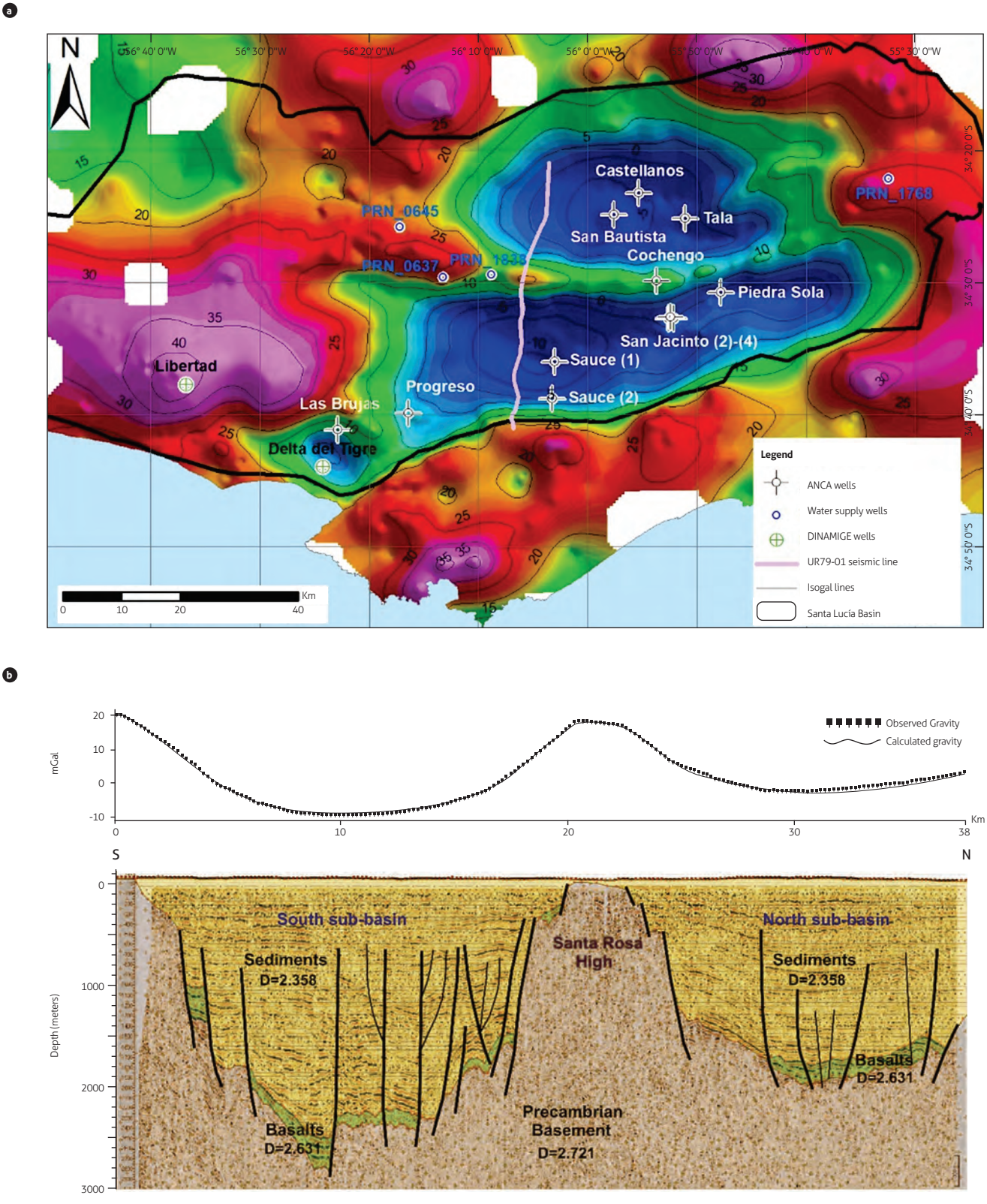

Figure 5. a) Bouguer anomaly map of the Santa Lucía basin, showing the arrangement of the two subbasins separated by the Santa Rosa high. b) Cross-sections of the 2D gravity model, supported by seismic line UR76-01
Source: adapted from Rodríguez et al. (2020)

Based on surface information, seismic surveys and several exploratory wells, Veroslavsky et al. (2004) proved the presence of pre-rift and rift records, which are assigned to the Upper Jurassic and Lower Cretaceous (Figure 6). Their rocky records, which exceed 2300 m in the Sauce 1 well, begin with a few basaltic eruptions that correspond to the Puerto Gómez Formation, which overlays the Precambrian basement in some sectors. These basalts are interspersed with thick continental sedimentary rocks of the Cañada Solís Formation that are interpreted as alluvial systems and are laterally and vertically related to the sandstones, conglomeratic sandstones and subordinate pelites of the Migues Formation. These lithological terms are interpreted as deposits of river and lake systems, with some associated wind episodes. The Castellanos Formation developed in the central sector of the basin, particularly in the domain of the northern subbasin, and consists of a sequence of pelites, claystones and gray sandstones, with occasional intercalated levels of anhydrite, the facies associations and paleontological content of which indicate a primarily lacustrine origin and an Aptian Albian age (Veroslavsky, 1999; Campos, 1998).

The structural configuration of the basin reveals potential stratigraphic traps (pinchout) combined with closure against a fault (particularly against the Santa Rosa high and other sectors with strong structural compartmentalization, *e.g.*, the Sauce depocenter of the southern subbasin, Figure 5).

Toward the Upper Cretaceous, the sedimentation changed to a continental siliciclastic sequence developed in a post-rift setting that exceeded the boundaries of the basin that controlled the sedimentation during the Lower Cretaceous. In the geographical area where the Santa Lucía basin developed, these continental records do not exceed 100 m and essentially gather fluvial deposits that meet in a) the Mercedes Formation, which consists of white and pink sandstones and conglomeratic sandstones of varied granulometry, with conglomeratic, pelitic and calcareous intercalations in strongly silicified sectors, and b) the Asencio Formation, which consists of whitish, fine, massive and laminated sandstones and has been affected by intense ferrification processes near the top (Figure 6). Some authors have included the limestone deposits caused by intense calcretization processes associated with the Mercedes Formation in the Queguay Formation (Spoturno et al., 2004).

From the Oligocene to the present, the Cretaceous sequences have been covered by continental and transitional sedimentary rocks, including pelites, fine-to-coarse sandstones and clays of the formations shown in Figure 6.

The Fray Bentos Formation is the first Cenozoic depositional event and is characterized by siliciclastic continental Oligocene deposits linked to arid and semiarid conditions, interspersed with short humid periods, including the following main lithologies: fine-to-medium-coarse sandstones, pinkish and somewhat sandy loessic silts, lutite and conglomerate and conglomeratic sandstone lenses (Spoturno et al., 2004). The sandstones and silts are generally cemented by calcium carbonate, which is either pulverulent or in sandstones with irregular shapes. In the basin, the unit has a thickness ranging from a few meters to slightly over 100 m and develops as a wedge that thickens toward the west (Spoturno et al., 2004).

The Camacho Formation corresponds to preserved, Upper Miocene marine transgressions, which are thicker (30-35 m) in the southwest region of the CSL, and is traditionally correlated with the Paraná Formation in the Argentinian territory (del Río and Martínez, 1998). This formation is represented by silty claystones, claystones with hues ranging from greenish gray to black, mudstones with a clayey siltitic matrix and sand, gravel and bivalve mollusk clasts with hues ranging from greenish dark gray to black, detrital and biodetrital sediments of lumachelles with a grayish fine-to-medium-coarse sandy matrix and fine-to-very-fine sandstones with a clayey matrix and calcareous cement.

The Raigón Formation encompasses fluvial and transitional continental Plio-Pleistocene sediments of sand and gravel, different from the Fray Bentos Formation but similar to the Camacho Formation, which is covered by the Libertad Formation. The Raigón Formation is located in the departments of Montevideo, Canelones, San José and Colonia in Uruguay, which support the important homonymous aquifer and display a gradual subsidence toward the SW (Figure 7).

The depth of the Raigón Formation peaks in the coastal areas, ranging from approximately 40 to 45 m, and has minimum values between 5 and 10 m in the continental zones (Pena et al., 2013). The main lithological compositions of the Raigón Formation in more than 70 wells include white, feldspathic fine-to-medium-coarse sands, thick arkosic sands, chippings, gravels and polymictic pebbles and boulders, all of which are interstratified with more or less continuous lenses of clays and fine clayey sands with hues ranging from brown to green (Heinzen et al., 1986; Carrión et al., 2011).

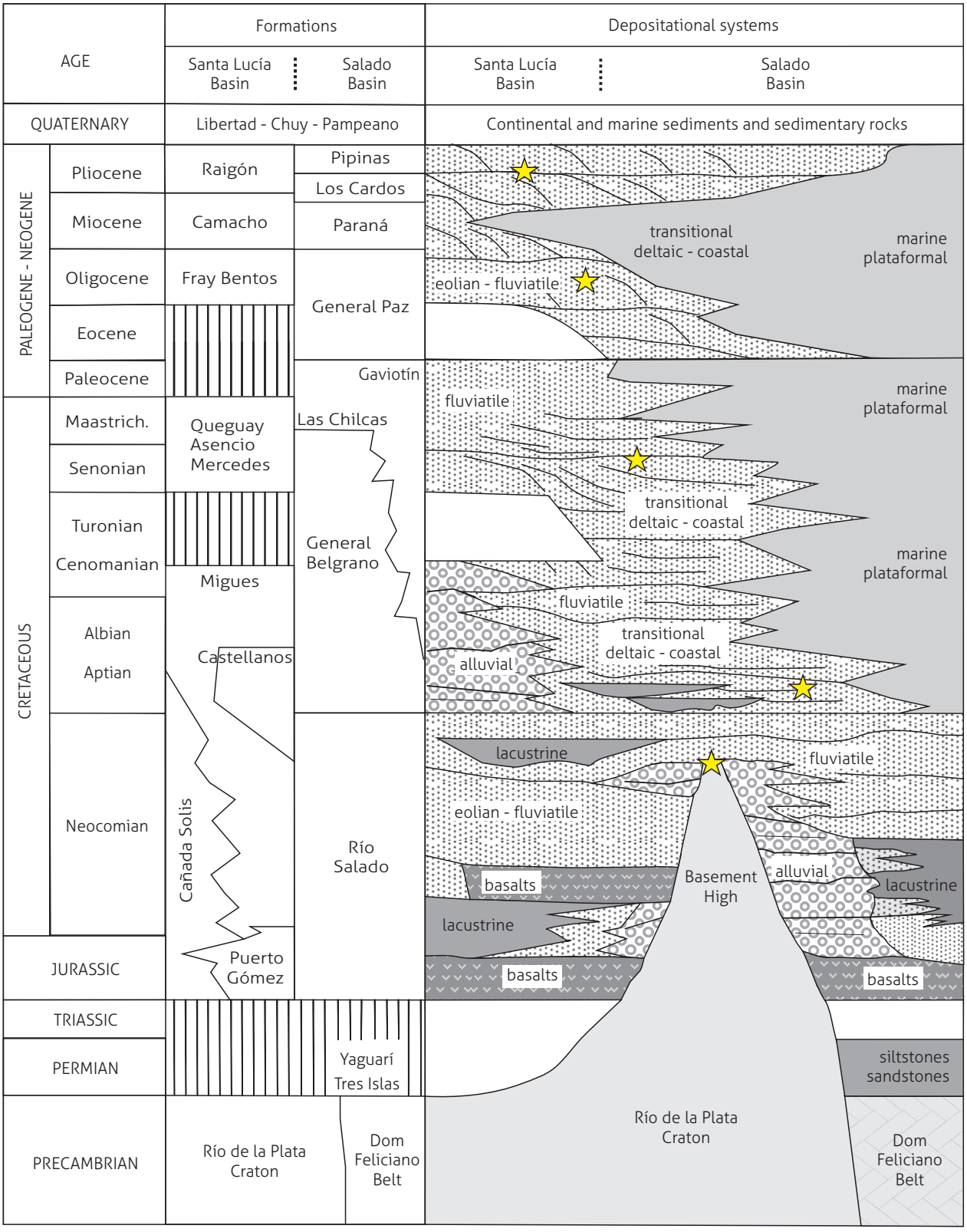

Figure 6. Chronolithostratigraphic columns of the Santa Lucía and Salado basins showing a tendency to develop more distal and deeper facies toward the south; the yellow stars in column A indicate the location of the levels with petrophysical quality that likely function as aquifers
Source: Rossello et al. (2017)

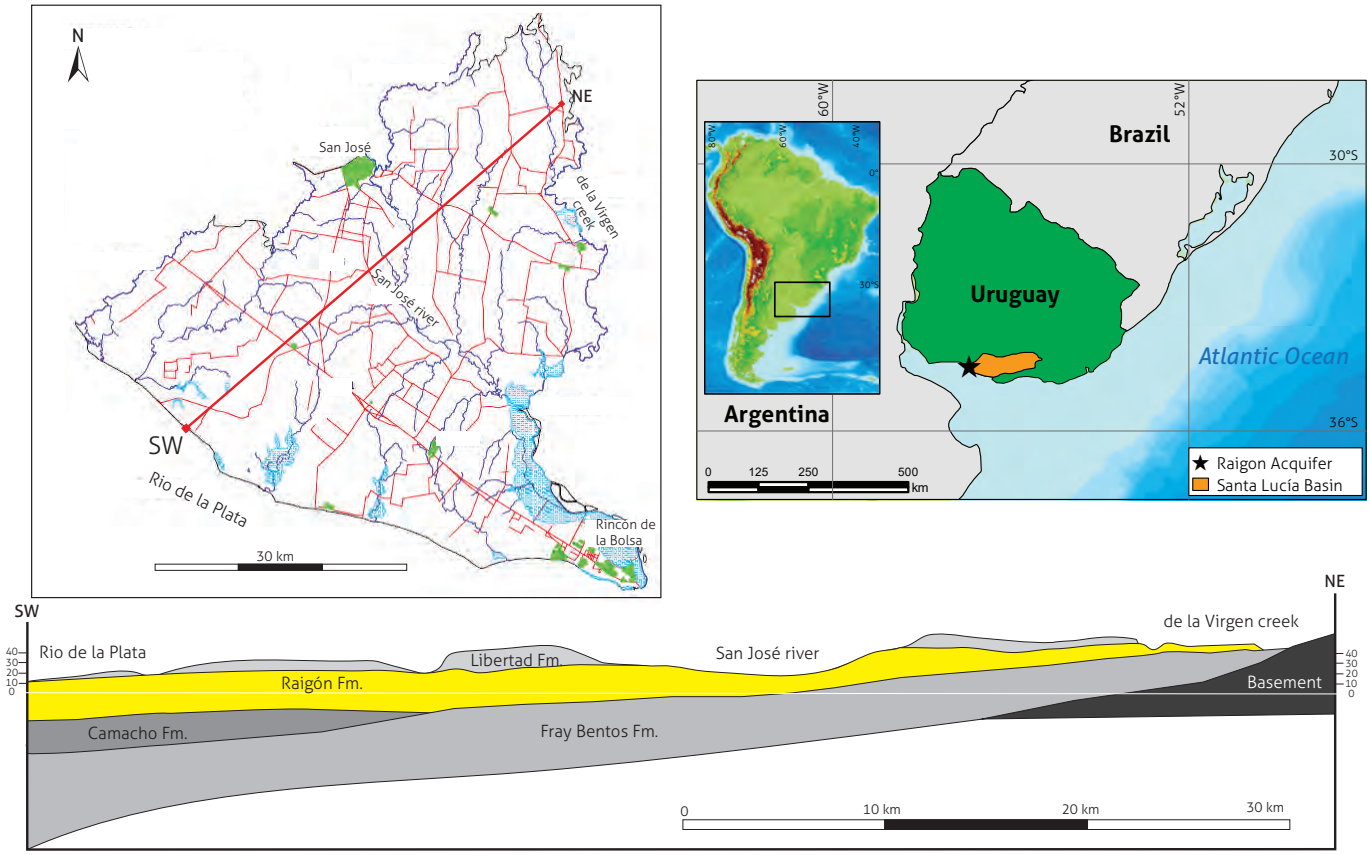

Figure 7. Location of the Raigón aquifer on the Uruguayan coast of the La Plata River (see its location in Figure 1) and a schematic cross-section
The cross-section shows the gradual subsidence of the sequences toward the SW.
Source: adapted from Los Santos-Gregoraschuk and Hernández García (2013)

3.3 Salado basin

The Salado basin is a Meso-Cenozoic depocenter that developed both inland and offshore in the province of Buenos Aires, extends for more than 700 km and has been explored for hydrocarbon resources (Tavella and Wright 1996; Yrigoyen, 1999; Tavella, 2005; Raggio et al., 2012). Among other deep wells, the General Belgrano well, drilled in 1948, ultimately bottomed out at 4012 m.b.w.h. in Cretaceous sequences without reaching the basement. In addition, exploratory seismic data on hydrocarbons in the domain of the Salado basin show a sustained and likely gradual deepening toward the Samborombón Bay, forming its deep Meso-Cenozoic depocenter (Figure 6).

The Salado basin infill shows two characteristic, predominantly continental lithofacies with maximum recorded thicknesses of 886 m: a) the first Neocomian lithofacies, with a sharp syn-rift character and thick clastic sequences, such as red beds, is represented by the Salado River Formation, and b) the second lithofacies is represented by post-rift levels of the General Belgrano Formation that are attributed to the Aptian-Santonian and overlay the previous formation with a well-marked angular unconformity in the seismic sections, albeit the lithological differentiation of the well samples is less pronounced.

These lithofacies are followed by the marine units of the Las Chilcas Formation (Maastrichtian-Paleocene) that are gradually overlaid with regressive, continental red beds assigned to the Eocene-Oligo-Miocene of the General Paz and Olivos-Los Cardos Formations, reaching depths of up to 800 m and transiently becoming deltaic and marine deposits toward the east and ultimately completely dominant before reaching the continental slope. The analysis of the offshore seismic sections shows a conformation that begins with Eocene deposits of the proximal platform and gradually, upwardly changes to a set of deltaic facies, which became alluvial plain deposits in the late Oligocene.

Another major marine advance occurred between the early and mid-Miocene. Similar to the previous marine advance in the Maastrichtian-Paleocene, this advance also transgresses deeply into this part of the continent, as represented by the Paraná Formation, with a maximum recorded thickness of 815 m. The Salado basin displays a gradual transition between the Miocene marine deposits and the underlying units; however, near the coast, this relationship is pseudoconcordant based on the clear evidence of a fracturing episode that dislocated the Olivos Formation without affecting the Paraná Formation and the loosely overlapping boundaries of previous continental deposits (Yrigoyen, 1999).

The Cenozoic sedimentary record ends at a depth of approximately 125 m, as represented by the inland continental clastic accumulations. There is a gradual marine influence toward the ocean. Reddish-brown terrigenous deposits (correlated with the Arroyo Chasicó Formation) have also been differentiated and assigned to the lower Pliocene for their rich faunal content, culminating in the upper Pliocene with the Puelches Formation, which is characterized by a conspicuous deposit of light and yellowish-brown quartz sands at a depth of a few tens of meters. Lastly, silts and loesses, assigned to the Pampeano Formation, top the stratigraphic column in the Quaternary and broadly cover the edaphic surface that dominates the Buenos Aires plain.

4. Hydrogeological framework of the aquifers of the Santa Lucía basin

The Santa Lucía basin contains three main aquifers that are used for various purposes, including drinking water, livestock water, agricultural irrigation and industrial uses (Dinamige, 2009).

The Raigón Aquifer System (*Sistema Acuífero Raigón* – SAR) is the most important system in a wide region of southwestern Uruguay due to its high levels of extraction (Bessouat et al., 2000). This aquifer consists of a Plio-Pliocene sequence of sandstones, sands and gravels, interspersed by thin levels of pelites and claystones, which occasionally act as confining or semiconfining units. The Camacho Formation in the south region and the Fray Bentos Formation to the north form the base of this aquifer. Although the Camacho Formation is considered impermeable, some perforation data suggest the existence of permeable zones within this formation, which enables hydraulic connection to the Raigón aquifer (Instituto Nacional de Investigación Agropecuaria, 2019). Therefore, based on its lithological and hydraulic characteristics, the Raigón aquifer may operate as a system of multiple interrelated layers (Gestión Sostenible del Acuífero Raigón, Uruguay, 2005).

The best aquifer conditions are found in the extreme southwest of the Santa Lucía basin (San José department) where the continuity, depth and hydraulic conductivity of the strata, the existence of considerable recharge and the well-defined physical boundaries enable the development of the SAR (INIA, 2019). In the region south of the city of San José, the minimum thickness of the aquifer ranges from 0.5 to 2 m, with low yields (2 to 5 m^3/h). The hydrogeological characteristics of the Santa Lucia basin change in the south-central region, where the yields reach high values (60-80 m^3/h), and the wells produce up to 10 m^3/h. In general, the thickness does not exceed 20 m, and the base of the aquifer is always less than 100 m from the ground surface. The transmissivity ranges from 100 to 2200 m^2/d, with values between 300 and 1400 m^2/d prevailing throughout the SAR. The storage coefficient ranges from 1.10-5 to 1.10-2 (Carrión et al., 2011; Gestión Sostenible del Acuífero Raigón, Uruguay, 2005).

The other two aquifers in the Santa Lucía basin, the Migues aquifer and the Mercedes aquifer, consist of Cretaceous geological units (Dinamige, 2009; Bossi et al., 1999; Montaño et al., 2006). Their groundwater layers are the most relevant antecedent streams for analyzing the performance of the Cretaceous aquifer units in the CSL, particularly in the central region of the department of Canelones.

The Mercedes aquifer is found at the surface and subsurface at shallow depths, with variable thicknesses, and has the characteristics of a free and semiconfined aquifer (Dinamige, 2009). In the central region of the basin, the aquifer consists of sandstones and conglomeratic sandstones, ranging from consolidated to friable and occasionally with strong silicification and carbonation processes, and acts as a partly porous and partly fissured aquifer. The Mercedes aquifer shows, in general, low discharges, ranging from 2 to 4000 l/h, except in areas of intense fracturing. According to Montaño et al. (2006), in the central region of the department of Canelones, the Mercedes aquifer performs as a free aquifer, and its average thickness is approximately 10 m, with mean transmissivity (T) values of approximately 50 m^2/day, ranging from 3 to 100 m^2/day, and a mean permeability (K) ranging from 1 to 10 m/day.

The Migues aquifer develops almost exclusively in the subsurface, and its main hydrogeological and hydrochemical

characteristics are only known up to depths of approximately 150-200 m due to the depth limitations of water well drilling companies; thus, its groundwater potential at greater depths remains unknown. Bossi et al. (1999) stated that, in some sectors, this aquifer can accumulate large volumes of groundwater, with discharges reaching 30 m^3/h at depths ranging from 40 to 80 m. The quality of this water can be good, although it is occasionally high in salinity. In the Juanicó region, Montaño et al. (2006) highlighted the presence of a sandy, semiconfined and multilayer aquifer, with occasional sandy conglomeratic levels and depths ranging from 30 to 120 m, that essentially consists of the Migues aquifer and the Mercedes aquifer in the first meters. In this region, the discharge of most wells ranges from 10 to 15 m^3/h, but several wells have discharges that exceed these values.

Although the hydrogeological characteristics of the Migues aquifer under shallow, semiconfined and confined conditions are somewhat known, its economic potential as a reservoir could be even higher at greater depths. The exploratory wells drilled in search of hydrocarbons, particularly in the southern subbasin, show the development of vast and considerably thick sandy bodies, which display excellent porosity and permeability characteristics for reservoir rocks at variable depths (Veroslavsky, 1999). Based on the study of well cores, cuttings and Sauce well logging (2450 m), Tomasini et al. (2019) reported good reservoir properties in at least three levels, with tops at depths ranging from 900 to 1500 m. The reservoir levels are outlined by the sandstones of the Migues Formation, with large thicknesses (> 100 m), mean porosities of 22% and permeability values ranging from 150 to 460 mD. These characteristics have led to several studies of these deep reservoirs aimed at analyzing their viability for gas storage (methane, hydrogen and CO_2) and as a geothermal resource (Tomasini et al., 2019).

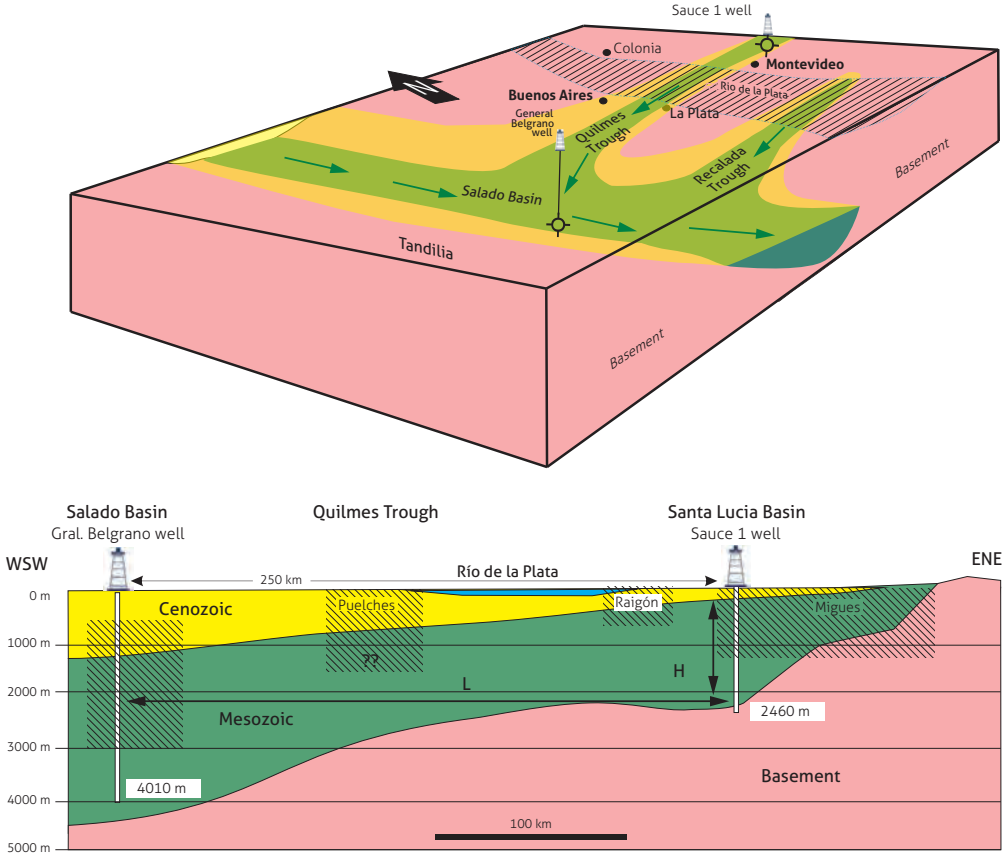

Figure 8. Above: three-dimensional diagram of the connection between the Santa Lucía Basin-FQ and the Recalada Trough with the Salado Basin. Below: schematic cross-section of the regional subsurface through the La Plata River
This cross-section shows the deepening of the Meso-Cenozoic sequences from the Santa Lucía basin (Sauce well 1) to the Salado basin (Gral. Belgrano well). L: distance between control wells; H: difference in level. Source: Modified from Rosello et al. (2017).

5. Discussion

A schematic correlation of the characteristics of the previously described sedimentary infills of the Santa Lucía and Salado basins reveals a regional slope in the pre-Mesozoic basement that deepens toward the southwest until reaching level differences of more than 1000 m (Figure 8). In the latter depocenter, excluding the Cretaceous and Oligocene-Pliocene formations, the sedimentary facies are more distal and are related to other sources located toward the NW (Rossello, 2018), which are generally thinner and show evaporitic intercalations. Therefore, given its unfavorable petrophysical conditions, the FQ is unlikely to have the hydrogeological conditions expected in the deepest sectors.

If the gravimetric surveys available for the FQ (Rossello et al., 2011; Perdomo et al., 2017) can be compared with those described in the Santa Lucía basin (Rodríguez et al., 2020), block tectonics, expressed as uplifted basement blocks separated by sedimentary volumes, may be active in the FQ.

If the favorable petrophysical characteristics of the aquifers known in Uruguay continue in the FQ, albeit at greater depths, conditions of natural upwelling and considerable geothermal temperatures could occur in this trough because the water from the aquifers of the Santa Lucía basin flows through saturated porous and permeable materials toward levels that are deeper than the infiltration levels. Due to the presence of superimposed sealing units, these discharges could naturally re-emerge as springs upon well drilling, in line with the vertical flow dynamics in a saturated porous medium established by Darcy's law (see definitions in Custodio and Lamas, 1976). Groeber (1945) recognized the upwelling and partial upwelling character of the aquifers in the sequences termed "Mesopotámico rojo" [Red Mesopotamic] reached by the wells drilled by Artaza (1943); however, no further petrophysical and hydrodynamic descriptions are available.

In the FQ, the aquifer would likely encompass levels with more proximal depositional characteristics, correlated with the

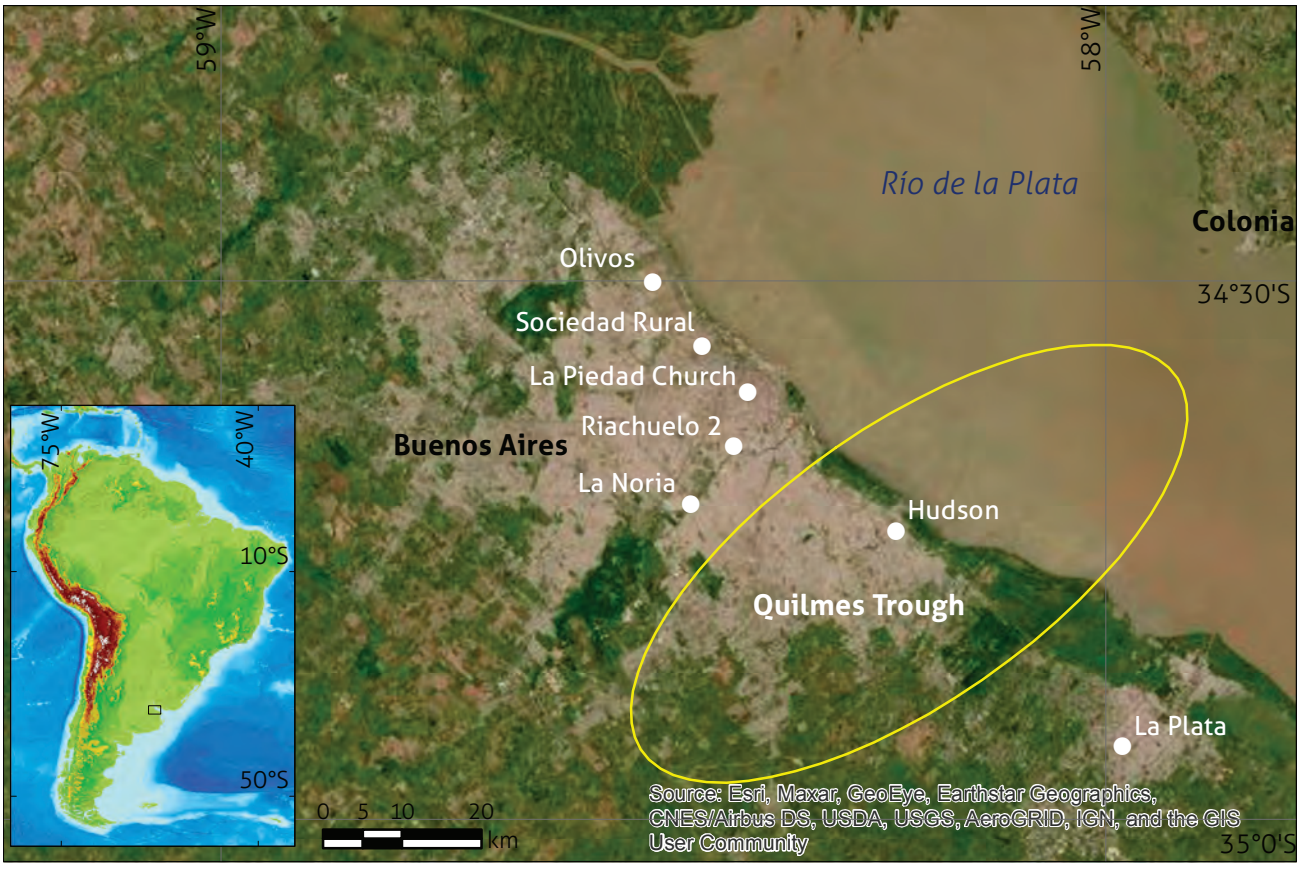

Figure 9. Estimated location of the possible aquifers in the FQ underneath the traditional Puelches and Pampeano aquifers in the metropolitan area of Buenos Aires
Source: Taken from Rosello et al. (2018).

Salado River and General Belgrano Formations, and favorable petrophysical characteristics for an aquifer.

If the FQ harbors deep aquifers below the well-known Puelches, Pampeano and Paraná aquifers (Santa Cruz, 1972; Santa Cruz et al., 1997; Amato and Silva Busso, 2006), with hydraulic, physical and chemical conditions similar to those of the aquifers of the Santa Lucía basin, these aquifers could be an excellent supply of alternative or complementary hydrogeological resources for the metropolitan area of Buenos Aires, where the trough is located (Figure 9).

6. Conclusions

The interpretation of the FQ as a depocenter with Mesozoic and Cenozoic sedimentary infills that reach an average depth of almost 900 m suggests the presence of significant sandstone and conglomeratic intervals that could be suitable for new hydrogeologic reservoirs that are deeper than current reservoirs, when compared to neighboring areas in Uruguay. Currently available gravimetric surveys allow us to establish a morphotectonic analogy with the Santa Lucía basin, which is much better known for its subsoil data from the exploration of its hydrocarbon resources.

New deep aquifers will likely be discovered based on knowledge of the petrophysical characteristics of the equivalent units of the Santa Lucía basin, the hydrodynamic conditions of which range from 12 to 15% effective porosity, with stratigraphic traps (pinchout) combined with (closure against a fault) and overlapped by fine sediments of excellent quality that can act as seals.

In addition, the FQ connects similar sedimentary sequences of the Santa Lucía basin with those of the Salado basin at deeper positions, likely providing favorable conditions for upwelling aquifers and even hydrothermalism. Based on the deepening upward sequences that are most likely to form aquifers, a topographic difference of approximately 700 to 900 m is calculated, which should generate an adequate gradient to facilitate underground flow from groundwater recharge zones located in Uruguay.

Considering the arguments described above, a specific hydrogeological study supported by noninvasive, rapid, low-cost geophysical exploration methods, such as magnetotellurics (MT), audio-frequency MT (AMT), the horizontal-to-vertical spectral ratio (HVSR) and transient electromagnetics (TEM), must be performed to complement the knowledge on the geological configuration of this region, which has been limited by the scope of gravimetric models. Drilling the necessary exploratory wells will enable us to determine if the spatial conditions and geochemical qualities of the deep aquifers can host the FQ.

For this reason, the present working hypothesis is proposed, which justifies the logistical costs of exploratory drilling in the FQ to verify the existence of thermal groundwater, its hydraulic, physical, chemical and isotope characteristics and, consequently, the technical-economic potential of this proposed aquifer system. Locating this aquifer system is very important given its strategic location below the large population centers in and around Buenos Aires.

Acknowledgments

The authors thank the anonymous reviewers for their valuable comments and suggestions, which helped improve this manuscript.

References

Amato, S., & Silva Busso, A. (2006). Relaciones estratigráficas e hidroquímicas de los acuíferos Pampeano y Puelches en el noreste de la provincia de Buenos Aires. *Revista Museo Argentino Ciencias Naturales*, *Nueva Serie*, *8*(1), 9-26.

Artaza, E. (1943). *Saneamiento urbano en la República Argentina, provisión de agua y desagües urbanos: Provisión de Agua.* Faculty of Physico-mathematical Sciences, Universidad Nacional de La Plata, Notebook 6. Thesis Series, 43-57.

Auge, M. P. (2005). Hidrogeología de La Plata, provincia de Buenos Aires. In R. E. de Barrio, R. O. Echeverry, M. E. Caballé y E. Llambías (eds.), *Geología y recursos minerales de la provincia de Buenos Aires* (pp. 293-311), Relatorio 16th Argentine Geological Congress (La Plata).

Bessouat, C., De Souza, S., Oleaga, A., & Pacheco, F. (2000). *Acuífero Raigón. Part 1: caracterización geohidrológica*. 1st Joint World Congress on Groundwater (Brazil), CD room.

Bossi, J., Morales, H., Brunetto, I., Martínez, M., & Arlo, L. (1999). *Evaluación de las posibilidades de aguas subterráneas en el centro y noreste del departamento de Canelones*. Final Report, Project CSIC-Udelar.

Cabassi, I. R., Gianibelli, J., Miranda, S., & Castiglione, B. (1996). *Nuevos aspectos tectónicos del borde norte de la cuenca del Salado (provincia de Buenos Aires, Argentina) a partir de resultados magnéticos*. 13th Argentine Geological

Congress-3rd Congress of Hydrocarbon Exploration (Buenos Aires). Acts 2, 443-451.

Campos, C. C. (1998). *Biocronoestratigrafía e inferências paleoambientais das formações Castellanos e Migues - bacia de Santa Lucía - Cretáceodo Uruguai, com base em palinologia* [dissertação de mestrado]. Universidade Guarulhos, Brasil.

Carrión, R., Heinzen, W., & Massa, E. (2011). Otra mirada al agua subterránea en el Uruguay: acuíferos: ubicación y detalles. *Ciencia*, (12), 9-12. (Data June, 2009). www.dinamige.gub.uy

Custodio, E., & Lamas, M. R. (1976). *Hidrología subterránea* (2 vols.). Ediciones Omega.

Dalla Salda, L. (1981). El basamento de la isla Martín García, Río de la Plata. *Revista de la Asociación Geológica Argentina*, *36*(1), 29-43.

De los Santos Gregoraschuk, J., & Hernández García, G. (2013). Modelación numérica de un acuífero mediante dos esquemas representativos: Raigón, Uruguay. *Tecnología y Ciencias del Agua*, *4*(4), 151-158.

De Santa Ana, H., Goso, C., Muzio, R., Oyhantçabal, P., & Veroslavsky, G. (1994). Bacia do Santa Lucía (Uruguai): evoluçaõ tectonica e sedimentar. *Geociências*, *13*(1), 37-52.

Del Río, C. J., & Martínez, S. (1998). Clase Bivalvia. In C. J. del Río (ed.), *Moluscos marinos miocenos de la Argentina y del Uruguay* (pp. 48-83). Monographs 15. Academia Nacional de Ciencias Exactas, Físicas y Naturales.

Dinamige. (2009). *Estimación de la extracción de agua subterránea: principales acuíferos del Uruguay*. https://www.miem.gub.uy/sites/default/files/estimacion_de_extraccion_anualde_aguas_subterraneas_en_los_principales_acuiferos_del_uruguay.pdf

Gestión sostenible del acuífero Raigón, Uruguay. (2005). Informe final del Proyecto RLA/8/031, Manejo Integrado y Sostenible de Aguas Subterráneas en América Latina, funded by IAEA.

Gianibelli, J. C., & Ríos, F. F. (1989). *Aspectos geofísicos y tectónicos de la cuenca del Salado.* 3rd meeting Geotransectas América del Sur (Mar del Plata). Acts, 31-39.

Gianibelli, J. C., Cabassi, I. R., Suárez, E. A., Barrio, L., Weisz, S., Petcoff, L., Cingolani, C. A., Sidoti, O., & Ríos, F. F. (1989). La anomalía del borde noreste de la cuenca del Salado: transecta. 3rd meeting Geotransectas América del Sur (Mar del Plata). Acts, 112-118.

González Bonorino, F. (1965). Mineralogía de las fracciones arcilla y limo del Pampeano en el área de la ciudad de Buenos Aires y su significado estratigráfico y sedimentológico. *Revista de la Asociación Geológica Argentina*, *20*(1), 67-150.

Groeber, P. (1945). Las aguas surgentes y semisurgentes del norte de la provincia de Buenos Aires. *Revista La Ingeniería*, *49*(6), 371-387.

Heinzen, W., Velozo, C., Carrión, R., Cardozo, L., Madracho, H., & Massa, E. (1986). Elementos del ciclo hidrológico. Carta hidrogeológica a escala 1:2000000. Ministerio de Industria y Energía, Dinamige, División Aguas Subterráneas (Montevideo).

INIA. (2019). *Gestión ambiental del sistema acuífero Raigón.* FPTA. Serie 78.

Instituto Nacional de Investigación Agropecuaria, Uruguay. (2019). *Gestión ambiental del sistema acuífero Raigón*. FPTA-INIA. Serie 78.

Montaño, J., Gagliardi, S., & Montaño, M. (2006). Recursos hídricos subterráneos del Uruguay. *Boletín Geológico y Minero*, *117*(1), 201-222.

Oyhantçabal, P., Siegesmund, S., & Wemmer, K. (2011). The Río de la Plata Craton: A review of units, boundaries, ages and isotopic signature. *International Journal of Earth Sciences*, (100), 201-220. https://doi.org/10.1007/s00531-010-0580-8

Pena, S., Techera, J., & Massa, E. (2013). *Monitoreo acuífero Raigón, departamento de San José, Uruguay*. Dinamige, División Geología, Área Hidrogeología, Technical report (Montevideo).

Perdomo, S., Späth, F., & Kruse, E. (2017). *Exploración gravimétrica y geoeléctrica del basamento cristalino en el umbral de Martín García, partido de La Plata*. Buenos Aires. 20th Argentine Geological Congress (S. M. de Tucumán). Acts.

Raggio, F., Gerster, R., & Welsink, H. (2012). Cuencas del Salado y Punta del Este. *Petrotecnia*, (12), 80-88.

Rodríguez, P., Marmisolle, J., Gristo, P., De Santa Ana, H., & Veroslavsky, G. (2020). *Bouguer anomaly map and 2D modeling case study from Santa Lucía Basin, onshore Uruguay.* Society of Exploration Geophysicists, SEG International Exposition and 90th Annual Meeting. https://doi.org/10.1190/segam2020-3426365.1

Rossello, E. A. (2018). Modificaciones neotectónicas de la red de drenaje de la región central pampeana (Argentina): consecuencias en el relleno de la cuenca del Salado. *Revista de la Sociedad de Geología de España*, *31*(1), 105-116.

Rossello, E. A., De Santa Ana, H., & Veroslavsky, G. (2001). La cuenca Santa Lucía (Uruguay): un pull-apart juro-cretácico

transtensivo dextral. *Revista de la Asociación Geológica Argentina*, *56*(1), 38-50

Rossello, E. A., Heit, B., & Bianchi, M. (2020). Shallow intraplate seismicity in the Buenos Aires province (Argentina) and surrounding areas: Is it related to the Quilmes Trough? *Boletín de Geología*, *42*(2), 31-48. https://doi.org/10.18273/revbol.v42n2-2020002

Rossello, E. A., Veroslavsky, G., & De Santa Ana, H. (2011). *La fosa de Quilmes: prolongación austral de la cuenca Santa Lucía (Uruguay) en la provincia de Buenos Aires (Argentina).* 18th Argentine Geological Congress (Neuquén, Argentina). Acts, 1044-1045.

Rossello, E. A., Veroslavsky, G., De Santa Ana, H., & Rodríguez, P. (2017). Depocentros meso-cenozoicos y rasgos tectónicos del basamento cristalino del Río de la Plata (Argentina y Uruguay). *Revista de la Asociación Geológica Argentina*, *74*(3), 283-294.

Rossello, E. A., Veroslavsky, G., De Santa Ana, H., & Rodríguez, P. (2018). Geology of the Río de la Plata and the surrounding areas of Argentina and Uruguay related to the evolution of the Atlantic margin. *Journal of South American Earth Sciences*, (83), 147-164. https://doi.org/10.1016/j.jsames.2017.12.010

Sala, J. M., & Hernández, M. A. (1993). *Contribución al mapa geohidrológico de la provincia de Buenos Aires, zona noreste*. Consejo Federal de Inversiones, Desarrollo and Manejo de Aguas Subterráneas (Dymas).

Santa Cruz, J. N. (1972). Estudio sedimentológico de la Formación Puelches en la provincia de Buenos Aires. *Revista de la Asociación Geológica Argentina*, *27*(1), 5-62.

Santa Cruz, J. N., Silva Busso, A., Amato, S., Guarino, M., Villegas, D., & Cernadas, M. (1997). Explotación y deterioro del acuífero Puelches en la región metropolitana de la República Argentina. *Ingeniería Sanitaria y Ambiental*, (31), 34-44.

Spoturno, J., Oyhantçabal, P., Goso, C., Aubet, N., & Cazaux, S. (2004). *Mapa geológico y recursos minerales del departamento de Canelones a escala 1:100000*. Dinamige, Science Faculty. Project Conicyt 6019, Montevideo.

Tavella, G. F. (2005). Cuenca del Salado. In R. E. de Barrio, R. O. Echeverry, M. E. Caballé, & E. Llambías (eds.). *Geología y recursos minerales de la provincia de Buenos Aires*. 16th Argentine Geological Congress (La Plata), pp. 459-472.

Tavella, G. F., & Wright, C. G. (1996). Cuenca del Salado. In V. A. Ramos & M. A. Turic (eds.), Geología y recursos naturales de la plataforma continental argentina. 13.° Congreso Geológico Argentino y 3rd Congress of Hydrocarbon Exploration (Buenos Aires), pp. 459-472.

Tomasini, J., De Santa Ana, H., Conti, B., & Rodríguez, P. (2019). *Almacenamiento geológico de gases en medios porosos de Uruguay: seguridad energética y sostenibilidad ambiental.* IX Uruguayan Congress of Geology. Abstracts, acts.

Veroslavsky, G. (1999). *Geología da bacia de Santa Lucía, Uruguai* (Ph. D thesis). Instituto de Geociências e Ciências Exatas, Universidade Estadual Paulista (São Paulo).

Veroslavsky, G., De Santa Ana, H., & Rossello, E. A. (2004). Origen y evolución tectosedimentaria de los depósitos juroeocretácicos de la región meridional del Uruguay: su vinculación con el lineamiento Santa Lucía-Aiguá-Merín. In G. Veroslavsky, M. Ubilla, & S. Martínez (eds.), *Cuencas sedimentarias de Uruguay: geología, paleontología y recursos minerales* (2nd ed., pp. 117-142). Mesozoico Ediciones Dirac, Science Faculty, Universidad de la República (Montevideo).

Yrigoyen, M. B. (1975). *Geología del subsuelo y plataforma continental*. 6th Argentine Geological Congress (Bahía Blanca). Rapporteurship 139-168.

Yrigoyen, M. R. (1999). Los depósitos cretácicos y terciarios de las cuencas del Salado y del Colorado. In R. Caminos (ed.), *Geología argentina*. Instituto de Geología y Recursos Minerales.

Zambrano, J. J. (1974). Cuencas sedimentarias en el subsuelo de la provincia de Buenos Aires y zonas adyacentes. *Revista de la Asociación Geológica Argentina*, *29*(4), 443-469.

Boletín Geológico

SERVICIO GEOLÓGICO COLOMBIANO

Boletín Geológico
Editorial Policy

Boletín Geológico is a serial scientific publication of the Servicio Geológico Colombiano (SGC), active since 1953, aiming to promote and disseminate research in the Earth sciences. *Boletín Geológico* publishes original scientific manuscripts of research, reflections, reviews, data and case reports on the Earth sciences, in Spanish or English.

Objective and scope

To disseminate scientific knowledge in the following fields of research:

- Stratigraphy, sedimentology, structure and evolution of basins.
- Geochemistry, geophysics, volcanology, igneous and metamorphic petrology.
- Tectonics, seismotectonic and geodynamic modeling.
- Hydrogeology, oceanography and geothermal energy.
- Economic geology, mineralogy, metallogenesis, hydrocarbon genesis and reservoirs.
- Geomorphology, geological hazards, environmental geology, soil research, climate change and geological heritage.
- Paleontology, paleoclimatology, Quaternary geology and geoarcheology.
- Software applications and artificial intelligence in Earth sciences.

Boletín Geológico may also include compilations, short notes and manuscripts on the state of knowledge and special research on critical and relevant issues.

Articles from authors linked or not linked to the Servicio Geológico Colombiano are accepted.

Periodicity

Biannual publication with online publishing in June and December of each year.

Publishing costs

The contents of the journal are freely available without charge to readers and can be reused after download with proper bibliographic reference.

The journal does not charge authors any fees for sending or receiving their article, for the editorial process, or for publishing. It is completely funded by the Servicio Geológico Colombiano.

Open Access Statement

The content of the journal is protected under a Creative Commons - attribution license. Consequently, the work may be copied, redistributed, remixed, adapted, transformed, and built upon to create new works from the content for any purpose (including commercial purposes). The journal guarantees open access to all published content, users can read, download, copy, distribute,

print, search or link the full texts of the articles. Whoever exercises any of the aforementioned rights must adequately credit the copyright on the original work and indicate if the work was modified.

The Servicio Geológico Colombiano is not responsible for any damage or harm derived from the exercise of the rights granted under the Creative Commons attribution license, nor does it offer guarantees of any kind in relation to the licensed material.

Attribution (CC BY)

Archive and preservation

Boletín Geológico uses the LOCKSS system to create a storage system that allows the creation of permanent files for conservation and restoration purposes.

Boletín Geológico

SERVICIO GEOLÓGICO COLOMBIANO

Instructions to Authors

Authorship

The authorship of a postulated article should include those who actively and substantially contributed to the intellectual content and the analysis or interpretation of the data; as such, the authors are publicly responsible for the article submitted. The list and order of the authors should be reviewed before submitting the work the first time for publication. After submitting an article, authorship changes are not accepted.

Transfer of patrimonial copyright to the Servicio Geológico Colombiano

The authors of an article approved for publication transfer patrimonial copyright to the Servicio Geológico Colombiano for its subsequent dissemination, reproduction and distribution in the printed and digital media available to the Servicio Geológico Colombiano, as well as for its inclusion in national or international databases and indexes.

Author requirements

- Understand the editorial policy of the *Boletín Geológico* and the derived processes, and be in agreement with them.
- Include all the people who contributed to the preparation of the manuscript as authors.
- Abide by all ethical guidelines for authors and reviewers.
- In the event that the reviewers of the article/publication suggest the need to make changes or adjustments before their approval, the authors agree to make such adjustments in the time required by the *Boletín Geológico*.

The obligations of the authors are included in the letter of authorship found HERE, or in the corresponding steps when submitting an article. Sending the letter of authorship is an essential requirement for the submission of an article.

1. Submission criteria

All articles submitted for consideration for publication must meet the following submission criteria:

- Only original and unpublished articles are accepted. The content of the articles must not have been published, totally or partially, in another journal or publication.
- Articles must be sent in Word format by the web page https://revistas.sgc.gov.co/index.php/boletingeo, in the "Submit article" tab.
- The title, in Spanish and English, should be concise and reflect the subject matter.
- The name, the complete institutional affiliation of each author, and the email of the corresponding author must be included.
- The abstract and keywords must be included in both Spanish and English. Images must be attached as individual graphics files, with a minimum resolution of 300 dpi.
- If acknowledgments, acknowledgments to entities, publication permits, etc., are required, they should be included at the end of the text and before the references.
- The text must comply with the references and style requirements indicated in the editorial standards.

2. Editorial guidelines

a. Tables

Tables must be submitted in an editable format, not as images, and they must be accompanied by an explicit legend and source. They must be referenced in the text, and they must be essential to explain or further support the argument of the article.

b. Figures

Figures, such as diagrams, photographs or maps, should be sent in graphics files with a minimum resolution of 300 dpi. Each figure must be cited in the text and be accompanied by an explanatory legend that includes the source.

Images from sources other than the authors of the article must have the permission from the authors of the original image, be free of copyright conflicts or have a Creative Commons license (for further information, please refer to: https://co.creativecommons.org/). Maps, aerial photographs and satellite images should include a graphic scale.

c. Citations

The citation format of *Boletín Geológico* is APA style (Seventh Edition). In the text, citations must include the author's name and date of publication, and all references must be listed in the references section.

When several works by the same author are cited, they must be organized in chronological order and will be shown separated by a comma: (Groat, 2014).

When a reference has two authors, the surnames of both authors must be cited and separated by the conjunction "&": (Pokrovski and Dubessy, 2014) or Pokrovski and Dubessy (2014).

When the reference has three or more authors, only the first author must be cited, followed by the abbreviation "et al.": (Feneyrol et al., 2013) or Feneyrol et al. (2013).

In the case of a corporate author, the name of the organization must be written the first time with the acronym in parentheses, followed by the year; subsequently, only the acronym will be mentioned (Servicio Geológico Colombiano (SGC), 2017).

When citing several references, they must be chronologically sorted and separated by semicolons: (Mantilla et al., 2013; Van der Lelij et al., 2016; Rodríguez et al., 2017). When a specific page of a reference is cited, the page number must be included after the year and be preceded by the abbreviation p., or pp. in the case of several pages: (Groat, 2014, p. 48).

d. Quotes

When the quote is shorter than forty words, it must be written within the paragraph, in quotation marks and without italics. The reference must be included at the end of the quote (Groat, 2014, p. 48).

When the quote is longer than forty words, it must be written in a separate paragraph, with a 2.5-cm left indent, without quotation marks or italics and with a font size one point smaller than the body text. The reference must be included at the end of the quotation (Groat, 2014, p. 48).

e. References

According to the APA format, only the first letter (initial) of the first names of the authors is provided. In the case where two surnames are included, they must not be separated by a hyphen. References must be written in single-space format and with a 1-cm hanging indent (in a hanging indent, the first line of the paragraph is not indented, and all subsequent lines are indented, in this case, 1 cm). If the documents have a Digital Object Identifier (DOI), this identifier must be included at the end of the reference.

Books

Only the first letter (initial) of the first word and of proper names, if any, in the titles of books are capitalized. The titles should be italicized, and the subtitle separated from the title by a colon, not by a period. In Spanish, the first letter of a word following a colon is written in uppercase font; in English, this letter is capitalized.

The information provided must strictly match that included in the following examples and follow the same rules of punctuation between each element of the reference:

Lee, M. S. (2012). *Mass Spectrometry Handbook* (Vol. 1). Wiley.

Bormann, P. (2013). *New Manual of Seismological Observatory Practice 2 (NMSOP-2)*. Deutsches GeoForschungsZentrum. https://doi.org/10.2312/GFZ.NMSOP-2_DS_3.1

Book chapters

Book chapters follow the same rules as those of book titles, except for one difference: the titles of book chapters must not be italicized. The title of the book must be italicized and preceded by the preposition "In".

The information provided must strictly match that included in the following examples and follow the same rules of punctuation between each element of the reference:

Horstwood, M. (2008). Data reduction strategies, uncertainty assessment and resolution of LA–(MC–) ICP–MS isotope data. In P. Sylvester (Ed.), *Laser ablation–ICP–MS in the Earth Sciences: Current practices and outstanding issues*. Mineralogical Association of Canada.

Reimann, C., Birke, M., Demetriades, A., Filzmoser, P., & O'Connor, P. (2014). The gemas project - concept and background. In C. Reimann, A. Demetriades, M. Birke, & I. Schoeters (Eds.). *Chemistry of Europe's Agricultural Soils, Part A*. Bundesanstalt fur Geowissenschaften und Rohstoffe.

Journal articles

Titles of journal articles follow the same rules as those of titles of book chapters, except for one difference: the first letters of all meaningful words (first word, names, verbs and adjectives) of titles of journal articles must be written in uppercase font and italicized, but they must not be preceded by the preposition "In".

The information provided must strictly match that included in the following examples and follow the same rules of punctuation between each element of the reference:

Domeier, M., & Torsvik, T. (2014). Plate tectonics in the late Paleozoic. *Geoscience Frontiers*, *5*(3), 303-350. https://dx.doi.org/10.1016/j.gsf.2014.01.002

Konstantinou, K. (2015). Tornillos modeled as self-oscillations of fluid filling a cavity: application to the 1992-1993 activity at Galeras volcano, Colombia. *Physics of the Earth and Planetary Interiors, 238*, 23-33. https://dx.doi.org/10.1016/j.pepi.2014.10.014

Thesis works

Saylor, J. (2008). *The Late Miocene Through Modern Evolution of the Zhada Basin, South-Western Tibet* (Ph. D. Thesis). The University of Arizona, Tucson.

Conferences, seminars and others

The titles of talks given in these contexts are written without italics, and only the first letter of the first word and proper nouns, if included, are capitalized. All meaningful words in event names are capitalized.

The information provided must strictly match that included in the following example and follow the same rules of punctuation between each element of the reference:

Sulochana, V., Francis, A., & Tickle, A. (2015). Morphology based radon processed neural network for transmission line fault detection. 2015 International Conference on Advances in Computing, Communications and Informatics (ICACCI).

Maps

The information provided must strictly match that included in the following example and follow the same rules of punctuation between each element of the reference:

Bacchin, M., Miligan, P. R., Wynne, P., & Tracey, R. (2008). *Gravity anomaly map of the Australian region, 3rd edn, 1:5,000,000*. Geoscience Australia.

Web pages

EURAQUEM/CITAC. (2016). *Guide to quality in analytical chemistry an aid to accreditation*. Retrieved from www.eurachem.org

Suggested links

- Keywords in the Geosciences: https://www.americangeosciences.org/georef/georef-thesaurus-lists
- Creative Commons: https://co.creativecommons.org/

Complejo Ígneo El Cerro. Autor: Arrubla y Silva.

CONTENTS

bg

SERVICIO GEOLÓGICO COLOMBIANO

El futuro es de todos | Minenergía

ISSN 0120-1425 48

9 770120 142003

www.sgc.gov.co